

Vibrational Spectroscopy of the  
Active Site and Iron Sulfur Clusters  
of the Membrane Bound  
Hydrogenase from *Ralstonia*  
*Eutropha*

vorgelegt von

Diplom Physikerin

**Elisabeth Siebert**

aus Zehdenick

der Fakultät II - Mathematik und Naturwissenschaften  
der Technischen Universität Berlin  
zur Erlangung des akademischen Grades  
Doktor der Naturwissenschaften  
- Dr. rer. nat. -

genehmigte Dissertation

Promotionsausschuss:

Vorsitzender:

Prof. Dr. R. Süßmuth

Berichter/Gutachter:

Prof. Dr. P. Hildebrandt

Berichter/Gutachter:

Prof. Dr. H. Dobbek

Berichter/Gutachter:

Dr. I. Zebger

Tag der wissenschaftlichen Aussprache:

04. September 2015

Berlin 2015



# Abstract

The need for an environmentally friendly, highly efficient energy source has brought hydrogenases into the center of attention in enzyme research. Hydrogenases catalyze the reversible cleavage of molecular hydrogen into two protons and two electrons and could therefore become a key component of future biological fuel cells. In this thesis, the oxygen-tolerant, membrane bound [NiFe] hydrogenase (MBH) from *Ralstonia eutropha* is investigated by means of Infrared (IR) and Resonance Raman (RR) spectroscopy. This enzyme is of particular technological interest, because it preserves catalytic activity even under ambient oxygen concentrations.

With IR spectroscopy, redox transitions of the [NiFe] active site were studied as a function of externally adjusted potentials. Thus, it was possible to make the interconversion of the active site redox states within the catalytic cycle visible. The results demonstrate that the reoxidation process is only reversible if the MBH is still attached to its natural electron acceptor cytochrome *b* in membrane fragments, as it is in its natural environment. The entire reoxidation process was successfully modeled with a set of coupled mono-exponential functions, confirming that the underlying processes are one-electron transitions. The solubilized MBH is not capable of reacting in a fully reversible fashion with hydrogen and oxygen, since the formation of the irreversible inactive species is also possible during the reoxidation process once the natural electron acceptor is lost. Comparative studies revealed that major fractions of such MBH samples can be reactivated in the presence of redox mediators and sufficiently high overpotentials. Additionally, IR component spectra involving the CO and CN stretching modes were determined for all catalytically active and inactive redox species of the [NiFe] active site.

With the present work RR spectroscopy is established as a powerful method complementary to IR and EPR (Electron Paramagnetic Resonance) spectroscopy to investigate the various cofactors of the MBH, i.e. the [NiFe] active site and the FeS clusters. A consistent assignment of the respective vibrational modes in the region from 300 to 700  $\text{cm}^{-1}$  was achieved by wavelength- and angle-dependent RR studies, statistical analyses on experimental RR spectra as well as isotopic labeling and quantum chemical calculations by Y. Rippers.

The detected vibrational modes of the active site were assigned to Fe-CO / CN modes of the redox states  $\text{Ni}_a\text{-S}$  and  $\text{Ni}_a\text{-L}$ . These two active species are formed via light-induced processes in the RR experiment. Due to this photo-induced reactivation of the active site the 'potential window of activity' for  $\text{H}_2$ -oxidation in a fuel cell might be broadened and thus the performance of the biofuel cell increased.

The most intense FeS stretching modes of all three FeS clusters were discriminated with angle-dependent RR spectroscopy and RR spectra from samples of MBH variants with genetically engineered FeS clusters. This also yields the first vibrational spectroscopic description of the superoxidized proximal cluster.

This proximal [4Fe3S] cluster is unique in oxygen-tolerant membrane bound hydrogenases and is thought to play a key role for protecting the active site from oxidative damage. RR spectroscopy revealed that the native configuration of the superoxidized cluster has a bound hydroxyl group at one Fe ion. This hydroxyl group is rebound in high amounts within the reoxidation process of the MBH. RR spectra of isotopically labeled MBH samples demonstrated that the hydroxyl ligand at the superoxidized proximal cluster is preferentially formed from molecular oxygen, which is reduced in a four-electron three-proton process. Solvent water molecules in the vicinity of the proximal cluster are an alternative source for the ligand, but this binding process is much slower. These mechanistic and structural insights even exceed the information derived from crystallographic data.

The advanced understanding of the experimental RR spectra of the MBH from *Ralstonia eutropha* will be the basis for future investigations of the wildtype enzyme and specific genetically engineered MBH variants with modifications at the [NiFe] active site or the FeS clusters. Further aspects of the catalytic cycle may be elucidated with systematically varied experimental conditions as well.

# Zusammenfassung

Die Suche nach einer umweltfreundlichen und effizienten Energiequelle hat die Hydrogenasen in den Mittelpunkt der Enzymforschung gebracht. Diese Enzyme könnten eine zentrale Komponente in zukünftigen Bio-Brennstoffzellen werden, da sie die reversible Oxidation von molekularem Wasserstoff in Protonen und Elektronen katalysieren. In dieser Arbeit wurde die sauerstofftolerante, membrangebundene [NiFe] Hydrogenase (MBH) von *Ralstonia eutropha* mittels Infrarot (IR) und Resonanz Raman (RR) Spektroskopie untersucht. Dieses Enzym ist für die technologische Anwendung von besonderem Interesse, da es seine katalytische Aktivität auch unter atmosphärischen Sauerstoffkonzentrationen beibehält.

Mit der IR Spektroskopie wurden die Redox-Übergänge des aktiven [NiFe] Zentrums als Funktion von externen Potentialen untersucht. Damit war es möglich die Umwandlung der verschiedenen Redox-Zustände des aktiven Zentrums innerhalb des katalytischen Zyklus sichtbar zu machen. Diese Untersuchungen zeigten, dass der Reoxidationsprozess nur dann vollständig reversibel ist, solange die MBH mit ihrem natürlichen Elektronen-Akzeptor Cytochrom *b* in den Fragmenten der Zellmembran verbunden ist. Der gesamte Reoxidationsprozess wurde erfolgreich mit gekoppelten mono-exponentiellen Gleichungen modelliert, was bestätigt, dass die zugrunde liegenden Prozesse Ein-Elektronen Übergänge sind. Der gelösten MBH, ohne natürlichen Elektronen-Akzeptor, ist es nicht möglich komplett reversibel mit Wasserstoff und Sauerstoff zu reagieren, da es teilweise zur Bildung einer irreversibel inaktiven Spezies während des Reoxidationsprozesses kommt. Vergleichende Untersuchungen unter anaeroben Bedingungen an solchen MBH Proben ergaben jedoch, dass ein überwiegender Teil dieser Spezies aktiviert werden kann, wenn ein hinreichend hohes Überpotential angelegt wird und Redox-Mediatoren zugegen sind. Weiterhin wurden die IR-Komponentenspektren, mit den entsprechenden CO und CN Streckschwingungen aller aktiven und inaktiven Redox-Zustände des aktiven [NiFe] Zentrums bestimmt.

Mit der vorliegenden Arbeit wurde die RR Spektroskopie, neben der IR und EPR (Electron Paramagnetic Resonance) Spektroskopie, als weitere leistungsfähige Methode etabliert um die verschiedenen Kofaktoren der MBH, das heißt die FeS Cluster und das aktive [NiFe] Zentrum, zu erforschen. Eine konsistente Zuordnung der entsprechenden Schwingungsmoden im Bereich von 300 bis 700  $\text{cm}^{-1}$  wurde durch wellenlängen- und winkelabhängige RR Studien, statistische Analysen der experimentellen RR Spektren, Isotopenmarkierung sowie durch quantenchemische Berechnungen (Y. Rippers) erreicht. Die detektierten Schwingungsmoden des aktiven Zentrums wurden als Fe-CO / CN Moden

des Ni<sub>a</sub>-S und Ni<sub>a</sub>-L Redox-Zustands identifiziert. Diese beiden aktiven Zustände werden durch einen lichtinduzierten Prozess im RR Experiment geformt. Mit dieser lichtinduzierten Reaktivierung des aktiven Zentrums könnte der Potentialbereich für die H<sub>2</sub>-Oxidation in einer zukünftigen Bio-Brennstoffzelle erweitert werden, was wiederum die Leistungsfähigkeit der Brennstoffzelle erhöhen würde.

Die intensivsten Schwingungsmoden aller drei FeS Cluster wurden mittels winkelabhängiger RR Spektroskopie sowie RR Spektren von MBH Varianten mit modifizierten FeS Clustern unterschieden. Somit konnte auch das Schwingungsspektrum des superoxidierten proximalen FeS Clusters extrahiert werden. Dieser [4Fe3S] Cluster ist einzigartig in den sauerstofftoleranten membrangebundenen Hydrogenasen und ihm wird eine zentrale Rolle für den Schutz des aktiven Zentrums vor oxidativer Schädigung zugeschrieben. Die RR Spektroskopie zeigte, dass in der natürlichen Konfiguration des superoxidierten Clusters ein Hydroxyligand an ein Fe Ion koordiniert ist und dieser Ligand während des Reoxidationsprozesses zu einem hohen Anteil erneut gebunden wird. Die RR Spektren von isotoopenmarkierten MBH Proben zeigten weiterhin, dass der Hydroxyligand bevorzugt aus molekularem Sauerstoff, der in einem Vier-Elektronen Drei-Protonen Prozess reduziert wurde, geformt wird. Wassermoleküle der Lösung in der Nähe des proximalen Clusters stellen eine alternative Quelle für diesen Liganden dar, aber der entsprechende Prozess ist wesentlich langsamer. Diese mechanistischen und strukturellen Einblicke gehen über die unmittelbar aus der Kristallstruktur zugänglichen Informationen hinaus.

Das erweiterte Verständnis der experimentellen RR Spektren der MBH von *Ralstonia eutropha* stellt die Basis für zukünftige Untersuchungen des MBH Wildtyps und seiner Varianten, mit Modifikationen an den FeS Clustern sowie des aktiven [NiFe] Zentrums, dar.

# Publications

## Parts of this thesis have been published before in the following articles in scientific journals:

E. SIEBERT, M. HORCH, Y. RIPPERS, J. FRITSCH, S. FRIELINGSDORF, O. LENZ, F. VELAZQUEZ ESCOBAR, F. SIEBERT, L. PAASCHE, U. KUHLMANN, F. LENDZIAN, M.A. MROGINSKI, I. ZEBGER AND P. HILDEBRANDT: “Resonance Raman spectroscopy as a novel tool to monitor the active site of hydrogenases: new insights into structure and reactivity”, *Angewandte Chemie, Int. Ed.* 52, 5162–65 **2013**

S. FRIELINGSDORF, J. FRITSCH, A. SCHMIDT, M. HAMMER, J. LÖWENSTEIN, E. SIEBERT, V. PELMENSCHIKOV, T. JAENICKE, J. KALMS, Y. RIPPERS, F. LENDZIAN, I. ZEBGER, C. TEUTLOFF, M. KAUPP, R. BITTL, P. HILDEBRANDT, B. FRIEDRICH, O. LENZ AND P. SCHEERER: “Redox-dependent structural and chemical transformation of the [4Fe3S] cluster in O<sub>2</sub>-tolerant [NiFe] hydrogenase”, *Nature Chemical Biology* 10, 378–385 **2014**

E. SIEBERT, Y. RIPPERS, S. FRIELINGSDORF, J. FRITSCH, A. SCHMIDT, J. KALMS, S. KATZ, O. LENZ, P. SCHEERER, L. PAASCHE, V. PELMENSCHIKOV, U. KUHLMANN, M.A. MROGINSKI, I. ZEBGER, P. HILDEBRANDT: “Resonance Raman Spectroscopic Analysis of the [NiFe] Active Site and the Proximal [4Fe-3S] Cluster of an O<sub>2</sub>-tolerant Membrane-bound Hydrogenase in the Crystalline State”, *The Journal of Physical Chemistry* published online, 23. July **2015**

## Additional publications that are not part of this thesis

J. FRITSCH, S. LÖSCHER, O. SANGANAS, E. SIEBERT, I. ZEBGER, M. STEIN, M. LUDWIG, A. DELACEY, H. DAU, B. FRIEDRICH, O. LENZ AND M. HAUMANN: “[NiFe] and [FeS] cofactors in the membrane-bound hydrogenase of *Ralstonia eutropha* investigated by X-ray absorption spectroscopy: insights into O<sub>2</sub>-tolerant H<sub>2</sub> cleavage”, *Biochemistry* 50(26), 5858–69 **2011**

I. BÜRSTEL, P. HUMMEL, E. SIEBERT, N. WISITRUANGSAKUL, I. ZEBGER, B. FRIEDRICH AND O. LENZ: “Probing the origin of the metabolic precursor of the CO ligand in the catalytic center of [NiFe] hydrogenase”, *Journal of Biological Chemistry*

286(50), 44937–44 **2011**

I. BÜRSTEL, E. SIEBERT, G. WINTER, P. HUMMEL, I. ZEBGER, B. FRIEDRICH AND O. LENZ: “A universal scaffold for synthesis of the  $\text{Fe}(\text{CN})_2(\text{CO})$  moiety of [NiFe]-hydrogenase”, *Journal of Biological Chemistry* 287(46), 38845–53 **2012**

J. FRITSCH, E. SIEBERT, J. PRIEBE, I. ZEBGER, F. LENDZIAN, C. TEUTLOFF, B. FRIEDRICH AND O. LENZ: “Rubredoxin-related Maturation Factor Guarantees Metal Cofactor Integrity during Aerobic Biosynthesis of Membrane-bound [NiFe] Hydrogenase”, *Journal of Biological Chemistry* 289(11), 7982–93 **2014**

T. WARMING, E. SIEBERT, A. SCHLIWA, E. STOCK, R. ZIMMERMANN AND D. BIMBERG: “Hole-Hole and Electron-Hole Exchange Interactions in Single InAs/GaAs Quantum Dots”, *Physical Review B* 79, 125316 **2009**

E. SIEBERT, T. WARMING, A. SCHLIWA, E. STOCK, M. WINKELNKEMPER, S. RODT AND D. BIMBERG: “Spectroscopic Access to Single Hole Energies in InAs/GaAs Quantum Dots”, *Physical Review B* 79, 205321 **2009**

# Contents

<b>Abstract</b>	<b>I</b>
<b>Zusammenfassung</b>	<b>III</b>
<b>Publications</b>	<b>V</b>
<b>1. Motivation and Overview</b>	<b>1</b>
<b>2. Current State of Hydrogenase Research</b>	<b>5</b>
2.1. The Crystal Structure of [NiFe] Hydrogenases . . . . .	7
2.2. Spectroscopic Characteristics of MBH-like [NiFe] Hydrogenases . . . . .	9
2.3. Catalytic Model for H <sub>2</sub> Conversion in the Presence of Oxygen . . . . .	17
<b>3. Vibrational Spectroscopy and Experimental Details</b>	<b>23</b>
3.1. Infrared Absorption Spectroscopy . . . . .	24
3.2. Instrumentation for Infrared Spectroscopy . . . . .	25
3.2.1. Infrared Transmission Spectroscopy . . . . .	26
3.2.2. Attenuated Total Reflection Spectroscopy . . . . .	27
3.3. Raman Scattering . . . . .	30
3.4. Resonance Raman Scattering . . . . .	34
3.5. Instrumentation for Raman Spectroscopy . . . . .	38
<b>4. Redox Transitions of the Active Site Monitored by FTIR</b>	<b>41</b>
4.1. The Reoxidation Process Tracked in Time . . . . .	42
4.2. Electrochemical Cycling of the Active Site Redox States . . . . .	49
4.3. Conclusion . . . . .	57
<b>5. Vibrational Spectroscopy on the Activated MBH at Cryogenic Temperatures</b>	<b>59</b>
5.1. Infrared Spectra under the Influence of Light . . . . .	60
5.2. Resonance Raman Characterization of the Reduced Active Site . . . . .	64
5.2.1. UV-vis Spectra of the MBH . . . . .	64
5.2.2. RR Spectra Under Different Reducing Conditions . . . . .	66
5.2.3. RR Spectra of MBH Variants . . . . .	68
5.2.4. RR Spectra Isotopically Labeled Samples . . . . .	69
5.2.5. RR Spectra at Different Excitation Wavelengths . . . . .	69

5.3. Calculated Raman Spectra . . . . .	71
5.4. Discussion . . . . .	74
<b>6. Vibrational Spectroscopy on Crystals of the As-isolated MBH</b>	<b>77</b>
6.1. Infrared Spectroscopy on Crystalline Samples . . . . .	79
6.2. Raman Active Modes of the Oxidized Active Site and the FeS Clusters .	80
6.2.1. Excitation Wavelength Dependent Resonance Raman Spectra . .	81
6.2.2. Component Analysis of Resonance Raman Spectra . . . . .	84
6.3. Comparison to Theoretical Raman Spectra . . . . .	92
6.4. Effect of Photo-Reduction in Fe(CN) <sub>6</sub> Treated Crystals . . . . .	97
6.5. Discussion and Summary . . . . .	98
<b>7. Resonance Raman Characterization of FeS Stretching Modes</b>	<b>103</b>
7.1. Preliminary Considerations . . . . .	104
7.2. Comparison of Crystalline and Solubilized MBH Samples . . . . .	105
7.3. Angular Dependence of Resonance Raman Spectra . . . . .	108
7.4. Attack of the Cluster Mutants . . . . .	114
7.5. Extraction of FeS Component Spectra . . . . .	117
7.6. Polarization Dependent Resonance Raman Spectra . . . . .	122
7.7. Conclusion . . . . .	126
<b>8. On the Origin of the OH<sup>-</sup> Ligand at the Proximal FeS Cluster</b>	<b>129</b>
8.1. Isotopic Labeling Experiments at Various Redox States . . . . .	130
8.1.1. Role of the His229 and Long Term Effects at 80 K . . . . .	134
8.2. Conclusion . . . . .	137
<b>9. Summary and Outlook</b>	<b>139</b>
<b>A. Protein Purification, Crystallization and Preparation</b>	<b>149</b>
<b>B. Appendix to Chapter 4</b>	<b>151</b>
<b>C. Appendix to Chapter 5</b>	<b>157</b>
<b>D. Appendix to Chapter 6</b>	<b>163</b>
<b>E. Appendix to Chapter 7</b>	<b>173</b>
<b>Acknowledgement</b>	<b>177</b>
<b>Bibliography</b>	<b>178</b>





# 1. Motivation and Overview

Proteins are, besides water, the most abundant molecules in all biological systems.[1] They consist of one or more peptide chains and have diverse functions within organisms. Proteins that act as catalysts for biochemical reactions are referred to as enzymes. Many reactions in nature, that are mediated by enzymes, occur at mild conditions and are characterized by high specificities and turnover rates. Similar reactions are often hardly accessible in synthetic chemistry and need harsh reaction conditions or noble-metal catalysts. Conversely, enzymes have a long and successful history as bio-catalysts for chemical reactions in the production of chemicals, in the pharmaceutical industry as well as in food production.[2, 3, 4, 5]

In view of the need for an environmentally-friendly energy source hydrogen has been proposed as an alternative to fossil fuels.[6, 7, 8, 9] In commercial fuel cells, which are still expensive and need platinum catalysts, hydrogen is converted to electric power. In this respect, one class of enzymes, the hydrogenases, has become the center of attention. Hydrogenases catalyze the reversible cleavage of molecular hydrogen into two protons and two electrons at high turnover rates, similar to platinum catalysts.[10, 11, 12, 13, 14, 15] Unfortunately, this reaction is inhibited in most hydrogenases in the presence of oxygen.[16] Only a few hydrogenases exhibit catalytic activities at ambient oxygen concentrations.[16, 17, 18, 19, 20] These oxygen-tolerant hydrogenases are of particular interest for biotechnological applications.

The Knallgas bacterium *Ralstonia eutropha* expresses four different oxygen-tolerant hydrogenases and they play a major role in the energy metabolism of this organism.[16, 21, 22, 23] The catalytic activity of hydrogenases depends on the presence of small non-proteic components, which are composed of small inorganic molecules or metal ions.[24] In the case of the hydrogenase, these cofactors, are the nickel-iron active site, where the hydrogen cleav-

age takes place, and three iron-sulfur clusters which transfer the electrons released during the catalytic cycle to an electron acceptor. In case of the membrane bound hydrogenase (MBH), the primary electron acceptor is the electron transfer protein cytochrome *b* within the cytoplasmic membrane. The hydrogenase activity and oxygen-tolerance is unchanged to some extent, if the MBH is isolated without this unit. This heterodimeric form of the MBH can be adsorbed on a graphite electrode, which then serves as an artificial electron acceptor.[25, 14] This is of particular interest for biotechnological applications in fuel cells. In fact, the catalytic activity of such a system is comparable to a platinum based catalyst.[25, 26] However, in living organisms, hydrogenases – like all other enzymes – are renewed to avoid a continuous accumulation of degraded enzymes and thus a decrease of catalytic performance. This cannot be implemented in technological applications. Therefore, the ultimate goal in hydrogenase research is a bio-mimetic catalyst.[27, 28] For the synthesis of such compounds a detailed study of the cofactor structure within the hydrogenase enzyme is a major concern. Also the role of the cofactors during the catalysis in the presence of oxygen has to be addressed.

A large variety of experimental techniques has helped to understand different aspects of these issues.[12, 13, 29, 30, 31, 32] Electron Paramagnetic Resonance and Infrared spectroscopy are well established techniques for probing the different states of the catalytic cycle.[12, 13] However, both methods have inherent limitations. With Electron Paramagnetic Resonance spectroscopy the electronic structures of the iron-sulfur clusters and the nickel-iron active site have been studied through the investigation of their paramagnetic states.[12, 33] But iron-sulfur clusters, as well as the active site iron ion with a total spin of zero, are inaccessible with this technique. Infrared spectroscopy is suitable for the detection of structural characteristics of the hydrogenase's nickel-iron active site. This vibrational spectroscopic method has been used to specify all diamagnetic and paramagnetic redox states of the nickel-iron active site in the catalytic cycle.[34, 13, 35, 36, 33] In this work it is used to monitor the interconversion of the redox states within the inactivation pathway of the catalytic cycle. (Chapter 4) Here, the stretching vibrations of the diatomic ligands at the active site iron ion are detected. The electron density distribution in this cofactor changes as a function of the redox potential. These alterations are traced with Infrared spectroscopy.

Resonance Raman spectroscopy is a powerful complementary vi-

brational spectroscopic method. It offers the possibility to selectively probe vibrational modes of the iron-sulfur clusters upon excitation in resonance with their electronic transition. Additionally, vibrational modes that involve metal ions, such as the iron ion of the active site, can be probed.[37] Thus, structural and electronic properties of the active site can be probed *in addition* to the iron-sulfur clusters.

Previous Raman studies were limited to hydrogenase model complexes of the active site.[38, 39, 40, 41] In the present work Resonance Raman spectroscopy is established as a research method for natural hydrogenase enzymes. To achieve this, different methods for the consistent analysis of highly complex biological systems, such as the MBH from *Ralstonia eutropha*, are developed. (Chapter 5, 6 and 7) The individual contributions of the four cofactors of the MBH to the Resonance Raman spectrum are separated in this work. Accordingly, structural and mechanistic insights are gathered by Resonance Raman spectroscopy. They include the direct photo-conversion of catalytically active and *inactive* redox states of the active site to two different activated redox states. (Chapter 5 and 6) Furthermore, a coordination of a hydroxide ligand at the iron-sulfur cluster proximal to the active site is verified with Resonance Raman spectroscopy. (Chapter 6 and 8) The structure of this proximal cluster differs from conventional clusters in oxygen-sensitive hydrogenases.[42, 43, 44, 45, 46, 47] As it is unique in oxygen-tolerant hydrogenases, it is considered to be important for the oxygen-tolerance of the entire enzyme.[43] With Resonance Raman spectroscopy the vibrational spectrum is resolved for this recently identified unusual proximal iron-sulfur cluster. (Chapter 7) These results complement findings from Infrared and Electron Paramagnetic Resonance spectroscopy as well as crystallographic investigations.

The advanced understanding of Resonance Raman spectra of the MBH from *Ralstonia eutropha* is the basis for future studies of this enzyme on questions regarding the structure-function relationship of the cofactors for the catalytic cycle in the presence of oxygen. (Chapter 8)

Finally, the methods developed in this work can be applied for the consistent analysis of other complex (biological) systems with a number of chemically different components.



## 2. Current State of Hydrogenase Research

Hydrogenases are metallo-enzymes that catalyze the oxidation of molecular hydrogen into two protons and electrons or the reverse reaction, the generation of molecular hydrogen [48]:



Hydrogenases are widespread in nature and can be found in bacteria, archaea and eukarya, where they mainly provide energy for the organism by oxidation of  $H_2$  or balance the redox potential of the cell through the generation or splitting of  $H_2$ . [49, 50, 51, 52, 53] The  $H_2$ -cycling is carried out at the active site of the enzyme, which is either a protein bound [Fe], [FeFe] or [NiFe] metal complex. The molecular nature of the active site determines the classification of the hydrogenases. [49, 50, 54, 55] [Fe] hydrogenases activate  $H_2$  only in the presence of a second substrate (methenyltetrahydromethanopterin) and are highly light-sensitive. [56, 57] [FeFe] and [NiFe] hydrogenases are the most common hydrogenases in nature. [58, 59, 60] [FeFe] hydrogenases are primarily involved in  $H_2$ -generation at high turnover frequencies (up to 20 000 hydrogen molecules per second) [14], but are irreversibly inactivated during catalysis by trace amounts of oxygen. [13, 42, 61] This property excludes an application under aerobic conditions.

The class of [NiFe] hydrogenases is often more active in  $H_2$ -oxidation to two protons and electrons. Turnover rates are as high as 10 000 hydrogen molecules per second, which is on the order of platinum based catalysts. [14, 26] Most [NiFe] hydrogenases are less sensitive to oxygen than their [FeFe] counterparts and are reversibly inactivated upon exposure to oxygen. [62]

The class of [NiFe] hydrogenases that is capable of a residual  $H_2$ -oxidation in the presence of oxygen, is called oxygen-tolerant. [14] In this respect hydrogenases, which maintain  $H_2$ -oxidation even at high oxygen-concentrations at the same turnover rates as un-

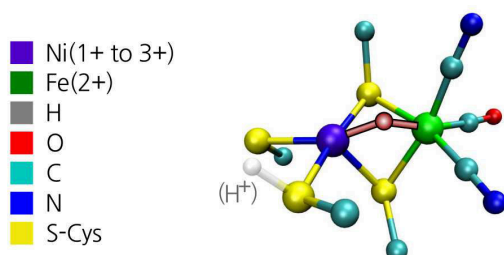
der anaerobic conditions, have to be considered to be oxygen-insensitive.[32] Nevertheless, both enzyme types are of major interest for biotechnological applications. This has triggered intense research efforts in the last decades towards the understanding of the structure, catalytic mechanism and the structure-function relationship with respect to the operation of the hydrogenase enzyme.

The entity of all [NiFe] hydrogenases is classified into five groups depending on their physiological function, location in the cell and their structure[49, 50]: The first group is bound to the cell membrane. Hydrogenases of three further groups are found in the cytoplasm, and include the energy converting, NAD(P)<sup>+</sup> reducing and H<sub>2</sub>-oxidizing / sensory hydrogenases. A fifth group has been defined recently.[63] Hydrogenases of this group have a high affinity towards H<sub>2</sub>-oxidation and they are capable to maintain activity even at H<sub>2</sub> concentrations as low as 0.5 ppmv.<sup>A</sup>[64]

<sup>A</sup>0.5 ppmv means 5 parts in 10 000 000 volume parts that is 0.00005 %. This corresponds to H<sub>2</sub> concentrations in the troposphere.

The group of the membrane bound hydrogenases (MBH) is the most studied form. The overall structure of this group of hydrogenases is divided into a large and small subunit and a cytochrome as an electron acceptor in the cytoplasmic membrane. The [NiFe] active site, where the molecular hydrogen is cycled, resides in the large subunit. The generated electrons are transferred via three FeS clusters in the small subunit to an electron acceptor. Here, the primary electron acceptors, which are in many cases cytochromes containing *c*- or *b*-type hemes, feed the electrons from the oxidation of H<sub>2</sub> to the respiratory chain of the cell.[52] The entity of the above characteristics defines the term 'standard' or oxygen-sensitive [NiFe] hydrogenases. The organisms *Desulfovibrio gigas*, *Desulfovibrio fructosovorans*, *Allochromatium vinosum* and *Desulfovibrio vulgaris* Miyazaki F are examples that comprise hydrogenases of this type.[31]

From other organisms oxygen-tolerant membrane bound hydrogenases have been isolated and characterized. The most studied ones are the hydrogenases from the aerobic thermophile *Aquifex aeolicus* (Hase I) [65], the bacterium *Escherichia coli* (Hyd-1)[66], the Knallgas bacteria *Ralstonia metallidurans* (MBH) and *Ralstonia eutropha* (MBH). [67, 68] In the following two Sections (2.1 and 2.2) the focus will lie on the structure and spectroscopic characteristics of the MBH from different organisms. Aspects that differ between oxygen-sensitive and -tolerant hydrogenases will be discussed. The MBH from *Ralstonia eutropha*, which is also investigated in the present work, will serve as a model system for the oxygen-tolerant case. In Section 2.3 the catalytic cycle of MBHs in



the presence of oxygen will be discussed.

## 2.1. The Crystal Structure of [NiFe] Hydrogenases

In 1996 Fontecilla-Camps *et al.* were the first to solve the crystal structure of the oxygen-sensitive standard hydrogenase *Desulfovibrio gigas* [69]. In a recent review from Lubitz *et al.* the crystal structures for further oxygen-sensitive hydrogenases that have been solved since then are summarized.[31]

The active site is buried deep in the protein matrix and thus gas and water channels for the substrates ( $H_2$ ), inhibitors ( $O_2$ , CO) and products ( $H_2O$ ,  $e^-$ ,  $H^+$ ) are needed that extend from the [NiFe] center to the protein surface. Potential gas channels that connect the active site with the substrate are discussed to be formed of hydrophobic cavities.[71] A water pathway has been discussed by Frielingsdorf *et al.*[47]

The sulfurs of four cysteine residues from the protein backbone bind the [NiFe] active site. These residues may act as an intermediate binding site for the protons derived from  $H_2$ -cycling.[31] Moreover, they can influence the spin and charge density of the nickel ion and thus alter the electronic properties of the entire active site. Two of these cysteine residues bridge the nickel ion with the low-spin iron ion in oxidation state 2+.[72, 73] The Fe ion is coordinated by three further inorganic ligands, one CO and two  $CN^-$ . [58] (Figure 2.1) A sixth ligand bridges the Fe ion with the Ni ion. This ligand varies depending on the redox state of the entire [NiFe] active site in the catalytic cycle. Notably, there is no conformational change of the entire protein matrix during the catalytic cycle.

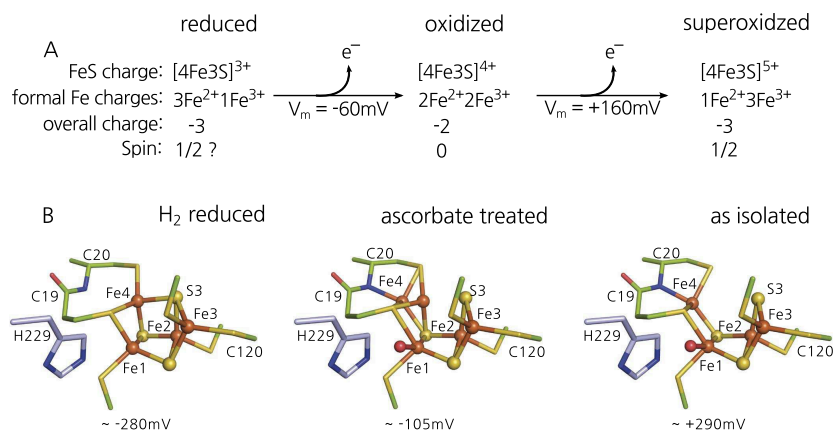
In oxygen-sensitive standard hydrogenases the electron transfer chain in the small subunit is composed of a [4Fe4S] cluster coordinated by four cysteines in the position proximal to the active site, a medial [3Fe4S] cluster coordinated by three cysteines and

**Figure 2.1.:** Ball-and-stick model of the [NiFe] active site. The Ni and Fe ions are bridged by two cysteinyl thiolates (yellow). The Fe ion, which remains in oxidation state 2+ for all redox states, is additionally coordinated by one CO and two  $CN^-$  ligands. Two further cysteine thiolates are bound to the Ni ion. One of these terminal cysteine residues is protonated in specific redox states ( $Ni_a-L$  and  $Ni_a-SR$ ). (See Reference [70] and Section 5.3) The redox state of the active site is largely defined by the oxidation state of the Ni ion (from 1+ to 3+) and the chemical nature of a third ligand (red/gray) in the bridging position between the two metal ions.

Figure, with slight modifications, generated by Y. Rippers.

**Figure 2.2.:** A) Core charge and total spin state of the proximal cluster in its three different redox states – reduced, oxidized and superoxidized. The approximate midpoint potentials for the two one-electron transitions are  $-60$  and  $160$  mV. B) Ball-and-stick model of the proximal FeS clusters generated from the crystal structure of the hydrogen reduced and as-isolated MBH from *Ralstonia eutropha*. [44, 47] The proximal cluster is coordinated by six cysteines and undergoes redox-dependent structural changes. These occur predominantly in the vicinity of Fe4 and Fe1. In the reduced form the sulfur of Cys19 substitutes the missing sulfide. With increasing potentials a conformational change is induced at this position. At a potential of  $\sim -105$  mV the Fe4 swaps its position between the sulfide of Cys19 and a peptide amide nitrogen. After a second redox transition, the cluster is stabilized in an asymmetric open form. Here, Fe4 is bound to the peptide amide nitrogen and an additional hydroxyl ( $\text{OH}^-$ ) ligand binds at Fe1.

Picture adapted from Reference [47].



distal  $[4\text{Fe}4\text{S}]$  cluster which is coordinated by three cysteines and one histidine residue. [74] The latter cluster transfers the electrons to the cytochrome. [50]

Crystal structures of the oxygen-tolerant membrane bound [NiFe] hydrogenases from *Ralstonia eutropha* [44, 47], *Hydrogenovibrio marinus* MBH [45] and *Escherichia coli* Hyd-1 [46] are available since 2011. The structure of the [NiFe] active site is very similar to that of oxygen-sensitive hydrogenases. [44, 45, 46, 75] But, all structures revealed an unprecedented  $[4\text{Fe}3\text{S}]$  cluster proximal to the active site. This cluster is coordinated by six cysteines, in contrast to four in oxygen-sensitive hydrogenases. [44, 45, 46] In the hydrogen-reduced form the  $[4\text{Fe}3\text{S}]$  cluster adopts a cubane-like structure. With increasing redox potential this cluster undergoes structural rearrangements. (Figure 2.2) At midpoint potentials of approximately  $-60$  mV, a conformational change is induced at the position of Fe4. The Fe4 swaps its position between the sulfur of the Cys19 residue and a peptide amide nitrogen. The  $[4\text{Fe}3\text{S}]$  cluster is stabilized in an asymmetric and open form and Fe4 is bound to the amide nitrogen after the second redox transition at a midpoint potential of  $160$  mV. In this superoxidized form an additional hydroxyl ligand ( $\text{OH}^-$ ) occurs at Fe1. (See Reference [47] and Section 6.2 and 7.1 of the present work) This ligand is hydrogen bonded to a histidine residue. Only a few of such redox dependent structural rearrangements have been reported so far. [44, 45] The six cysteine coordinated  $[8\text{Fe}7\text{S}]$  P cluster in the nitrogenase is accompanied by ligand exchanges at two Fe ions upon oxidation. [76, 77] In addition, this cluster is also capable of two consecutive one-electron reaction. [78]

## 2.2. Spectroscopic Characteristics of MBH-like [NiFe] Hydrogenases

Structural differences between oxygen-sensitive and -tolerant hydrogenases from various organisms have been elucidated on the basis of their respective crystal structures. With spectroscopic [13, 12], electrochemical [14], theoretical [15] and biochemical [43, 79] investigations valuable information on the redox properties of the hydrogenases as well as the reactions with their substrates and inhibitors are gathered. The combination of all information yields a comprehensive understanding of the hydrogenase's structure-function relationship, with respect to their redox states, catalytic cycle and the origin of the oxygen-tolerance.

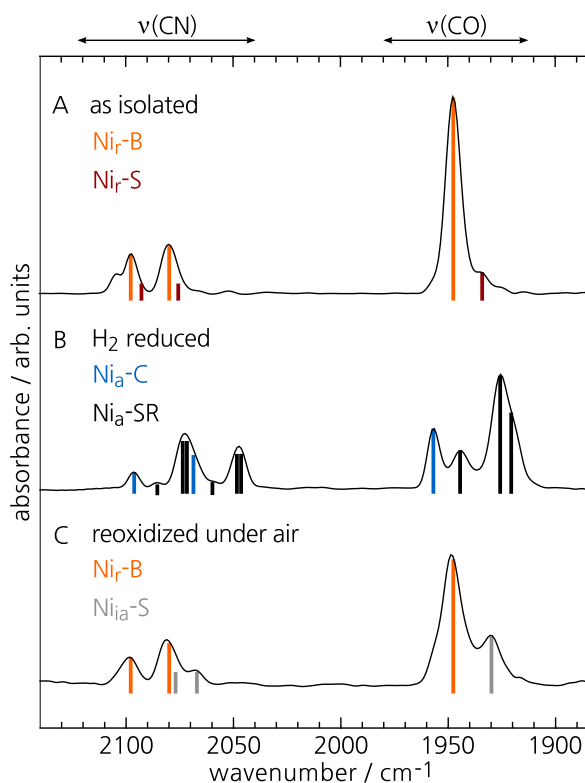
### The [NiFe] Active Site: Redox States within the Catalytic Cycle

Various catalytically active and inactive redox states of the [NiFe] active site can be probed with FTIR and EPR spectroscopy.[13, 80] With both techniques most [NiFe] redox states of oxygen-sensitive and -tolerant hydrogenases have been identified. EPR spectroscopy is limited to the paramagnetic Ni states ( $\text{Ni}^{1+}$  or  $\text{Ni}^{3+}$ ) of the active site and cannot access information on the Fe ion ( $\text{Fe}^{2+}$ ,  $S = 0$ ) at all.

FTIR spectroscopy is a suitable method for a detailed study of the active site structure for all possible redox states.[13, 81, 34, 82, 83, 29, 84, 85] This technique probes the intra-ligand stretching modes of the CO and the two  $\text{CN}^-$  ligands bound to the Fe ion.[60, 58, 84] The frequencies of these three modes lie in a spectral region between 1870 and 2120  $\text{cm}^{-1}$ , free of interfering modes from the protein backbone and water. A frequency shift of the CO and CN stretching modes correlates characteristically with the redox state of the enzyme. These modes are sensitive to the electron density at the Fe ion, which is altered in accordance to the nature of the bridging ligand and the oxidation state of the nickel ion.

The diversity of the [NiFe] redox states is exemplary shown in typical infrared absorbance spectra in Figure 2.3. Here, the MBH from *Ralstonia eutropha* is chosen as an example, but spectra with the same characteristics have been measured for other MBHs from other organisms. The spectra are obtained from three different MBH samples: The as-isolated,  $\text{H}_2$  reduced and reoxidized with air form. The interconversion – as-isolated (oxidized)  $\rightarrow$   $\text{H}_2$  reduced

**Figure 2.3.:** Infrared absorbance spectra of a heterodimeric MBH sample from *Ralstonia eutropha* at a pH of 5.5, as studied in this work. Depending on the treatment of the sample with oxygen and hydrogen, different mixtures of redox states at the active site are populated. A) The Ni<sub>r</sub>-B redox state is the major detected species in aerobically isolated sample. B) Incubation of the sample with 100 % H<sub>2</sub> yields mixtures of the activated Ni<sub>a</sub>-C and Ni<sub>a</sub>-SR species. C) A reoxidation of the reduced samples with air results in the formation of Ni<sub>r</sub>-B, as the major redox species. Depending on the preparation up to 30 % of the irreversibly inactive species Ni<sub>ia</sub>-S are formed as well.



→ reoxidized – is accompanied by a change of the redox potential within the sample. The population of the various redox states correlates directly with the redox potential and their related midpoint potentials have been determined in spectro-electrochemical titration experiments.[81, 34] The CO and CN stretching modes of each redox state are indicated by three vertical bars of the same color. (See also Reference [33])

Depending on their role in the catalytic cycle, the various redox states of the active site are divided into inactive ready (oxidized) and activated (reduced) states. Only the latter form catalyzes H<sub>2</sub>-oxidation.[86] A redox scheme for several hydrogenases has been developed and is presented in Figure 2.4 [13, 12, 83, 85, 29]

*Inactive states:* Purified heterodimeric MBH samples, where the membrane has been removed, exhibit some portion of an irreversibly inactive species Ni<sub>ia</sub>-S, which is EPR silent. The total amount of this species strongly depends on the purification conditions and can be as high as 80 %.[87, 33] Interestingly, the absence of the cytochrome unit does influence the hydrogenase activity, oxygen sensitivity and spectroscopic properties.[88, 85, 89] For typical MBH samples, as used in the present work, Ni<sub>r</sub>-B is, with relative portions of up to 90 %, the major redox state in the as-isolated form of the enzyme.[33] In this redox state the nickel ion is in oxidation state 3+ and a hydroxyl ligand bridges the

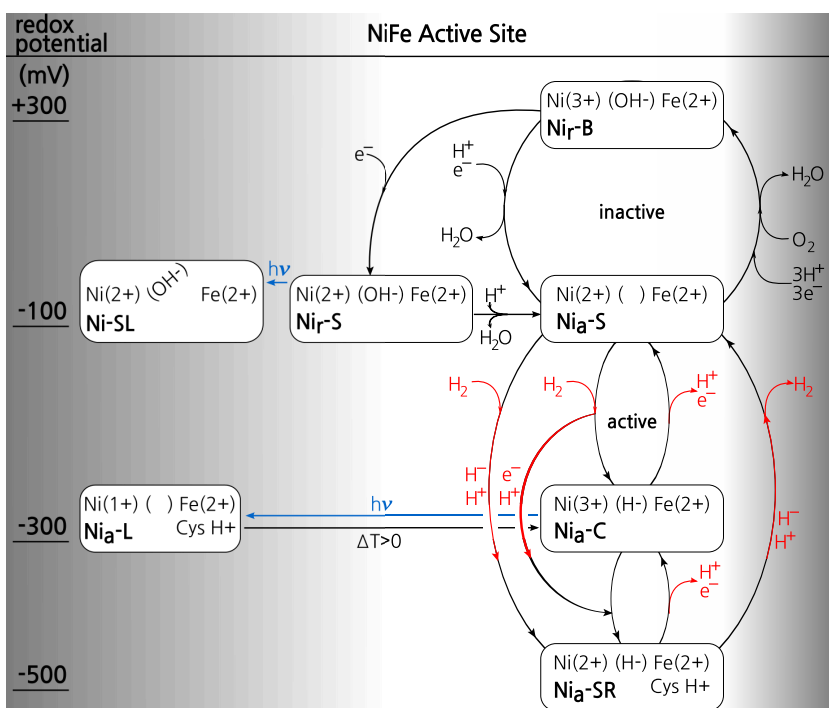


**Figure 2.4.:** Redox states of the active site in the catalytic cycle of an oxygen-tolerant MBH. Oxidation states of the Ni and Fe ion are given in parenthesis, as well as the nature of the bridging ligand. On the left hand side the approximate redox potentials for each species are shown vs. standard hydrogen electrode.

In the presence of  $\text{H}_2$  the inactive species  $\text{Ni}_r\text{-B}$  and  $\text{Ni}_r\text{-S}$  are activated and reduced to the  $\text{Ni}_a\text{-S}$  redox state. A formal one-electron reduction and proton transfer of this state yields the  $\text{Ni}_a\text{-C}$  species with a bridging  $\text{H}^-$ . This state is in redox equilibrium with the fully reduced species  $\text{Ni}_a\text{-SR}$ .  $\text{Ni}_a\text{-C}$  photoconverts to the  $\text{Ni}_a\text{-L}$  species after illumination at temperatures below 120 K. The activated species of the  $[\text{NiFe}]$  active site splits  $\text{H}_2$  into protons ( $\text{H}^+$ ) and electrons ( $\text{e}^-$ ). (red arrows)

In the presence of  $\text{O}_2$  the  $\text{Ni}_r\text{-B}$  species is formed with an  $\text{OH}^-$  in the bridge. This process requires three protons and four electrons and releases one water molecule.

Photo-conversion of  $\text{Ni}_a\text{-C}$  and  $\text{Ni}_r\text{-S}$  at temperatures below 120 K are marked with blue arrows. Scheme adapted with modifications from References [31].

nickel and iron ions.[90, 91, 92] In accordance to other oxygen-tolerant hydrogenases, the MBH does not exhibit the  $\text{Ni}_u\text{-A}$  redox state.[85, 33, 93] This paramagnetic ( $\text{Ni}^{3+}$ ) redox state is only observed in oxygen-sensitive hydrogenases.[87, 33] For the  $\text{Ni}_u\text{-A}$  a hydroperoxide was proposed as the bridging ligand, but has not yet been unambiguously identified.[90, 91, 94]

The  $\text{Ni}_r\text{-B}$  redox state is activated in a  $\text{H}_2$  atmosphere within less than a minute into the active  $\text{Ni}_a\text{-S}$  redox state, whereas it takes about an hour to activate  $\text{Ni}_u\text{-A}$ .[95, 96, 14]<sup>B</sup> Both redox states may pass through the intermediate state  $\text{Ni}_r\text{-S}$  before the catalytic cycle is entered. This redox state is observed in oxygen-tolerant hydrogenases only with amounts on the order of ten percent, due to the fast activation of  $\text{Ni}_r\text{-B}$  to the active redox state  $\text{Ni}_a\text{-S}$ . (See Figure 2.3A)

When a proton and an electron enter the active site, the  $\text{Ni}_r\text{-S}$  is formed upon one-electron reduction of  $\text{Ni}_r\text{-B}$  (and  $\text{Ni}_u\text{-A}$ ) whereby the oxidation state of the nickel ion changes to 2+. This redox state may exist in two isoelectronic forms, one with a hydroxyl in the bridge and one with a water molecule loosely bound to the active site.[97, 21] However, no reliable structural information exists to date to prove this. The  $\text{Ni}_r\text{-S}$  is further activated to  $\text{Ni}_a\text{-S}$ , whenever the bridging oxygenic species reacts with a proton and leaves the active site as a water molecule. The entire reaction is nominally identical to the reaction of  $\text{Ni}_r\text{-B}$  with one proton and electron. (See Figure 2.6)

<sup>B</sup>The subscripts r and u in  $\text{Ni}_r\text{-B}$  and  $\text{Ni}_u\text{-A}$  refer to active-ready and -unready, respectively.

*Activated states:* The Ni<sub>a</sub>-S is considered as the first active state of the catalytic cycle. Its nickel ion is in oxidation state 2<sup>+</sup> and the bridge is empty.[98] Upon further incubation with H<sub>2</sub> the bridging position is rapidly occupied by a hydride (H<sup>-</sup>) and the oxidation state of the nickel ion becomes 3+.[99, 100, 101] This is the Ni<sub>a</sub>-C redox state – the key species in the process of catalytic H<sub>2</sub> splitting. Upon further reduction of the potential the fully reduced species Ni<sub>a</sub>-SR is populated by a formal addition of a proton and electron. The electron changes the oxidation state of the nickel ion to 2+.[102, 100] The Ni<sub>a</sub>-SR species carries the products of the heterolytic H<sub>2</sub> splitting: The proton is attached to the terminal cysteine [97, 103, 104] and the hydride (H<sup>-</sup>) remains in the bridging position.[80, 96, 105, 106, 104] Under catalytic turnover conditions the Ni<sub>a</sub>-SR is supposedly the only state in equilibrium with the Ni<sub>a</sub>-C. This redox state can exist in up to three isoelectronic forms Ni<sub>a</sub>-SR, Ni<sub>a</sub>-SR' and Ni<sub>a</sub>-SR'', as indicated by three different CO stretching bands in Figure 2.3B. The three forms of the Ni<sub>a</sub>-SR possibly differ in their protonation and spin state or their interaction with the protein environment.[80, 13, 12]

Specific redox states of the [NiFe] active site are highly light-sensitive at temperatures below 120 K and their photo-conversion is reversible in the dark at temperatures above ~ 200 K.[107]

*Light-induced states:* The Ni<sub>a</sub>-C redox state is highly light-sensitive and converts to the paramagnetic Ni<sub>a</sub>-L redox state. This photo-conversion was first identified by EPR spectroscopy in the hydrogenase from *Allochromatium vinosum* [107] and later in oxygen-tolerant and -sensitive hydrogenases from other organisms [108, 109, 99, 110, 103]. Under the influence of light the bridging hydride of Ni<sub>a</sub>-C is liberated as a proton and the nickel ion of the resulting Ni<sub>a</sub>-L redox state is left in a formal oxidation state 1+ and a spin of S = 1/2.[108, 102, 100, 99] The released proton binds to a terminal cysteine of the active site. (See Reference [111, 103] and Section 5.1 of the work on hand) As a result of the depleted bridging site the electron density at the iron ion increases and the infrared active CO and CN stretching modes of the Ni<sub>a</sub>-L are red-shifted with respect to the bands of the Ni<sub>a</sub>-C species.[112, 113] The entire process is reversible in the dark and temperatures above 200 K. Depending on the organism of the investigated hydrogenase two further Ni<sub>a</sub>-L redox states, with different protonation states of the active site, have been identified.[99, 109, 108] Pandelia *et al.* showed for hydrogenase I from *Aquifex aeolicus* that the Ni<sub>a</sub>-L1 and Ni<sub>a</sub>-L3 species form at temperatures below 100 K even in the

absence of light.[110]

It is worth to note that the bridging hydride of the Ni<sub>a</sub>-C redox state is bound weaker in oxygen-tolerant than in oxygen-sensitive hydrogenases. Therefore, the Ni<sub>a</sub>-C redox state shows an increased sensitivity towards light in comparison to oxygen-sensitive hydrogenases.[110]

The Ni<sub>r</sub>-S redox state, which is rarely observed in oxygen-tolerant hydrogenases, was shown to be light-sensitive in the oxygen-sensitive hydrogenase from *Desulfovibrio vulgaris* Miyazaki F.[114, 83, 82] The active site changes its binding configuration upon illumination, whereby the coordination structure of the iron ion is perturbed significantly, while the nickel ion experiences only small changes. The bond between the Fe ion and the bridging ligand is believed to be broken, while that to the Ni ion supposedly remains intact.[115, 114] The population of this Ni-SL state increases with illumination time and is wavelength-dependent, with local maxima at 490 and 600 nm.[114] These maxima are associated with electronic transitions in the nickel center of the active site. Osuka *et al.* showed for the same organism, that 15% of the initial Ni<sub>u</sub>-A undergoes a photo-conversion under the same conditions.[115] With a photo-conversion of 4% of Ni<sub>r</sub>-B, this redox state of the oxygen-sensitive hydrogenase of *Desulfovibrio vulgaris* Miyazaki F is slightly light-sensitive too.[114, 83]

In contrast to that, a photo-conversion of Ni<sub>r</sub>-B at high potentials was observed in electrochemical experiments on the oxygen-tolerant hydrogenase from *Aquifex aeolicus*. [116] Ciaccafava *et al.* propose that a loss of the bridging hydroxyl ligand is promoted by the illumination and the photo-induced Ni-SL state is formed.

## The FeS Clusters: Structural Insights and Redox Behavior

The current state of knowledge on the FeS clusters of oxygen-sensitive and -tolerant hydrogenases is mainly based on EPR spectroscopy.[117, 118, 119] This technique can detect only paramagnetic states of the individual FeS clusters and, likewise paramagnetic Ni states of the active site.<sup>C</sup> Thus, also the interaction between these cofactors can be studied to some extent.

For oxygen-sensitive standard hydrogenases in the as-isolated form the FeS clusters are in their highest oxidation states: The proximal and distal [4Fe4S] have an oxidation state of 2+ and thus both a total spin of S = 0. The medial [3Fe4S] cluster is in oxidation state

<sup>C</sup>paramagnetic states of the [NiFe] active site are: Ni<sub>u</sub>-A, Ni<sub>r</sub>-B, Ni<sub>a</sub>-C and Ni<sub>a</sub>-L

1+ with  $S = 1/2$ . [120, 121] In accordance to that, the medial cluster is detected as a narrow signal, together with weak signals from the Ni<sub>r</sub>-B species, in EPR spectra measured at temperatures below 80 K. [122] In H<sub>2</sub>-treated standard hydrogenases the medial cluster is reduced to a diamagnetic species [3Fe4S]<sup>0</sup>. Simultaneously the proximal (and distal) [4Fe4S] cluster is reduced to an oxidation state of 1+. This paramagnetic species can be detected with EPR spectroscopy. [33] The paramagnetic Ni<sub>a</sub>-C redox species of the active site can interact with the spatially nearby reduced proximal cluster through a spin coupling. Therefore, the EPR signal of an H<sub>2</sub>-reduced hydrogenase is split. [123, 107]

The proximal cluster of oxygen-tolerant hydrogenases is a six cysteine coordinated [4Fe3S] cluster, instead of a standard [4Fe4S] cubane with a four cysteine configuration. [44, 45, 46] In addition, it undergoes two one-electron redox transitions at physiological conditions accompanied by structural rearrangements (Figure 2.2). [47, 43, 124] In contrast, regular [4Fe4S] clusters are capable of single one-electron redox transitions only. [125]

Thus, the proximal [4Fe3S] cluster of the oxygen-tolerant hydrogenases constitutes an additional paramagnetic species ([4Fe3S]<sup>5+</sup>,  $S = 1/2$ ) in the as-isolated, oxidized form of the enzyme. [125, 33, 93] The spin of this species couples with the spin of the medial cluster and gives rise to characteristic split signals for both cofactors in the EPR spectra of the MBH from *Ralstonia eutropha* and related [NiFe] hydrogenases (Figure 2.5A). [68, 43, 124] The distal [4Fe4S] cluster remains with a spin of  $S = 0$  in the as-isolated enzyme EPR silent. [126] This cluster, as well as the medial [3Fe4S] cluster is structurally similar to the respective cluster in standard hydrogenases. [44, 45, 46]

Upon mild reduction with 50 mM excess sodium ascorbate, which coincides with a redox potential of approximately 70 mV, a well defined narrow signal of the medial [3Fe4S] cluster is found in the EPR spectrum of the wildtype MBH (Figure 2.5B). This indicates that the oxidation state of the proximal cluster is reduced such that it resides in an EPR silent diamagnetic state with [4Fe3S]<sup>4+</sup> and  $S = 0$ . A further reduction of the MBH with hydrogen again yields an EPR signal similar to that of standard hydrogenases, were a split signal of the paramagnetic Ni<sub>a</sub>-C redox state and the proximal [4Fe3S]<sup>3+</sup> (and distal) cluster is observed (Figure 2.5C). These EPR spectroscopic observations also point to a [4Fe3S] cluster that is capable to access three redox states with two one-electron transitions under physiological conditions. [43, 124]

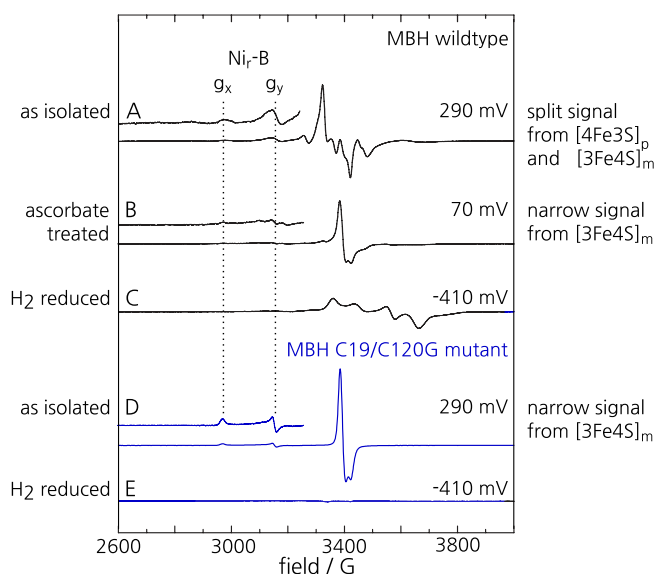


**Figure 2.5.:** EPR spectra of the MBH wildtype and MBH C120G/C19G variant measured at a temperature of 20 K. Traces A and D correspond to the as-isolated samples; traces C and E display the spectra of the hydrogen reduced samples. The sample of the wildtype MBH was mildly reduced with sodium ascorbate, which coincides with a redox potential of  $\sim 70$  mV. This spectrum shows essentially the narrow signal of the medial [3Fe4S] cluster in oxidation state 1+, which is likewise observed in the EPR spectrum of the as-isolated C120G/C19G mutant of the MBH. In contrast, the EPR spectrum of the as-isolated MBH wildtype exhibits as split signal from the medial [3Fe4S] and proximal [4Fe3S] cluster, as well as some contribution of the paramagnetic  $\text{Ni}_r\text{-B}$ .  $g_x$  and  $g_y$  signals of this [NiFe] redox state are indicated with dotted lines. All redox potentials are given with respect to standard hydrogen electrode.

Figure adapted from Reference [43].

To prove that it is the proximal cluster responsible for the split EPR signal and the additional redox transition, the two additional cysteine residues Cys19 and Cys120 were exchanged for glycine residues by site directed mutagenesis.[43] The resulting MBH variant C120G/C19G mimics the structure of an oxygen-sensitive [NiFe] hydrogenases, since the proximal standard cubane [4Fe4S] cluster is likewise coordinated with four cysteine residues. Additionally, this variant is oxygen-sensitive. It forms the  $\text{Ni}_u\text{-A}$  redox state and an oxidatively damaged EPR-silent Ni-S species upon long-term incubation with  $\text{H}_2/\text{O}_2$  mixtures.[43] Nevertheless, the cysteine exchange variants of *Ralstonia eutropha* MBH and *Escherichia coli* Hyd-1 sustained residual  $\text{H}_2$ -oxidation activity in the presence of short pulses of  $\text{O}_2$  for several minutes.[13, 14, 43, 127]

Also, the EPR spectra revealed that the additional paramagnetic species vanishes at high potentials, because essentially only the narrow signal of the medial [3Fe4S]<sup>1+</sup> is observed (Figure 2.5D). Incubation of this variant with hydrogen, again, results in the split signal from the paramagnetic  $\text{Ni}_a\text{-C}$  redox state and the proximal [4Fe4S] cluster (Figure 2.5E). Thus, the proximal [4Fe4S] cluster in the C120G/C19G variant possess two redox states with a single one-electron redox transition, similar to regular clusters in standard hydrogenases.

The two particular cysteine residues Cys19 and Cys120 in the coordination sphere of the proximal [4Fe3S] cluster seem to occur only in MBHs [43, 128] and are missing in the amino acid sequence of the oxygen-sensitive variants[43]. Thus, hydrogen reduction in the presence of oxygen is correlated with the existence

of these two additional residues Cys19 and Cys120, whereby the Cys19 residue seems to have the largest influence on the oxygen-tolerance.[127, 46, 30] This is in accordance to the central role of the Cys19 residue in the redox dependent structural rearrangements in the vicinity of the Fe4 ion.[46, 47] In contrast, the C120G variant of the MBH behaves more similar to the wildtype MBH in electrochemical investigations.[127] But, according to electrochemical experiments, none of the cysteine exchange variants behaved as sensitive towards O<sub>2</sub> as the standard hydrogenases under equivalent conditions.[43, 127, 32] Thus, this cluster seems to be not the only feature that contributes to the oxygen-tolerance.[32]

Further spectroscopic studies that probe the electronic and ligation structure of the proximal cluster are discussed in References [127, 124, 126, 129, 47] and the work on hand (Section 6.2, 7.2 and 8.1). These insights complement the structural data discussed above and prove that the unusual architecture of the proximal [4Fe3S] cluster facilitates two one-electron redox transitions at physiological relevant redox potentials. The two redox transitions between the as-isolated and hydrogen reduced form are accomplished through structural rearrangements in the vicinity of the Fe4 ion of this cluster.[43, 124, 44, 45, 46, 30, 47] In Figure 2.2 the structure of the [4Fe3S] cluster in all three redox states is shown. The two electrons released through the oxidation of the proximal cluster from [4Fe3S]<sup>3+</sup> to [4Fe3S]<sup>5+</sup> are crucial for the protection of the [NiFe] active site from oxidative damage. For this reason, the oxygen-tolerance of specific hydrogenases is partly ascribed to the proximal cluster.

Here, it is worth to note that the redox potentials of all three FeS clusters in the MBH from *Ralstonia eutropha* and its homologues from other organisms are considerably higher than the ones in oxygen-sensitive standard hydrogenases.[120, 16, 68, 124] Based on EPR and Mössbauer spectroscopy the midpoint potentials have been determined.[32] For the proximal cluster the two one-electron transitions have midpoint potentials of -60 to 98 mV and 160 to 240 mV.[43] The midpoint potential of the [3Fe4S]<sup>0</sup> → [3Fe4S]<sup>1+</sup> transition in the medial cluster is in the range of 25 to 130 mV.[125, 124, 126] The redox transition of the distal cluster [4Fe4S]<sup>1+</sup> → [4Fe4S]<sup>2+</sup> lies between -180 and -65 mV.[124, 126]

### 2.3. Catalytic Model for H<sub>2</sub> Conversion in the Presence of Oxygen

For another hydrogenase from *Ralstonia eutropha* it was suggested that a limited access of oxygen to the active site causes the oxygen-tolerance, which is incompatible the fact that the rate of impinging oxygen is not the controlling factor.[130]<sup>D</sup> Genetic modifications of hydrophobic gas channels connecting the solvent with the active site, led to a restricted diffusion of O<sub>2</sub> to the active site. But these enzyme variants do not sustain H<sub>2</sub>-oxidation activity under ambient O<sub>2</sub> partial pressures.[22, 131]

<sup>D</sup>Here the regulatory hydrogenase (RH) is meant.

In addition, the oxygen-tolerance is not linked to modifications of the [NiFe] active site itself, since the crystal structures of oxygen-tolerant and -sensitive MBHs revealed almost identical coordination spheres at this cofactor.[44, 45, 46, 75]

These observations show that the oxygen-tolerance of the MBH is determined neither by a restricted access of oxygen to the active site nor a finite ability of the active site to react with oxygen. In fact, there is a crucial link between oxygen-tolerance and the FeS clusters, as will be discussed below. But first, the term oxygen-tolerance will be defined with electrochemical observation and their implications for the function of the hydrogenase enzyme.

#### Electrochemical Definition of Oxygen-Tolerance

As electrons are part of the catalytic cycle, Protein Film Electrochemistry (PFE) is an excellent method to study the catalytic behavior of the hydrogenases.[13] Based on this method Armstrong *et al.* studied the oxygen-sensitive hydrogenase from *Allochromatium vinosum* electrochemically.[25] In PFE the hydrogenase is immobilized on a graphite electrode which allows to vary the potential in a wide range. Thus, H<sub>2</sub>-oxidation and -generation is induced at high and low potentials, respectively. The current, derived from the direct electron transfer between the protein and the electrode, is proportional to the catalytic activity of the protein in the presence of a substrate. PFE thus also allows to investigate the inactivation characteristics of the hydrogenases, revealing that these enzymes can be inactivated under two conditions:

Under anaerobic conditions and high potentials oxygen-sensitive hydrogenases inactivate to a mixture of the Ni<sub>r</sub>-B and Ni<sub>u</sub>-A redox states. In contrast, oxygen-tolerant hydrogenases exclusively

form the  $Ni_r$ -B redox state.[132, 33, 85, 20] Once the potential is lowered  $Ni_r$ -B readily reactivates to the  $Ni_a$ -S and  $Ni_a$ -C redox state [133], whereby the reactivation rate is more than two orders of magnitude faster for the oxygen-tolerant hydrogenases.[85, 132] This reaction is characterized by the switch potential  $V_{switch}$ , which defines the potential where the maximal slope in catalytic current recovery is observed. The switch potential of the MBH from *Ralstonia eutropha* is +130 mV and thus approximately 200 mV higher than that of standard hydrogenases.[11] The highly positive  $V_{switch}$  of the oxygen-tolerant hydrogenases allows to maintain  $H_2$ -oxidation in the presence of oxygen at physiologically accessible potentials.[132] Therefore, the MBH is catalytically active in a wide potential window. This behavior has been observed for other oxygen-tolerant hydrogenases from *Ralstonia metallidurans*, *Aquifex aeolicus* and *Escherichia coli*. [11, 23, 20]

Hydrogenases can be inactivated under a second condition: The presence of oxygen. In oxygen-sensitive hydrogenases,  $H_2$ -oxidation is rapidly inactivated by traces of oxygen at low potentials. The catalytic current is not recovered once oxygen is replaced with hydrogen. Only a further decrease of the potential can partially reactivate the enzyme.[134] This is in agreement with the spectroscopically observed formation of the slowly activating  $Ni_u$ -A along with portion of the  $Ni_r$ -B species.[26, 11] Oxygen-tolerant hydrogenases maintain, on the contrary, a decreased catalytic current in the presence of oxygen at low potentials.[135, 23] Here, only the inactive ready species  $Ni_r$ -B is formed and no  $Ni_u$ -A species. The current is almost fully recovered once the oxygen leaves the electrochemical cell, which is in accordance to the exclusive formation of the rapidly reactivating species  $Ni_r$ -B.[11, 23]

Interestingly, the onset potential for  $H_2$ -oxidation is circa 100 mV higher for oxygen-tolerant than oxygen-sensitive hydrogenases.[11, 85, 20] Similarly, the cysteine exchange variants of *Ralstonia eutropha* MBH and *Escherichia coli* Hyd-1 show an unchanged overpotential for  $H_2$ -oxidation and regained activity at similar switch potentials after inactivation, as their wildtype counterparts. Thus, the onset potential for  $H_2$ -oxidation as well as the switch potential are independent of the proximal cluster.[43, 127]

## Catalytic Model

The entire catalytic cycle of a hydrogenase involves not only reactions of the substrate with the active site, but also binding of the

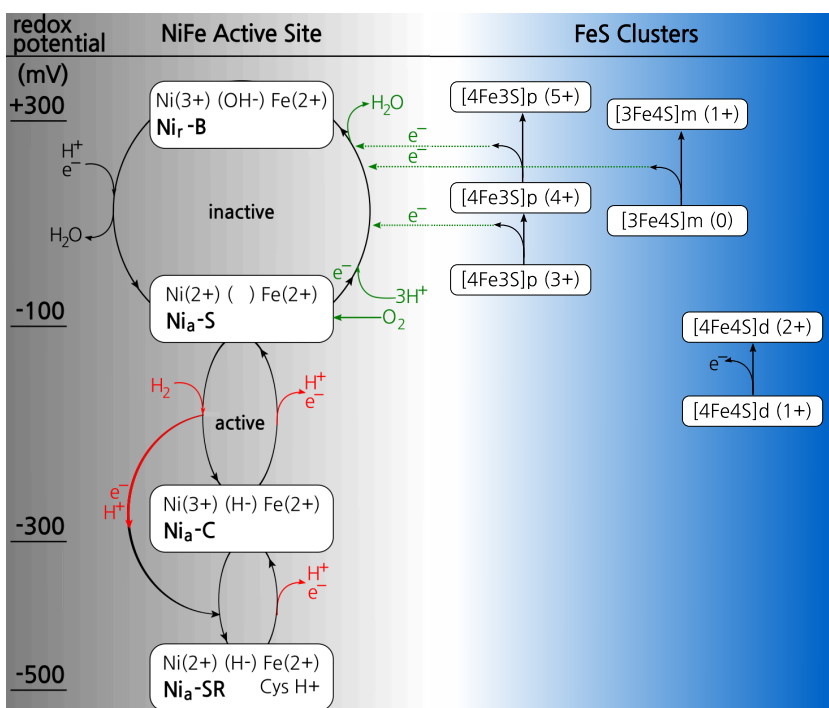


**Figure 2.6.:** Redox states of the [NiFe] active site and the three FeS clusters in the catalytic cycle of an oxygen-tolerant MBH. In the presence of  $H_2$  the inactive species  $Ni_r$ -B and  $Ni_r$ -S are activated and reduced to the  $Ni_a$ -S redox state. Formal one electron reduction of this state yields the  $Ni_a$ -C species with a bridging  $H^-$ . This state is in equilibrium with the fully reduced species  $Ni_a$ -SR. The activated species of the [NiFe] active site split  $H_2$  into protons ( $H^+$ ) and electrons ( $e^-$ ).

In the presence of  $O_2$  the  $Ni_r$ -B species is formed with an  $OH^-$  in the bridge. Four electrons and three protons are required for this reversible inactivation and detoxification of the  $O_2$ , which is accompanied with a formation of  $H_2O$ . Three electrons are provided from two redox transition of the proximal [4Fe3S] cluster and one redox transition of the medial [3Fe4S] cluster.[47] The fourth electron derives from the active site.

Red Cycle: Formal hydrogenase cycle. Green: Oxygenase function of the hydrogenase. Redox potential lowered from top to bottom of picture. Scheme adapted with modifications from References [30, 31].

substrate and release of the catalytic products, with a subsequent transfer of electrons and protons within the protein. Thus, the catalytic function relies on an inseparable interplay between the different redox active cofactors, i.e. the [NiFe] active site and the FeS clusters for the transfer of electrons.

The current catalytic model for oxygen-tolerant MBHs relies on a close alliance of the [NiFe] active site and the FeS clusters. This enables the enzyme to cope with the oxygen once it reaches the active site by forming the oxidized redox state  $Ni_r$ -B. The  $Ni_r$ -B can be rapidly reactivated and the enzyme re-enters the catalytic cycle for  $H_2$  oxidation. This cycle contains three redox states:  $Ni_a$ -S,  $Ni_a$ -C and  $Ni_a$ -SR.

The catalytic model for oxygen-tolerant hydrogenases is sketched in Figure 2.6.[43]

The natural target for molecular oxygen is the electron rich environment of the [NiFe] active site.[136] Oxygen-tolerant hydrogenases exclusively form the  $Ni_r$ -B redox state, which is easily reactivated to the active species  $Ni_a$ -S and  $Ni_a$ -C under mildly reducing conditions.[11, 132, 85, 20] The prerequisite for the exclusive formation of  $Ni_r$ -B is that  $O_2$  is reduced to water and a hydroxide in a four-electron – three-proton reaction.[43, 132, 68, 44, 46, 30] The water leaves the protein and the hydroxyl ligand stays in the bridging position between Ni and Fe ion to form the  $Ni_r$ -B redox state. This oxidase activity of the hydrogenase avoids the formation of reactive oxygen species that may damage or block the

active site, as in the case of  $Ni_u$ -A population in oxygen-sensitive hydrogenases.[132] For the soluble hydrogenase (SH) from *Ralstonia eutropha* this oxidase activity has been recently proven.[137] It is likely that the electrons are transferred one by one to the  $O_2$  at the active site. This electron transfer is possibly coupled to a transfer of protons. From a redox titration of Hyd1 from *Aquifex aeolicus*, which revealed one pH dependent redox transition of the proximal cluster,[124] a proton coupled electron transfer is anticipated for the MBH from *Ralstonia eutropha* as well.

The first electron for the oxidase process is derived from the  $[NiFe]$  active site in the  $Ni_a$ -S redox state. This raises the oxidation state of the nickel ion to 3+. The remaining three electrons originate from the FeS clusters, which are in their *reduced* states at the time of the  $O_2$  attack. Accordingly, the redox potentials of all three FeS clusters are higher than those of their counterparts in oxygen-sensitive hydrogenases.[87, 125, 43, 124, 126] Thus, the corresponding redox transitions lie in a potential range of the cytochrome *b*, which connects the MBH with the ubiquinone pool in the cytoplasmic membrane at +90 mV.[138] Consequently, the electrons can be transferred rapidly to the active site before the  $Ni_u$ -A species is formed.[43, 31]

The second and third electron result from the redox transitions of the proximal  $[4Fe3S]^{3+} \rightarrow [4Fe3S]^{4+}$  and the medial cluster  $[3Fe4S]^0 \rightarrow [3Fe4S]^{1+}$ . One of these electrons formally breaks the O–O bond. With the three additional protons a water molecule and hydroxyl radical (OH) is formed. The hydroxyl radical is highly reactive. It has been suggested that this is the step where oxygen-sensitive standard hydrogenases are trapped in the  $Ni_u$ -A redox state, since they have only access to two electrons from the FeS clusters.[43, 31] But oxygen-tolerant hydrogenases can acquire a fourth electron from the second redox transition  $[4Fe3S]^{4+} \rightarrow [4Fe3S]^{5+}$  of the proximal cluster to the superoxidized form at a high potential.[30, 29, 124, 43, 44, 45, 46] This electron reduces the hydroxyl radical to a hydroxide ion ( $OH^-$ ), which forms the bridging ligand of the  $Ni_r$ -B species. Once in the  $Ni_r$ -B state, an electron and proton are required to remove the hydroxyl ( $OH^-$ ) from the bridge in the form of a second water molecule. The active site 'recovers' to the activated redox species  $Ni_a$ -S and  $Ni_a$ -C. Here, the  $H_2$  is split into protons and electrons and the electrons are transferred through the FeS clusters to the cytochrome *b* at the cytoplasmic membrane.

Thus, the proximal cluster has in fact two functions: It transfers

the electrons during H<sub>2</sub> oxidation and stores two of the four electrons for the rapid reduction of O<sub>2</sub> to water and a hydroxide ion in the oxidase process. Accordingly, the redox potentials of the three FeS clusters have to be higher than their counterparts in oxygen-sensitive standard hydrogenases, as stated above.[43, 124, 126]

This catalytic model predicts a continuous formation of water in both, the oxidase and hydrogenase process. The crystal structures of *Ralstonia eutropha* [47] and *Hydrogenovibrio marinus* MBH [45] suggest that there is a network of hydrophilic cavities connecting the active site with the protein surface. A water pathway has been discussed by Frielingsdorf *et al.*[47]

The above statements lead to a conclusive definition of oxygen-tolerance:

Oxygen-tolerant hydrogenases are not inhibited or irreversibly damaged by oxygen, but are able to maintain H<sub>2</sub>-oxidation activity under aerobic conditions.[135, 11] In other words, only oxygen-tolerant hydrogenases are able to continuously remove oxygen from the active site and avoid the formation of the slowly recovering Ni<sub>u</sub>-A species. Therefore oxygen may be considered, along with hydrogen, as a second substrate of the hydrogenase. That is, oxygen has access to the active site where it is reduced.

The current catalytic model for H<sub>2</sub>-oxidation in the presence of oxygen predicts a continuous formation of water as a result of the immediate reduction of O<sub>2</sub> at the [NiFe] active site. Three of the required four electrons are provided by the modified proximal and medial FeS clusters.[132, 68, 43, 44, 45, 46, 139] Accordingly, hydrogenases are bifunctional enzymes with hydrogenase and oxidase activities.[30]

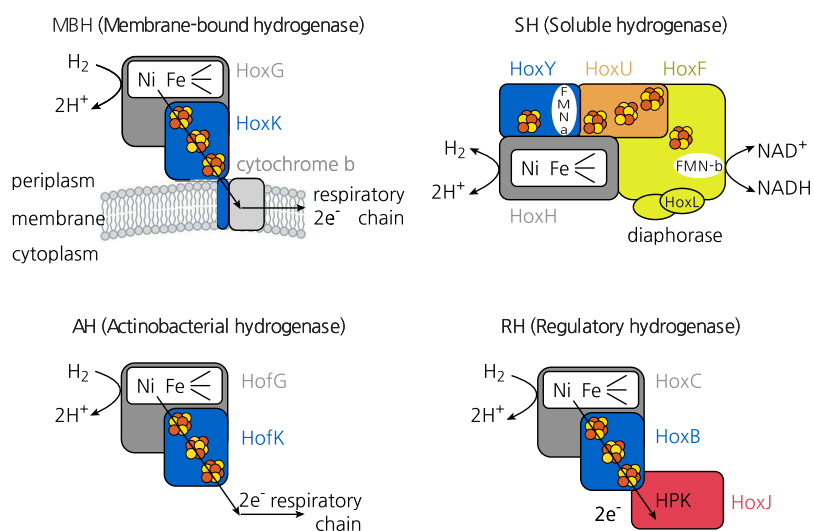
### Synopsis: Oxygen-Tolerance of *ReSH* and *ReRH*

The model organism *Ralstonia eutropha* hosts three further oxygen-tolerant hydrogenases (Figure 2.7).[16, 32]

The actinobacterial hydrogenase (AH) belongs to the recently established fifth group of [NiFe] hydrogenases.[140] These oxygen-insensitive hydrogenases have a high affinity towards H<sub>2</sub>-oxidation at atmospheric concentrations of molecular hydrogen.

The soluble hydrogenase (SH) is a six-subunit enzyme that couples H<sub>2</sub>-oxidation with the reduction of NAD(P)<sup>+</sup>. [141, 16] It belongs to group 3 of the [NiFe] hydrogenases and maintains decreased H<sub>2</sub>-oxidation and H<sup>+</sup>-reduction activities at atmospheric

**Figure 2.7.:** Scheme of the modular structure of the four [NiFe] hydrogenases from *Ralstonia eutropha*. The [NiFe] active site is located in the large subunit (gray), whereby the Fe ion is coordinated by one CO and two  $CN^-$  ligands. (See Figure 2.1 for a more detailed description.) The small subunit (blue) contains one or more FeS clusters. The proposed electron transfer pathways are indicated by straight arrows. Curved arrows indicate the splitting of  $H_2$  to protons and electrons at the active site. Figure adapted from Reference [32].



$O_2$  concentrations.[141, 137] In addition the SH shows oxidase (oxygen reduction) activity at the [NiFe] active site.[142, 143] The presence of a sulfenate species at the oxidized active site cysteines was detected as a split IR spectrum, only in oxygen-tolerant SH proteins.[21, 143] Therefore, the reversible sulfoxxygenation may play a role for the oxygen-tolerance of this particular enzyme.[143] The regulatory hydrogenase (RH) controls hydrogenase gene expression depending on the concentration of  $H_2$ . It is insensitive towards oxygen and belongs to group 2 of the [NiFe] hydrogenases. The  $H_2$ -oxidation activity of the RH is two orders of magnitude lower than that of the MBH.[144] The hydrophobic gas channel, that connects the active site with the protein surface, has been shown to be occupied with bulky amino acids in the RH homologous from *Ralstonia eutropha* and *Ralstonia capsulatus*. [22, 131] This triggered the hypothesis that a limited access of oxygen is caused by the small size of the gas channel. In fact, it was possible to construct amino acid exchange variants of organisms, that normally express oxygen-sensitive hydrogenases, with a narrowed gas channel. These hydrogenase variants showed similarities to oxygen-tolerant hydrogenases, but it has not been possible so far to convert a oxygen-sensitive to a oxygen-tolerant hydrogenase through the gas channel approach.[145, 146, 147, 32]

# 3. Vibrational Spectroscopy and Experimental Details

Various experimental techniques are available to determine the structure of molecules, such as x-ray diffraction[148], Electron Paramagnetic Resonance spectroscopy[149], Mass Spectroscopy[150] and vibrational spectroscopy[151]. The two major representatives of the latter technique are Infrared (IR) and Raman spectroscopy. Both techniques rely on the interaction of electromagnetic radiation with molecules, which results in transitions between different vibrational modes of the molecule. The structural information gathered with both techniques may be complementary, since the underlying mechanisms differ. In IR spectroscopy electromagnetic radiation in the infrared spectral region (from 10 to 12500 cm<sup>-1</sup>) is absorbed, whereby Raman spectroscopy relies on the inelastic scattering of the incident photons.

In the case of IR spectroscopy the system under study is irradiated with polychromatic light. Incident photons with an energy  $h\nu_k^{IR}$  matching the energy difference between an initial and final vibrational state of a specific mode  $k$  are absorbed:<sup>A</sup>

$$h\nu_k^{IR} = h\nu_k^f - h\nu_k^i. \quad (3.1)$$

The basis for Raman spectroscopy is inelastic scattering of photons with a discrete energy  $h\nu$  defined by the incident laser. The energy difference between the incident electromagnetic light  $h\nu$  and the inelastically scattered photons  $h\nu^R$  is, according to the law of energy conservation, equal to the energy difference of the initial and final vibrational states of the  $k^{th}$  normal mode

$$h\nu - h\nu_k^R = h\nu_k^f - h\nu_k^i \quad (3.2)$$

The final vibrational state may be energetically higher or lower than the initial vibrational state. In this respect Stokes- and Anti-

<sup>A</sup>The superscripts  $i$  and  $f$  refer to the initial and final vibrational state of the  $k^{th}$  normal mode.

Stokes-Raman Scattering are defined.

Both, IR and Raman spectroscopy provide information about the vibrational energy levels of the electronic ground state  $|e^g\rangle$ . This is derived directly from the measured intensities resulting from transitions between vibrational levels  $|v_k^i\rangle$  and  $|v_k^f\rangle$ . The measured intensity is proportional to the transition probability  $W_{if}$ :

$$I^{IR/R} \sim W_{if} \sim \left| \langle \Psi_f | \hat{\Omega} | \Psi_i \rangle \right|^2, \quad (3.3)$$

whereby  $\Psi_f$  and  $\Psi_i$  are the wavefunctions of the final and initial vibrational states. The operator  $\hat{\Omega}$  is different for the IR and Raman process and describes the perturbation of the studied system by the incident electromagnetic radiation.

In Section 3.1 and 3.3 equations for the expected IR and Raman intensity of a vibrational mode will be introduced. They directly imply that infrared active modes change the electronic dipole moment  $\mathbf{P}^e$ , while Raman active modes change the polarizability  $\alpha$  of the studied system.

### 3.1. Infrared Absorption Spectroscopy

Electromagnetic radiation in the mid-infrared region from 4000 to 400  $\text{cm}^{-1}$  (2.5 to 25  $\mu\text{m}$ ) lies energetically in the range of vibrational modes. An absorption of incident radiation with an energy of  $h\nu_k^{IR}$  results in the transition  $|v_k^i\rangle \rightarrow |v_k^f\rangle$  for all infrared active modes  $k$ . (See Equation 3.1) The perturbation of the studied system is described by the electronic dipole moment operator  $\hat{\Omega} = \hat{\mathbf{P}}^e$ , which reads as:

$$\mathbf{P}^e = \sum_j e_j \cdot \mathbf{q}_j \quad (3.4)$$

where  $e_j$  is the effective charge of the electron cloud at the  $j^{\text{th}}$  atom. The internal coordinate  $\mathbf{q}_j$  describes the distance of the nuclei to the center of gravity of the molecule in Cartesian coordinates  $x_j, y_j, z_j$ . The mass-weighted internal coordinates can be converted into the normal coordinates  $Q_k$  for each vibrational mode  $k$ . Then, the electronic dipole moment is expanded as a Taylor Series along  $Q_k$ :

$$\tilde{\mathbf{P}}^e \approx \mathbf{P}_0^e + \sum_k \left( \frac{\partial \mathbf{P}^e}{\partial Q_k} \right)_0 Q_k + \dots \quad (3.5)$$

Inserting this expression into Equation 3.3 yields:

$$I^{IR} \sim W_{if} \sim \left| \langle \Psi_f | \tilde{\mathbf{P}}^e | \Psi_i \rangle \right|^2 \approx \left| \mathbf{P}_0^e \langle \Psi_f | \Psi_i \rangle + \sum_k \left( \frac{\partial \mathbf{P}^e}{\partial Q_k} \right)_0 \langle \Psi_f | \hat{Q}_k | \Psi_i \rangle \right|^2 \quad (3.6)$$

The first integral is always zero as the wavefunction  $\Psi_i$  and  $\Psi_f$  are orthogonal by definition. The second term is non-zero and contributes to the absorbed infrared intensity  $I^{IR}$ , if  $\partial \mathbf{P}^e / \partial Q_k$  and the integral  $\langle \Psi_f | \hat{Q}_k | \Psi_i \rangle$  are non-zero. From the derivative it can be inferred that an interaction between the molecule and the electromagnetic radiation arises whenever a specific normal mode  $k$  changes the electronic dipole moment  $\mathbf{P}^e$  of the molecule. These modes are termed as infrared active. The integral  $\langle \Psi_f | \hat{Q}_k | \Psi_i \rangle$  is non-zero within the harmonic approximation when the vibrational quantum numbers  $i$  and  $f$  differ by  $\pm 1$ . The latter term also determines symmetry-based selection rules.

With Equation 3.6 the IR intensity of the  $k^{th}$  normal mode is proportional to:

$$I_k^{IR} \sim \left| \left( \frac{\partial \mathbf{P}^e}{\partial Q_k} \right)_0 \langle \Psi_f | \hat{Q}_k | \Psi_i \rangle \right|^2. \quad (3.7)$$

This quantity determines the portion of the absorbed incident light  $A$  in Lambert-Beer's law:

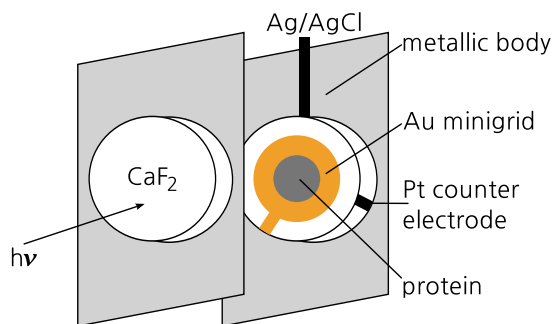
$$A(\nu_k) = -\log_{10} \frac{I_k^{IR}}{I_o} = \epsilon(\nu_k) \cdot c \cdot d \quad (3.8)$$

where  $I_o$  is the intensity of the light source. The sample is characterized by its concentration  $c$ , thickness  $d$  and extinction coefficient  $\epsilon(\nu_k)$ . The extinction coefficient describes how incident electromagnetic radiation of a given frequency  $\nu_k$  is absorbed by the investigated sample. Thus, scanning the frequency over a certain spectral range yields an infrared absorption spectrum  $A(\nu)$ .

### 3.2. Instrumentation for Infrared Spectroscopy

In this work IR spectra are measured with a Bruker Tensor 27 Fourier Transform Infrared (FTIR) spectrometer, which uses polychromatic radiation of an incandescent source and a photo-conductive liquid nitrogen cooled MCT-detector. The central part of this spectrometer is the Michelson interferometer[152] which allows to probe  $A(\nu)$  for all frequencies simultaneously through a

**Figure 3.1.:** Scheme, adapted from Reference [153], of the optically transparent thin layer transmission cell as used in this work. Potential control is achieved in a three electrode geometry, with a Ag/AgCl reference electrode, a less than  $10\ \mu\text{m}$  thick and 70% transparent gold working electrode as well as a platinum sheet counter electrode. To improve the electron transfer between the sample and the working electrode redox mediators are used.[125, 81]



Fourier transformation of the measured interferogram  $I(\delta)$  to  $I(\nu)$ . Whereby  $\delta$  is the optical path difference defined by movement of one mirror in the interferometer.

### 3.2.1. Infrared Transmission Spectroscopy

In infrared transmission spectroscopy the sample is placed into the optical path between the interferometer and detector. Typical transmission cells, as used in this work, consist of a metal body, where the sample is sandwiched between two  $\text{CaF}_2$  windows. The sample volume of  $10\ \mu\text{L}$  is defined by a thin polytetrafluoroethylene (PTFE) spacer of  $50\ \mu\text{m}$  and a sealing ring ensures adequate tightness of the construction. An aperture with a diameter of 4 mm controls the optical path. The temperature of the entire cell is typically adjusted to  $10\ ^\circ\text{C}$  for all measurements shown in this work. By convention the absorbance given by Equation 3.8 is plotted as a function of the wavenumber  $\bar{\nu}[\text{cm}^{-1}]$ . The FTIR spectra are acquired in the region between  $4000$  and  $1000\ \text{cm}^{-1}$  with a spectral resolution of  $2\ \text{cm}^{-1}$ , via 200 consecutive scans. Subsequently the spectra are evaluated with OPUS 5.5 and home-written GNU-octave scripts.

### Spectro-Electrochemistry

Optically transparent thin layer electrochemical cells (Figure 3.1) allow infrared spectroscopic studies in combination with electrochemical control of the potential at the investigated sample.[153] With this technique, referred to as IR Spectro-Electro-Chemistry (IR-SEC), systems with more than one redox state are probed as a function of an applied potential. Structural changes are monitored directly in the infrared spectrum as the relative absorbance  $A^i(V)$  for a specific redox state  $i$  depends on the applied potential  $V$ . [153, 34] Between the measured quantity  $A^i(V)$  and the Nernst

Equation<sup>B</sup>

$$V = V_m + \frac{RT}{zF} \frac{c_{ox}}{c_{red}} \quad (3.9)$$

the following relation is defined, where  $C$  is a constant offset:

$$A^i(V) = \frac{A_{max}^i}{1 + \exp\left(\frac{zF}{RT} \cdot (V - V_m)\right)} + C. \quad (3.10)$$

A fit of this equation to the data yields the midpoint potential  $V_m$  of the redox couple. Additionally, the number of transferred electrons  $z$  involved in a given redox transition can be determined. Similar to the transmission spectra, the IR-SEC spectra are acquired in the region between 4000 and 1000  $\text{cm}^{-1}$  with a spectral resolution of 4  $\text{cm}^{-1}$ . For one spectrum 400 scans are averaged.

Equilibration times of the system to changes of the external potential were twenty to thirty minutes. The open-circuit potential of the aerobically isolated MBH in this setup was determined to be between 15 and 33 mV (vs. Ag/AgCl).<sup>C</sup> In order to investigate the possibility of activating of the sample in the IR-SEC cell the potential was decreased to -700 mV in steps of 100 mV. Whether this activation process is reversible was tested by (re)oxidizing the samples with increasing potentials of up to 150 mV (vs. Ag/AgCl).

$${}^B R = 8.314 \text{ CV K}^{-1} \text{ mol}^{-1}$$

$$F = 9.449 \cdot 10^4 \text{ C mol}^{-1}$$

T: Temperature

z: number of transferred electrons

V: redox potential

$V_m$ : mid point potential

$c_{ox}/c_{red}$ : proportion of oxidized and reduced form of the species

<sup>C</sup>This is equivalent to values of 225 and 243 mV vs. the Standard Hydrogen Electrode (SHE)

### 3.2.2. Attenuated Total Reflection Spectroscopy

To obtain IR spectra from surfaces of liquid or solid samples attenuated total reflection (ATR) spectroscopy is employed. In this technique the absorbed IR radiation is determined by its penetration depth into the sample instead of the absolute sample thickness. For biological samples this is of great importance since they can be covered with an aqueous layer for a full hydration without increasing water absorption bands in the respective spectrum recorded from the sample surface. In this sense, ATR spectroscopy can be applied independent of the buffer composition or the gas phase over the sample during the measurement itself.[151]

The ATR technique[154, 155] is based on the effect of total internal reflection.<sup>D</sup> The incident infrared beam is directed through an optically thin medium with a refractive index  $n_L$  onto a crystal with a high refractive index  $n_H$  at a certain angle of incidence  $\theta$ . If  $\theta$  is larger than the critical angle

$$\theta_c = \arcsin\left(\frac{n_L}{n_H}\right), \quad (3.11)$$

<sup>D</sup>Total internal reflection only occurs when electromagnetic radiation propagates from an optically dense to a thin medium. If no angle  $\theta_L$  fulfills Snell's law, such that  $n_H/n_L \sin \theta \geq 1$ , light is reflected at the interface.

the light is internally reflected within the crystal. Behind the reflecting interface, in the optically thin medium, evanescent waves are formed. The amplitude  $E$  of their electric field decays exponentially with the distance  $x$  normal to the surface

$$E(x) = E_o \exp\left(-\frac{x}{d_p}\right) \quad (3.12)$$

Here,  $E_o$  is the amplitude at the interface and  $d_p$  the penetration depth, which is defined as:

$$d_p = \frac{\lambda}{2\pi \sqrt{n_H^2 \sin^2 \theta - n_L^2}}. \quad (3.13)$$

For electromagnetic radiation with  $\lambda = 5000 \text{ nm}$  ( $2000 \text{ cm}^{-1}$ ) and an incident angle of  $\theta = 45^\circ$  at the germanium-air interface, a penetration depth  $d_p$  of  $0.29 \mu\text{m}$  is calculated according to the above equation.<sup>E</sup> However, the penetration depths of the infrared radiation into typical samples in close contact with the ATR-crystal are between  $0.5$  and  $3.0 \mu\text{m}$  since  $n_L$  is typically larger than one. Moreover, a dispersion of the refractive index as well as the absorption of the electromagnetic radiation within the investigated sample has to be considered by defining the complex index of refraction  $\tilde{n}_L(\lambda) = n_L(\lambda) + i\kappa_L(\lambda)$ . Then the penetration depth  $d_p(\tilde{n}_L(\lambda))$  becomes a function of the wavelength. At wavelengths where the sample absorbs infrared energy  $h\nu_k^{IR}$  the dispersion  $\tilde{n}_L(\lambda)$  is anomalous. With the corresponding change of the penetration depth  $d_p$  the evanescent wave is attenuated and the reflectance of the infrared radiation at the interface is modified. The latter is detected as a function of wavelength (or wavenumber) and forms the IR spectrum of the investigated samples.

<sup>E</sup>With  $n_H = 4.10$  and  $n_L = 1.0$  for the germanium-air interface the critical angle is  $\theta_c = 14^\circ$ .

IR spectra of as-isolated MBH crystals were measured with a Bruker Tensor 27 FTIR spectrometer connected to a Hyperion 2000 infrared microscope. The microscope is equipped with a  $20 \times$  ATR objective optimized for a measurement area of  $100 \mu\text{m}$  in diameter. This setting is ideal for IR measurements on single MBH crystals. The exact position of the MBH crystal to the tip of the ATR Germanium crystal is aligned in the visible mode of the objective. In the measurement mode of the objective a proper contact between the ATR crystal tip and the sample is ensured by the observation of strong amide bands in the FTIR spectrum, as compared to the background of the surrounding atmosphere. An internal pressure sensor ensures an optimal contact between the ATR crystal and

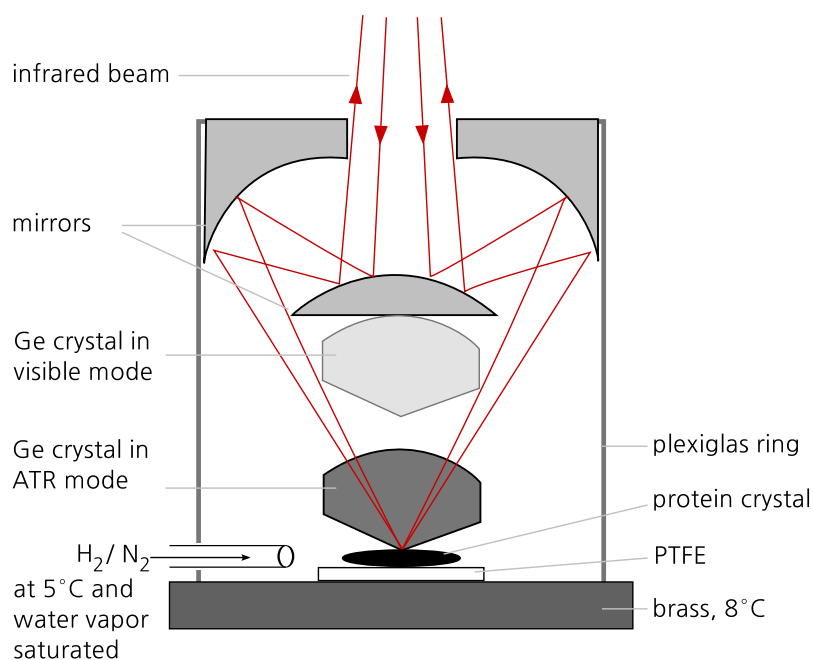


**Figure 3.2.:** Sketch of the ATR-crystal in contact with the sample. To ensure optimal storage conditions, the protein crystal is placed on a cooled brass plate with a PTFE spacer in between. Additionally, the small volume around the crystal is purged with water vapor saturated gaseous nitrogen, cooled to approximately 5 °C. For visible inspection of the crystal the ATR crystal is moved to the upper position. The Figure is adapted with some modifications from Reference [156].

the sample.

To avoid damages on the ATR tip, the sample itself is placed loosely on a 1 mm thick PTFE support. To ensure an optimal environment for the MBH crystals during the measurement, the PTFE support with the sample is placed on a Peltier cooled brass plate at 8 °C. Furthermore, a small volume between the brass plate and the objective housing is purged with gaseous nitrogen saturated with water vapor. (See Figure 3.2) To avoid condensation of the water vapor, the nitrogen itself was cooled to approximately 5 °C. The remaining parts of the microscope were purged with dry nitrogen. This setup allows FTIR measurements on one single MBH crystal for at least three days.

### 3.3. Raman Scattering

An extensive review of the Raman effect can be found in the book by D.A. Long [157], which is also the main source of this Section.

The Raman effect is a two photon process of inelastic light scattering by matter, whereby the energy of the scattered light is modified with respect to that of the incident electromagnetic field. (Equation 3.2) This effect was predicted theoretically in 1923 by A. Smekal and experimentally proven by C.V. Raman five years later.[158, 159] Classically, the Raman effect is described on the basis of first-order induced electronic dipole moments  $\mathbf{P}^{ind}$ ,

$$\mathbf{P}^{ind} = \boldsymbol{\alpha} \cdot \mathbf{E} \quad (3.14)$$

which are generated when the oscillating electric field vector  $\mathbf{E}(\omega)$  of the incident light interacts with the electron cloud of the scattering center. The electric field oscillates with the frequency  $\omega$  and the amplitude  $\mathbf{E}_o$ <sup>F</sup>

$$\mathbf{E}(\omega) = \mathbf{E}_o \cos \omega t. \quad (3.15)$$

The magnitude and direction of the induced electronic dipole moment vector depends on the polarizability  $\boldsymbol{\alpha}$  of the molecule.  $\boldsymbol{\alpha}$  is a tensor of second rank and is regarded as a measure of the ease with which electrons of the irradiated molecule can be displaced from their equilibrium positions to produce an electronic dipole moment  $\mathbf{P}^{ind}$ . This also depends on the position of the nuclei with respect to the electron cloud in the electric field  $\mathbf{E}(\omega)$  and is thus sensitive to vibrations of the molecule. The  $k^{th}$  normal mode at a frequency of  $\omega_k$  is described with the normal coordinate  $Q_k$  as a simple harmonic oscillation of the form

$$Q_k = Q_{k_o} \cos (\omega_k t + \delta_k). \quad (3.16)$$

The polarizability of the molecule changes with its vibration and can be expanded as a Taylor series with respect to all normal coordinates  $Q_k$ :

$$\tilde{\boldsymbol{\alpha}} = \boldsymbol{\alpha}_o + \sum_k \left( \frac{\partial \boldsymbol{\alpha}}{\partial Q_k} \right)_0 Q_k + \dots \quad (3.17)$$

Inserting the last three equations into Equation 3.14 and neglecting the phase  $\delta_k$  yields:

<sup>F</sup>with the relation  $\lambda = \frac{c}{\nu} = \frac{2\pi c}{\omega}$

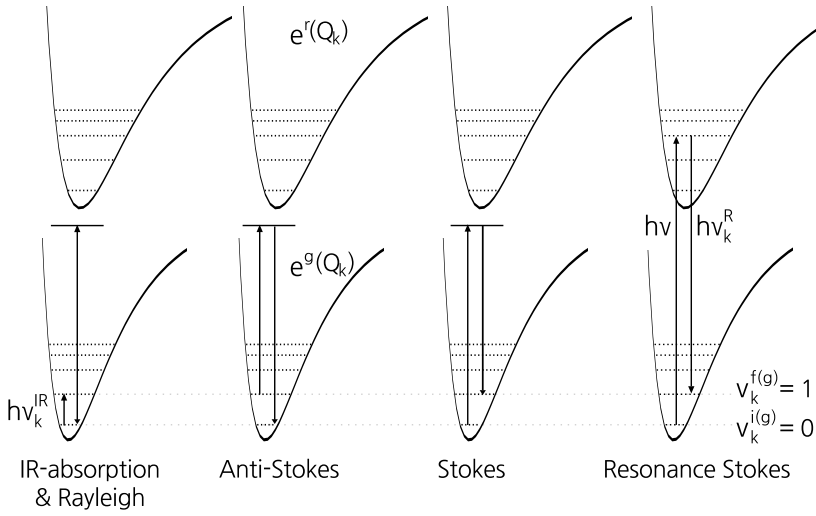


**Figure 3.3.:** Schematic illustration of (vibrational) transitions associated with IR absorption, Rayleigh and Raman scattering. For the latter, Anti-Stokes, Stokes and Resonance Raman Scattering is depicted for one vibrational mode  $k$ . The potential energy surfaces for the ground and excited electronic states are labeled with  $e^g(Q_k)$  and  $e^r(Q_k)$  and are shifted by  $\Delta Q_k$ . The energy levels of the initial and final vibrational state of the  $k^{\text{th}}$  normal mode are labeled with  $v_k^{i(g)}$  and  $v_k^{f(g)}$ . The energy of the scattered radiation is represented by a  $\downarrow$  with the label  $h\nu_k^R$ .

The Figure is reproduced with slight modifications from Reference [157].

$$\begin{aligned}
 \mathbf{P}^{ind} &= \alpha_o \mathbf{E}_o \cos \omega t \\
 &+ \sum_k \left( \frac{\partial \alpha}{\partial Q_k} \right)_0 Q_{k_o} \cos \omega_k t \cdot \mathbf{E}_o \cos \omega t \\
 &= \underbrace{\alpha_o \mathbf{E}_o \cos \omega t}_{\text{Rayleigh}} \\
 &+ \frac{1}{2} \sum_k \left( \frac{\partial \alpha}{\partial Q_k} \right)_0 Q_{k_o} \mathbf{E}_o \cdot \left[ \underbrace{\cos(\omega - \omega_k) t}_{\text{Stokes}} + \underbrace{\cos(\omega + \omega_k) t}_{\text{Anti-Stokes}} \right]
 \end{aligned} \tag{3.18}$$

The first term is related to the dominant Rayleigh scattering, where the scattered photons have the same energy as the incoming ones. The second term corresponds to Stokes and Anti-Stokes Raman scattering. (See Figure 3.3)

A significant Raman intensity can be observed for the  $k^{\text{th}}$  vibrational mode if

$$\alpha' = \left( \frac{\partial \alpha}{\partial Q_k} \right)_0 \neq 0, \tag{3.19}$$

i.e., if the polarizability changes with the vibration of the molecule. This quantity is also called the derived polarizability or Raman tensor. Its symmetry is directly related to the symmetry of the normal coordinate  $Q_k$ , which means that both quantities belong to the same representation of the molecule's symmetry group.

Within the classical description of the Raman effect, the frequencies of the scattered radiation are predicted correctly. But, only by a quantum mechanical treatment the intensity of the scattered light can be described. Furthermore, conclusions about the molecule's properties, such as the symmetry of the vibrational

modes and molecular orientations within the specimen [160], can be drawn from the quantum mechanical description of the Raman effect.

The quantum mechanical treatment of the induced electronic dipole moment  $\mathbf{P}^{ind}$  is based on second order perturbation theory. With <sup>G</sup>

<sup>G</sup> $\Psi'_f(t), \Psi'_i(t)$ : disturbed wavefunctions of the initial and final state  
 $\hat{\mathbf{P}}$ : electronic dipole moment operator  
 $W_{if}$ : transition probability  
 $I^R$ : Raman intensity

$$I^R \sim W_{if} \sim \left| \underbrace{\langle \Psi'_f | \hat{\mathbf{P}} | \Psi'_i \rangle}_{\mathbf{P}_{fi} = \mathbf{P}^{ind} = \alpha \cdot \mathbf{E}} \right|^2 \quad (3.20)$$

the probability  $W_{if}$  for the transition between the initial and final vibrational states  $|i\rangle$  and  $|f\rangle$  can be determined.[161] This transition involves a virtual state  $|r\rangle$  with an energy  $\mathcal{E}_r$ . The polarizability tensor  $\alpha$  is obtained from the solution of Equation 3.20 and comparison to the classical case described in Equation 3.14. Then the components  $\rho, \sigma = x, y, z$  of the tensor are calculated by: <sup>H</sup>

<sup>H</sup> $\omega_{fi} = \omega_f - \omega_i$   
 $\hat{P}_\rho, \hat{P}_\sigma$ : component of electronic dipole moment operator in  $\rho, \sigma$  direction  
 $i\Gamma_r$ : finite lifetime of  $|r\rangle$

$$(\alpha_{\rho\sigma})_{fi} = \frac{1}{\hbar} \sum_{r \neq i, f} \frac{\langle f | \hat{P}_\rho | r \rangle \langle r | \hat{P}_\sigma | i \rangle}{\omega_{ri} - \omega - i\Gamma_r} + \frac{\langle f | \hat{P}_\sigma | r \rangle \langle r | \hat{P}_\rho | i \rangle}{\omega_{rf} + \omega + i\Gamma_r} \quad (3.21)$$

Thus, Raman scattering can be regarded as a transition from  $|r\rangle \leftarrow |i\rangle$  (absorption of light) to  $|f\rangle \leftarrow |r\rangle$  (emission of light), involving all possible virtual states  $|r\rangle$ . This process is a property of the electronic ground state, where the initial and final vibrational level lie. No information about the state  $|r\rangle$  can be obtained from non-resonant Raman scattering, as it is not a solution of the time-dependent Schrödinger equation,

An electronic transition to a state  $|r\rangle$  is involved in the Raman process. In the framework of the Born-Oppenheimer Approximation  $|r\rangle$  can be separated into nuclear wavefunctions  $|v^r\rangle$  and those of the electrons  $|e^r\rangle$ .[162]<sup>I</sup> Therefore, the general transition polarizability tensor for Raman scattering can be further simplified to

<sup>I</sup> $|r\rangle = |e^r\rangle |v^r\rangle$   
 $\omega_r = \omega_{e^r} + \omega_{v^r}$   
 $\omega_{v(r_i)} = \omega_{v^r} - \omega_{v^i}$   
 $\omega_{e(r_i)} = \omega_{e^r} - \omega_{e^i}$   
the summation is restricted to the states  $|r\rangle$

$$(\alpha_{\rho\sigma})_{fi} = \frac{1}{\hbar} \sum_{r \neq i, f} \left[ \frac{\langle v^f | P_\rho^{e(fr)} | v^r \rangle \langle v^r | P_\sigma^{e(rg)} | v^i \rangle}{\omega_{e(r_i)} + \omega_{v(r_i)} - \omega - i\Gamma_r} + \frac{\langle v^f | P_\sigma^{e(fr)} | v^r \rangle \langle v^r | P_\rho^{e(rg)} | v^i \rangle}{\omega_{e(rf)} + \omega_{v(rf)} + \omega + i\Gamma_r} \right]. \quad (3.22)$$

$P_\rho^{e(fr)} = \langle e^f | \hat{P}_\rho | e^r \rangle$  is the  $\rho$  component of the pure electronic transition dipole moment for the electronic transition  $|e^f\rangle \leftarrow |e^r\rangle$ . To account for their dependence on the nuclear vibrations, the pure electronic transition dipole moments are expanded as a Taylor series along  $Q_k$  and finally combined with Equation 3.22. Additionally, for non-resonant Raman scattering  $\omega \ll \omega_{ri}$  applies and the

term becomes relatively insensitive to  $\omega_{v(r_i)}$ . The resulting terms  $\omega_{e(rg)} - \omega$  and  $\omega_{e(rg)} + \omega$  are much larger than the damping factor  $\Gamma_r$ , which is thus neglected. Then:

$$(\alpha_{\rho\sigma})_{fi} = A_{\rho\sigma}^R + B_{\rho\sigma}^R + \dots,$$

$$A_{\rho\sigma}^R = \frac{1}{\hbar} \sum_{r \neq g} P_{\rho_0}^{e(fr)} P_{\sigma_0}^{e(rg)} \langle v^f | v^i \rangle \cdot \left[ \frac{1}{\omega_{e(rg)} - \omega} + \frac{1}{\omega_{e(rf)} + \omega} \right],$$

$$B_{\rho\sigma}^R = \frac{1}{\hbar^2} \sum_{r \neq g} \sum_k \left[ P_{\rho_0}^{e(fr)} \left( \frac{\partial P_{\sigma}^{e(rg)}}{\partial Q_k} \right)_{Q_0} + \left( \frac{\partial P_{\rho}^{e(rg)}}{\partial Q_k} \right)_{Q_0} P_{\sigma_0}^{e(fr)} \right] \cdot \left[ \frac{1}{\omega_{e(rg)} - \omega} + \frac{1}{\omega_{e(rg)} + \omega} \right] \langle v^f | Q_k | v^i \rangle.$$

Here the superscript R indicates that the case of pure vibrational Raman scattering is considered. Higher terms than A and B are neglected.

In a more simplified manner that is rewritten as

$$(\alpha_{\rho\sigma})_{fi} = \underbrace{(\alpha_{\rho\sigma})_0 \langle v^f | v^i \rangle}_{A_{\rho\sigma}^R} + \underbrace{\sum_k \left( \frac{\partial \alpha_{\rho\sigma}}{\partial Q_k} \right)_0 \langle v^f | Q_k | v^i \rangle}_{B_{\rho\sigma}^R}. \quad (3.23)$$

which is equivalent to the result of the classical treatment in Equation 3.18. The first term in Equation 3.23 refers to Rayleigh scattering and contributes to the scattered intensity when  $|v^f\rangle$  is degenerate with  $|v^i\rangle$ , that is  $|v^f\rangle = |v^i\rangle$  and thus  $\omega_{fi} = 0$ . The second term refers to Raman scattering and should not be confused with the Raman tensor in Equation 3.19. Usually the Raman intensity is by a factor of  $10^6$  smaller than the intensity of the Rayleigh scattered light. Significant contributions to the scattered Raman intensity are expected whenever the terms  $\partial \alpha_{\rho\sigma} / \partial Q_k$  and  $\langle v^f | Q_k | v^i \rangle$  are non-zero for the  $k^{th}$  vibrational mode. The latter is true when the vibrational quantum numbers of the initial and final state differ by  $\pm 1$ . For Stokes Raman scattering the vibrational quantum numbers are set to  $|v_k^i\rangle = 0$  and  $|v_k^f\rangle = +1$ , such that the vibrational wavefunction  $\Theta_{v^i}^k$  of the initial state contains the totally symmetric representation  $\tilde{\Gamma}_1$  of the molecules symmetry group. The final vibrational wavefunction  $\Theta_{v^f}^k$  belongs to the same representation  $\tilde{\Gamma}_\diamond$  as the  $k^{th}$  normal mode. If in addition the direct product  $\tilde{\Gamma}_\diamond(\Theta_{v^f}^k) \otimes \tilde{\Gamma}_\diamond(Q_k)$  is equal to the totally symmetric representation  $\tilde{\Gamma}_1$ , the  $k^{th}$  normal mode is Raman-active and the energy of the scattered radiation is equal to  $\hbar\omega - \hbar\omega_{fi}$  for this

mode. (See Equation 3.2)

### 3.4. Resonance Raman Scattering

In case of Resonance Raman (RR) scattering the energy of the incident light  $\hbar\omega$  approaches that of an *electronic* transition with  $\hbar\omega_{ri}$ . Thus,  $\omega \approx \omega_{ri}$  and the denominator with  $\omega_{ri} - \omega - i\Gamma_r$  in Equation 3.21 dominates the sum. In such a way, the transition polarizability tensor then simplifies to:

$$(\alpha_{\rho\sigma})_{fi} = \frac{1}{\hbar} \sum_{r \neq i, f} \frac{\langle f | \hat{P}_\rho | r \rangle \langle r | \hat{P}_\sigma | i \rangle}{\omega_{ri} - \omega - i\Gamma_r} \quad (3.24)$$

With the Born-Oppenheimer Approximation [162] the transition polarizability tensor is further simplified to:

$$(\alpha_{\rho\sigma})_{fi} = \frac{1}{\hbar} \sum_{r \neq i, f} \left[ \frac{\langle v^f | P_\rho^{e(fr)} | v^r \rangle \langle v^r | P_\sigma^{e(rg)} | v^i \rangle}{\omega_{e(r)} + \omega_{v(r)} - \omega - i\Gamma_r} \right], \quad (3.25)$$

where  $P_\rho^{e(fr)} = \langle e^f | \hat{P}_\rho | e^r \rangle$  is the  $\rho$  component of the pure electronic transition dipole moment for the electronic transition  $|e^f\rangle \leftarrow |e^r\rangle$ . They are expanded in a Taylor series along  $Q_k$  and finally combined with Equation 3.25. Different terms contribute to  $\alpha$ : <sup>J</sup>

$$(\alpha_{\rho\sigma})_{fi} = A_{\rho\sigma} + B_{\rho\sigma} + C_{\rho\sigma} + D_{\rho\sigma},$$

$$A_{\rho\sigma} = \frac{1}{\hbar} \underbrace{P_{\rho 0}^{e(gr)} P_{\sigma 0}^{e(rg)}}_{\text{electronic}} \sum_{v_k^r} \underbrace{\left[ \frac{\langle v_k^{f(g)} | v_k^{r(r)} \rangle \langle v_k^{r(r)} | v_k^{i(g)} \rangle}{\omega_{e(r)} + \omega_{v_k(r)} - \omega - i\Gamma_r} \right]}_{\text{vibrational}},$$

$$B_{\rho\sigma} = \frac{1}{\hbar^2} P_{\rho 0}^{e(gr)} \left( \frac{\partial P_{\sigma 0}^{e(rg)}}{\partial Q_k} \right)_{Q_0} \cdot \sum_{v_k^r} \left[ \frac{\langle v_k^{f(g)} | Q_k | v_k^{r(r)} \rangle \langle v_k^{r(r)} | v_k^{i(g)} \rangle + \langle v_k^{f(g)} | v_k^{r(r)} \rangle \langle v_k^{r(r)} | Q_k | v_k^{i(g)} \rangle}{\omega_{e(r)} + \omega_{v_k(r)} - \omega - i\Gamma_r} \right].$$

The A-term contains products of two unperturbed pure electronic transition dipole moments  $P_{\rho 0}^{e(gr)}$  for the transition  $|e^g\rangle \rightarrow |e^r\rangle$  with the nuclei in their equilibrium configurations. These moments are large for electronically allowed transitions between electronic states of opposite parity. This term defines the efficient resonance enhancement of the scattered Raman intensity. In addition, A-

<sup>J</sup> $v_k^{f(g)}$  indicates that the final vibrational state of the  $k^{\text{th}}$  normal mode lies in the electronic ground state. For most experimental conditions it is sufficient to assume that the scattering is associated with transitions of the form  $e^g v^f \leftarrow e^g v^i$ . That is the initial and final electronic state lie in the electronic ground state of the system. This is termed pure vibrational Raman scattering. Depending on the nature of  $e^r$  it maybe 'normal Raman Scattering' or 'Resonance Raman Scattering'.

term RR scattering requires that the Franck-Condon overlap integrals  $\langle v_k^{f(g)} | v_k^{r(r)} \rangle$  and  $\langle v_k^{r(r)} | v_k^{i(g)} \rangle$  are non-zero for at least one of the normal modes  $k$ . This is most pronounced for electronic transitions between a ground and an excited state with different potential energy surfaces, that are shifted by  $\Delta Q_k$  to each other. The B-term has a product of one unperturbed and one perturbed pure electronic transition dipole moment  $\partial P_{\rho_0}^{e(rg)} / \partial Q_k$ . Here, the perturbed moment describes the strength of Herzberg-Teller vibronic coupling between the excited electronic state  $|e^r\rangle$  to another electronic state induced by a vibrational mode  $Q_k$ . The B-Term is only important, when there is no significant RR scattering from the A-Term. In most cases the contribution of Franck-Condon RR scattering, i.e. the A-Term scattering, to the intensities is the largest one.

Accordingly, the RR intensity for A-term scattering is approximated to

$$\begin{aligned}
 I^{RR} &\sim W_{if} \sim \left| \underbrace{\langle \Psi'_f | \hat{\mathbf{P}} | \Psi'_i \rangle}_{\mathbf{P}_{fi} = \mathbf{P}^{ind} = \alpha \cdot \mathbf{E}} \right|^2 \\
 &\sim \left| \langle \Psi'_f | \hat{\alpha} \mathbf{E} | \Psi'_i \rangle \right|^2 \\
 &\sim \left| \mathbf{P}_0^{e(gr)} \mathbf{P}_0^{e(rg)} \mathbf{E} \right|^2 \frac{\left| \langle v_k^{f(g)} | v_k^{r(r)} \rangle \langle v_k^{r(r)} | v_k^{i(g)} \rangle \right|^2}{(\omega_{e(rg)} + \omega_{v_k(r)} - \omega)^2 + \Gamma_r^2} \quad (3.26)
 \end{aligned}$$

### Angle-Dependent Resonance Raman Scattering

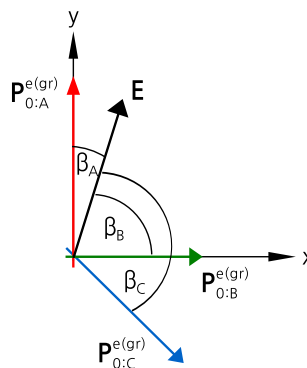
The probability for the electronic transition  $|e^r\rangle \leftarrow |e^g\rangle$  is given by:[161]

$$W_{rg} \sim \left| \mathbf{P}_0^{e(rg)} \cdot \mathbf{E} \right|^2 \sim \cos^2 \beta, \quad (3.27)$$

where  $\beta$  is the angle between the vectorial quantities  $\mathbf{P}^{e(rg)}$  and the electric field vector  $\mathbf{E}$  of the incident electromagnetic radiation. Thus, the transition probability  $W_{rg}$  is maximal when both vectors are parallel. In other words, the angle-dependent RR intensity is controlled by the scalar product between the pure electron transition dipole moments and the incident electric field.

This effect will be used in this work to distinguish the vibrational modes of the three different FeS clusters in the MBH's small subunit. Under the prerequisite that the pure electronic transition dipole moments for all three FeS clusters point in different directions in space, an angle  $\beta$  exists where the transition probab-

**Figure 3.4.:** Illustration of the pure electronic transition dipole moments  $\mathbf{P}_{0:\diamond}^{e(gr)}$  for three different components  $\diamond = A, B$  or  $C$  in a Cartesian coordinate system. The electric field vector  $\mathbf{E}$  of the incident light encloses an angle of  $\beta_\diamond$  with the pure electronic transition dipole moment  $\mathbf{P}_{0:\diamond}^{e(gr)}$  and induces an electronic transition  $|e^r\rangle \leftarrow |e^g\rangle$ . For the illustrated case the transition probability for  $W_{rg} \sim |\mathbf{P}_{0:A}^{e(gr)} \cdot \mathbf{E}|^2$  is maximal, due to its  $\cos^2 \beta$  dependence.



ity  $W_{rg}$  is maximal for the electronic transition in only one particular FeS cluster. That is illustrated in Figure 3.4 for three different pure electronic transition dipole moments  $\mathbf{P}_{0:\diamond}^{e(gr)}$  and the electric field vector  $\mathbf{E}$  in a Cartesian coordinate system. Here, the different dipole moments correspond to three independent molecular components  $\diamond = A, B$  or  $C$  in one investigated sample. Depending on the angle  $\beta_\diamond$  between the two vectorial quantities the transition probability follows a  $\cos^2 \beta_\diamond$  function. In view of Equation 3.26 the contribution of the vibrational modes for each component A, B, C to the measured RR intensity likewise depends on  $\beta_\diamond$ .

### Polarization-Dependent Raman Scattering

For non-resonant Raman scattering, R. Loudon [163] was the first who correlated the Raman scattering tensor with the crystal structure of solids. R. Roe [164] introduced spherical harmonics to explain its orientation within the coordinate system of the solid sample. In the early 1970s polarized Raman spectroscopy was applied for the study of molecular orientations in uniaxial polymers.[165, 166, 167, 160] The directional information on the Raman scattering tensor is determined by the angular distribution of the scattered intensity by means of a polarized incident laser beam and an analyzer in the detection pathway. Hereby, the choice of the incident polarization turned out to be crucial for distinguishing various species in the polymeric sample.[165]

The components of the transition polarizability tensor  $(\alpha_{\rho\sigma})_{fi}$  can be determined from polarization dependent Raman measurements. In principle that enables conclusions on the symmetry of specific vibrational modes  $k$ . With regard to the tensorial nature of the polarizability Equation 3.14 can be written in the Cartesian coor-

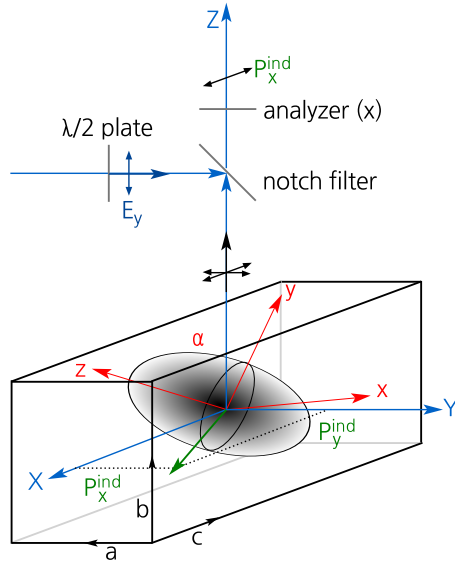


**Figure 3.5.:** The laboratory coordinate system ( $XYZ$ ) used in this work with respect to the  $(abc)$  unit cell of the MBH crystal and the principal axes  $(xyz)$  of the transition polarizability tensor  $\alpha$  for one vibrational mode  $k$ . The laser propagates in the  $Z$ -direction and its electric field vector  $\mathbf{E}$  lies in the  $XY$ -plane as adjusted by the half-wave plate. Correspondingly, only the  $X$  and  $Y$  components of the induced electronic dipole moment  $\mathbf{P}^{ind}$  can be determined in a  $180^\circ$  backscattering geometry. The analyzer, in the detection pathway, selects either of the two components.

dinate system as:

$$\begin{pmatrix} P_X \\ P_Y \\ P_Z \end{pmatrix} = \begin{pmatrix} \alpha_{XX} & \alpha_{XY} & \alpha_{XZ} \\ \alpha_{YX} & \alpha_{YY} & \alpha_{YZ} \\ \alpha_{ZX} & \alpha_{ZY} & \alpha_{ZZ} \end{pmatrix} \cdot \begin{pmatrix} E_X \\ E_Y \\ E_Z \end{pmatrix} \quad (3.28)$$

In this work a  $180^\circ$  backscattering geometry and a propagation in the  $Z$ -direction ( $E_Z = 0$  and  $P_Z = 0$ ) is chosen for the RR measurements. (See Figure 3.5). Then the above equation simplifies to

$$\begin{aligned} P_X &= \alpha_{XX}E_X + \alpha_{XY}E_Y, \\ P_Y &= \alpha_{YX}E_X + \alpha_{YY}E_Y. \end{aligned}$$

According to Equation 3.20 the measured scattered intensity  $I(\cdot^s)$  in the  $X$  or  $Y$ -direction is proportional to

$$\begin{aligned} I(X^s) &\sim P_X^2 = (\alpha_{XX}E_X + \alpha_{XY}E_Y)^2, \\ I(Y^s) &\sim P_Y^2 = (\alpha_{YX}E_X + \alpha_{YY}E_Y)^2. \end{aligned}$$

If the electric field vector of the incident light is aligned either along the  $X$ -axis ( $\mathbf{E} = E_X\mathbf{e}_X$ ) or the  $Y$ -axis ( $\mathbf{E} = E_Y\mathbf{e}_Y$ ) four different configurations for the scattered intensity can be obtained:

$$\begin{aligned} I_{\parallel} &= I(X^e X^s) \sim \langle (\alpha_{XX})^2 \rangle, \\ I_{\perp} &= I(X^e Y^s) \sim \langle (\alpha_{YX})^2 \rangle, \\ I_{\perp} &= I(Y^e X^s) \sim \langle (\alpha_{XY})^2 \rangle, \\ I_{\parallel} &= I(Y^e Y^s) \sim \langle (\alpha_{YY})^2 \rangle, \end{aligned}$$

where  $I(\cdot^e \cdot^s)$  denotes that the incident electric field is polarized in the  $(\cdot^e)$  direction and the scattered radiation is detected in the  $(\cdot^s)$  direction of the laboratory coordinate system.

For gaseous or liquid substances the molecular orientation is perfectly random and the measured intensity corresponds to a mean value over all possible orientations. In this case, the Raman scattering tensor can be expressed in the form of two invariants  $\bar{\alpha}'$  and  $\bar{\gamma}'$  and the Raman intensity is proportional to:  $I_{\perp} \sim 1/15\bar{\gamma}'^2$  and  $I_{\parallel} \sim \bar{\alpha}'^2 + 4/45\bar{\gamma}'^2$ . [168]

The depolarization ratio is defined as  $\rho_D = I_{\perp}/I_{\parallel}$ . It is zero for polarized bands and 0.75 for unpolarized bands for the theoretical case. However, this only applies for the case of vibrational Raman scattering and not for the case of RR scattering on solids with (partial) orientation of the inherent structural groups.

In case of polarized RR spectroscopy the measured intensity not only depends on the symmetry of the molecular vibrations (see discussion in previous section) but also on the orientation of the pure electronic transition dipole moments of the specimen. In view of Equation 3.26 this results in a rather complex function which cannot be easily determined from the experimentally obtained polarized RR intensity. Therefore, the components of the transition polarizability tensor  $(\alpha_{\rho\sigma})_{fi}$  for a vibration mode  $k$  cannot be determined and no information about its orientation within the sample can be obtained.

### 3.5. Instrumentation for Raman Spectroscopy

In Figure 3.6A the setup for RR measurements is shown schematically. The 458, 514 and 568 nm line of an Argon continuous wave (cw) laser as well as the 413 nm line of a Krypton cw laser are used as excitation lines. To remove plasma lines a plasma filter (F) corresponding to the selected wavelength is placed into the laser beam. Within the confocal Raman spectrometer (LabRam HR-800, Jobin Yvon) the laser light is focused onto the sample surface with a Nikon 20 × microscope objective (20.5 mm working distance, 0.35 numeric aperture). The Raman signal is collected in a 180° backscattering geometry through the same objective and Rayleigh scattered light is suppressed by an edge or holographic notch filter (N) in the detection pathway. Afterwards the scattered light is focused onto the entrance slit of the spectrograph unit. A grating with 1200 lines/mm disperses the light, which is then refocused with a curved mirror onto the liquid nitrogen cooled CCD

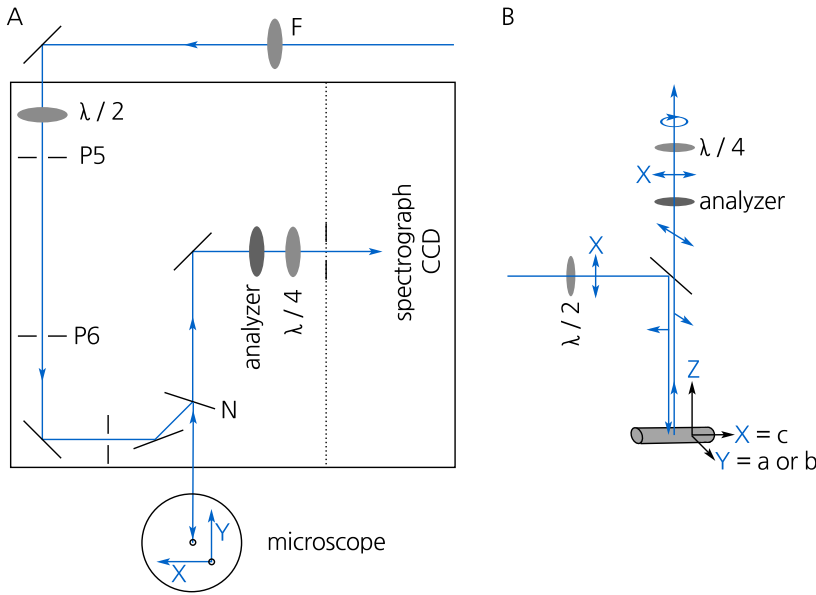


**Figure 3.6.:** A) Sketch of the RR setup as used in this work. B) Declaration of the laboratory coordinate system ( $XYZ$ ) with respect to the  $(abc)$  unit cell of the MBH crystal.

for detection. For most experiments a binning factor of two was used, that is the intensities of two adjacent pixels of the CCD chip are summed up. This setting yields increments per camera pixel of 1.23, 0.95 and  $0.77 \text{ cm}^{-1}$  for wavelengths of 458, 514 and 568 nm, respectively. Thus, the reported frequencies for an excitation at 458 nm are accurate within roughly  $\pm 1 \text{ cm}^{-1}$ .

For RR measurements of the MBH the laser power at the sample surface is set to 1 – 2 mW and the sample temperature is kept at 80 K with a Linkam THMS600 microscope stage. Laser induced damage of the samples is excluded on the basis of a comparison of consecutively measured spectra from the same sample. Accumulation times are 120 – 300 seconds with up to 30 repetitions. For RR measurements of crystalline MBH samples the  $c$ -axis is always aligned parallel to the electric field vector of the incident laser beam. In Figure 3.5 and 3.6B the laboratory ( $XYZ$ ) and the immanent crystal coordinate system  $(abc)$  are declared. A half-wave plate in the excitation pathway allows to turn the electric field vector of the laser in the  $XY$ -plane. In this respect, the excitation angle  $\beta'$  is defined as the angle between the  $c$ -axis of the crystal and the electric field vector of the incident laser, i.e.  $\beta' = 0$  and  $90^\circ$  correspond to an excitation along  $X$  and  $Y$ , respectively. Together with the analyzer in the detection pathway polarization-dependent RR measurements can be carried out. To reduce polarization-dependent intensity losses in the spectrograph, the analyzer is backed up with a quarter-wave plate at a fixed angle of  $45^\circ$  between its slow axis and the analyzer axis. Thus light entering the spectrograph is always circularly polarized.

The measured RR spectra were carefully calibrated to an internal reference band at  $274.0\text{ cm}^{-1}$  of water ice and/or the phenylalanine vibration of the protein at  $1003.4\text{ cm}^{-1}$  (for non-labeled samples only). Linear baselines were subtracted via GNU-octave and if necessary, the spectra were integrated numerically and normalized with home-written GNU-octave scripts from H. Naumann and E. Siebert. Peak fitting was carried out with FitYK [169]. Component analyses and calculation of RR difference spectra were done with the Python based software SpecMate[170].

For the RR experiments, the concentration of MBH samples in solution was adjusted  $0.9 - 1.3\text{ mM}$ . The samples were transferred as  $1.5\text{ }\mu\text{L}$  drops to the quartz sample holder and frozen in liquid nitrogen prior to the measurements. Similarly, MBH crystals for RR experiments were transferred from the mother liquor with a nylon loop to the quartz sample holder and frozen in liquid nitrogen. Prior to that, excess amounts of the mother liquor were removed to reduce the probability of its freezing in the amorphous phase. This procedure also ensured, that further additives, such as polyethylene glycol (PEG), are removed from the surface of the crystal. The vibrational modes of the PEG would otherwise overlap with modes of the MBH.

## 4. Redox Transitions of the Active Site Monitored by FTIR

The solubilized heterodimeric form of the MBH ( $\text{MBH}_{\text{sol}}$ ) can be obtained by detaching the enzyme from the cytoplasmic membrane with detergent. Thereby, it is also separated from the primary electron acceptor cytochrome *b*. The  $\text{MBH}_{\text{sol}}$  has been extensively characterized in electrochemical and electro-catalytic studies.[11, 135] In fact, even the potential for biotechnological applications was demonstrated, as the  $\text{MBH}_{\text{sol}}$  was successfully implemented as an anodic component in enzymatic fuel cells for light-driven hydrogen production.[171, 172] Within the catalytic cycle of the hydrogenases the structural and electronic properties of the [NiFe] active site are altered. These can however, not be probed by pure electrochemical methods. Therefore, suitable spectroscopic techniques, such as Fourier Transform Infrared (FTIR) spectroscopy, have to be applied.[60, 173, 34, 81] In a combined approach of FTIR and Electron Paramagnetic Resonance (EPR) spectroscopy Saggi *et al.* showed 2009 that the redox behavior of the heterodimeric  $\text{MBH}_{\text{sol}}$  is modified due to the detachment of the enzyme from the cytoplasmic membrane.[33] Although the active site of the  $\text{MBH}_{\text{sol}}$  exhibits all redox states known from oxygen-tolerant hydrogenases, except the unready  $\text{Ni}_{\text{u}}\text{-A}$  state, a significant portion resides in a permanently catalytically inactive form. This non-native  $\text{Ni}_{\text{ia}}\text{-S}$  redox state cannot be activated even after prolonged incubation of the  $\text{MBH}_{\text{sol}}$  with hydrogen. In contrast, the MBH in its natural environment attached to the cytoplasmic membrane ( $\text{MBH}_{\text{mem}}$ ) reacts fully reversible with hydrogen and oxygen and no  $\text{Ni}_{\text{ia}}\text{-S}$  species is formed. The infrared spectrum after reoxidation with air is identical to the one obtained prior to hydrogen reduction. In other words, the infrared spectra of the oxidized and reoxidized  $\text{MBH}_{\text{mem}}$  samples show an active site that resides to at least 90 % in the  $\text{Ni}_{\text{r}}\text{-B}$  redox state. As a consequence of this study

an improved purification protocol for the  $\text{MBH}_{\text{sol}}$  was developed by Fritsch *et al.*[79] The procedure resulted in a stable heterodimeric  $\text{MBH}_{\text{sol}}$ , where the  $[\text{NiFe}]$  active site resides with up to 90% in the  $\text{Ni}_r\text{-B}$  redox state as well.[79, 43] (See also Figure 2.3) Similar portions of the  $\text{Ni}_r\text{-B}$  redox state are observed from  $\text{MBH}_{\text{mem}}$  samples.

Heterodimeric  $\text{MBH}_{\text{sol}}$  samples at a pH of 5.5 from this improved purification protocol are investigated in the present work. In the first part of this Chapter, the reoxidation process of the  $\text{MBH}_{\text{sol}}$ , obtained by the new purification protocol, is compared in a time resolved manner to the one of the heterodimeric MBH still attached to the cytoplasmic membrane ( $\text{MBH}_{\text{mem}}$ ). Afterwards, the Spectro-Electrochemical (SEC) characteristics of the  $\text{MBH}_{\text{sol}}$  at pH 7.0 are investigated. The obtained results are compared to infrared spectroscopic data of the new  $\text{MBH}_{\text{sol}}$  preparation after reductions with hydrogen and fast reoxidation with air.[43]

#### 4.1. The Reoxidation Process Tracked in Time

Potential-dependent infrared measurements on redox active enzymes, such as hydrogenases, allow insights into their catalytic cycle and (in)activation processes.[153, 34] Additionally, the identity of the involved redox states can be investigated. The redox state of the enzyme can either be altered chemically (e.g. with dithionite or ferricyanide), by externally applied potentials in a SEC infrared transmission cell or with different natural substrates (such as  $\text{H}_2$  and  $\text{O}_2$ ).

This section aims to elucidate differences in the catalytic cycle of the heterodimeric MBH attached to the inner membrane ( $\text{MBH}_{\text{mem}}$ ) and the solubilized heterodimeric form of the MBH ( $\text{MBH}_{\text{sol}}$ ). The redox potential is changed with varying partial pressures of the natural substrates hydrogen and oxygen. In the present experiment, this is achieved by a continuous and very slow gas exchange between hydrogen and oxygen inside the FTIR transmission cell over the course of seventeen hours. Although the redox potential at the sample cannot be determined in this setup, this technique has several advantages: The steady gas exchange is a convenient way to study the reoxidation behavior of the MBH as the redox potential increases continuously from reducing to oxidizing potentials. During that time FTIR spectra are constantly acquired in intervals of 150 seconds. Moreover, due to the extremely slow gas exchange in the sample compartment equilibrium conditions are

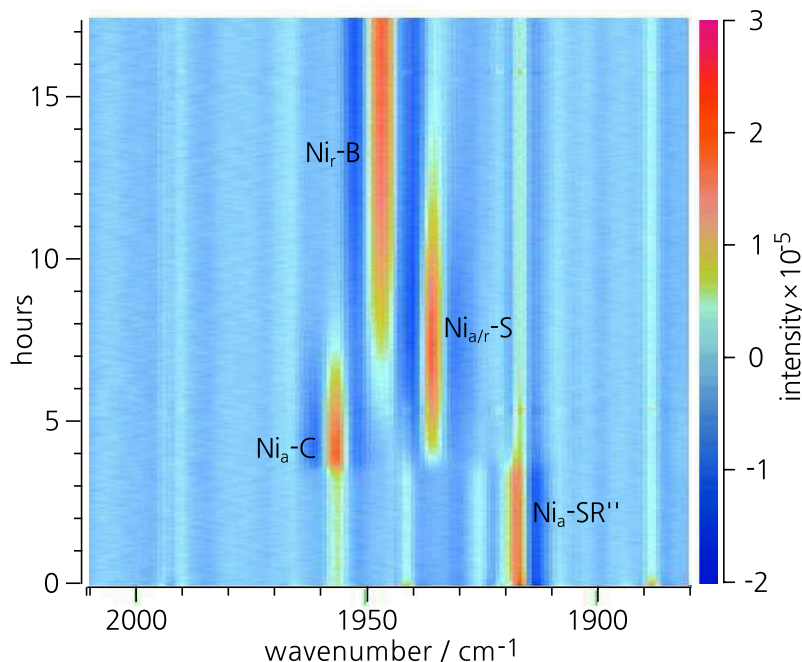


**Figure 4.1.:** Three dimensional representation of the second derivative absorbance spectra of a  $\text{MBH}_{\text{mem}}$  sample during the reoxidation process. The evolution of the CO band intensity for all detected redox species is shown in Figure 4.3 as a function of time (in arbitrary but normalized units). The CO bands of the different redox species  $\text{Ni}_a\text{-SR}''$ ,  $\text{Ni}_a\text{-C}$ ,  $\text{Ni}_{a/r}\text{-S}$  and  $\text{Ni}_r\text{-B}$  are indicated.

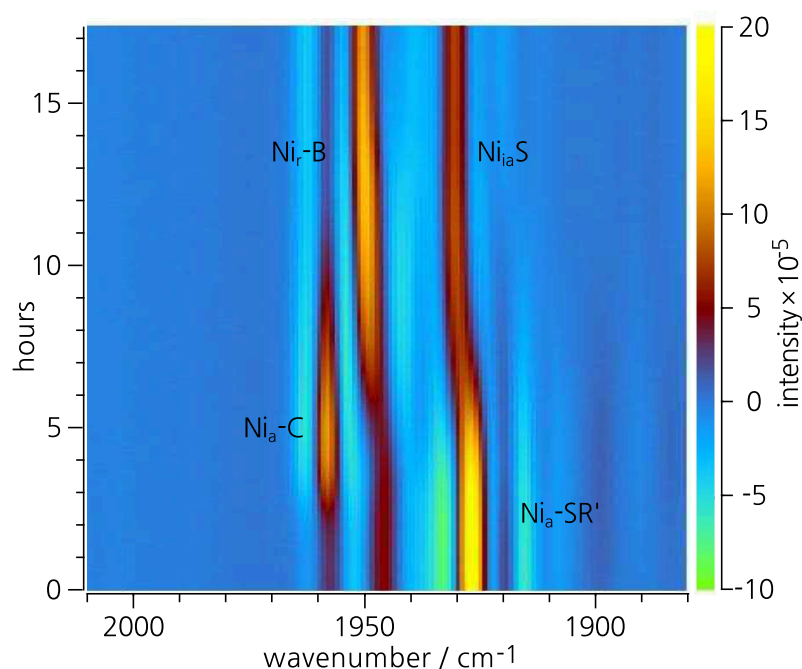
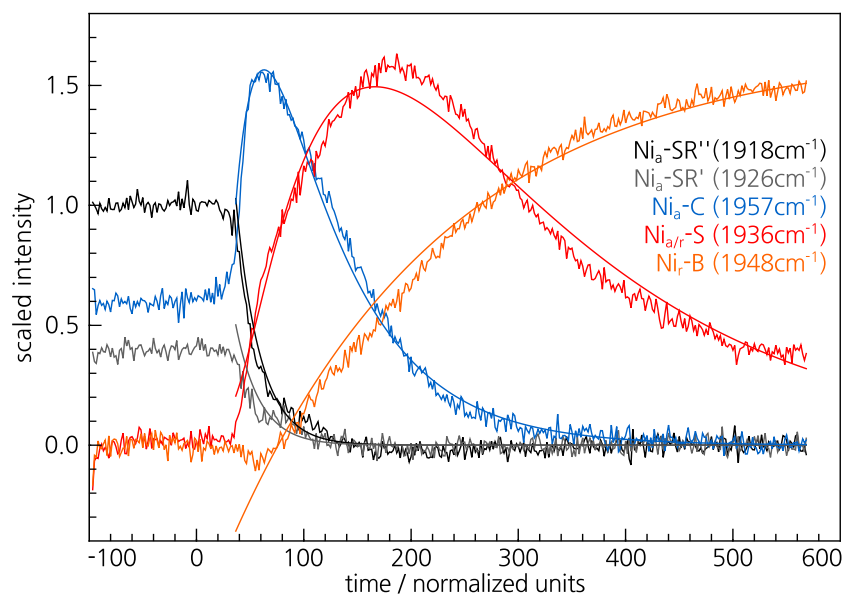


**Figure 4.2.:** Three dimensional representation of the second derivative absorbance spectra of a  $\text{MBH}_{\text{sol}}$  sample during the reoxidation process. The evolution of the CO band intensity for all detected redox species is shown in Figure 4.4 as a function of time (in arbitrary but normalized units). The CO band positions of the different redox species  $\text{Ni}_a\text{-SR}'$ ,  $\text{Ni}_a\text{-C}$ ,  $\text{Ni}_{ia}\text{-S}$  and  $\text{Ni}_r\text{-B}$  are indicated. The CO band of  $\text{Ni}_r\text{-B}$  species is shifted by 1 to  $2\text{ cm}^{-1}$  to higher energies than for the inner membrane sample. Moreover, the  $\text{Ni}_{a/r}\text{-S}$  species is hardly detectable.

met for every single measurement. The relative intensities of the various redox states from the  $[\text{NiFe}]$  active site can be inferred at every time of the reoxidation process. Thus, the interconversion of the redox states is monitored.

The reoxidation process is illustrated for the  $\text{MBH}_{\text{mem}}$  and  $\text{MBH}_{\text{sol}}$ , both at a pH of 5.5, in Figure 4.1 and 4.2, respectively. For these contour plots 400 infrared spectra à 200 scans, were continuously measured after the reduction of the corresponding sample with 100% hydrogen. Thus, the spectrum numbers from 1 to 400 rep-

**Figure 4.3.:** The CO band intensity for all detected redox species in the second derivative absorbance spectra is displayed as a function of time. The time axis is arbitrary but normalized to the decay of the Ni<sub>a</sub>-SR'' species (see text). The time axis relates to the redox potential at the sample with a linear function. Continuous lines correspond to the results of a fit with coupled mono exponential functions to the experimental data set. The reoxidation curves correspond to the contour plot of the MBH<sub>mem</sub> shown in Figure 4.1.



represent a measure of time after the reduction. Due to the large number of single absorbance spectra a manual baseline correction could not be carried out. Therefore, the corresponding inverted second derivatives of the CO stretching bands in the characteristic spectral region, are displayed in the contour plots. In such a way, the evolution of the various redox states of the active site can still be followed for both sample types. Several differences in their reoxidation behavior can be readily summarized: No inactive species Ni<sub>ia</sub>-S is detected in the MBH<sub>mem</sub> and the reoxidized form exhibits predominantly vibrational modes of the Ni<sub>r</sub>-B redox state. In contrast to that, shows the reoxidized MBH<sub>sol</sub> sample considerable amounts of the irreversibly inactive species Ni<sub>ia</sub>-S along with the Ni<sub>r</sub>-B state. The spectra of the reduced MBH<sub>sol</sub> sample comprises major fractions of the Ni<sub>a</sub>-SR' (1926 cm<sup>-1</sup>) whereas Ni<sub>a</sub>-SR'' (1918 cm<sup>-1</sup>) dominates the reduced Infrared spectrum of the MBH<sub>mem</sub>. The corresponding other reduced species with band positions at 1918 cm<sup>-1</sup> or 1926 cm<sup>-1</sup> as well as the Ni<sub>a</sub>-SR (1944 cm<sup>-1</sup>) related CO stretching mode can be detected only with very weak intensities. Besides, the expected redox state interconversion from the fully reduced Ni<sub>a</sub>-SR, SR', SR'' species via the central intermediate Ni<sub>a</sub>-C to the active or ready silent Ni<sub>a/r</sub>-S redox state is observed.<sup>A</sup> Finally Ni<sub>a/r</sub>-S decays and Ni<sub>r</sub>-B is formed. It should be noted, that the related infrared spectral intensities of the MBH<sub>sol</sub> are, due to significantly lower concentrations in the MBH<sub>mem</sub> samples, at least one order of magnitude more higher, as can be deduced from the intensity scale bars on the right hand side of contour plots.

<sup>A</sup>Under the present conditions Ni<sub>a</sub>-S and Ni<sub>r</sub>-S cannot be distinguished. Both redox states are characterized by a nickel ion in oxidation state 2+. However, the bridging ligand is different: Ni<sub>a</sub>-S has an empty bridge and Ni<sub>r</sub>-S either bound OH<sup>-</sup> or H<sub>2</sub>O.

Since the diffusion of the substrates in and out of the measurement

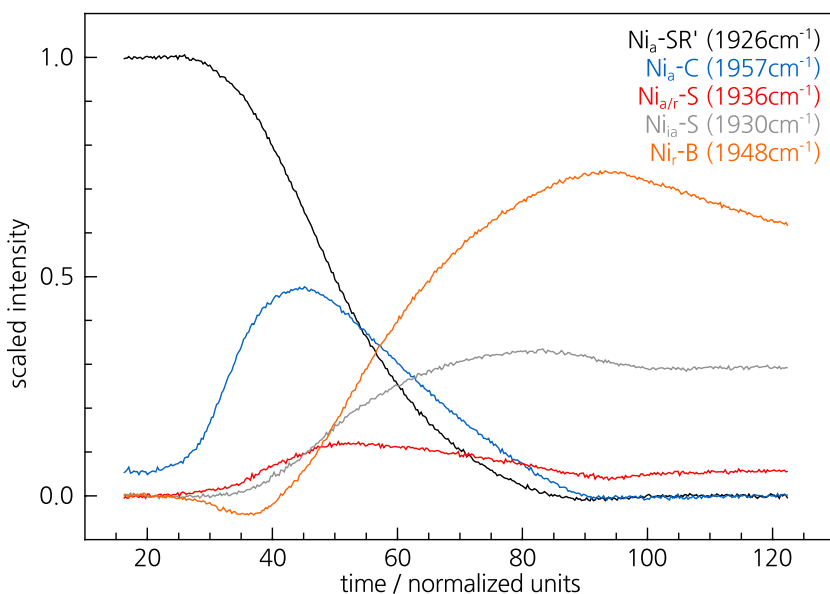


**Figure 4.4.:** The CO band intensity for all detected redox species in the second derivative absorbance spectra is displayed as a function of time. The time axis is arbitrary but normalized to the decay of the Ni<sub>a</sub>-SR' species. (See text) The time axis relates to the redox potential at the sample with a linear function. The reoxidation curves correspond to the contour plot of the MBH<sub>sol</sub> shown in Figure 4.2.

cell, and thus the respective partial gas pressures or the resulting inherent potentials, cannot be externally controlled or measured adequately, a comparative and quantitative analysis of both reoxidation process is prevented. In a first approximation of the slow gas exchange in the measurement cell, the partial pressure of hydrogen decreases and that of oxygen increases mono-exponentially till the upper limit of 20%. If the partial pressures could be determined, a conversion by means of the modified Nernst Equation to the respective redox potentials would be possible.<sup>B</sup> In this way, a potential axis with a linear relation to the time axis could be provided. However, this function cannot be obtained with the current setup. Therefore, the following reoxidation curves can be only interpreted on a qualitative level.

For the sake of comparability, time and intensity axes were normalized with the following procedure: The diffusion constants of the gases, which flow in and out of the cell, determine the progress of the reoxidation process in time. Thus, the time axis is normalized relative to two reference points of the reoxidation curve from the Ni<sub>a</sub>-SR' (for MBH<sub>sol</sub>) or Ni<sub>a</sub>-SR'' (for MBH<sub>mem</sub>) species. As a reference the intensity values for 80 and 50% of the measured Ni<sub>a</sub>-SR' / Ni<sub>a</sub>-SR'' CO band intensity of the second derivative were chosen. In between those points ten units are set in the new 'normalized' time-axis. Additionally the time-values of all curves were shifted in such way that the 50% value of Ni<sub>a</sub>-SR' / Ni<sub>a</sub>-SR'' lies at 50 units on the normalized time-axis.<sup>C</sup> Thus the 80% intensity value of Ni<sub>a</sub>-SR' / Ni<sub>a</sub>-SR'' is found at 40 units on the normalized time-axis.

The intensity-offsets of the reoxidation curves were corrected to

<sup>B</sup>

$$V = V_o + \frac{RT}{nF} \ln \left( \frac{a(H^+)^2}{p(H_2)} \right)^{1/2}$$

with:  $n=2$ ,  $F=9.648 \cdot 10^4 \text{ C/mol}$ ,  
 $R=8.314 \text{ J/K mol}$  and  $T=300 \text{ K}$ ,  
 $\ln(a(H^+))=2.302 \cdot \log(a(H^+))=$   
 $-2.302 \cdot \text{pH}$   
 $p(H_2)=1.00$  to  $0$  for  $100\%$  to  $0\%$   
hydrogen in the atmosphere

<sup>C</sup>The value of 50 units on the normalized time axis is chosen arbitrarily

reasonable values as well. Right after the reduction, i.e. at the beginning of the measurement, the intensities of the  $\text{Ni}_{a/r}\text{-S}$ ,  $\text{Ni}_{ia}\text{-S}$  and  $\text{Ni}_r\text{-B}$  are zero. Conversely, the intensities of the curves at  $\text{Ni}_a\text{-SR}''$ ,  $\text{Ni}_a\text{-SR}'$  and  $\text{Ni}_a\text{-C}$  are zero after the reoxidation process is completed, i.e. at the end of the measurement. Finally the intensities of all curves were normalized such that  $\text{Ni}_a\text{-SR}'$  (for  $\text{MBH}_{\text{sol}}$ ) /  $\text{Ni}_a\text{-SR}''$  (for  $\text{MBH}_{\text{mem}}$ ) have an initial intensity value of one. The measured intensities of the other curves are scaled accordingly.

**Table 4.1.:** Phenomenological comparison of time traces shown in Figure 4.1 and 4.2 for the MBH samples attached to the inner membrane and in the heterodimeric form, respectively.

membrane attached MBH	heterodimeric MBH
$I^{\text{max}}(\text{Ni}_a\text{-SR}'') > I^{\text{max}}(\text{Ni}_a\text{-SR}')$	$I^{\text{max}}(\text{Ni}_a\text{-SR}'') \ll I^{\text{max}}(\text{Ni}_a\text{-SR}')$
$I^{\text{max}}(\text{Ni}_a\text{-C}) > I^{\text{max}}(\text{Ni}_a\text{-SR}'')$ $I^{\text{max}}(\text{Ni}_a\text{-C}) > I^{\text{max}}(\text{Ni}_a\text{-SR}')$	$I^{\text{max}}(\text{Ni}_a\text{-C}) < I^{\text{max}}(\text{Ni}_a\text{-SR}')$
$I^{\text{max}}(\text{Ni}_{a/r}\text{-S}) \approx I^{\text{max}}(\text{Ni}_a\text{-C})$	$I^{\text{max}}(\text{Ni}_{a/r}\text{-S}) \approx 0.3 \cdot I^{\text{max}}(\text{Ni}_a\text{-C})$
$I(\text{Ni}_r\text{-B}) = \text{maximal}$ after completed reoxidation	$I(\text{Ni}_r\text{-B}) = \text{maximal}$ if $I(\text{Ni}_a\text{-C})$ and $I(\text{Ni}_{a/r}\text{-S})$ zero $I(\text{Ni}_r\text{-B}) = 50$ to $60\%$ after completed reoxidation
No $\text{Ni}_{ia}\text{-S}$	$I(\text{Ni}_{ia}\text{-S}) = 30$ to $40\%$ after completed reoxidation $\text{Ni}_{ia}\text{-S}$ formed from decaying $\text{Ni}_a\text{-SR}$ and $\text{Ni}_a\text{-C}$ .

With respect to this procedure, the CO band intensities of the various redox species are plotted as a function of 'normalized' time after the hydrogen-reduction in Figure 4.3 and 4.4 for the  $\text{MBH}_{\text{mem}}$  and the  $\text{MBH}_{\text{sol}}$ , respectively. These data sets were acquired with home written GNU-octave scripts. The intensity at the various CO band positions is calculated in the limits of  $\pm 1$  wavenumber for all 400 second derivative absorption spectra. These are only approximations of the true band intensities, as will be discussed in more detail in the next section (Figure 4.6).

In total, reoxidation processes for six  $\text{MBH}_{\text{sol}}$  and four  $\text{MBH}_{\text{mem}}$  samples were acquired and compared to each other. Similarities in the reoxidation process observed for both kind of MBH samples are: The fully reduced species  $\text{Ni}_a\text{-SR}'$  and  $\text{Ni}_a\text{-SR}''$  have approximately the same redox potential. The intermediate  $\text{Ni}_a\text{-C}$  redox

state is generated upon the decay of the Ni<sub>a</sub>-SR' / Ni<sub>a</sub>-SR'' species. Likewise, is the Ni<sub>a/r</sub>-S species formed on the expense of the Ni<sub>a</sub>-C species. The reoxidation process is completed with the formation of the fully oxidized Ni<sub>r</sub>-B from Ni<sub>a/r</sub>-S.

The reoxidation curves for the MBH<sub>sol</sub> samples are in principle similar to each other, but deviate in parts from the curves of the MBH<sub>mem</sub>, and vice versa. Table 4.1 summarizes the differences observed for the reoxidation processes of both kind of samples.

Apparently, the composition of the redox species varies at comparable potentials (normalized time units) and thus the reoxidation process differs in certain aspects significantly. This is presumably related to the fact that the MBH<sub>sol</sub> samples lack the primary electron acceptor cytochrome *b* at the end of the FeS-cluster electron transport chain in the small subunit. This may influence the redox potentials of the individual redox species. Moreover, the loss of the electron acceptor affects the reversibility of the redox process, the overall stability as well as oxygen tolerance of the entire enzyme.

The most prominent discrepancy is the presence of an irreversibly inactive redox species Ni<sub>ia</sub>-S [33], which only occurs in the reoxidation curves for the MBH<sub>sol</sub> samples. The species is populated upon the decay of the reduced species Ni<sub>a</sub>-SR' and Ni<sub>a</sub>-C and contributes up to 40% of the total CO band intensity after complete reoxidation of the samples. For the as-isolated MBH<sub>sol</sub> samples at pH 5.5 this contribution is less than ten percent, since these samples are grown under strongly oxidizing conditions.[43, 174]

Based on the observations summarized in Table 4.1 a set of coupled mono-exponential equations is derived to describe the decay and formation of the various redox species. In Appendix B a reaction scheme for the interconversion of the redox states during the reoxidation process is given, also simplifications leading to the rate equations below are specified.

$$\frac{dSR''(t)}{dt} = -k_1'' \cdot SR''(t) \quad (4.1)$$

$$\frac{dSR'(t)}{dt} = -k_1' \cdot SR'(t) \quad (4.2)$$

$$\frac{dC(t)}{dt} = +k_1'' \cdot SR''(t) + k_1' \cdot SR'(t) - k_2 \cdot C(t) \quad (4.3)$$

$$\frac{dS_{a/r}(t)}{dt} = +k_2 \cdot C(t) - k_3 \cdot S_{a/r}(t) \quad (4.4)$$

$$\frac{dB(t)}{dt} = +k_3 \cdot S_{a/r}(t) \quad (4.5)$$

Here,  $k_1$  denotes the decay constant of the normalized time units  $t$  (potential) dependent second derivative intensity  $SR''(t)$  of the

**Table 4.2.:** Parameters from a fit of simple coupled exponentials (Equations 4.1 to 4.5) to the reoxidation curves shown in Figure 4.3 of the MBH<sub>mem</sub>.  $SR''(0)$  denotes the normalized second derivative intensity of the Ni<sub>a</sub>-SR'' redox species at time zero.

$k_1''$	$k_1'$	$k_2$	$k_3$	
0.044	0.044	0.013	0.005	
$SR''(0)$	$SR'(0)$	$C(0)$	$S_{a/r}(0)$	$B(0)$
1.02	0.50	1.01	0.20	-0.36

CO stretching band from the Ni<sub>a</sub>-SR'' redox state. This quantity is proportional to the concentration of the Ni<sub>a</sub>-SR'' species during the reoxidation process. Similar notations apply for the other redox states. The model is constructed in such a way that the decaying Ni<sub>a</sub>-SR'' and Ni<sub>a</sub>-SR' populate the Ni<sub>a</sub>-C redox state. The Ni<sub>a/r</sub>-S redox state is formed on the expense of Ni<sub>a</sub>-C, which decays with a constant of  $k_2$ . Similarly the Ni<sub>r</sub>-B redox state is formed upon the decay of Ni<sub>a/r</sub>-S with  $k_3$ .

Modeling of these rate equations to the reoxidation curves shown in Figure 4.3 was executed with modified scripts from H. Naumann in GNU octave. The obtained reaction constants are summarized in Table 4.2. The presented data is the first successful kinetic model of the entire reoxidation process. It proves that the involved processes are mainly one-electron transitions between two redox species.

In view of the kinetic model the preferred reaction pathway for the MBH<sub>mem</sub> is sketched in Figure 4.5 with black arrows. These transitions are in accordance to the processes described theoretically in Section 2.2, except that that there is no distinction between Ni<sub>a</sub>-S and Ni<sub>r</sub>-S possible under the present experimental conditions.

The reoxidation behavior of MBH<sub>sol</sub> samples is altered in some aspects, as summarized in Table 4.1. Blue arrows in Figure 4.5 indicate the modified reoxidation process in the MBH<sub>sol</sub>. Here, the transient Ni<sub>a</sub>-S and Ni<sub>r</sub>-S redox states are hardly detectable. Possibly because these species decay almost instantaneously to the Ni<sub>r</sub>-B, when they are formed from the decaying Ni<sub>a</sub>-C species. During the reoxidation process of the MBH<sub>sol</sub> the irreversibly inactive redox state Ni<sub>ia</sub>-S is populated from the decaying reduced species Ni<sub>a</sub>-C and possibly even Ni<sub>a</sub>-SR. This process cannot be modeled with the above mono-exponential rate equations, here coupled sigmoidal functions would be more appropriate. To this point, first attempts in this direction have been made, albeit without satisfactory results for the entire process.

In summary, this section showed the first visualization of the time dependent reoxidation process for the MBH in the solubilized heterodimeric form and for heterodimeric MBH samples attached to the cytoplasmic membrane. In principle both kind of samples show

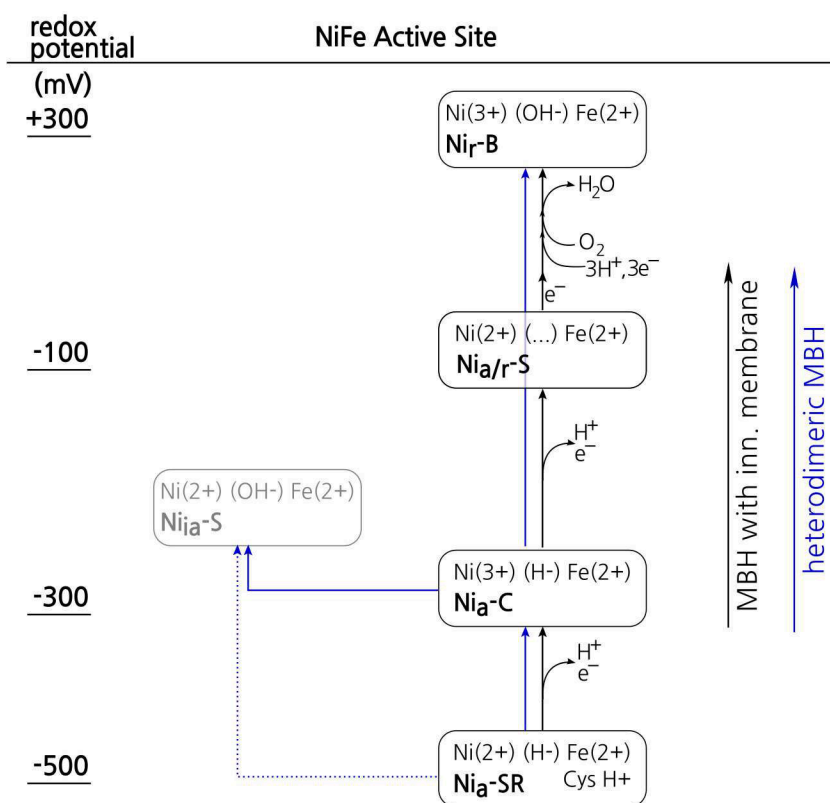


**Figure 4.5.:** Preferred reoxidation pathways for the MBH attached to the membrane (black) and the heterodimeric MBH (blue), derived from relative composition of redox species at comparable time units (potentials) in Figure 4.3 and 4.4. Continuous / dotted blue lines indicate more / less favored redox transitions. Notably, the irreversibly inactive species  $\text{Ni}_{\text{ia}}\text{-S}$  is populated only for heterodimeric MBH samples and it is formed from decaying reduced redox species.

the same redox transitions, but only the solubilized heterodimeric MBH exhibits the inactive redox species  $\text{Ni}_{\text{ia}}\text{-S}$  during and after the completion of the reoxidation process. A qualitative analysis revealed that this species evolves from the decaying reduced redox states  $\text{Ni}_{\text{a}}\text{-C}$  and maybe even  $\text{Ni}_{\text{a}}\text{-SR}$  upon their exposure to oxygen.

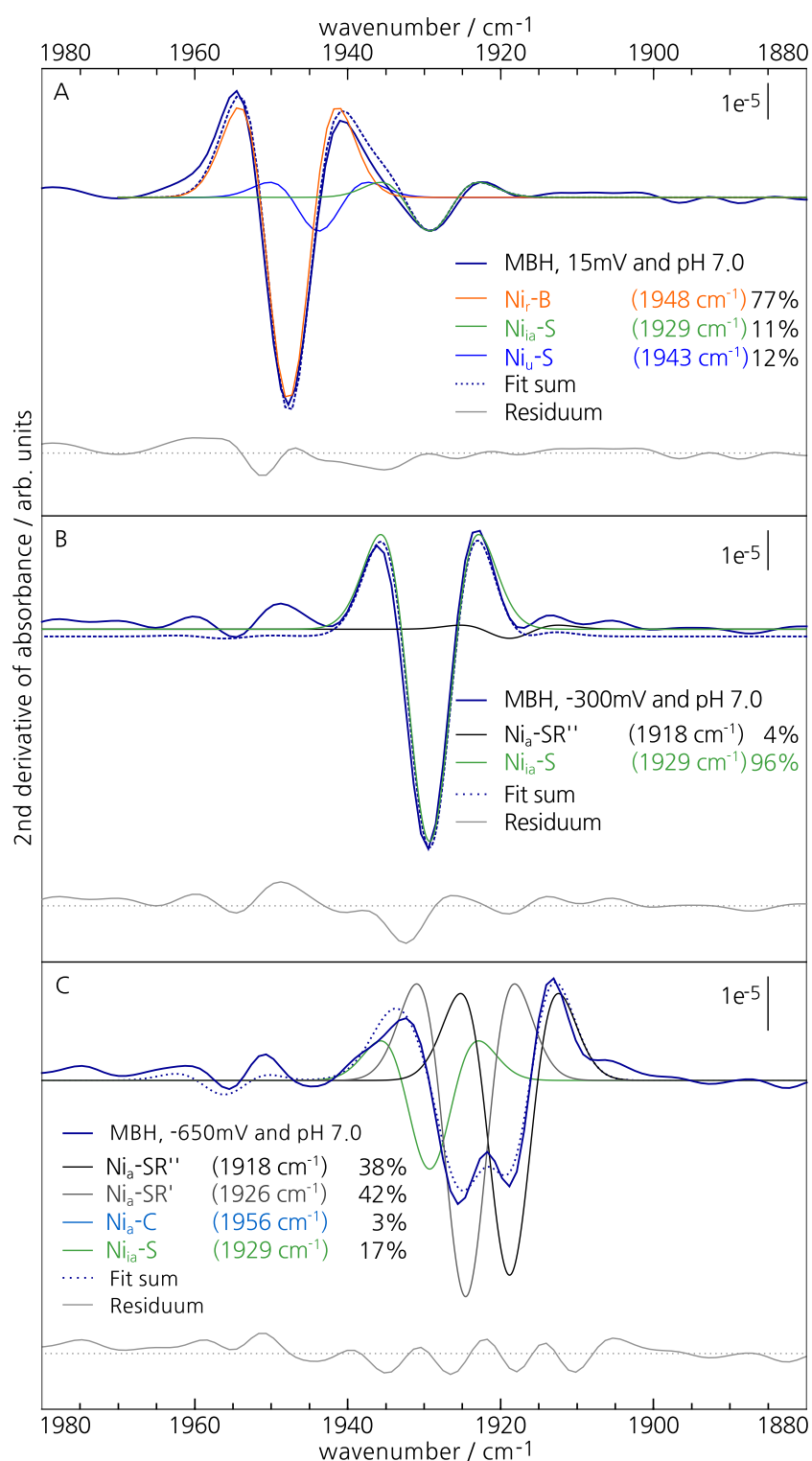
In addition, the reoxidation process for heterodimeric MBH samples attached to the inner membrane was successfully modeled with coupled mono exponential rate equations for the first time. This confirms, that the involved redox transitions are one-electron processes.

## 4.2. Electrochemical Cycling of the Active Site

### Redox States

In this section the redox titration of the oxygen-tolerant  $\text{MBH}_{\text{sol}}$  from *Ralstonia eutropha* at pH 7.0 is described. The determined midpoint potential and number of transferred electrons for the  $\text{Ni}_{\text{a}}\text{-SR}$ – $\text{Ni}_{\text{a}}\text{-C}$  redox couple is compared to values obtained from similar experiments on other oxygen-sensitive and oxygen-tolerant hydrogenases.[34, 81, 85] Moreover, component spectra comprising the CO and CN band positions as well as their relative

**Figure 4.6.:** Second derivative absorption spectra of one  $\text{MBH}_{\text{sol}}$  sample at pH 7.0, 15 °C and different externally applied potentials. A superposition of second derivative Gaussian functions as defined in Equation 4.6 is fitted to the spectral region of the CO stretching bands. The band areas  $A_i$  were fitted, while band positions  $\nu_i$  and widths  $\sigma_i$  are constant. The relative band area is given in percent for each redox species.



absorption intensities are consistently determined for all redox species of the  $[\text{NiFe}]$  active site.

The redox titrations, with *in situ* control of the potential, were performed at a temperature of 15 °C and in the presence of redox mediators [125]. Further experimental details can be found in Section 3.2.

The fraction of the Ni<sub>r</sub>-B species was ca. 90% at the open-circuit potential (OCP) of the aerobically isolated MBH<sub>sol</sub>, indicating fully oxidized samples at pH 7.0.

The following analysis of the relative amount of each redox species as a function of applied potential is aggravated by the fact that no pure redox species can be observed and that the bands of various redox species show a strong superposition due to their inherent wide band widths of up to 14 cm<sup>-1</sup>. In addition, the overall absorbance of the CO and CN stretching modes is low and the spectrum exhibits broad bands related to the mediator cocktail in the spectral region of the CO and CN absorptions. The latter two obstacles are circumvented by using the spectrum of the protein after four days at 15 °C in the very same measurement cell as a background. This spectrum does not show any CO and CN modes of the active site, but the spectral features of the mediator cocktail and possible contaminations at the cell windows are maintained. In such a way all impurities are eliminated from absorbance spectra and the spectral quality is significantly improved as illustrated in Figure B.2. Moreover, as the same protein sample in the same cell is used, both the background and the sample measurement refer to an identical sampling thickness. The second derivatives of the corresponding infrared absorption spectra lack all constant and linear fractions of the spectral background, but the band positions of the CO and CN stretching modes are preserved.

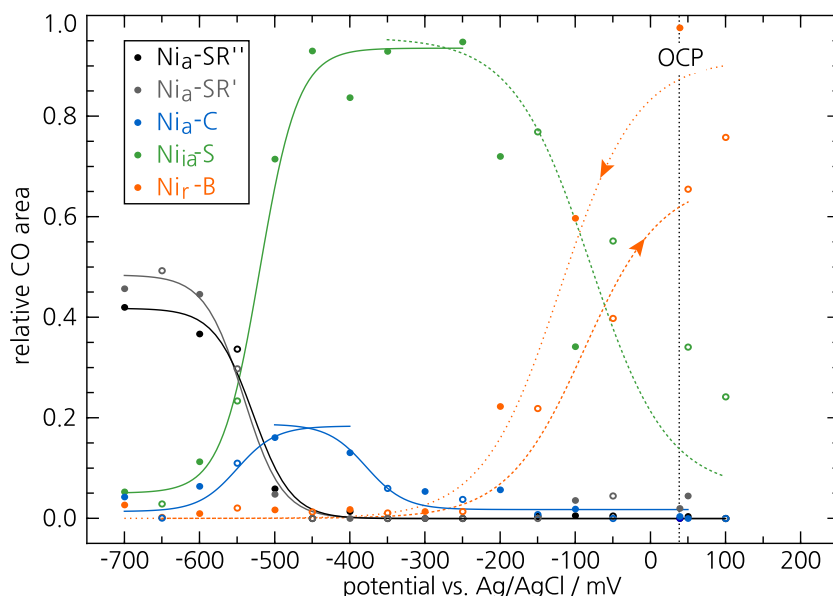
In the need of a reproducible calculation of the relative fraction for each redox species as a function of applied potential, the analysis of the second derivatives absorbance spectra was chosen, in favor of a manual and error-prone baseline correction of a large number of infrared absorbance spectra. A superposition of *i* second derivative Gaussian functions, whereby *i* stands for each redox state of the active site, was fitted to the measured second derivative spectra.<sup>D</sup>

$$\begin{aligned}
 a_i(\nu) &= \frac{A^i \cdot \sqrt{2\pi}}{\sigma_i} \cdot \exp \left[ -2 \cdot \left( \frac{x - \nu_i}{\sigma_i} \right)^2 \right] \\
 a_i''(\nu) &= \frac{4\sqrt{2\pi} \cdot A^i}{\sigma_i^2 \cdot \sigma_i} \cdot \exp \left[ -2 \cdot \left( \frac{\nu - \nu_i}{\sigma_i} \right)^2 \right] \cdot \left( \frac{4}{\sigma_i^2} \cdot (\nu - \nu_i)^2 - 1 \right) \\
 fit(\nu) &= \sum_i a_i''(\nu) \tag{4.6}
 \end{aligned}$$

<sup>D</sup> $a_i(\nu)$  Gauss function and its second derivative  $a_i''(\nu)$   
 $\nu_i$  band position for species *i*  
 $A^i$  = area / integrated intensity  
 $\sigma_i$  = 14.4 cm<sup>-1</sup> band width

The fitted integrated intensity or area  $A^i$  of the band readily corresponds to the relative fraction  $A_{rel}^i$  when calculated with respect to the total area of the CO stretching bands. The fitting routine was executed in GNU octave with home written scripts from H.

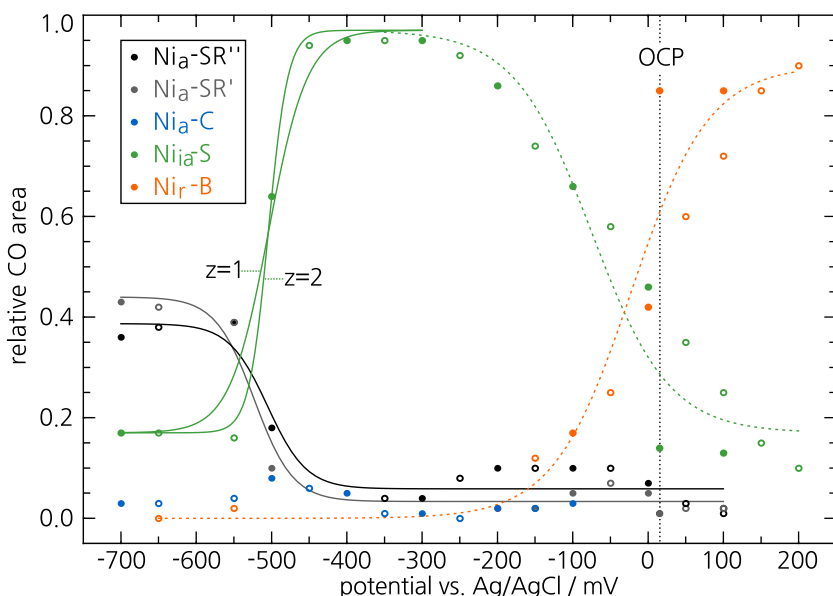
**Figure 4.7.:** Relative absorption  $A_{rel}^i$  as a function of externally applied potential  $V$  for all detected redox species from the active site of one  $MBH_{sol}$  sample at pH 7.0 and 15 °C. Potential steps from the OCP to  $-700$  mV (vs. Ag/AgCl) are marked with  $\bullet$ , likewise potential steps from  $-700$  mV to more positive potentials with  $\circ$ . The values ( $\bullet/\circ$ ) were obtained from fits of Equation 4.6 to the second derivative absorption spectra. See also Figure 4.6. Afterwards, Equation 4.7 was fitted to the  $A_{rel}^i$  (continuous lines). In case, this fit could not be carried out due to a small number of  $A_{rel}^i$  values, dashed lines are given as a guide to the eye.



Naumman, D. v. Stetten and E. Siebert. The results shown in Figure 4.6 prove its feasibility for the spectra under investigation. As demonstrated in Figure 4.6C an absolute quantification of the intensities in the region of the CO stretching modes is not possible solely from the second derivatives. A fit with functions of the form in Equation 4.6 illustrates, that the real band intensities of adjacent bands are larger than shown in the spectrum due the positive shoulders of the second derivative gauss functions.

However, the widely used form for the presentation of IR data are the baseline corrected absorbance spectra. Therefore, three absorbance spectra were baseline corrected and compared to the superposition of Gaussian functions calculated from the fitted values of the corresponding second derivative spectra. (Figure B.4) Clearly, these spectra match the fitted bands very well. Thus, the manual baseline correction of a large number of IR spectra is obsolete. The integrated intensities or areas of the CO bands of the individual redox species from the MBH can be determined with fits of the second derivative FTIR spectra.

The relative absorbance for each redox species is obtained as a function of the applied potential for two heterodimeric  $MBH_{sol}$  samples at pH 7.0 and displayed in Figure 4.7 and 4.8. These values  $A_{rel}^i(V)$  are obtained from the CO stretching bands, as their absorbance is larger than that of the CN stretching vibration.



To determine the midpoint potentials  $V_m$  of the redox couples and the number of transferred electrons  $z$  for each transition, equation:

$$A^i(V) = \frac{A_{max}^i}{1 + \exp\left(\frac{zF}{RT} \cdot (V - V_m)\right)} + C. \quad (4.7)$$

is fitted to the experimental  $A_{rel}^i(V)$ . Due to the limited number of data points the parameter  $z$ , describing the number of transferred electrons for a redox couple, was set to constant values of 0.5, 1.0 or 2.0. Only the  $Ni_a$ -SR– $Ni_a$ -C redox couple could be satisfactorily fitted as a one-electron reaction in Figure 4.7. In contrast, the  $Ni_a$ -C redox state was not populated in the IR-SEC titration of the second  $MBH_{sol}$  sample from a comparable preparation shown in Figure 4.8. Thus, at pH 7.0  $Ni_a$ -C is a transient state between  $Ni_a$ -SR and  $Ni_{ia}$ -S. If the related redox state conversion happens sufficiently fast, the formally dominating redox transition is the one from  $Ni_a$ -SR to  $Ni_{ia}$ -S. This transition might take place as a multiple electron transition. (See Figure 4.8)

The obtained midpoint potential for the  $Ni_a$ -SR– $Ni_a$ -C couple in the  $MBH_{sol}$  at pH 7.0 is compared to the values for another oxygen-tolerant and two oxygen-sensitive hydrogenases in Table 4.3 and actually matches the one of the oxygen-tolerant hydrogenase from *Aquifex aeolicus* reasonably well.[85] The corresponding midpoint potential of the oxygen-sensitive hydrogenases are up to 100 mV lower than those of the two oxygen-tolerant hydrogenases from *Aquifex aeolicus* [85] and the MBH from *Ralstonia eutropha*.

Whenever the intensity of the  $Ni_a$ -SR'/ $Ni_a$ -SR'' species reaches its minimum value the maximal fraction of the  $Ni_{ia}$ -S redox state is detected at a potential of -300 (-90) mV (vs. Ag/AgCl (SHE)). With

**Figure 4.8.:** Similar to Figure 4.7 but relative absorptions  $A_{rel}^i$  were obtained from another  $MBH_{sol}$  sample at pH 7.0 and 15 °C. The values (●/○) were obtained from fits of Equation 4.6 to the second derivative absorption spectra. Afterwards, Equation 4.7 was fitted to the  $A_{rel}^i$ . In case, this fit could not be carried out due to a small number of  $A_{rel}^i$  values, dashed lines are given as a guide to the eye.

Only the species (light green dots and lines) with a CO stretching band at 1929  $cm^{-1}$  shows a considerable offset, which indicates that it is composed of an  $Ni_{ia}$ -S that can be reactivated electro-chemically (under the present conditions) and entirely inactive  $Ni_{ia}$ -S' redox species. In contrast to Figure 4.7 essentially no  $Ni_a$ -C is detected here.

$$^E R = 8.314 \text{ CV K}^{-1} \text{ mol}^{-1}$$

$$F = 9.449 \cdot 10^4 \text{ C mol}^{-1}$$

T[K]: Temperature

z: number of transferred electrons

V[mV]: applied potential vs. Ag/AgCl

$V_m$ [mV]: midpoint potential

$A_{max}^i$ : maximal fraction of species i

C: intensity offset

**Table 4.3.:** Mean values of the midpoint potential of a selected redox-couple derived for the  $\text{MBH}_{\text{sol}}$  from *Ralstonia eutropha* at pH 7 compared to literature values from *Aquifex aeolicus* at pH 7.4, *Desulfovibrio vulgaris* Miyazaki F at pH 6.8 and *Desulfovibrio gigas*.

	redox couple	$V_m$ (mV) vs. SHE
MBH	$\text{Ni}_a\text{-SR}-\text{Ni}_a\text{-C}$ ( $\text{Ni}_{\text{ia}}\text{-S}$ )	$-330$ ( $-304$ ) $\pm 10$
Aquifex	$\text{Ni}_a\text{-SR}-\text{Ni}_a\text{-C}$	$-300 \pm 10$
	$\text{Ni}_a\text{-C}-\text{Ni}_a\text{-S}$	$-295 \pm 10$
	$\text{Ni}_a\text{-S}-\text{Ni}_r\text{-B}$	$-105 \pm 10$
Miyazaki	$\text{Ni}_a\text{-SR}-\text{Ni}_a\text{-C}$	$-432 \pm 20$
	$\text{Ni}_a\text{-C}-\text{Ni}_a\text{-S}$	$-311 \pm 11$
	$\text{Ni}_a\text{-S}-\text{Ni}_r\text{-B}$	$-136 \pm 1$
D. gigas	$\text{Ni}_a\text{-SR}-\text{Ni}_a\text{-C}$	$-430 \pm 5$
	$\text{Ni}_a\text{-C}-\text{Ni}_a\text{-S}$	$-365 \pm 5$
	$\text{Ni}_a\text{-S}-\text{Ni}_r\text{-B}$	$-135 \pm 5$

increasing potentials the redox transition to the  $\text{Ni}_r\text{-B}$  redox state is triggered. However, Equation 4.7 cannot fit this interconversion to a satisfactory level, as two or three electrons are presumably, consecutively transferred in this reaction. This is kind of an artificial reaction and probably pH-dependent.[33, 89]

However, an increase of the potential up to 150 mV above the initial open circuit potential, reveals that the  $\text{Ni}_r\text{-B}$  state can be almost completely restored to its initial level. Thus, the entire electrochemical process is still reversible.

Previous studies characterized the  $\text{Ni}_{\text{ia}}\text{-S}$  state by a CO stretching band at  $1929\text{ cm}^{-1}$  and this state is irreversibly inactive in the presence of hydrogen as a natural substrate.[33] A further inspection of Figure 4.8 reveals that a major fraction of the  $\text{Ni}_{\text{ia}}\text{-S}$  state can be activated under the current experimental conditions, i.e. external applied potentials in the presence of redox mediators. A certain amount, however, remained even here in the irreversibly inactive form, which can be deduced from the constant offset of  $C = 0.17$  obtained in the fit (Table B.1). An explanation for this unexpected behavior might be that an initial (oxidative) damage may happen at the proximal cluster. This affects the electron transport chain.[43] But a direct interaction of the active site with the redox mediators can lead to a reactivation of the enzyme within the externally applied electric field. For residual amounts a more severe damage at or in the vicinity of the active site may have happened, such that the enzyme remains inactive. Although the CO stretching mode of both redox species exhibit the same frequency, the CN stretching modes vary and can be distinguished.

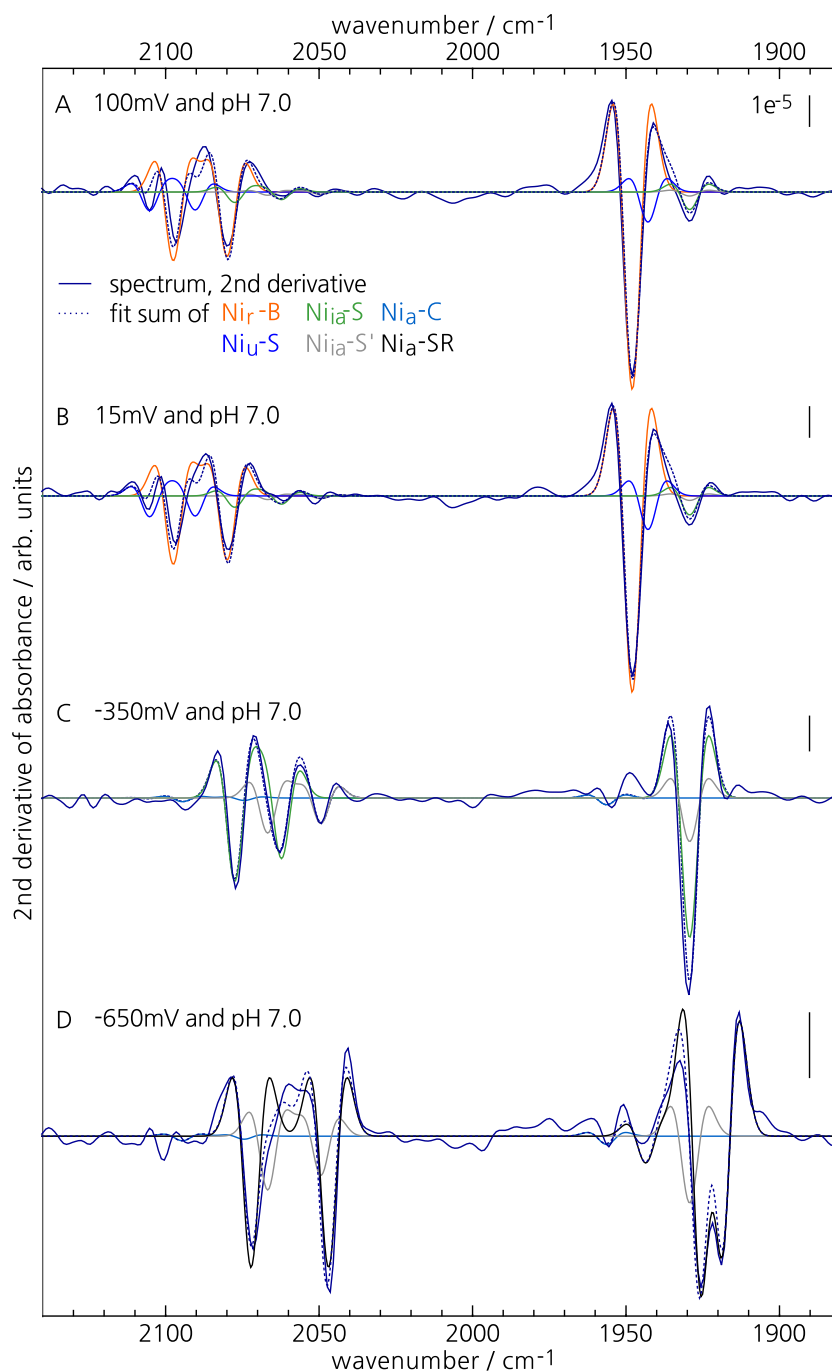
	position $\pm 0.5 \text{ cm}^{-1}$	area $\cdot 10^{-3}$ $\pm 5 \%$	FWHM $\pm 1.0 \text{ cm}^{-1}$
Ni <sub>f</sub> -B	1947.9	1.00	14.4
	2079.7	0.30	14.0
	2097.2	0.32	14.0
Ni <sub>u</sub> -S	1942.8	1.00	14.4
	2090.1	0.55	14.0
	2104.9	0.57	14.0
Ni <sub>a</sub> -C	1956.2	1.00	14.4
	2074.2	0.33	14.0
	2094.2	0.50	14.0
Ni <sub>ia</sub> -S	1929.2	1.00	14.4
	2062.0	0.40	14.0
	2077.2	0.54	14.0
Ni <sub>ia</sub> -S'	1929.2	1.00	14.4
	2049.2	0.54	14.0
	2066.5	0.74	14.0
Ni <sub>a</sub> -SR	1918.9	0.90	14.4
	1925.3	1.00	14.4
	1943.5*	0.10*	14.4*
	2046.7	0.45	14.0
	2071.9	0.45	14.0

**Table 4.4.:** Averaged band parameters for the individual Gaussian shaped bands of each spectral component. The individual envelopes for each species were fitted to the spectra shown in Figure 4.9 according to Equation 4.8.

Note, that the two CN bands of the Ni<sub>a</sub>-SR'' and Ni<sub>a</sub>-SR' redox state are, within 2 to 3 cm<sup>-1</sup>, at the same positions and not distinguished here. Moreover, the relative intensity of the CO band from the Ni<sub>a</sub>-SR redox state is too weak and no CN bands can be spectroscopically resolved.

In an iterative process with fits of the second derivatives of the absorbance spectra obtained with IR-SEC, the CO *and* CN band positions as well as their intensity ratios were determined for all redox species, including the two Ni<sub>ia</sub>-S species, of the MBH<sub>sol</sub> at pH 7.0. The values for each observed redox state are summarized in Table 4.4. Indeed, the re-activable Ni<sub>ia</sub>-S and the entirely irreversibly inactive Ni<sub>ia</sub>-S' species have different CO band positions at 2062 / 2077 and 2049 / 2066 cm<sup>-1</sup>, respectively. The fully reduced species Ni<sub>a</sub>-SR is composed of three CO stretching bands at 1919, 1926 and 1944 cm<sup>-1</sup>. Whereby the latter band contributes only with a relative intensity of ten percent with respect to most intense CO band of Ni<sub>a</sub>-SR' at 1926 cm<sup>-1</sup>. The CN stretching vibrations of Ni<sub>a</sub>-SR' and Ni<sub>a</sub>-SR'' exhibit similar frequencies at 2046 and 2072 cm<sup>-1</sup>. The CN bands at 2090 and 2105 cm<sup>-1</sup> occurring

**Figure 4.9.:** Second derivative absorption spectra of a heterodimeric MBH<sub>sol</sub> sample at pH 7, 15 °C and different externally applied potentials. A component fit for the spectral region of the CO and CN stretching vibrations to the determined components for each redox species as summarized in Table 4.4 is illustrated for different external voltages. The intensities  $A^{i(CO)}$  and  $A^{i(CN)}$  of the CO and CN bands for each species  $i$  are constant, only the scaling factors  $K_i$  are fitted to match the spectrum.



mostly in spectra of oxidized samples are assigned to a CN stretching mode at  $1943\text{ cm}^{-1}$  of an EPR silent Ni<sub>U</sub>-S redox species, that resembles an 'unready' state, with a yet unknown structure, which can be activated to another ready state.[33]

A linear superposition of the derived spectral components for the various redox species of the [NiFe] active site provides a good description of the second derivatives of the absorbance spectra (Figure 4.9) as well as the baseline corrected absorbance spectra (Figure B.4). Again, the superposition of Gaussian functions shown in Figure B.4 is calculated from fitted values of the corresponding

second derivatives.

The global fit of all spectra was executed in GNU octave, with fixed values for band positions and widths.<sup>F</sup>

$$fit(\nu) = \sum_i K_i \left( a''_{i(CO)}(\nu) + a''_{i(CN_1)}(\nu) + a''_{i(CN_2)}(\nu) \right) \quad (4.8)$$

<sup>F</sup>  $a''_{i(\diamond)}(\nu)$  second derivative Gauss function for the CO or CN bands of species  $i$ . With fixed band position  $\nu_i$ , area  $A_i$  and band width  $\sigma_i$ . See Equation 4.6

The intensities  $A^{i(CO)}$  and  $A^{i(CN)}$  of the CO and CN bands for each species  $i$  were kept fixed as well, only the scaling factors  $K_i$  were fitted to match the spectrum.

In summary: With potential dependent IR measurements the midpoint potentials of active site transitions within the MBH<sub>sol</sub> at pH 7.0 could be estimated. Thereby, the values for the Ni<sub>a</sub>-SR–Ni<sub>a</sub>-C redox couple were in satisfactory agreement with previous results on the oxygen-tolerant hydrogenase from *Aquifex aeolicus*.<sup>[85]</sup> Furthermore, the CO and CN band positions as well as their intensity ratios were consistently determined for all redox states. In addition, two Ni<sub>ia</sub>-S species could be distinguished, one reactivable Ni<sub>ia</sub>-S and the entirely irreversibly inactive Ni<sub>ia</sub>-S'. The assignment of the CN band positions of the Ni<sub>u</sub>-S species could be confirmed as well.

A reproducible procedure to analyze a large number of IR spectra, based on the evaluation of the second derivative absorbance spectra is presented. This approach avoids the error-prone manual baseline correction for infrared absorptions of the CO and CN stretching vibrations of the active site, as shown here for analysis of the IR-SEC data. Future data obtained in IR-SEC experiments at different pH values can be evaluated more efficiently.

### 4.3. Conclusion

At a pH value of 5.5 the MBH embedded in its natural environment, i.e. attached to the cytoplasmic membrane (MBH<sub>mem</sub>), reacts completely reversible with hydrogen and oxygen. Moreover, the time dependent reoxidation process can be modeled with coupled first order exponential equations for the decay and rise of the involved redox states. This, confirms that the corresponding transitions between the various species are one-electrons processes.

A loss of the natural electron acceptor cytochrome  $b$  at the end of the electron transport chain alters the reoxidation behavior and the formation of the irreversibly inactive redox species Ni<sub>ia</sub>-S is triggered in the heterodimeric MBH<sub>sol</sub>. The Ni<sub>ia</sub>-S redox state is

presumably formed from the reduced redox state  $\text{Ni}_a\text{-C}$  concomitant with the  $\text{Ni}_{a/r}\text{-S}$  species. Thus, the heterodimeric  $\text{MBH}_{\text{sol}}$  cannot react in a fully reversible way with hydrogen and oxygen anymore. However, compared to earlier preparations [33, 43, 79] the quality of the as-isolated protein samples has been significantly improved. Nevertheless the inherent instability of the solubilized enzyme still has to be overcome.

At pH 7.0 the oxidative damage appears to be more pronounced, as no  $\text{Ni}_{a/r}\text{-S}$  is formed during the aerobic reoxidation.[43, 89] This might be related to the fact that  $\text{Ni}_a\text{-C}$  is not or only weakly accumulated under these conditions. The  $\text{MBH}_{\text{sol}}$  samples at pH 7.0 showed maximal  $\text{Ni}_a\text{-C}$  fractions of less than 15 %. In contrast, the  $\text{Ni}_a\text{-C}$  portion can be as high as 50 % in heterodimeric  $\text{MBH}_{\text{sol}}$  samples at pH 5.5. Interestingly, major amounts of the  $\text{Ni}_{ia}\text{-S}$  species, that does not react with the natural substrate hydrogen, can still be activated in the presence of redox mediators and under externally applied potentials in a SEC cell. A residual amount remains entirely inactive. The initial oxidative damage, leading to the formation of the  $\text{Ni}_{ia}\text{-S}$ , may happen at the proximal FeS cluster and thus affects the electron transport chain.[43] This may be overcome by a direct interaction of the active site and the redox mediators, resulting in the activation of  $\text{Ni}_{ia}\text{-S}$  to  $\text{Ni}_r\text{-B}$  at externally applied overpotentials. Thus, the studied catalytic reactions of the  $\text{MBH}_{\text{sol}}$  are reversible under the chosen experimental conditions. A more severe oxidative damage leads to the formation of the entirely inactive  $\text{Ni}_{ia}\text{-S}'$  species. The two species  $\text{Ni}_{ia}\text{-S}$  and  $\text{Ni}_{ia}\text{-S}'$  exhibit the same band position for the CO , while those of the CN stretching vibrations differ.

# 5. Vibrational Spectroscopy on the Activated MBH at Cryogenic Temperatures

All MBH samples referred to in the next Chapters were purified in the solubilized heterodimeric form, without the primary electron acceptor cytochrome *b*. Therefore, the abbreviation MBH is equivalent to MBH<sub>sol</sub>, without further notice.

Parts of this Chapter have been published in Reference [103] and were obtained in a collaboration between E. Siebert, Y. Rippers and M. Horch. Individual contributions are indicated by the initials. Contributions from J. Fritsch and F. Lenzian are credited likewise.

In this chapter Resonance Raman (RR) spectroscopy will be introduced as an additional vibrational spectroscopic method to characterize the active site of [NiFe] hydrogenases. In concert with further spectroscopic techniques, such as Electron Paramagnetic Resonance (EPR) Spectroscopy, Infrared (IR) Spectroscopy and UV-vis methods as well as quantum mechanical / molecular mechanical (QM/MM) calculations, the potential of this tool will demonstrated to gain further structural and mechanistic insights on the catalytic center. These findings exceed in parts even the capabilities of the x-ray crystallographic data. The first studies in this context were carried on the activated membrane bound hydrogenase (MBH) from *Ralstonia eutropha*.

Before the RR spectra of the activated (H<sub>2</sub>-reduced) MBH are presented, the IR spectra of such MBH samples are studied at temperatures of 80 K and under illumination. (Section 5.1) Under such conditions the Ni<sub>a</sub>-C is transferred to the light-induced Ni<sub>a</sub>-L redox state for hydrogenases from other organisms.[107, 108, 109, 99, 110, 103] The conditions of the IR experiment mimic the measure-

ment conditions of the subsequent RR experiments in Section 5.2 to some extent. Therefore, the RR spectra will be shown to be dominated by vibrational modes from the Fe-CO / CN moiety of the Ni<sub>a</sub>-L redox state. This finding is supported by RR studies on MBH samples at different redox potentials, with genetic variations at the FeS clusters and isotopically labeled <sup>13</sup>C and <sup>15</sup>N samples. In addition, excitation wavelength-dependent RR spectra of the reduced MBH are discussed.

In concert with QM / MM calculations carried out by Y. Rippers it is possible to assign specific modes in the experimental RR spectrum to Fe-CO / CN stretching and bending modes of the active site and confirm a Fe-CO charge transfer as the origin of the resonance enhancement of the Ni<sub>a</sub>-L vibrational modes. (Section 5.3)

### 5.1. Infrared Spectra under the Influence of Light

Similar to most other hydrogenases, the H<sub>2</sub>-reduced MBH from *Ralstonia eutropha* exhibits a mixture of the catalytically active redox states, Ni<sub>a</sub>-SR and Ni<sub>a</sub>-C. Their relative contribution to the active site can be monitored with Fourier Transform Infrared (FTIR) spectroscopy through the detection of their CO and CN stretching modes.[33] The exact composition of these species depends on the redox potential externally applied to the protein. According to the modified Nernst's equation<sup>A</sup> it may be tuned by the pH value and the H<sub>2</sub> partial pressure.[175] Hence, increasing the fraction of the H<sub>2</sub> in the gas mixture from 5 to 100 % lowers the redox potential of the protein at pH 5.5 from -286 mV to -325 mV (vs. Standard Hydrogen Electrode SHE). The FTIR spectra of MBH samples prepared under both conditions are depicted in Figure 5.1. The fully reduced Ni<sub>a</sub>-SR redox state is a mixture of three substates that presumably differ in their degree of protonation and spin state or their interaction with the protein environment.[80, 13] The Ni<sub>a</sub>-SR species are EPR silent (Ni<sup>2+</sup>, S = 1) and most likely carry a hydride ligand in the bridging position between Ni and Fe.[176, 177] The infrared active CO stretching bands of the Ni<sub>a</sub>-SR species are marked in black and their integral amount decreases from 82 to 26 %, at the expense of an increasing Ni<sub>a</sub>-C fraction, when the partial pressure of the H<sub>2</sub> is reduced to 5 %. Further redox species, like the Ni<sub>a/r</sub>-S and Ni<sub>ia</sub>-S, are accumulated under these conditions.

The catalytically active Ni<sub>a</sub>-C redox state is formally reached via one-electron oxidation of the Ni<sub>a</sub>-SR species. With the Nickel in

A

$$V = V_o + \frac{RT}{nF} \ln \left( \frac{a(H^+)^2}{p(H_2)} \right)^{1/2}$$

with: n=2, F=9.648·10<sup>4</sup> C/mol,  
R=8.314 J/K mol and T=300 K,  
ln(a(H<sup>+</sup>))=2.302·log(a(H<sup>+</sup>))=  
-2.302·pH  
p(H<sub>2</sub>)=0.05 or 1.00 for 5 % or 100 %  
hydrogen in atmosphere

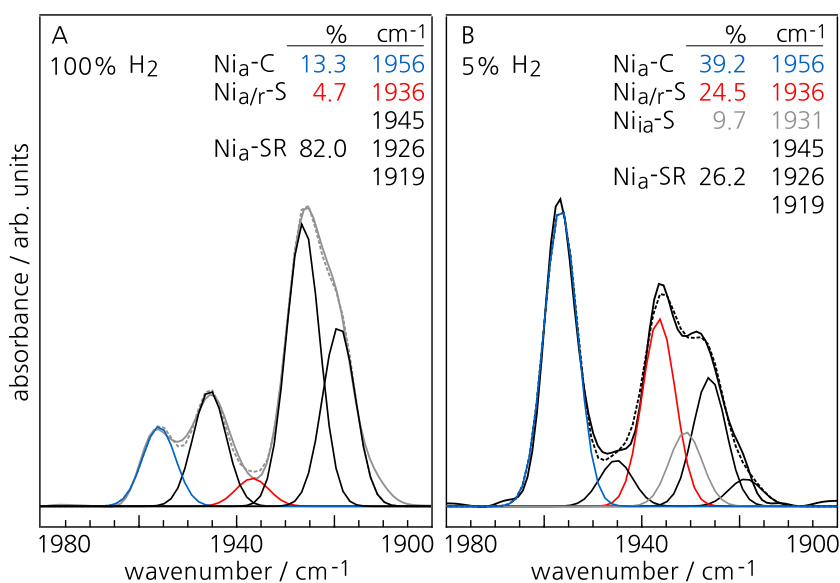


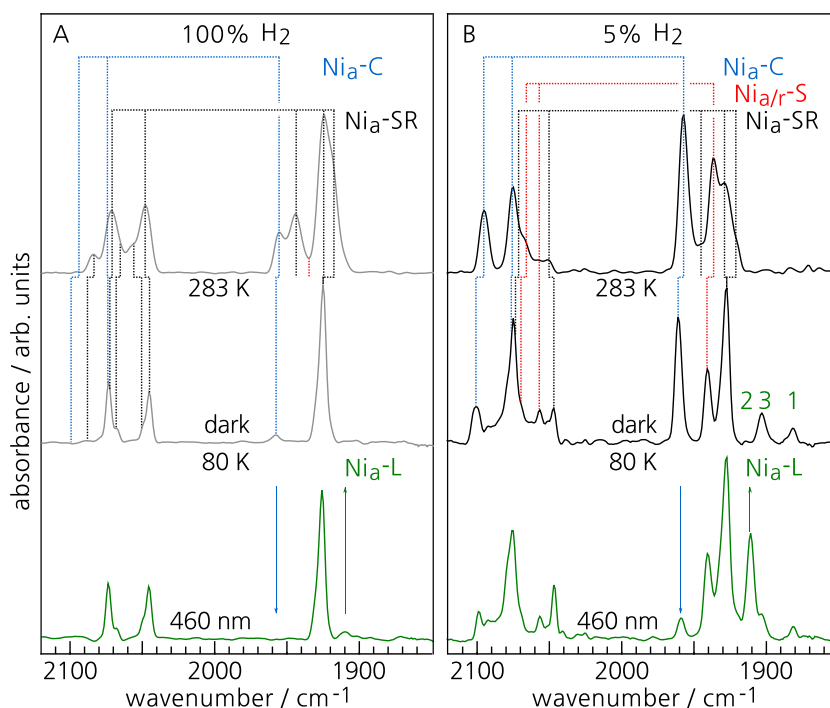
**Figure 5.1.:** FTIR spectra of the MBH at 283 K, either reduced by A) bare hydrogen or B) forming gas (5% H<sub>2</sub>, 95% N<sub>2</sub>). Both spectra were fitted with Gaussian shaped bands with a FWHM of 8 cm<sup>-1</sup>. The band positions of the CO stretching modes and relative intensities of the Ni<sub>a</sub>-C, Ni<sub>a/r</sub>-S and the Ni<sub>a</sub>-SR redox states are given on the right hand side of each panel. In addition, two other EPR silent species with CO band positions at 1936 and 1931 cm<sup>-1</sup> were detected. The first is ascribed to a active ready species Ni<sub>a/r</sub>-S and the the latter species can be assigned to an irreversibly inactive species Ni<sub>ia</sub>-S.[33]

Both samples were solubilized at pH 5.5 and have protein concentrations between 200 and 500 μM.

oxidation state 3+ and a spin  $S = 1/2$ , it is paramagnetic and therefore EPR-active. Due to the charge localization at the active site the electronic transition from Ni<sub>a</sub>-SR to Ni<sub>a</sub>-C is also accompanied by a small decrease of electron density at the Fe ion, which is in agreement with a blue-shift of the infrared active CO and CN stretching modes of the Ni<sub>a</sub>-C.[83] The bridging site between the two metals of the active site has been shown to be occupied by a hydride ligand (H<sup>-</sup>).[99, 100, 101, 102] In oxygen-tolerant hydrogenases this ligand is bound weaker than in the Ni<sub>a</sub>-C redox state of standard hydrogenases. Therefore, the respective redox potentials are approximately 100 mV more positive and the Ni<sub>a</sub>-C state of oxygen-tolerant hydrogenases shows an increased light-sensitivity.[110]

Already in 1985 it has been shown that the [NiFe] active site of the anaerobic working hydrogenase of *Chromatium vinosum* is highly light-sensitive at temperatures below 180 K and that this photoreaction includes a breaking of a nickel-hydrogen bond.[107] This reaction seems to be common feature of all [NiFe] hydrogenases, as it was later observed for hydrogenases of several other organisms [108, 99, 178, 101, 179] and is best described by a photoconversion from the Ni<sub>a</sub>-C to the Ni<sub>a</sub>-L redox state. Hereby, the bridging hydride ligand of the Ni<sub>a</sub>-C is liberated as a proton and the Ni ion in the resulting paramagnetic Ni<sub>a</sub>-L redox state is left in a formal 1+ oxidation state and a spin of  $S = 1/2$ . [108, 99, 102, 100] As a result of the depleted bridging site, the electron density at the iron ion is increased and the infrared active CO and CN stretching modes of the Ni<sub>a</sub>-L are red-shifted with respect to the bands of the Ni<sub>a</sub>-C species.[113]

**Figure 5.2.:** FTIR spectra of the MBH at 283 and 80 K of the MBH, either reduced by A) bare hydrogen or B) forming gas (5 % H<sub>2</sub>, 95 % N<sub>2</sub>). The CO and CN band positions of the Ni<sub>a</sub>-C, Ni<sub>a/r</sub>-S and Ni<sub>a</sub>-SR redox state at both temperatures are indicated by vertical lines. The green trace at the bottom of the figure shows the FTIR spectra under constant LED illumination at 460 nm and 80 K. Here, the Ni<sub>a</sub>-L redox state forms at the expense of the Ni<sub>a</sub>-C state. ES and MH prepared samples and measured spectra from panel B)



The Ni<sub>a</sub>-C to Ni<sub>a</sub>-L conversion is reversible in the dark and at temperatures above 120 to 180 K, depending on the organism.[107, 100, 99] The rebinding of the hydride to the Ni<sub>a</sub>-C redox state is a first order process with an activation energy of 46 kJ/mol in the hydrogenase of *Dv Miyazaki F*. [112] Therefore, the energy of the Ni<sub>a</sub>-L state is higher than that of the Ni<sub>a</sub>-C redox state.[108]

For the MBH photo-dissociation of the bridging hydride of the Ni<sub>a</sub>-C state can be followed by FTIR spectroscopy [114] which is illustrated in Figure 5.2. Here, the displayed region of the spectra shown in Figure 5.1 is expanded to show the CN stretching bands as well. The middle traces show the FTIR spectra of both samples, treated with 100 and 5 % hydrogen, at 80 K. Due to the decreased thermal mobility at these temperatures, the band widths are reduced and the band positions are shifted. The three CO bands of the Ni<sub>a</sub>-SR species merge to one CO band at 1927.0 cm<sup>-1</sup> and two pairs of adjacent CN bands at 2046.5 / 2074.3 cm<sup>-1</sup> and 2049.8 / 2068.8 cm<sup>-1</sup>. (Panel A) This indicates that only two very similar of the three Ni<sub>a</sub>-SR configurations are energetically favored at 80 K. The FTIR spectrum at 80 K of the MBH reduced by 5 % H<sub>2</sub> in panel B exhibits two further CO bands at 1880 and 1903 cm<sup>-1</sup>. They are assigned to the CO stretching modes of the Ni<sub>a</sub>-L1 and Ni<sub>a</sub>-L3 species, in accordance to the nomenclature for Hydrogenase I from *Aquifex aeolicus* in Reference [110]. The Ni<sub>a</sub>-L1 species is known to form at temperatures below 100 K even in the absence of light.[125] Depending on the temperature and du-

ration of illumination a third light-induced Ni<sub>a</sub>-L2 state has been identified for hydrogenases from different organisms.[110, 108, 99, 109] Illuminating these H<sub>2</sub>-reduced MBH samples with continuous light from a diode (LED) emitting at 460 nm results in the spectra shown as blue traces at the bottom of Figure 5.2. Under these conditions the Ni<sub>a</sub>-L2 species forms at the expense of the Ni<sub>a</sub>-C to about 80%. The population of the other two species Ni<sub>a</sub>-L1 and Ni<sub>a</sub>-L3 remains unchanged.<sup>B</sup>

That finding is depicted in a different way in the light-minus-dark FTIR difference spectrum in panel A of Figure 5.3 of the samples reduced by 5% hydrogen. Here, negative bands mark light-sensitive states and positive bands light-induced states. Clearly, the Ni<sub>a</sub>-C state is converted to the Ni<sub>a</sub>-L state. The fully reduced state Ni<sub>a</sub>-SR remains unchanged under these conditions, although a conversion to Ni<sub>a</sub>-L was claimed to be possible.<sup>C</sup> Even after prolonged illumination no conversion of Ni<sub>a</sub>-SR to Ni<sub>a</sub>-L was observed. In turn this implies, that the depletion of the Ni<sub>a</sub>-C species at 80 K is not followed by a redox transition from Ni<sub>a</sub>-SR to Ni<sub>a</sub>-C, to restore the chemical equilibrium between the two redox states.[55, 180, 181, 182] However, the intensity one CO stretching mode at 1932.6 cm<sup>-1</sup> increases under prolonged illumination of the frozen sample. This band possibly belongs to a Ni-S-like redox state of the active site. The rather weak effect of the LED illumination on the FTIR spectra is discussed in more detail in Appendix C.

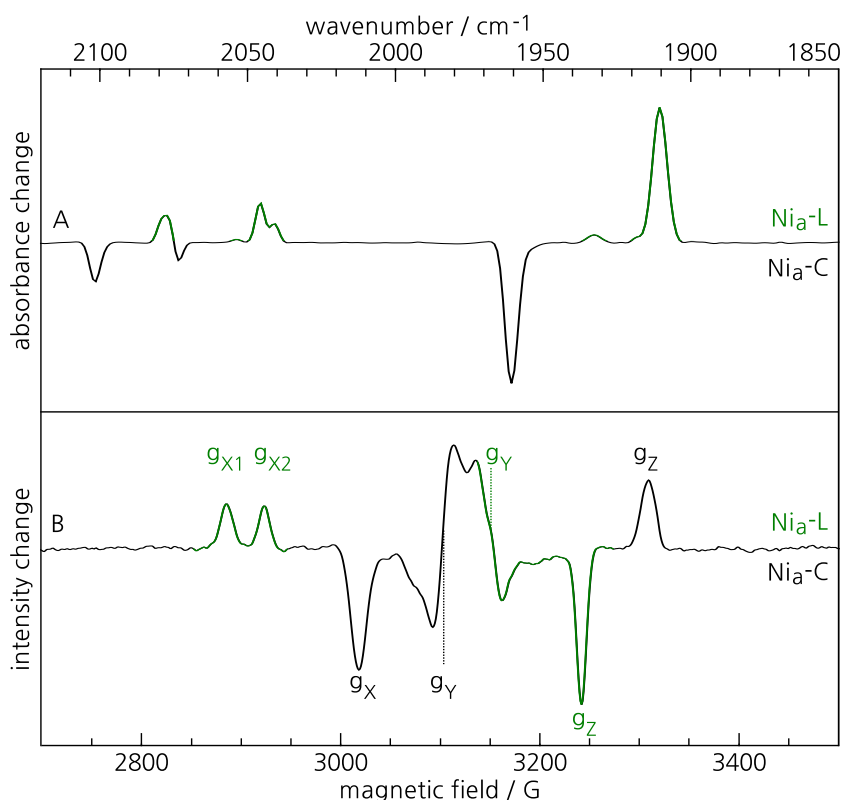
A sample of the MBH prepared under the same conditions was measured with EPR spectroscopy at 80 K under LED illumination at 455 nm. The light-minus-dark difference spectrum is shown in panel B of Figure 5.3. The g-tensor components of the Ni<sub>a</sub>-C and Ni<sub>a</sub>-L are marked in black and green, respectively. Again, the Ni<sub>a</sub>-C to Ni<sub>a</sub>-L photo-conversion is observed. The diamagnetic species Ni<sub>a</sub>-SR and Ni-S cannot be detected in EPR spectroscopy.

These experiments indicate that only vibrational modes of the Ni<sub>a</sub>-L and maybe of the Ni<sub>a</sub>-SR can be detected in RR spectra of similar samples. As the Ni<sub>a/r</sub>-S species also contributes with up to 24% to the FTIR spectrum of the 5% H<sub>2</sub>-reduced MBH (Figure 5.1B), its vibrational modes are anticipated, as well.

<sup>B</sup>In the following Ni<sub>a</sub>-L will refer to Ni<sub>a</sub>-L2 without further notice.

<sup>C</sup>Personal communication between M.E. Pandelia and K. Bagley in 2009 [83]

**Figure 5.3.:** Light-Minus-Dark difference spectra of the MBH reduced by 5% H<sub>2</sub>, measured at 80 K with A) FTIR and B) EPR spectroscopy. Black signals refer to Ni<sub>a</sub>-C and green signals to Ni<sub>a</sub>-L. A weak positive band at 1932.6 cm<sup>-1</sup> in the FTIR spectrum possibly belongs to the CO stretching mode of a Ni-S species of the active site. (See Appendix C) ES and MH prepared the samples and measured the spectra in panel A), FL measured the spectra in panel B).



## 5.2. Resonance Raman Characterization of the Reduced Active Site

Vibrational spectra of the MBH contain contributions from the protein backbone and its cofactors: the three different FeS clusters of the electron transport chain and the [NiFe] center of the active site. The inherent complexity of a Raman spectrum can be reduced by tuning the wavelength of the exciting laser beam to a absorption maximum of one specific cofactor. In the corresponding RR spectrum the vibrational modes of this cofactor are resonantly enhanced, while modes of other cofactors have decreased intensities or are even completely omitted. With this procedure certain Raman active modes may be readily assigned to specific cofactors of the studied protein.

### 5.2.1. UV-vis Spectra of the MBH

In order to obtain the main electronic absorption bands of the MBH, UV-vis spectra of the as-isolated and H<sub>2</sub>-reduced enzyme were measured at 283 K by J. Fritsch prior to the RR experiments. Due to their high extinction coefficients, the corresponding absorption bands of the protein, i.e. the peptide bonds (190 to 230 nm) and the amino acids (250 to 280 nm) [183], are not shown in the

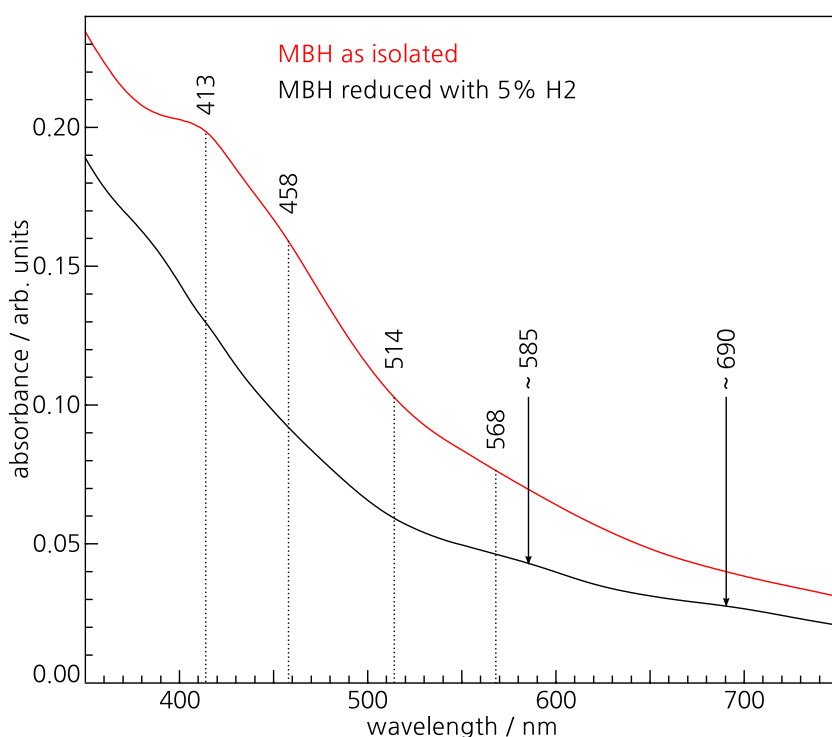


**Figure 5.4.:** UV-vis spectra of the as-isolated and H<sub>2</sub>-reduced MBH sample at 283 K, in red and black respectively.

The spectral region below 500 nm is dominated by a broad absorption through the FeS clusters, which significantly decrease for the reduced MBH. In contrast, two shallow absorption bands at approximately 585 and 690 nm are better resolved here. Dotted lines indicate the laser positions for the subsequent RR experiments at 80 K on similar samples.

Spectra measured by JF

spectral window displayed in Figure 5.4.

While the UV-vis spectrum of the as-isolated MBH is dominated by a broad absorption related to a S  $\rightarrow$  Fe charge transfer in the three FeS clusters ([4Fe3S], [3Fe4S], [4Fe4S]) between 400 and 500 nm, the corresponding absorption band of the hydrogen-reduced enzyme is significantly decreased. This is in agreement with previous studies on iron sulfur proteins, where oxidized [3Fe4S] and [4Fe4S] clusters have been shown to absorb between 415 to 455 nm and at  $\sim$  390 nm and with extinction coefficients of up to  $16000 \text{ M}^{-1} \text{ cm}^{-1}$ .<sup>D</sup> Upon reduction the extinction coefficients of the [3Fe4S] clusters drop to  $\sim 9600 \text{ M}^{-1} \text{ cm}^{-1}$ , while the [4Fe4S] clusters merely exhibit broad and weak absorption bands.[186, 187, 37] Such studies are not yet available for [4Fe3S] cluster, which was recently in the MBH from *Ralstonia eutropha* and other oxygen-tolerant hydrogenases.[44, 45, 46, 47]

In contrast to the absorption spectrum of the as-isolated MBH, two shallow absorption bands at approximately 585 and 690 nm are resolved for the reduced enzyme. Such bands have also been observed for *Desulfovibrio vulgaris* Miyazaki F and were assigned to electronic transitions in the [NiFe] active site exclusively.[38, 70] EPR measurements on these samples illuminated with 10 Hz laser pulses between 355 and 1064 nm proved that the Ni<sub>a</sub>-C to Ni<sub>a</sub>-L photoconversion is maximal at 590 and 700 nm. Although incident light with wavelengths below 400 nm is essentially absorbed

<sup>D</sup>In comparison, the extinction coefficients of cytochrome *c* can be as high as  $100\,000 \text{ M}^{-1} \text{ cm}^{-1}$ . [184, 185]

through the FeS clusters [186, 187], the Ni<sub>a</sub>-C to Ni<sub>a</sub>-L conversion was saturated at 355 nm with increased pulse powers. This indicates, that the conversion is only weakly influenced by the absorption of light through the FeS clusters.[70] Hence, continuous illumination of H<sub>2</sub>-reduced MBH samples with (laser) light between approximately 350 and 700 nm causes an essentially complete photo-conversion of the Ni<sub>a</sub>-C to the Ni<sub>a</sub>-L redox state of the [NiFe] active site. In accordance to the UV-vis spectra, excitation wavelengths at 413, 458, 514 and 568 nm were chosen for the following RR experiments. RR spectra of the reduced and oxidized MBH samples obtained at 413 nm turned out to be dominated by vibrational modes from the buffer solution and will not be considered in the following discussion. For the sake of completeness these spectra can be found in Appendix C Figure C.2.

In contrast to the UV-vis spectra, which were recorded at 283 K, all RR measurements were performed at 80 K. In general, it is observed that the main absorption bands in the UV-vis spectrum narrow and shift in wavelengths with decreasing temperatures. Since the oscillator strength remains constant, an increase of the extinction coefficient is observed with decreasing temperature.[188] Anyhow, the main absorption bands remain in a spectral region between 400 and 600 nm.

### 5.2.2. RR Spectra Under Different Reducing Conditions

Initially, RR spectra from MBH samples either reduced with 5% or 100% hydrogen were obtained at sample temperatures of 80 K and an excitation wavelength of 458 nm. The MBH samples are, apart from the increased protein concentration of up to 1000  $\mu$ M, identical to the samples used for the FTIR measurements shown in Figure 5.2. The corresponding RR spectra are shown in Figure 5.5 and may be divided into two characteristic spectral regions.

The first region from 250 to 400  $\text{cm}^{-1}$  comprises stretching, bending and breathing modes of the FeS clusters. Due to the low extinction coefficients bands of the reduced FeS clusters hardly contribute to this spectral region. Upon increasing the partial hydrogen pressure in the reducing gas mixture, contributions of the FeS stretching modes to the RR spectrum are further suppressed. This effect can be clearly observed in Figure 5.5 for the spectral region of the FeS bands. And at least one band at 342  $\text{cm}^{-1}$  significantly drops in intensity upon further reduction with 100% hydrogen,

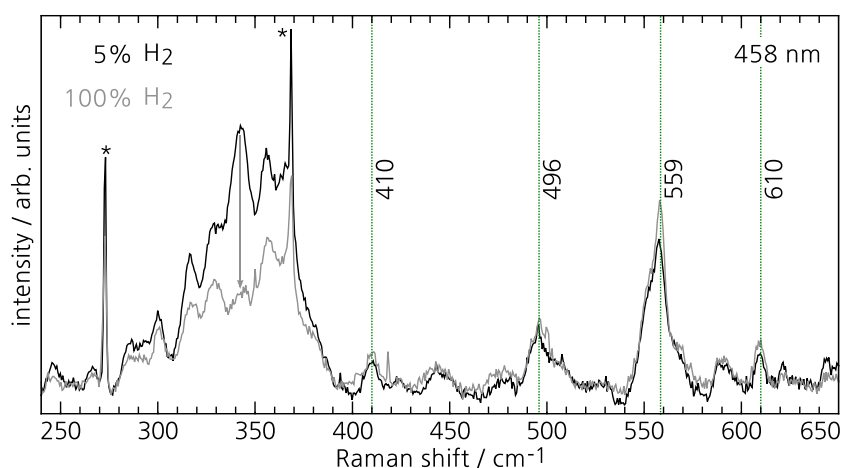


**Figure 5.5.:** RR spectra of two MBH samples, either incubated with forming gas (5 % H<sub>2</sub>, 95 % N<sub>2</sub>, black trace) or bare hydrogen (gray trace). The spectra are essentially identical with respect to the four marked bands between 400 and 650 cm<sup>-1</sup>. On the contrary, at least one band in the region below 400 cm<sup>-1</sup> of the FeS bands modes significantly drops in intensity upon further reduction with 100 % hydrogen.

Peaks labeled with an asterisk correspond to a photoluminescence of the quartz sample holder and ice. Both samples were solubilized at pH 5.5 and have a concentration of 900 μM. The spectra were recorded at a sample temperature of 80 K and an excitation wavelength of 458 nm. The corresponding FTIR spectra of the same samples can be found in Figure 5.2.

leaving a broad superposition of vibrational modes from the three fully reduced FeS clusters. Due to the low resonance enhancement of the reduced FeS clusters, also cluster related modes such as Fe-OH modes which are expected beyond 400 cm<sup>-1</sup> can be excluded as additional contributions to the RR spectrum.[186, 187, 37, 113] Nevertheless, the second spectral region of the RR spectra from 400 to 650 cm<sup>-1</sup> displays a set of pronounced vibrational bands. This spectral region is characteristic for Fe-CO / CN stretching and bending modes[113], consistent with previous findings on hydrogenase model compounds.[41, 39, 40] The detected vibrational bands at 410, 496, 559 and 610 cm<sup>-1</sup> for RR spectra of the hydrogen-reduced MBH, are not observed in this form in the RR spectra of the as-isolated MBH samples, measured under the same conditions. (See Chapter 6) Therefore, the observed vibrations are characteristic for the [NiFe] active site of the H<sub>2</sub>-reduced MBH from *Ralstonia eutropha*. With respect to the results discussed in Section 5.1 only modes of the Ni<sub>a</sub>-L, Ni<sub>a</sub>-SR and a Ni-S like species may contribute to these RR spectra excited at 458 nm. The observed bands for the H<sub>2</sub>-reduced MBH between 400 and 650 cm<sup>-1</sup> are, in terms of band positions and relative intensities, independent of the Ni<sub>a</sub>-C to Ni<sub>a</sub>-SR ratio prior to the RR measurement. This indicates that equal amounts of the same species are probed and that the equilibria of all reduced species are altered in favor for the detected species in the RR experiment. This is best explained by a efficient photo-conversion of the Ni<sub>a</sub>-C and the Ni<sub>a</sub>-SR redox state to the Ni<sub>a</sub>-L state under the high photon flux of the laser beam.<sup>E</sup> Thus, the RR spectrum of the reduced MBH reveals the Raman active bands of the Ni<sub>a</sub>-L redox state. Minor contributions of a Ni-S like redox state cannot be ruled out at this point.

The assignment of the bands between 400 and 650 cm<sup>-1</sup> to modes

<sup>E</sup>FTIR: 12 LEDs a 11 mW illuminate an area with a diameter of 15 mm → power/area = 12 × 11 mW/176 mm<sup>2</sup> = 0.75 mW/mm<sup>2</sup>

RR: Laser at 2 mW illuminates an area of 2 μm<sup>2</sup> → power/area = 2 mW/2 · 10<sup>-6</sup> mm<sup>2</sup> = 1 · 10<sup>6</sup> mW/mm<sup>2</sup> → increased by more than six orders of magnitude

of the [NiFe] active site is further supported by comparing RR spectra of MBH wildtype samples to MBH samples with modified FeS clusters but intact active sites. Also,  $^{13}\text{C}$  and  $^{15}\text{N}$  labeling experiments and excitation wavelength-dependent RR studies are considered.

### 5.2.3. RR Spectra of MBH Variants

To rule out (minor) contributions of FeS cluster modes in the spectral region from 400 to  $650\text{ cm}^{-1}$ , RR spectra of MBH variants with exchanged amino acid residues in the vicinity of the FeS clusters were examined. Originally, these MBH variants were developed by T. Goris, J. Fritsch, S. Frielingsdorf and O. Lenz [43, 47] to unravel the influence of the proximal [4Fe3S] cluster on the remarkable oxygen-tolerance of the MBH from *Ralstonia eutropha*.

Two genetically engineered MBH variants are considered for the decryption of the RR spectra of the  $\text{H}_2$ -reduced MBH: In the C120G/C19G variant two cysteines at the proximal cluster were exchanged by two glycines. As a consequence the proximal FeS cluster of this variant is formed as a [4Fe4S] instead of a [4Fe3S] cluster.[43] Exchanging the His229, which is in hydrogen bonding distance to the hydroxyl ligand of the superoxidized proximal cluster, with a methionine does not change the overall structure of the proximal cluster as compared to the superoxidized wildtype, but the hydroxyl ligand is missing in that H229M variant of the MBH.[189] The active site of both MBH variants remained unaffected.

The RR spectra of the two MBH variants reduced with 5% hydrogen are compared to the respective MBH wildtype sample in Figure 5.6. Due to the weak resonance enhancement of the reduced FeS clusters, the RR signals between 250 and  $400\text{ cm}^{-1}$  are almost identical for the three samples. Minor differences are attributed to the modifications at the proximal FeS cluster. The marked bands between 400 and  $650\text{ cm}^{-1}$ , that were initially attributed to modes of the [NiFe] active site, do not change with respect to band position and relative intensity ratio. Thus, these bands are independent of modifications at the proximal cluster and they are definitely related to modes of the active site, which was not affected in the MBH variant samples.

Five additional bands between 400 and  $650\text{ cm}^{-1}$  are identified in the RR spectra of the MBH wildtype and both MBH variant samples. They are marked with red lines in Figure 5.6 and Chapter 6

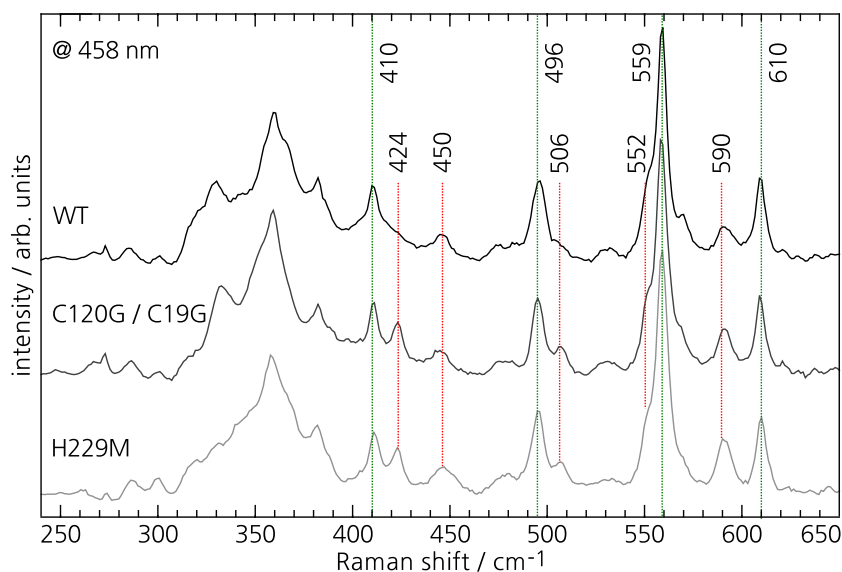


**Figure 5.6.:** RR spectra of 5% hydrogen-reduced samples from the MBH wildtype, C120G/C19G and H229M variant of the MBH recorded at 458 nm. Green vertical lines mark the band positions of the  $\text{Ni}_a$ -L redox state of the active site and red lines of a further cofactor of the MBH.

All spectra were obtained from crystalline samples, further details on that in Chapter 6.

is concerned with their origin.

#### 5.2.4. RR Spectra Isotopically Labeled Samples

To confirm that the vibrational modes between 400 and 650  $\text{cm}^{-1}$  originate from vibrations of the Fe-CO / CN moiety of the active site,  $^{13}\text{C}$ - and  $^{15}\text{N}$ -labeled MBH was purified from cells cultivated in a media either containing  $^{13}\text{C}$ -labeled glycerol or  $^{15}\text{N}$ -labeled  $^{15}\text{NH}_4\text{Cl}$ , respectively. [43, 103] Through the isotopic shifts of the CO and CN bands monitored in FTIR spectra of these samples (Figure 5.7), it can be deduced that the  $^{15}\text{N}$  is completely and the  $^{13}\text{C}$  is to circa 85% incorporated into the protein. As for the CO and CN bands in FTIR spectroscopy, the RR spectrum of the  $^{13}\text{C}$ -labeled and  $\text{H}_2$ -reduced MBH shows clear isotopic shifts from  $\Delta\nu = -8$  to  $-13 \text{ cm}^{-1}$  of the bands between 400 and 650  $\text{cm}^{-1}$  (Figure 5.8). Only small isotopic shifts on the order of  $\Delta\nu = -1 \text{ cm}^{-1}$  are observed for  $^{15}\text{N}$ -labeled MBH samples. Thus, the Raman bands have contributions from vibrations of the CO and  $\text{CN}^-$  ligands bound to the Fe atom of the active site and a Fe-CO metal-to-ligand charge transfer might be the origin of the resonance enhancement of these modes.

#### 5.2.5. RR Spectra at Different Excitation Wavelengths

In addition to the alternated absorption bands of the FeS clusters, the UV-vis spectrum of the hydrogen-reduced MBH showed two further shallow absorption bands at 585 and 690 nm. According

**Figure 5.7.:** FTIR spectra of MBH samples reduced by 100 % hydrogen at room temperature. The traces refer to A) non-labeled, B)  $^{15}\text{N}$ - and C)  $^{13}\text{C}$ -labeled protein. Isotopic shifts are given with respect to the absolute frequencies of the CO and CN absorption bands of the non-labeled protein, which are characteristic for the  $\text{Ni}_a\text{-C}$  (1956  $\text{cm}^{-1}$ ) and the  $\text{Ni}_a\text{-SR}$  states (1926, 1944, 2047 and 2071  $\text{cm}^{-1}$ ).

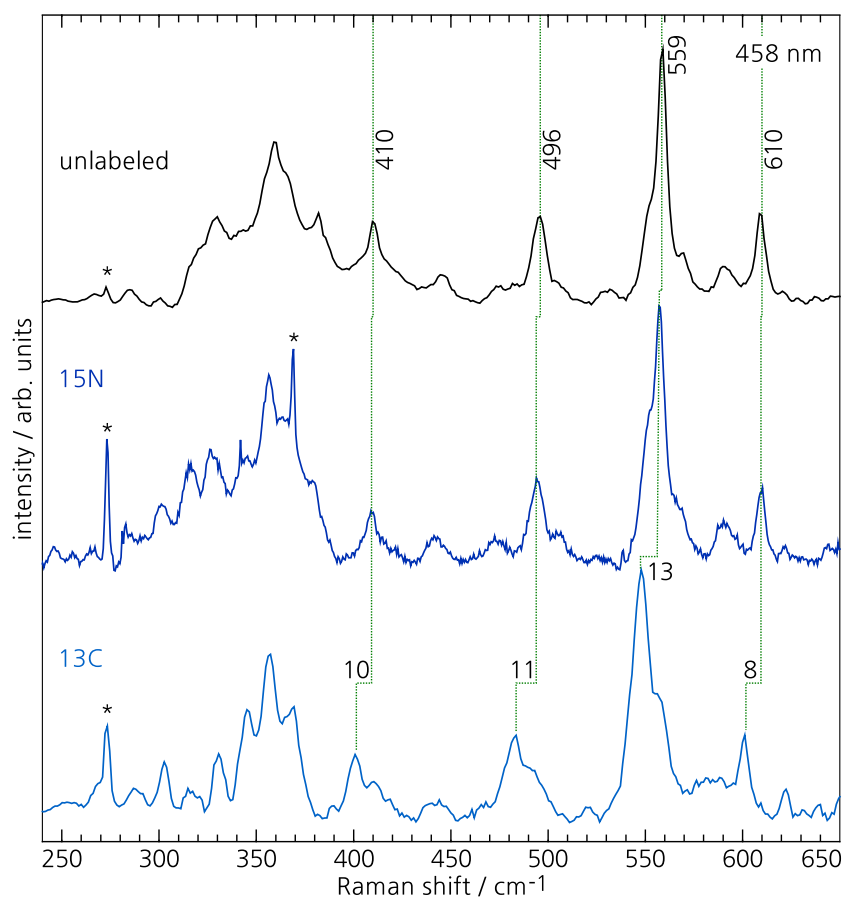
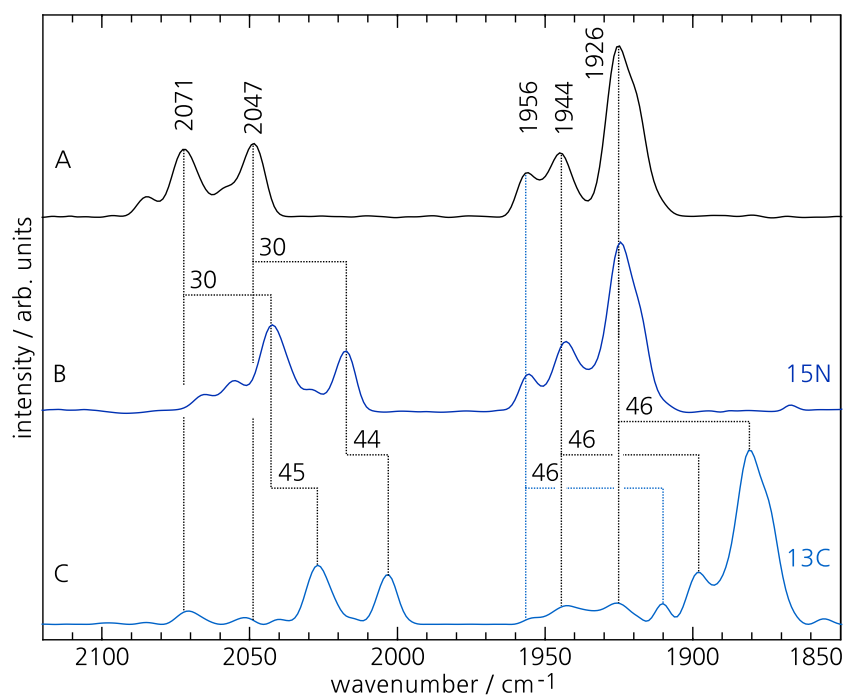
Accordingly, the CN absorption bands of the  $^{15}\text{N}$ -labeled sample reveal a complete labeling. In contrast,  $^{13}\text{C}$  is incorporated to approximately 85 % into the protein, as a fraction of both, the CO and CN bands, does not show an isotopic shift. All samples were solubilized at pH 5.5 and have concentrations between 200 and 500  $\mu\text{M}$ . The FTIR spectra were recorded in transmission geometry at a sample temperature of 283 K.

MH measured the  $^{13}\text{C}$  spectrum

**Figure 5.8.:** RR spectra of 100 %  $\text{H}_2$ -reduced MBH samples at 458 nm and 80 K. Non-labeled wildtype in black,  $^{15}\text{N}$  and  $^{13}\text{C}$ -labeled in dark-blue and blue, respectively. Only small isotopic shifts on the order of  $1\text{ cm}^{-1}$  are observed for  $^{15}\text{N}$ -labeled samples. In contrast, the  $^{13}\text{C}$ -labeled samples show distinct isotopic shifts from -8 to -13  $\text{cm}^{-1}$ , with respect to the non-labeled reference spectrum.

Peaks marked with an asterisk correspond to a photoluminescence of the quartz sample holder and ice.

MH measured the  $^{13}\text{C}$  spectrum



to the work of Fichtner *et al.* on *Desulfovibrio vulgaris* Miyazaki F a maximal Ni<sub>a</sub>-C to Ni<sub>a</sub>-L photo-conversion is expected at these wavelengths.[70] Therefore, an excitation wavelength of 568 nm was chosen in (pre-) resonance with the first electronic absorption band of the reduced MBH. To examine the evolution of the various RR bands detected with excitation wavelengths of 458 and 568 nm, 514 nm was selected as an intermediate wavelength. The RR spectra recorded at these wavelengths on the same MBH sample, reduced with 5 % hydrogen, are shown in Figure 5.9.

The most dramatic changes in the RR spectra are detected between 250 and 400 cm<sup>-1</sup>. At excitation wavelengths larger than 458 nm the broad signal, related to overlapping bands of the reduced FeS clusters decreases, as these modes are no longer resonantly enhanced. Two sharp bands of high intensities at 317 and 361 cm<sup>-1</sup> emerge in the RR spectrum measured at 568 nm. They presumably originate from vibrational modes of the [NiFe] active site as well. The RR spectrum of the regulatory hydrogenase measured at 568 nm exhibits a number of weak bands in the spectral window from 345 to 385 cm<sup>-1</sup>. They were likewise attributed to modes of the active site.[190]

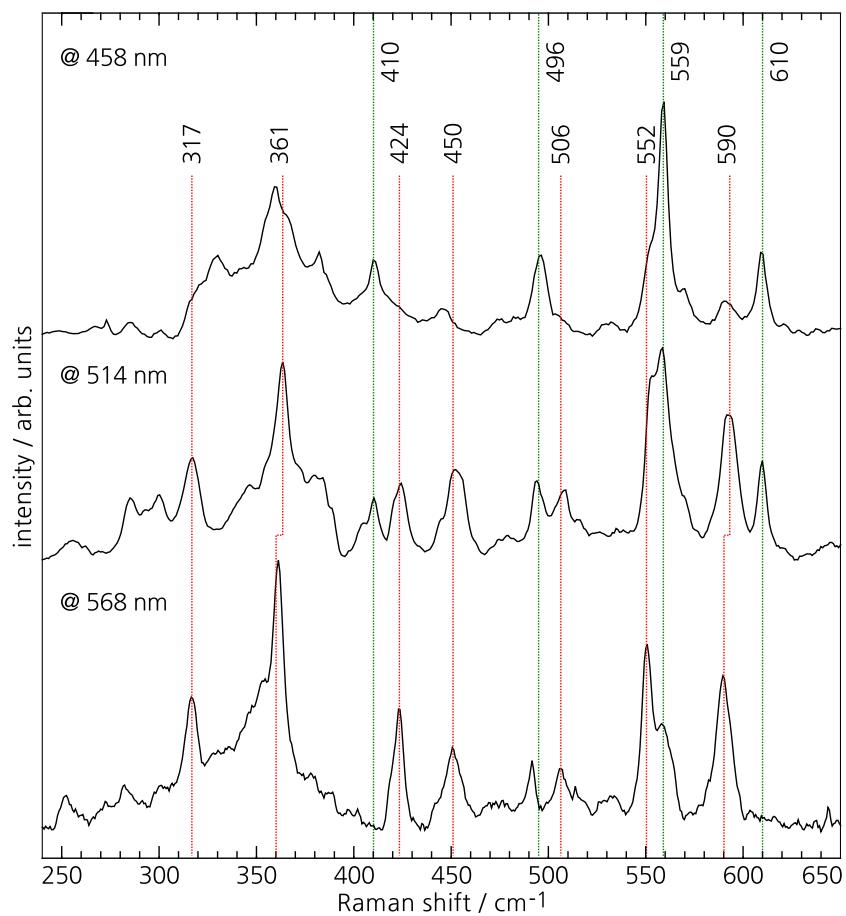
In the spectral region above 400 cm<sup>-1</sup> green vertical lines again indicate the positions of the bands that are assigned to modes of the Ni<sub>a</sub>-L redox state. The intensities of these bands decrease with increasing excitation wavelength and cannot be detected in the RR spectrum recorded at 568 nm. Thus, vibrational modes of the Ni<sub>a</sub>-L redox state are no longer resonantly enhanced at excitation wavelengths equal to or larger than 568 nm. Instead a new set of bands arises, as indicated by red lines. These bands were observed for the RR spectra of the C120G/C19G and H229M variants of the MBH as well (Figure 5.6) and their origin is discussed in the Chapter 6.

### 5.3. Calculated Raman Spectra

In the framework of the present experimental Raman studies Y. Rippers has derived calculated Raman spectra of the reduced active site by means of a hybrid quantum mechanical / molecular mechanical (QM / MM) model that was constructed on the basis of a computationally refined crystal structure of the H<sub>2</sub>-reduced MBH.[103, 44, 191] Since the experimental Raman bands show a sensitivity towards <sup>13</sup>C labeling, a resonance enhancement through

**Figure 5.9.:** Comparison of the RR spectra from 5% hydrogen reduced MBH wildtype samples excited at 458, 514 and 568 nm, respectively. Green vertical lines mark the band positions of the Ni<sub>a</sub>-L redox state of the active site.

At excitation wavelengths larger than 458 nm the signal of the overlapping bands from the reduced FeS cluster decreases - as the clusters no longer experience a resonant enhancement. With increasing laser wavelength a set of new bands emerges in the RR spectra, at the expense of decreasing intensities for the Ni<sub>a</sub>-L bands. The nature of these bands, marked in red, will be discussed in the Chapter 6.



a Fe-CO metal-to-ligand charge transfer transition is assumed. To mimic this, the calculated Raman intensities of the individual modes were approximated according to the contribution of the Fe-CO bending and stretching coordinates to the potential energy distribution (PED).[192] Such spectra were calculated for various oxidation, spin, and coordination states of the [NiFe] active site and different protonation states of the terminal Cys597 ligand of the nickel ion. The influence of these parameters on the calculated Raman spectra of the Ni<sub>a</sub>-L redox state is illustrated in Figure C.4. All calculated spectra indeed display distinct bands in the 400 to 650 cm<sup>-1</sup> spectral region, but most of them differ substantially from the experimental spectrum. Thus, a more detailed inspection is restricted to the calculated spectra of the Ni<sub>a</sub>-C, Ni<sub>a</sub>-L and Ni<sub>a</sub>-SR states (Figure 5.10). Hereby, the latter two are protonated at the Cys597 sulfur. The calculations for all three species reveal two closely spaced modes of predominant Fe-CO bending and stretching character, in agreement with the strongest band at 559 cm<sup>-1</sup> in the experimental spectrum. In accordance to the labeling experiments presented in Figure 5.8 <sup>15</sup>N and <sup>13</sup>C isotopic shifts were calculated for the Raman active modes of the Ni<sub>a</sub>-C, Ni<sub>a</sub>-SR and

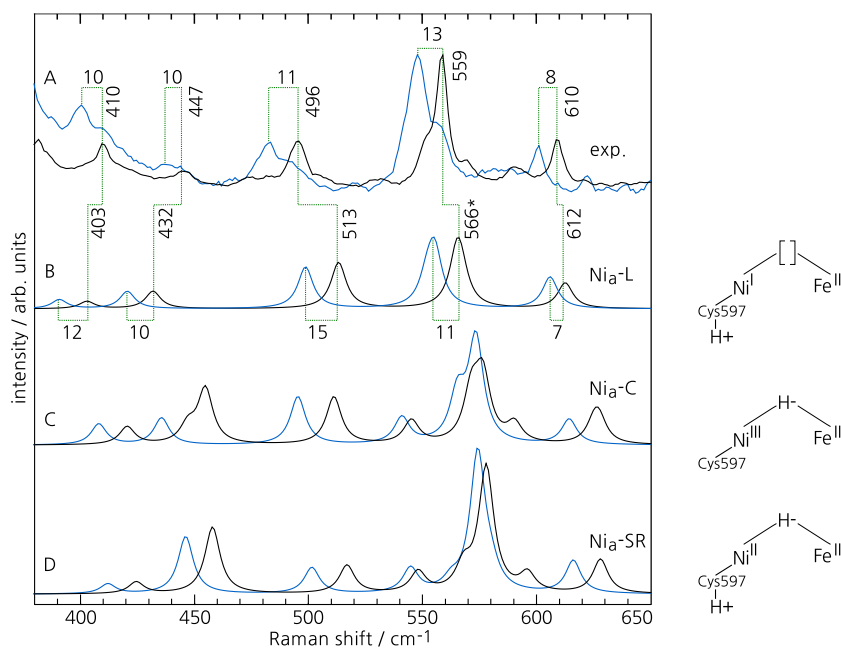


**Figure 5.10.:** A) Experimental RR spectrum of the MBH reduced by 5%  $\text{H}_2$  and calculated Raman spectra of the  $[\text{NiFe}]$  active site in the  $\text{Ni}_a\text{-L}$  (B),  $\text{Ni}_a\text{-C}$  (C) and  $\text{Ni}_a\text{-SR}$  (D) redox state. Black traces correspond to non-labeled samples and blue traces to  $^{13}\text{C}$  labeled samples. The band at  $566\text{ cm}^{-1}$  of the  $\text{Ni}_a\text{-L}$  redox state is related to the superposition of two normal modes at  $565$  and  $567\text{ cm}^{-1}$  and is therefore marked with an asterisk. MH measured the  $^{13}\text{C}$  spectrum, YR calculated all Raman spectra.

$\text{Ni}_a\text{-L}$  redox states, as well. Only small isotopic shifts on the order of  $1\text{ cm}^{-1}$  were calculated upon  $^{15}\text{N}$  labeling, which is in line with the experimental RR data. However, only calculations for  $\text{Ni}_a\text{-L}$  reproduce both, the experimental frequencies and the  $^{13}\text{C}$  isotopic shifts very well. In contrast, the calculations for  $\text{Ni}_a\text{-C}$  and  $\text{Ni}_a\text{-SR}$  over- and underestimate the frequency and the isotopic shift, respectively. Also the prominent Fe-CO stretching mode, observed at  $610\text{ cm}^{-1}$  ( $\Delta\nu^{13\text{C}} = -8\text{ cm}^{-1}$ ) in the experimental spectrum, is in good agreement with the calculated one for  $\text{Ni}_a\text{-L}$  at  $612\text{ cm}^{-1}$  ( $\Delta\nu^{13\text{C}} = -7\text{ cm}^{-1}$ ), which is in contrast to the distinctly overestimated values for  $\text{Ni}_a\text{-C}$  and  $\text{Ni}_a\text{-SR}$ . The calculated spectrum of  $\text{Ni}_a\text{-L}$  also provides the best agreement for the Fe-CN bending (and stretching) modes in the RR spectrum below  $550\text{ cm}^{-1}$ . In Table C.1 the normal coordinate contributions to the PED of the calculated modes for  $\text{Ni}_a\text{-L}$  with a protonated cysteine are summarized.

The comparison with the calculated spectra confirms that RR spectra obtained at  $458\text{ nm}$  essentially display the Raman active modes of  $\text{Ni}_a\text{-L}$  species. Note, that the good agreement with the spectrum calculated for  $\text{Ni}_a\text{-L}$  only refers to the species with a protonated Cys597, as it was proposed in Reference [70]. Thus, the experimentally observed Raman bands can be evidentially assigned to bending and stretching modes of the Fe-CO / CN moiety, which was also proposed in a recent nuclear resonance vibrational spectroscopy (NRVS) study.[193] Additionally, the Fe-CO charge transfer can be confirmed as the origin of the resonance enhancement, because

the Raman intensities of the individual modes, scaled according to the contribution of Fe-CO coordinates to the PED, match the experimentally observed relative intensity ratios remarkably well.

#### 5.4. Discussion

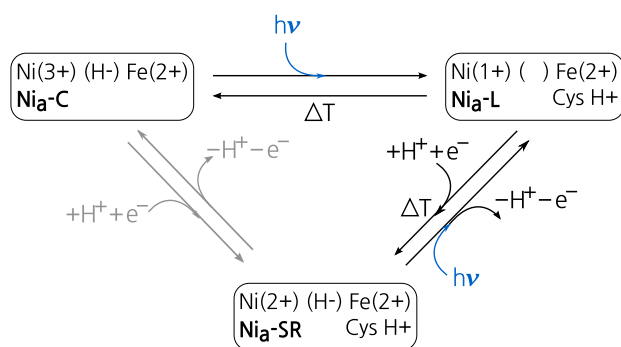
In this chapter the first characterization of Raman active modes from the reduced [NiFe] active site of the oxygen-tolerant MBH from *Ralstonia eutropha* has been presented. By comparison to calculated Raman spectra, the experimentally observed bands have been readily assigned to bending and stretching modes of the Fe-CO / CN moiety of the Ni<sub>a</sub>-L redox state. The characterization of the active site with RR spectroscopy has been backed up by complementary FTIR, EPR and UV-vis experiments on similar samples and conditions. In detail, the following insights have been obtained:

1. FTIR and EPR experiments on the H<sub>2</sub>-reduced MBH at temperatures of 80 K and under the influence of 460 nm LED light showed that 80% of the Ni<sub>a</sub>-C redox species is converted to the Ni<sub>a</sub>-L species, but none of the Ni<sub>a</sub>-SR species. This indicates, that the equilibrium between Ni<sub>a</sub>-C and Ni<sub>a</sub>-SR cannot be changed by the thermal Ni<sub>a</sub>-SR to Ni<sub>a</sub>-C redox transition at 80 K.

Thus, if the [NiFe] active site exhibits Raman active modes, they originate from the Ni<sub>a</sub>-L or the Ni<sub>a</sub>-SR, but not from Ni<sub>a</sub>-C species.

2. The present RR spectra show distinct bands in the spectral region characteristic for Fe-CO and Fe-CN bending and stretching modes. Contributions from the reduced FeS clusters can be excluded, because these bands are insensitive towards modifications of the FeS clusters. In contrast, a sensitivity towards <sup>15</sup>N and <sup>13</sup>C labeling was shown, which proves an association of these bands with Fe-CO and Fe-CN vibrations at the active site and also indicates that a Fe-CO metal-to-ligand charge transfer might be the origin of the pronounced resonance enhancement of these modes.

Since band positions and intensities are independent of the Ni<sub>a</sub>-C to Ni<sub>a</sub>-SR ratio prior to the RR experiments, equal amounts of the same species of the active site are probed. This is best explained by an efficient and direct photo-conversion of Ni<sub>a</sub>-C and Ni<sub>a</sub>-SR to Ni<sub>a</sub>-L under the high photon flux



during the RR experiments, i.e. the equilibria of all reduced states are altered in favor of the photo-converted species detected in the RR experiment.

- Using QM/MM calculations the experimentally observed Raman bands were readily assigned to Fe-CO/CN bending and stretching modes of the Ni<sub>a</sub>-L redox species. Notably, only the Ni<sub>a</sub>-L species with a protonated Cys597 is in excellent agreement with the experimental data in terms of band position and intensities. This is the first indication for the previously proposed protonation of a terminal cysteine ligand at the active site of [NiFe] hydrogenases.[70] Possibly, this cysteine is protonated in the Ni<sub>a</sub>-SR species as well. This has been recently concluded from a high resolution x-ray crystallographic structure from *Desulfovibrio vulgaris* Miyazaki F.[104]

The relative intensities of the calculated Raman bands for the Ni<sub>a</sub>-L redox state are in good agreement with the experimental data. This confirms that a Fe-CO metal-to-ligand charge transfer is the origin of the resonance enhancement as the calculated Raman intensities were scaled according to the contribution of the Fe-CO bending and stretching coordinates to the PED of the individual modes.

Based on these results a reaction mechanism for the H<sub>2</sub>-reduced [NiFe] active site under illumination and at temperatures as low as 80 K is developed and illustrated in Figure 5.11. As known from previous studies, Ni<sub>a</sub>-C converts to the Ni<sub>a</sub>-L under these conditions and the bridging hydride ligand (H<sup>-</sup>) is liberated.[108, 99, 102, 100] Two electrons formally remain at the Nickel site, thereby changing the oxidation state from 3+ to 1+. The remaining proton (H<sup>+</sup>) binds to the terminal Cys597. This depletion of the Ni<sub>a</sub>-C species at 80 K is not followed by a redox transition from Ni<sub>a</sub>-SR to Ni<sub>a</sub>-C, to restore the thermodynamic equilibrium between the two.

**Figure 5.11.:** Proposed reaction mechanism at 80 K and illumination in the blue spectral range.  $\Delta T$  marks transitions that need an increase in temperature.[110] Light-induced transitions are indicated with  $h\nu$ .

In contrast to the Ni<sub>a</sub>-C  $\rightarrow$  Ni<sub>a</sub>-L transition, the Ni<sub>a</sub>-SR  $\rightarrow$  Ni<sub>a</sub>-L transition presumably requires high photon fluxes as provided by laser excitation. As the chemical equilibrium between Ni<sub>a</sub>-C and Ni<sub>a</sub>-SR is not restored at 80 K the corresponding transitions are colored in gray.

But under the high photon flux of the incident laser beam the Ni<sub>a</sub>-SR is directly photo-converted to Ni<sub>a</sub>-L with a net removal of one proton (H<sup>+</sup>) and one electron. Formally, this is the same reaction as Ni<sub>a</sub>-SR → Ni<sub>a</sub>-C → Ni<sub>a</sub>-L.

Altogether, it was shown that the combination of RR spectroscopy with QM/MM calculations based on crystal structures derived from the very same preparations of the MBH as used for RR measurements, yields structural and electronic details of the active site, that are beyond the capabilities of x-ray crystallography. This technique might also be applied for the characterization of [Fe] and [FeFe] hydrogenases of other organisms.

# 6. Vibrational Spectroscopy on Crystals of the As-isolated MBH

Parts of this Chapter have been submitted to 'The Journal of Physical Chemistry' and were obtained in a collaboration between E. Siebert and Y. Rippers. All QM / MM calculations were carried out by Y. Rippers.

Unlike oxygen-sensitive [Fe], [FeFe] and [NiFe] hydrogenases, the oxygen-tolerant subgroup of the [NiFe] hydrogenases is able to oxidize molecular hydrogen to two protons and two electrons even under aerobic conditions.[14] Recently, biofuel cells based on the oxygen-tolerant subgroup of [NiFe] hydrogenases have been reported to deliver more than 1 mW/cm<sup>2</sup>. [194, 195, 196] To efficiently use these enzymes for biofuel cells, a comprehensive understanding of the structure-function relationship of the different cofactors, in particular the active site and the FeS clusters, is needed. Structural features of the FeS cluster, located approximately 11 Å proximal to the [NiFe] active site, are ascribed to the remarkable oxygen-tolerance of the hydrogenase.[44, 45, 46, 47] This newly found [4Fe3S] cluster is coordinated by six cysteines, instead of four as in oxygen-sensitive hydrogenases.[44] It undergoes structural rearrangements in a narrow but physiological potential range. In the so called superoxidized form one iron is bound to a backbone nitrogen and another iron is bound to a hydroxyl ligand.[47] It is believed that this cluster is one of the keys for the oxygen-tolerance, as it enables the fast reduction of oxygen to water.[197] Oxygen-sensitive and -tolerant hydrogenases differ in yet another aspect: In the latter only the Ni<sub>r</sub>-B, but not the Ni<sub>t</sub>-A redox state is formed. The Ni<sub>r</sub>-B species is reactivated two orders of magnitude faster to the active redox species of the active site under H<sub>2</sub>

or reducing conditions via the Ni<sub>r</sub>-S redox state, than for oxygen-sensitive hydrogenases.[198, 85, 199] Therefore, Ni<sub>r</sub>-S is rarely observed in oxygen-tolerant hydrogenases.

However, under anaerobic conditions these enzymes are inactivated via Ni<sub>r</sub>-B formation at high potentials, which causes a decrease in the performance of the biofuel cells.[11, 132, 20] This reversible inactivation defines an upper limit at which molecular hydrogen can be oxidized to two protons and two electrons. However, several studies report that an illumination of the hydrogenase may overcome this limitation.[114, 83, 116, 115]

In view of this anaerobic inactivation of the hydrogenases at high potentials and the reported reactivation under the influence of light, I have investigated the light-sensitivity of the oxidized active site with Resonance Raman (RR) spectroscopy. The previous chapter showed that the experimental conditions of RR spectroscopy are ideal for the photo-conversion of the active site. Moreover, it allows probing of the Fe-CO / CN modes in the spectral region between 400 and 700 cm<sup>-1</sup>. [103] However, modes of the proximal FeS cluster, such as the Fe-OH stretching and bending modes are expected in a similar spectral range.[113] Thus, this key spectral region contains marker bands of all catalytically relevant cofactors of the MBH. The main objective of this work is therefore to disentangle the region from 400 to 700 cm<sup>-1</sup> in terms of contributions from the different redox states, of both, the [NiFe] active site and the proximal FeS cluster.

The vibrational modes of both cofactors are discriminated by various methods of spectra analysis in Section 6.2 and the respective component spectra are consistently determined for an excitation at 458 nm. In this way, RR spectroscopy on hydrogenases offers a second experimental technique, apart from EPR spectroscopy, to investigate the FeS clusters and the active site at once.

The entire study is carried out with aerobically grown MBH crystals and represents the first comprehensive RR spectroscopic analysis of hydrogenase crystals. This approach offers the unique advantage that the individual cofactor spectra (component spectra) derived from this analysis originate from the same state to which the crystallographic models refer to. These models served as a basis for the calculation of Raman spectra with a quantum mechanical / molecular mechanical (QM/MM) hybrid method. A combination of the experimental and calculated Raman spectra allows to reliably determine the structure and electronic configuration of various cofactor states (Section 6.3). In turn, this improves the

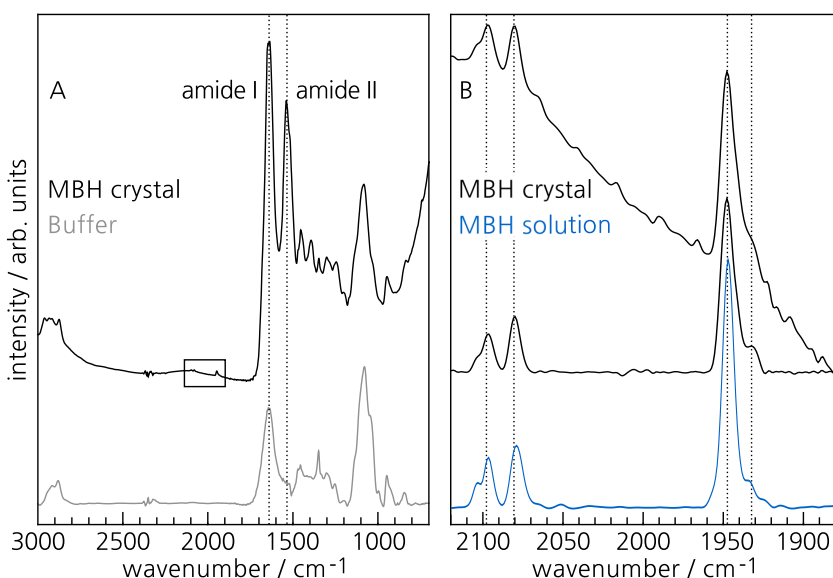


**Figure 6.1.:** A) Comparison of the FTIR spectrum of a single as-isolated MBH crystal (black) to the spectrum of its dried 'mother liquor' in gray. The amide bands of the protein backbone of the MBH are indicated by vertical lines.

B) Spectral region of the CO and CN stretching modes of the MBH. In black the spectrum of the MBH crystal with and without a manual baseline correction is shown. A typical spectrum of the MBH in solution at 10 °C is shown in blue. Both spectra exhibit a maximal fraction of the Ni<sub>r</sub>-B redox state (1949, 2080 and 2098 cm<sup>-1</sup>). The spectrum of the crystal shows a minor amount of the Ni<sub>r</sub>-S in the region of the CO stretching modes – as indicated by the vertical line at 1936 cm<sup>-1</sup> for the CO stretching mode.

understanding of the interplay between the MBH cofactors during catalysis and may further support the structural refinement of the crystallographic models, in particular for those states of the enzyme that are not accessible to x-ray crystallography.[103]

Apart from RR spectroscopy, the as-isolated MBH crystals are investigated with infrared spectroscopy in Section 6.1 as well. These infrared spectra are the first of a single protein crystal and thus, demonstrate another spectroscopic tool for the analysis of single protein crystals.

### 6.1. Infrared Spectroscopy on Crystalline Samples

As presented in Chapter 4 and Reference [60, 13, 173, 34, 81], Fourier Transform Infrared (FTIR) spectroscopy is capable to probe all redox states of the active site by detecting the stretching modes of the CO and the two CN<sup>-</sup> ligands, which coordinate the Fe atom of the active site. This has been studied extensively on the samples of the heterodimeric MBH in solution.[33, 43, 79] However, transmission FTIR spectroscopy in its established form cannot be applied for single protein crystals of the MBH, due to their high packing density and comparable small average dimensions of 1.4 × 0.3 × 0.3 mm. To cope with the dimensions of the crystalline sample, the spectra were accumulated with a 20 × ATR objective mounted to an infrared microscope equipped with an internal liquid nitrogen cooled Mercury Cadmium Telluride detector, as described in Section 3.1.

Figure 6.1 A displays the FTIR spectra of a single as-isolated MBH

crystal in black and of the dried 'mother liquor' of the crystals in gray, both with respect to a background of gaseous nitrogen atmosphere saturated with water vapor. The high intensity at the amide I and II band of the protein backbone at 1642 and 1533  $\text{cm}^{-1}$  in the spectrum of the as-isolated MBH crystal proves the proper contact between ATR tip and sample. The spectral region of the CO and CN stretching modes is highlighted with a box between 2140 and 1880  $\text{cm}^{-1}$  and the corresponding spectrum of the as-isolated MBH crystal in that region is shown in panel B of the same figure in black, with and without a manual baseline correction. For comparison a typical transmission FTIR spectrum of the as-isolated MBH in solution at 10 °C is shown in blue. This spectrum is the average of 50 single spectra à 200 scans, in contrast to that of the crystal with  $1 \times 400$  scans.

In view of the good agreement between the FTIR spectra of the crystalline and solubilized MBH, crystallization artifacts can be excluded to perturb the active site. Additionally, both spectra show a maximal fraction of the  $\text{Ni}_r\text{-B}$  redox state, with a normalized integral intensity of 90 and 83% for the CO stretching mode, respectively. The minor contribution originates from a  $\text{Ni-S}$  species, which has been observed in previous studies of the MBH as well.[33, 79] According to these investigations it might be a 'ready' species ( $\text{Ni}_r\text{-S}$ ) with either a hydroxyl or a water molecule in the bridging position. An alternative assignment can be a structure, designated as  $\text{Ni}_a\text{-S}$ , with an open coordination site. This state is supposed to be one central intermediate of the catalytic cycle. However, the formation of the  $\text{Ni}_r\text{-S}$  species in the as-isolated enzyme is in line with the presumed reactivity of  $\text{Ni}_a\text{-S}$  towards oxygen. Moreover, the crystal structures of the superoxidized MBH indicate a full occupancy of the bridging position by an oxygen species.[47] Thus, assignment of the CO stretching mode at 1936  $\text{cm}^{-1}$  to  $\text{Ni}_r\text{-S}$  is more likely.

## 6.2. Raman Active Modes of the Oxidized Active Site and the FeS Clusters

To complement the vibrational spectroscopic investigations of the oxidized active site, the following analysis will be broadened to Raman active modes. In the previous chapter it was shown that the reduced active site is accessible via RR spectroscopy. Hereby, the  $\text{Ni}_a\text{-L}$  redox state is detected in the RR spectrum of the reduced samples, via a light induced dissociation of the bridging hydride

of the Ni<sub>a</sub>-C redox state and a subsequent protonation of the terminal Cys597. Under the high photon fluxes of the incident laser beam in RR spectroscopy even the Ni<sub>a</sub>-SR redox state seems to be photo-converted to the Ni<sub>a</sub>-L redox state. The Raman active Fe-CO / CN bending and stretching modes of the Ni<sub>a</sub>-L were found in a spectral range characteristic for metal-ligand vibrations from 400 to 650 cm<sup>-1</sup>.<sup>[113]</sup> A similar spectral range is therefore expected for vibrational modes of the oxidized active site.

As shown by FTIR spectroscopy on as-isolated MBH samples at 10 °C, the redox state of [NiFe] active site is dominated by the Ni<sub>r</sub>-B redox state. Minor contributions originate from the Ni<sub>r</sub>-S redox state. The following analysis intends to elucidate whether one of these redox states can be accessed via RR spectroscopy or if yet another redox state is detected through a photo-induced process at the active site, as observed for the reduced active site.

In addition to the modes of the active site, stretching modes of the FeS cluster will contribute to the RR spectra of the oxidized MBH samples. They occur at frequencies from approximately 250 to 400 cm<sup>-1</sup> and thus, will only weakly superimpose with the modes from the active site. Thus, only Fe-OH modes of the proximal cluster are expected in a spectral range similar to that of the Fe-CO / CN stretching modes.<sup>[113]</sup>

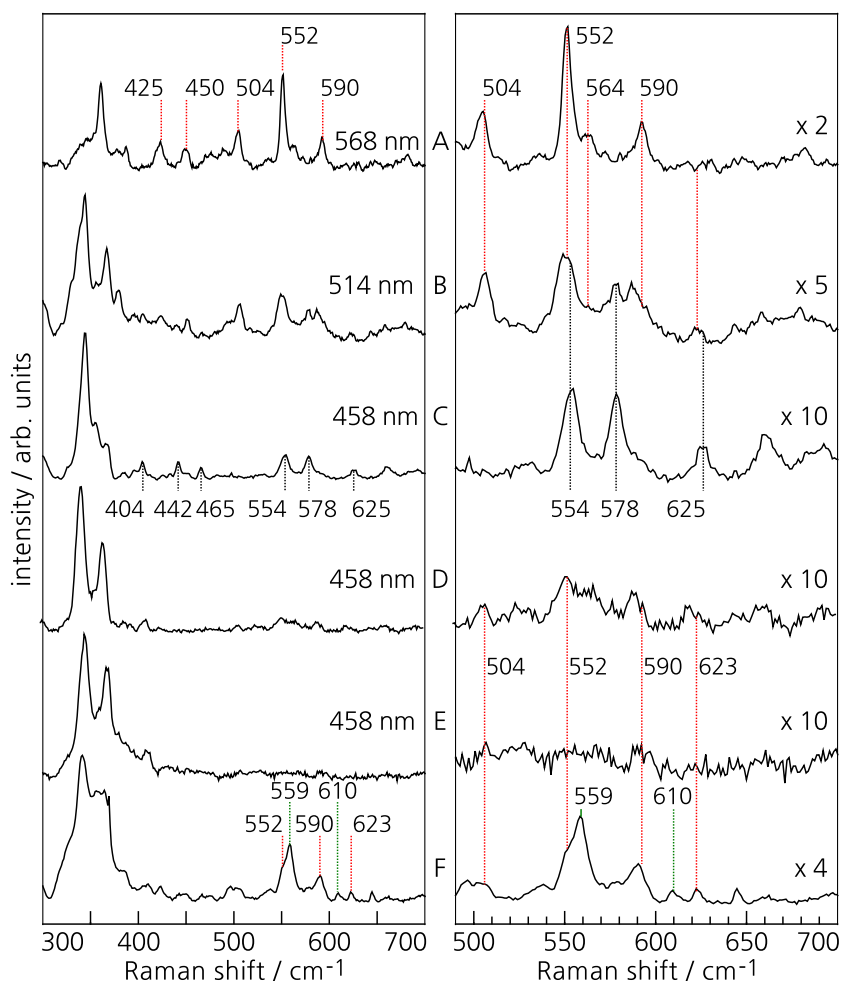
Therefore, the subject of the following analysis is to distinguish between modes originating from the [NiFe] active site and the proximal FeS cluster.

### 6.2.1. Excitation Wavelength Dependent Resonance Raman Spectra

Due to the chemical and structural difference of the three FeS clusters and the [NiFe] active site with the bound CO and CN<sup>-</sup> ligands, the energy range for the electronic transition within the latter cofactor differs from that of the FeS clusters. The UV-vis absorption spectrum of the as-isolated MBH at 300 K in Figure 5.4 exhibits a broad absorption between 410 and 460 nm which is associated with an absorption of the incident light by the FeS clusters. Shallow absorption bands at approximately 585 and 690 nm arise and were assigned to absorptions via the [NiFe] center.<sup>[70]</sup> All RR spectra were obtained from samples held at 80 K.

According to the UV-vis spectra an excitation wavelength of 458 nm was chosen for a resonant enhancement of vibrational modes containing FeS coordinates. Vibrational modes of the [NiFe] active

**Figure 6.2.:** Experimental RR spectra of a single crystal from the as-isolated MBH, measured at excitation wavelengths of (A) 568 nm, (B) 514 nm and (C) 458 nm. The spectra region between 490 and 700  $\text{cm}^{-1}$  is expanded to illustrate the effect of the excitation wavelengths on selected bands (marked in black, red and green). The different intensity scaling factors are indicated in the right panel. Traces D, E and F represent RR spectra obtained with 458 nm excitation from other MBH crystals of the same protein preparation. These spectra demonstrate inherent spectral variations.



site were resonantly enhanced at an excitation wavelength of 568 nm. Additionally, RR spectra at 514 nm were recorded to follow the changes of the bands. In this way, the complexity in the RR spectrum was reduced and the identification of individual bands to specific cofactors was supported.

Figure 6.2 shows the corresponding RR spectra of a single as-isolated MBH crystal excited at 568, 514 and 458 nm in trace A, B and C. The *c*-axis, i.e. the long axis of the crystal, was aligned parallel to the electric field vector of the incident laser beam. The same conditions apply to all following RR measurements.

RR spectra recorded at 458 and 514 nm show typical signatures of FeS stretching modes in the spectral region between 300 and 400  $\text{cm}^{-1}$ , which is consistent with the UV-vis spectra. In contrast, the RR spectrum of the sample excited at 568 nm shows an intense band at 362  $\text{cm}^{-1}$  on a broad background. Therefore, the RR spectra at 458 and 514 nm are dominated by modes which contain FeS coordinates and the spectrum recorded at 568 nm by modes from another cofactor of the protein, presumably the [NiFe]

active site. In Chapter 7 the FeS stretching modes will be analyzed in detail, the following analysis focuses on the bands between 400 and 700  $\text{cm}^{-1}$ .

In Figure 6.2 this region is scaled up with respect to the low frequency region to illustrate the different wavelength-dependence of the bands marked by black, red and green vertical lines. The signature of the spectrum taken at 568 nm clearly differs from the spectra excited at lower wavelengths. It exhibits distinct bands at 362, 425, 450, 504, 552, 564 and 590  $\text{cm}^{-1}$ , as marked by red vertical lines. The intensity of these bands is significantly reduced in the spectrum taken at 514 nm. For excitation at 458 nm of the very same sample this group of bands diminishes significantly. Hence, this first group of bands must originate from the [NiFe] active site of the as-isolated MBH.

Through the resonant enhancement of the FeS stretching modes another set of bands at 404, 442, 465, 554, 578 and 625  $\text{cm}^{-1}$  appears in spectrum C at 458 nm excitation, as indicated by black vertical lines. This group of bands is, together with the FeS stretching modes, enhanced at 514 nm excitation but not at 568 nm – where none of the FeS stretching modes are detected. Thus, this second group of bands must originate from modes associated with modes related to the additional functionalities of the proximal cluster, i.e. modes of the Fe-OH moiety, which in general exhibit a little less resonant enhancement as compared to the FeS stretching modes.[200, 201]

Yet, a selection of three further RR spectra excited at 458 nm from different as-isolated MBH crystals shown in trace D, E and F, demonstrates that the first group of bands (red lines) can be subject to a minor enhancement. Moreover, vibrational modes of the Ni<sub>a</sub>-L redox state (green lines) can appear. (See Chapter 5) Also the spectral signature of the FeS stretching region shows some variation depending on the chosen crystalline sample. Formally, all investigated as-isolated MBH crystals were prepared under the very same conditions but subtle deviations in sample preparation and handling, that cause minor structural changes and in turn the spectral distribution as shown in trace C to F, cannot be ruled out. In summary, the wavelength-dependent measurements suggest that there are at least three independent components with vibrational modes above 400  $\text{cm}^{-1}$ . One component with bands at 404, 442, 465, 554, 578 and 625  $\text{cm}^{-1}$  is related to the proximal FeS cluster, therefore this group of bands will be denoted as the  $C_{\text{FeS}}$  component. Furthermore, Raman bands at 425, 450, 504, 552, 564

and  $590\text{ cm}^{-1}$  will be shown to belong to Fe-CO / CN vibrations of the active site redox species of yet unknown structure. This spectral component is named  $C_{\text{NiX}}$ . The third spectral component was already identified with Fe-CO / CN vibrations of the  $\text{Ni}_a\text{-L}$  redox state, occasionally it will be denoted as  $C_{\text{NiL}}$ .

Only for the  $\text{Ni}_a\text{-L}$  species a relatively pure RR component spectrum ( $C_{\text{NiL}}$ ) can be measured at 458 nm, whereas few bands can be unambiguously identified with the other two components  $C_{\text{FeS}}$  and  $C_{\text{NiX}}$ . It is therefore not possible to derive the entire component spectra of the proximal cluster and the oxidized active site on the basis of wavelength-dependent RR spectra, also because the RR cross section does not vary uniformly with the excitation line for all bands of one cofactor.

### 6.2.2. Component Analysis of Resonance Raman Spectra

The results from the previous section show that excitation of the as-isolated MBH sample between 458 and 514 nm equally enhances modes of the active site, in the oxidized and reduced form, as well as modes of the iron sulfur clusters. (See also Figure 5.9)

In this section, bands of the active site and the proximal FeS cluster are discriminated for an excitation at 458 nm, where all involved species can be detected. Moreover, the spectral weights for each component are determined. This is achieved through a threefold analysis: A statistical analysis in the spectral range from 400 to  $700\text{ cm}^{-1}$ , which ultimately results in the component spectra for the superoxidized proximal FeS cluster, the oxidized and the reduced active site. This assignment is confirmed with RR spectra of different genetically engineered variants of the MBH. Moreover, using calculated Raman spectra from QM / MM calculations (by Y. Rippers) the bands of all component spectra are assigned to specific modes of either one of the two relevant cofactors of the MBH.

This type of analysis might turn out to be useful for other (complex biological) systems where different cofactors cannot be selectively enhanced and signal intensities are rather low. However, a large set of spectra from samples in various redox states has to be accumulated.

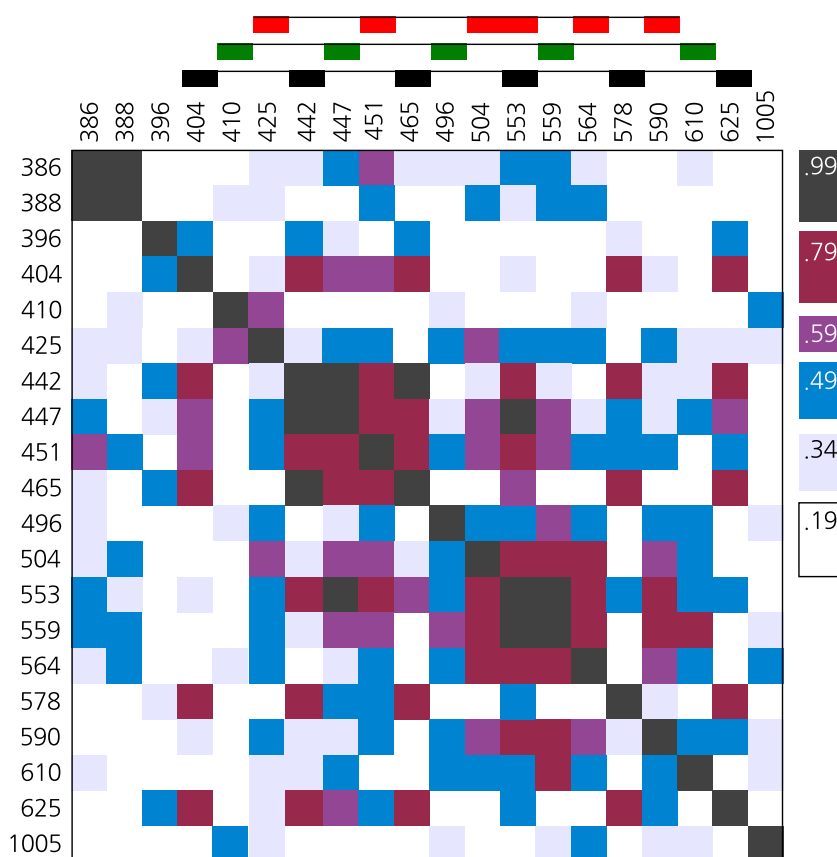


**Figure 6.3.:** Graphical illustration of the calculated Spearman's Rank cross-correlation coefficients  $\rho_S$  for the intensity correlation between 20 selected bands in 65 different RR spectra of the MBH. The 20 band positions are found at the top and left hand side of the matrix. The color code for the  $\rho_S$  coefficient is found at the right hand side. At the very top of the figure the proposed band positions of the  $C_{FeS}$ ,  $C_{NiL}$  and  $C_{NiX}$  components are marked in black, green and red, respectively. The calculated p-values for each  $\rho_S$  can be found in Figure D.2.

### Statistical Analysis

The spectra of the as-isolated MBH crystals (Figure 6.2 C-F) exhibit, a superposition of the three proposed components and possibly vibrational modes of the protein backbone. All normal modes of one specific vibrating cofactor exhibit a fixed relative intensity ratio to each other. In a mathematical sense this means that the intensity ratio between each two modes from one cofactor in a number of single spectra can be described by a monotone function. Then these modes are cross-correlated to each other.

To test this, a set of 65 RR spectra of different MBH samples, including the crystalline and solubilized MBH wildtype in the (re)oxidized and reduced redox-state, as well as the as-isolated MBH incubated in 50 mM ascorbic acid, for a partial reduction of the proximal cluster, were measured. Then, the mean intensities at the band positions of 19 vibrational modes between 380 and 650  $\text{cm}^{-1}$ , as found in the previous section, and the phenylalanine band of the protein backbone at 1005  $\text{cm}^{-1}$ , were computed numerically. The cross-correlation between the intensity relation of all two pairs of bands in this  $65 \times 20$  matrix is described by their Spearman's Rank correlation coefficient  $\rho_S$  in a  $20 \times 20$  matrix.[202] As the vibrational modes in the Raman spectra typically have linewidths of up

to  $10\text{ cm}^{-1}$ , cross-correlations between two selected modes closer than their linewidth should be neglected in this type of analysis, as solely the mean intensity is determined. All details and limitations of this statistical analysis can be found in Appendix E.

The  $20 \times 20$  matrix of the calculated Spearman's Rank correlation coefficient  $\rho_S$  is illustrated graphically in Figure 6.3. Initially I found that the selected bands between  $380$  and  $650\text{ cm}^{-1}$  must belong to modes of the cofactors of the MBH and not the protein backbone, as none of them, except the weak bands at  $410$  and  $564\text{ cm}^{-1}$ , is correlated with the phenylalanine band at  $1005\text{ cm}^{-1}$ . Bands that were assigned to the  $C_{\text{FeS}}$  component are indicated by black boxes at the top of Figure 6.3. They show a clear cross-correlation with  $\rho_S > 0.50$ .<sup>A</sup> Furthermore, the band at  $625\text{ cm}^{-1}$  seems to belong to this species as well ( $\rho_S = 0.67$ ), though it interferes with a nearby broad band at  $623\text{ cm}^{-1}$  of yet unknown origin (Figure 6.2). With cross-correlation coefficients of  $\rho_S < 0.35$  none of the bands of the  $C_{\text{FeS}}$  species, except the band at  $553\text{ cm}^{-1}$ , is related to the bands at  $425, 504, 564, 590\text{ cm}^{-1}$  as well as  $410, 496, 559, 610\text{ cm}^{-1}$ . Consequently, those bands must belong to (two) other components. Indeed, the vibrational modes at  $425, 504, 564$  and  $590\text{ cm}^{-1}$  were linked to modes of the active site in an oxidized redox state ( $C_{\text{NiX}}$ ) and the modes of the latter set to Fe-CO / CN modes of the reduced active site ( $C_{\text{NiL}}$ ).<sup>[103]</sup> Both sets of bands are marked by red and green boxes at the top of Figure 6.3, respectively. A (minor) cross-correlation between these two sets of bands results from the fact that the reduced species is always superimposed with the species of bands at  $504$  and  $590\text{ cm}^{-1}$ , but not necessarily the other way around. The statistical analysis has jet another facet: The band at  $553$  wavenumbers seems to be weakly correlated to the modes at  $425, 504, 564, 590\text{ cm}^{-1}$  ( $C_{\text{NiX}}$ ) as well as with the modes at  $442, 465, 578\text{ cm}^{-1}$  ( $C_{\text{FeS}}$ ). Hence, this band might be related to a mode of an oxidized redox state of the active site and the FeS cluster, and would thus be composed of two close-by modes.

All in all the statistical analysis on a large variety of RR spectra of the MBH confirmed that these spectra are composed of at least three different major components. The spectral component  $C_{\text{NiL}}$  exhibits bands at  $411, 496, 559$  and  $610\text{ cm}^{-1}$  and was already assigned to the light induced  $\text{Ni}_a\text{-L}$  redox state of the active site.<sup>[103]</sup> Vibrational modes at  $425, 504, (552), 564$  and  $590\text{ cm}^{-1}$  are linked to vibrations of an oxidized redox state ( $C_{\text{NiX}}$ ). Finally a species with bands at  $404, 442, 465, (554), 578$  and  $625\text{ cm}^{-1}$  is identified

<sup>A</sup>This lower limit was chosen to account for the relatively small number of samples investigated and weak intensities of specific bands.

to belong to vibrations of the proximal FeS cluster ( $C_{\text{FeS}}$ ).

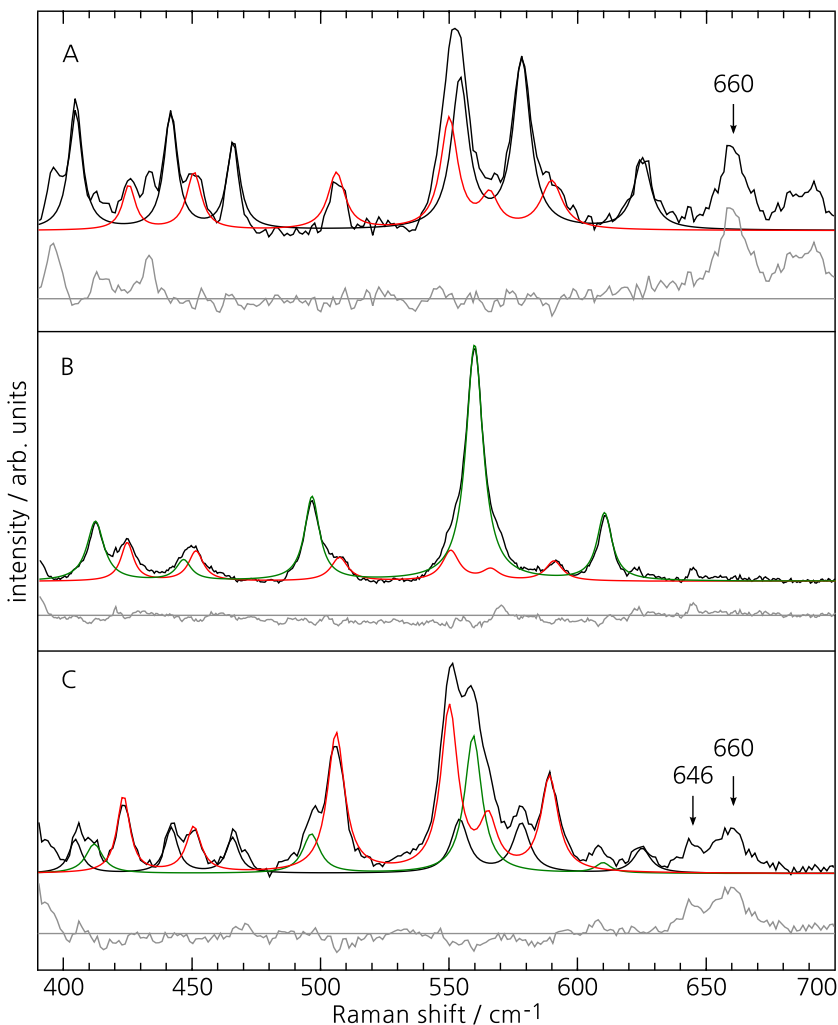


**Figure 6.4.:** For the initial component analysis three selected spectra with maximal intensity fraction at the band positions for the A)  $C_{\text{FeS}}$  component, B)  $C_{\text{NiL}}$  component and C)  $C_{\text{NiX}}$  component were fitted to Lorentzian bands. For the sake of clarity only the resulting envelopes for each found component are shown in black for  $C_{\text{FeS}}$ , red for  $C_{\text{NiX}}$  and green for  $C_{\text{NiL}}$ . The parameters for each individual species can be found in Table D.1. The residuals for each fit are shown in gray with a negative offset, they include unassigned bands at 649 and 660  $\text{cm}^{-1}$  not included in the component spectra, yet.

### Component Fits

The following spectra analysis is complementary to the statistical analysis, but is based on the same idea that vibrational modes belonging to one cofactor have a fixed intensity ratio to each other. For an initial definition of the component spectra for the proximal FeS cluster ( $C_{\text{FeS}}$ ) and those of the active site ( $C_{\text{NiX}}$  and  $C_{\text{NiL}}$ ), individual spectra with a maximal fraction of either of the three components were selected. Lorentzian shaped bands with linewidths of up to 10  $\text{cm}^{-1}$  were fitted to the respective three spectra at the previously determined band positions. This is shown in Figure 6.4. For the sake of clarity only the envelopes for the bands of one proposed component are shown, the actual values of each individual band can be found in the first three columns of Table D.1. The individual bands are ordered in groups according to the proposed components. The last three columns of the table show, for each

**Table 6.1.:** Optimized band parameters from component fits and difference spectra shown in Figures D.3 and 6.6 for the  $C_{\text{FeS}}$ ,  $C_{\text{NiX}}$  and  $C_{\text{NiL}}$  spectral component.

	position $\pm 0.5 \text{ cm}^{-1}$	relative area $\pm 20 \%$	FWHM $\pm 1.0 \text{ cm}^{-1}$
$C_{\text{FeS}}$	404	0.55	6
	433	0.27	6
	442	0.58	6
	452	0.22	6
	465	0.47	6
	554	0.83	8
	578	1.00	8
	625	0.41	8
	660	0.48	8
$C_{\text{NiX}} = C_{\text{NiS}}$	425	0.40	8
	450	0.21	8
	504	0.44	8
	552	1.11	8
	564	0.70	8
	590	1.00	10
	623	0.37	6
	646	0.40	6
$C_{\text{NiL}}$	411	0.24	6
	496	0.32	6
	559	1.00	6
	569	0.14	6
	610	0.50	6

spectrum of Figure 6.4A-C, the values of all fitted band areas normalized to the area of a marker band of each proposed component. That is, the band at  $559 \text{ cm}^{-1}$  for the  $C_{\text{NiL}}$ ,  $578 \text{ cm}^{-1}$  for the  $C_{\text{FeS}}$  and  $590 \text{ cm}^{-1}$  for the  $C_{\text{NiX}}$  component. If the intensity ratio for a group of bands with respect to one of the marker bands is comparable for all three selected spectra A-C, then this group must result from modes of one specific cofactor. As an example we may compare the normalized band areas of the  $C_{\text{FeS}}$  and  $C_{\text{NiX}}$  component in block A and C of Table D.1. In both blocks bands of the  $C_{\text{FeS}}$  component have comparable values when normalized to the marker band at  $578 \text{ cm}^{-1}$  but differ by an order of magnitude when normalized to  $590 \text{ cm}^{-1}$ . The situation is reversed when we turn to the last column of Table D.1, where only the group of bands proposed to belong to  $C_{\text{NiX}}$  have comparable ratios. Subsequently,

the experimental component spectra are generated, for an excitation at 458 nm. For the  $C_{\text{FeS}}$  and  $C_{\text{NiX}}$  component the envelope of the fitted Lorentzian shaped bands from Figure 6.4A and C were normalized to 578 and 590  $\text{cm}^{-1}$ , respectively and then averaged. The component spectrum  $C_{\text{NiL}}$  for the reduced active site is generated from the normalized and averaged fits of Figure 6.4A and C. The experimentally determined spectral weights for each component are summarized in Table 6.1.

Altogether a superposition of these three experimentally found components matches random RR spectra of the as-isolated MBH under various redox treatments accumulated at 458 nm excitation. This is shown in Figure D.3. The resulting residuals basically represent the spectral background with random noise and some minor positive bands, that are identified later in the text.

Thus, linear superpositions of the three fitted spectral components reproduce the measured RR spectra very well. With the knowledge of the true nature of these bands, conclusions on the composition as well as structural and functional details of the MBH samples can be drawn. One important example will be shown in Chapter 8.

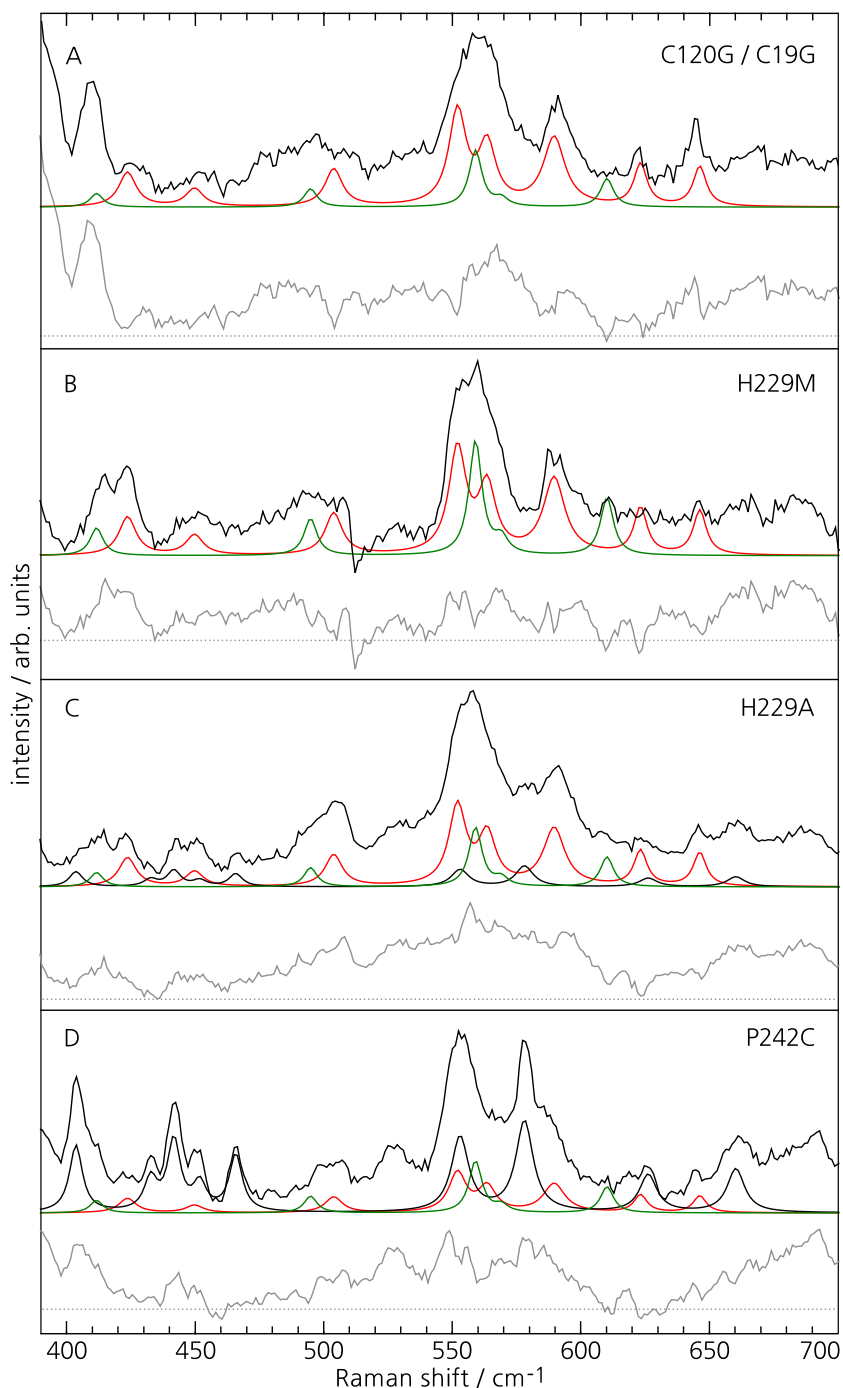
### Spectra of genetically engineered MBH variants

With reference to the analysis carried out in Chapter 5 the  $C_{\text{NiL}}$  component is identical to Fe-CO / CN vibrations of the active site in the  $\text{Ni}_a\text{-L}$  redox state. To determine the nature of the vibrational modes of the  $C_{\text{NiX}}$  and  $C_{\text{FeS}}$  component, a component analysis of RR spectra from as-isolated MBH samples with selected mutations of specific amino acids at the FeS clusters will further corroborate the initial assignment of the  $C_{\text{FeS}}$  component to vibrations of the superoxidized proximal cluster and the  $C_{\text{NiX}}$  component to Fe-CO / CN vibrations of another active site related redox state.

Using site-directed mutagenesis specific amino acid residues in the vicinity of the proximal or medial FeS cluster were substituted. A cubane like  $[\text{4Fe4S}]$  cluster is formed in the proximal or medial position, for the C120G/C19G or P242C variant, respectively.[43] In case of the histidine variants H229A and H229M a loss of the hydroxyl group at the proximal cluster is found in the respective x-ray crystal structures.[47, 203]

The RR spectra of these four MBH variants in the oxidized redox state are shown in Figure 6.5. They are fitted to a linear superposition of the three component spectra gathered in the previous section. The resulting residuals are shown in gray. The

**Figure 6.5.:** Spectra of engineered MBH variants with substitutions at the proximal and medial cluster. A detailed description of each MBH variant can be found in the text. The experimentally found spectral components ( $C_{FeS}$  in black,  $C_{NiX}$  in red and  $C_{NiL}$  in green) were fitted to all RR spectra, subsequently the baseline was corrected. The resulting residuals (gray) are shifted by a negative offset with respect to the experimental spectrum (black). The  $C_{NiX}$  and  $C_{NiL}$  component fit all spectra, except the P242C variant. Note that the bands at  $623$  and  $646\text{ cm}^{-1}$  are now included in the  $C_{NiX}$  and  $660\text{ cm}^{-1}$  in the  $C_{FeS}$  component, as summarized in Table 6.1. Buffer spectrum was subtracted prior to component analysis

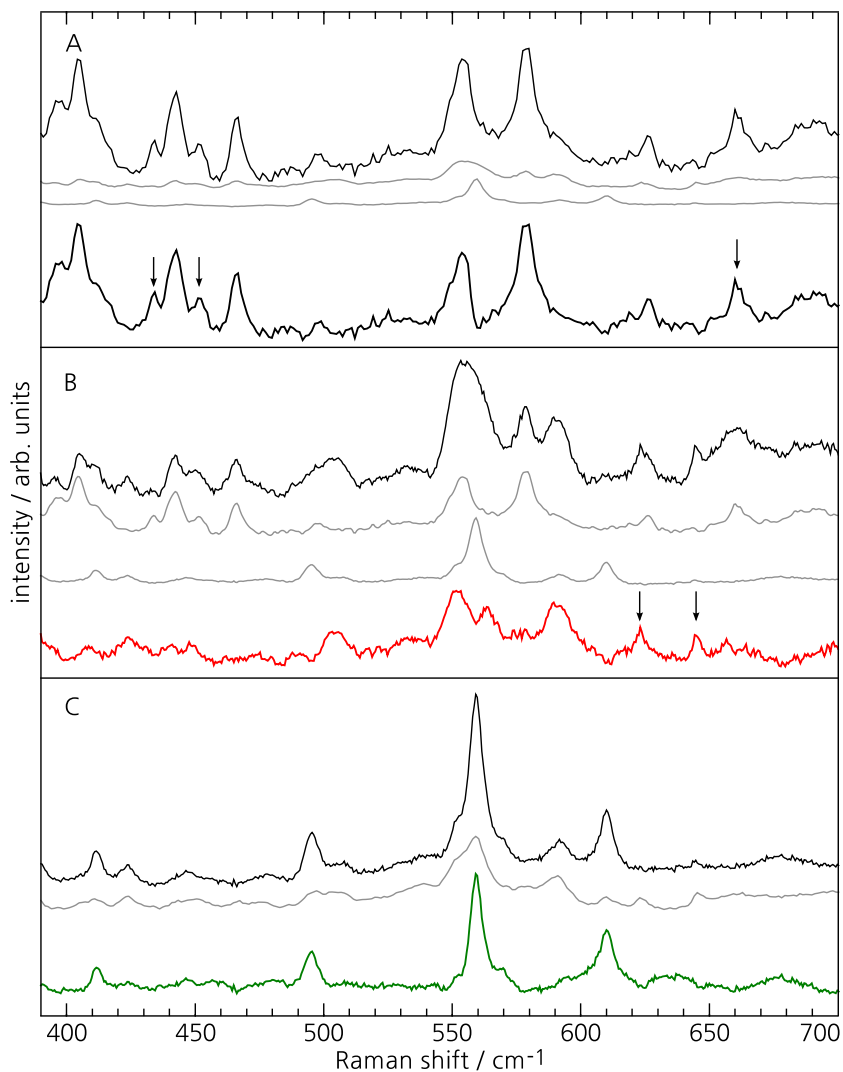


RR spectra of the C120G/C19G and both histidine variants could be simulated solely by the  $C_{NiX}$  and  $C_{NiL}$  component spectra, as the three spectra exhibit no contributions of the  $C_{FeS}$  component. Only the RR spectrum of the P242C variant exhibits a major fraction of  $C_{FeS}$  component. That finding confirms that the bands of this  $C_{FeS}$  component originate from the proximal cluster, as it is unchanged in the P242C variant, in contrast to the C120G/C19G, H229M and H229A variants, where this component is not observed. Since the active site was not subject to any structural changes in all of the four variants [189] and their corresponding RR spectra showed essential contributions of the  $C_{NiX}$  and  $C_{NiL}$  component, both components must belong to modes of the active site.

## Difference Spectra

Figure 6.5 and D.3 presented seven examples that a linear superposition of the found component spectra satisfactory describes the experimental spectra. The respective residuals display deviations from the noise level essentially only at the positions of those few bands that remained unassigned and were not included in the component spectra. Thus, these component spectra do not correspond to the complete spectra of the cofactors. However, since each component spectrum includes the most characteristic bands of the respective cofactor in a particular redox state, the component analysis provides a reliable determination of the relative spectral weights of the cofactors in the experimental spectra that involve overlapping contributions of the individual species. Once these spectral weights for the various components are known, the complete spectra can be evaluated by mutual subtraction of different experimental spectra. That is depicted in Figure 6.6. The resulting difference spectra are in general similar to the component spectra, but additional low intensity bands are found at 433, 452 and 660  $\text{cm}^{-1}$  for the  $C_{FeS}$  component in panel A and the  $C_{NiX}$  component exhibits further bands 623 and 646  $\text{cm}^{-1}$ . These bands are included in the final component spectra (Table 6.1). The difference spectrum shown in panel C displays the pure  $Ni_a$ -L spectrum, that differs slightly from the one shown in Ref-

**Figure 6.6.:** RR difference spectra showing the pure spectral components for  $C_{FeS}$ ,  $C_{NiX}$  and  $C_{NiL}$  in panel A to C. The baseline was corrected after the mutual subtraction of selected experimental spectra. Additional modes (arrows) with respect to Figure 6.4 can be identified for the  $C_{FeS}$  and  $C_{NiX}$  component spectrum in panel A and B, respectively. Accordingly, the component spectra are expanded to bands at 433, 452 and 660  $\text{cm}^{-1}$  for  $C_{FeS}$  as well as 623 and 660  $\text{cm}^{-1}$  for  $C_{NiX}$  (Table 6.1).



erence [103].

In the following, these spectra will be used for the structural assignment by comparison with theoretical Raman spectra, obtained via QM/MM calculations. [204]

### 6.3. Comparison to Theoretical Raman Spectra

Raman spectra for the proximal FeS cluster and the [NiFe] active site were calculated by Y. Rippers by means of molecular dynamic (MD) simulations in combination with a hybrid QM/MM model, based on the crystal structure of the oxidized MBH of *Ralstonia eutropha*. [47] The entire method is described in particular detail in Reference [204]. The calculated spectra will be compared to the complete component spectra, obtained in the previous section. In such a way, the experimental Raman bands can be associated with specific modes of the two cofactors, namely the proximal cluster

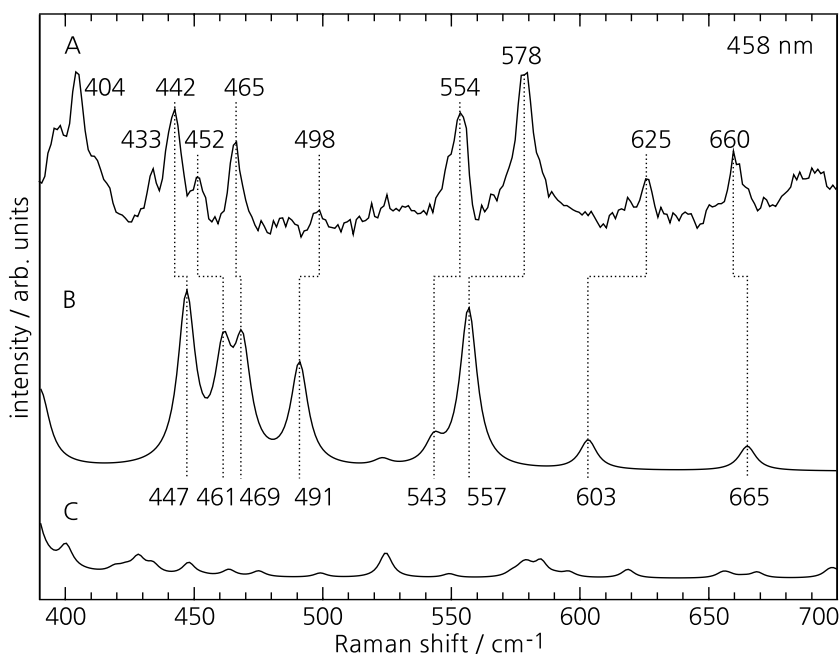


**Figure 6.7.:** (A) Complete component spectrum  $C_{FeS}$  of the  $[4Fe_3S]$  cluster, derived by mutual subtraction of selected experimental RR spectra measured at 458 nm (Figure 6.6A). The corresponding calculated spectrum of this cluster with (B) and without (C) a bound hydroxyl ligand at Fe1. All spectra are scaled to the maximal intensity of the FeS stretching bands between 300 and 400  $cm^{-1}$ .

and the active site.

When comparing the calculated modes with the experimentally determined bands, two criteria have to be considered. The inherent accuracy of the QM/MM method for frequency calculations is approximately  $10\text{ cm}^{-1}$ , but isotopic shifts are calculated with a much higher precision. Secondly, the calculated Raman intensities are expected to provide only a qualitative description for the experimental RR intensities.

The Proximal  $[4Fe_3S]$  Cluster:

The QM model of the proximal FeS cluster in the superoxidized state consists of four iron and three inorganic sulfur atoms from the FeS cluster core (Figure D.4). This cluster is coordinated by six cysteine residues (17, 19, 20, 115, 120 and 149) and a hydroxyl group at Fe1 which is hydrogen bonded to His229, which itself is protonated on  $N\tau$ .<sup>[47]</sup> A second structure was found in the crystallographic analysis, where this hydroxyl ligand is missing. A special feature of the FeS cluster in the superoxidized state is the bond between Fe4 and the backbone nitrogen of Cys20. This bond, as well as two conserved water molecules in the vicinity of the cluster were also considered in the QM models.

In Figure 6.7A the experimental component spectrum  $C_{FeS}$  component is shown again. It is compared to calculated spectra based on the two structures, with and without the hydroxyl ligand at Fe1 in trace B and C, respectively. Both calculated spectra are normalized to the mean intensities of the FeS stretching modes.

For the structure without the  $\text{OH}^-$  ligand only very weak bands are predicted for the region between  $400$  and  $700\text{ cm}^{-1}$ , as opposed to the experimental data shown in trace A. In contrast, the calculated Raman spectrum derived from the structure with a hydroxyl ligand at Fe1 displays a satisfactory agreement with a root-mean-square-deviation (rmsd) of  $12.8\text{ cm}^{-1}$  that is close to the intrinsic uncertainty of  $\pm 10\text{ cm}^{-1}$  for the QM method.

But, there are some notable deviations which mainly refer to the modes including the Fe-OH stretching coordinates predicted at  $543$  and  $557\text{ cm}^{-1}$ . These modes are readily assigned to the experimental bands at  $554$  and  $578\text{ cm}^{-1}$  on the basis of the significant D/H and  $^{18}\text{O}/^{16}\text{O}$  isotopic shifts. (Figure 8.1 and 8.2) A discrepancy is found for the magnitude of the  $^{18}\text{O}/^{16}\text{O}$  shifts. It is predicted to be larger for the  $557\text{ cm}^{-1}$  than for the  $543\text{ cm}^{-1}$  mode ( $20$  vs.  $11\text{ cm}^{-1}$ ) in contrast to the experimental findings of  $7$  vs.  $23\text{ cm}^{-1}$  for the corresponding  $578$  and  $554\text{ cm}^{-1}$  bands. The shifts are summarized in Table D.2. Altogether, the sum of the shifts is essentially the same, such that this deviation may be related to the intrinsic error associated with the PED calculation for closely spaced modes of similar character. In addition, the calculated nearly pure Fe-OH stretching mode at  $557\text{ cm}^{-1}$  and the mode at  $603\text{ cm}^{-1}$ , dominated by the C-S stretching of Cys19, show quite substantial frequency deviations of approximately  $20\text{ cm}^{-1}$ , with respect to their experimental counterparts. This may reflect shortcomings of the method in adequately describing hydrogen bonded systems involving fluctuating water molecules. In fact, for the [NiFe] active site, which does not include water molecules, such large deviations were not observed.

#### The [NiFe] Active Site:

The QM model for the  $\text{Ni}_a\text{-L}$  state of the [NiFe] active site includes the [NiFe] core with the  $\text{CN}^-$  and CO ligands, four cysteine residues (75, 78, 597 and 600), Arg530, Thr553 and His82 (Figure D.5). Also the protonation of one cysteine is considered. As shown previously the RR spectrum of the hydrogen-reduced [NiFe] active site largely reflects the  $\text{Ni}_a\text{-L}$  redox state, photo-converted from the  $\text{Ni}_a\text{-C}$  and  $\text{Ni}_a\text{-SR}$  redox states during the RR experiment. The calculated spectrum including the  $^{13}\text{C}/^{15}\text{N}$  isotopic shifts are in very good agreement with the experimental RR spectrum, corresponding to a rmsd of  $7.3\text{ cm}^{-1}$ , as shown in Figure 5.10 and 6.8. Even the very weak bands at  $530$  and  $445\text{ cm}^{-1}$  can be assigned on the basis of their distinct  $^{13}\text{C}$  isotopic shifts, that are in line with

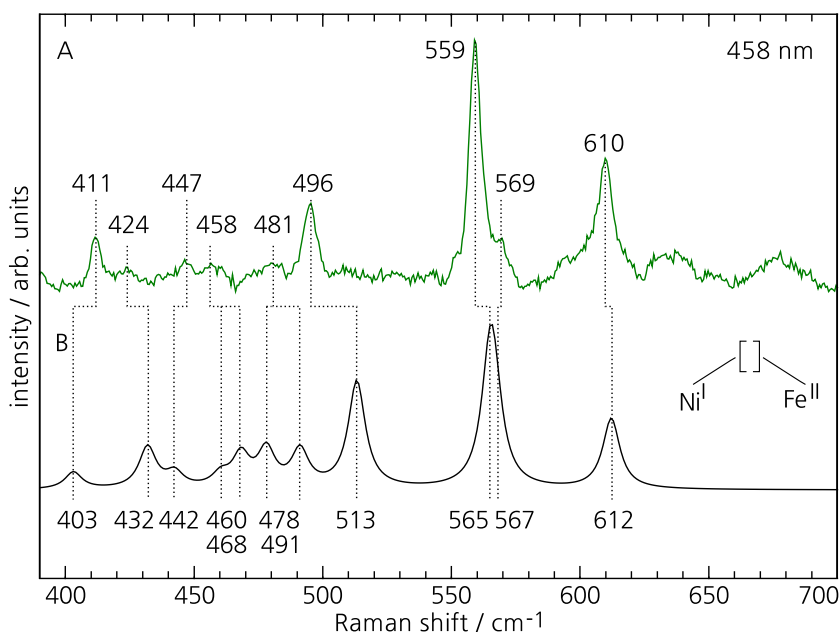


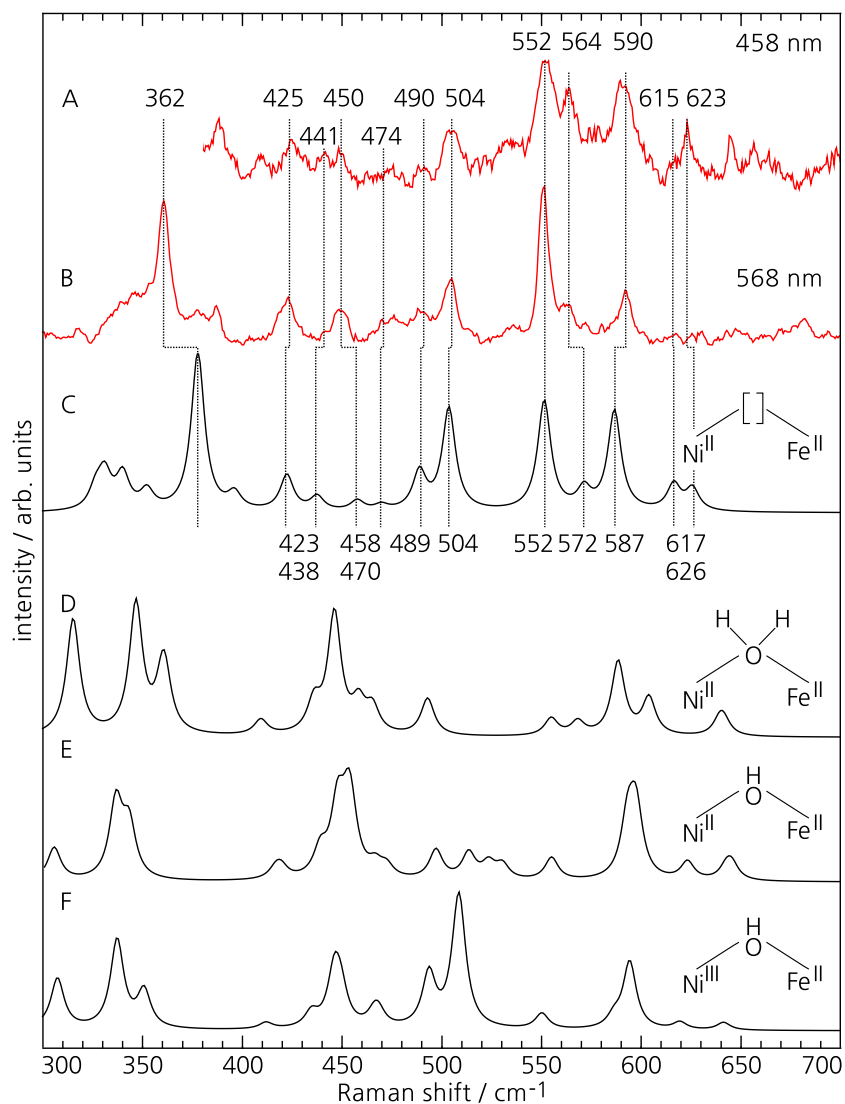
**Figure 6.8.:** (A) Complete component spectrum  $C_{NiL}$  of the  $Ni_a$ -L redox state, derived by mutual subtraction of selected experimental RR spectra measured at 458 nm (Figure 6.6C), compared to the calculated Raman spectrum (B).

the calculations. The remaining calculated modes at 478, 468, 460, and  $432\text{ cm}^{-1}$  are correlated with experimental bands solely based on the frequency match. However, the assignments are not unambiguous in each case due to close frequency spacing and the very low RR intensity slightly above the signal to noise level.

For the oxidized form of the active site, the same QM partition was employed but the calculations were carried out for different bridging ligands and oxidation states of the Ni ion. That is,  $Ni_r$ -B in oxidation state 3+ with a bridging hydroxyl ligand and the Ni-S species with Ni in oxidation state 2+ and either a hydroxyl, a water or no ligand in the bridging position. Other proposed configurations were tested as well, but they were not stable and relaxed back to  $Ni_a$ -S. The Fe remained in oxidation state 2+ in all of these redox states.

Figure 6.9 compares the various calculated spectra with the component spectrum  $C_{NiX}$  obtained at 458 nm and the RR spectrum directly measured at 568 nm, where only the Raman bands of the active site are enhanced. Clearly, the best agreement with the experimental spectra is achieved by the spectrum calculated for  $Ni_a$ -S. This spectrum nicely reproduces the three banded pattern between 550 and  $590\text{ cm}^{-1}$  in the experimental spectra and also correctly predicts the doublets at 490 and  $504\text{ cm}^{-1}$  as well as 615 and  $623\text{ cm}^{-1}$ , which is only detected at 458 nm excitation. In general, the different relative enhancements of the individual bands with excitations at 458 and 568 nm support the assignments, such that also most of the bands observed below  $500\text{ cm}^{-1}$  can be readily correlated with calculated modes and only a few uncertainties

**Figure 6.9.:** (A) Complete component spectrum  $C_{NiX}$ , derived by mutual subtraction of selected experimental RR spectra measured at 458 nm (Figure 6.6B). (B) Experimental RR spectrum obtained from an as-isolated MBH crystal with 568 nm excitation (Figure 6.2A). (C – F) Calculated Raman spectra for different oxidation states of the Nickel ion and different ligation patterns of the dinuclear center (see simplified structures on the right). Only the spectrum calculated for the  $Ni_a$ -S redox state (Trace C) agrees with the experimental RR spectra. Thus, the component spectrum  $C_{NiX}$  is renamed to  $C_{NiS}$ , to indicate the true nature of the Fe-CO / CN bands.



remain due to low band intensities. For the assignments in Figure 6.9, the rmsd is only  $4.4\text{ cm}^{-1}$  (Table D.4). In contrast, the calculated spectra of all other configurations provide a much worse description of the experimental spectra. This is in particular true for the  $Ni_r$ -B state which, according to the Infrared spectra (Figure 6.1), was the prevailing state of the oxidized samples studied in this work.

In summary, the component spectrum  $C_{NiX}$  is associated with Fe-CO / CN vibrations of the [NiFe] active site in the  $Ni_a$ -S redox state and the corresponding component spectrum is renamed to  $C_{NiS}$ .

#### 6.4. Effect of Photo-Reduction in $\text{Fe}(\text{CN})_6$ Treated Crystals

Ferricyanide  $[\text{Fe}(\text{CN})_6]^{-3}$  is widely used in biochemistry and chemistry as an oxidant. It has a strong absorption band at 420 nm and residual absorption at 458 nm.[205]

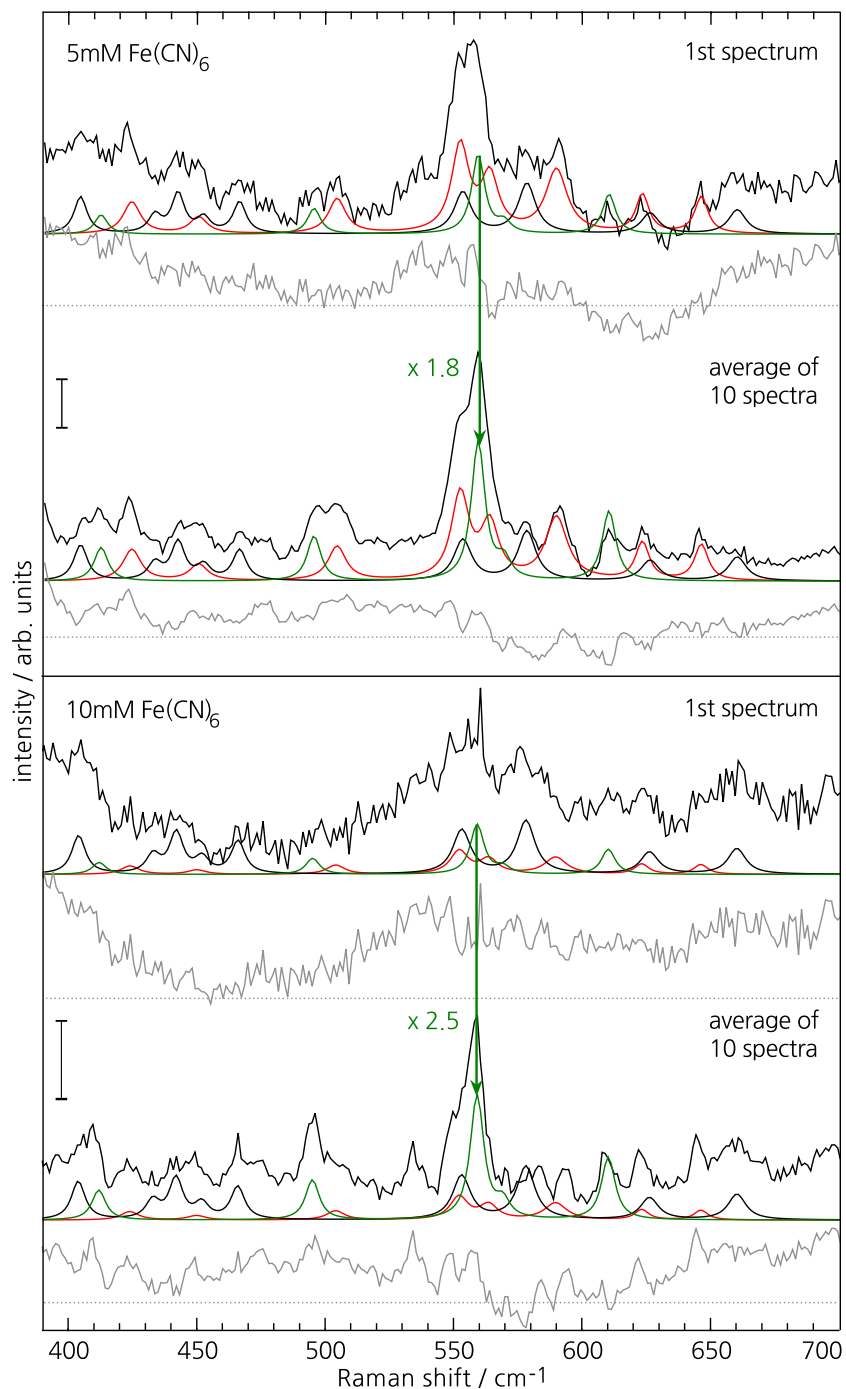
In order to enrich the amount of the superoxidized species with an  $\text{OH}^-$  bound to the proximal cluster, as-isolated samples of MBH crystals were treated with various amounts of ferricyanide (Appendix A). Figure 6.10 shows the corresponding RR spectra recorded at an excitation wavelength of 458 nm for two crystals soaked for three and a half hours in a mother liquor enriched with either 5 mM or 10 mM ferricyanide. Both graphs display the average of ten subsequently measured RR spectra, as for all other spectra shown in this work. In addition, also each first measured spectrum is plotted. Clearly the spectral intensity of the  $C_{\text{NiL}}$  component increases from the first to the averaged spectrum. A component analysis yields an intensity increase of a factor of 1.8 and 2.5 for the crystal soaked in 5 mM and 10 mM ferricyanide, respectively. Due to limitations with respect to the low signal to noise ratio a quantitative comparison of the relative intensity changes of the  $C_{\text{NiS}}$  and  $C_{\text{FeS}}$  components appears difficult for both crystals. No significant changes occurred in the spectral signature of the FeS stretching modes the region from 300 to 400  $\text{cm}^{-1}$  (not shown).

Photo-degradation products of ferricyanide are known to act as reducing agents [206, 207, 208, 209, 210, 211] and thus may reduce the nickel ion. This reaction may be followed by a photo-dissociation of the bridging hydroxyl ligand from the  $[\text{NiFe}]$  active site to form the  $\text{Ni}_a\text{-S}$  or leads to the accumulation of the further reduced  $\text{Ni}_a\text{-L}$  redox state.

Ferricyanide was present to various amounts in many of the samples used in this work. Not necessarily it was distributed homogeneously on the crystal surface and high local concentration of ferricyanide are possible. This provides a possible explanation for the detection of the  $\text{Ni}_a\text{-L}$  redox state in the RR spectra of crystals obtained from the as-isolated MBH. But also explains why RR spectra measured at different spots of the same crystal or different crystals from the same protein preparation exhibit different cofactor states (Figure 6.2C–F). Here, it is worth to note that the RR spectra do not allow conclusions about the quantitative distribution of the various active site states in the crystalline samples.

The

**Figure 6.10.:** Effect of photo-reduction for two crystals soaked in 5 or 10 mM ferricyanide. In both cases the intensity of the  $C_{NiL}$  component is increased, while it is difficult to compare the relative intensity changes for the  $C_{NiS}$  and  $C_{FeS}$  component spectra in a quantitative manner in the first and average spectrum.



RR spectra solely reflect the existence of those states, which are Raman active (i.e.  $Ni_a-S$  and  $Ni_a-L$  for the  $[NiFe]$  active site).

## 6.5. Discussion and Summary

In view of the two photo-activated species  $Ni_a-L$  and  $Ni_a-S$  observed in the RR spectra of the as-isolated MBH samples the pro-

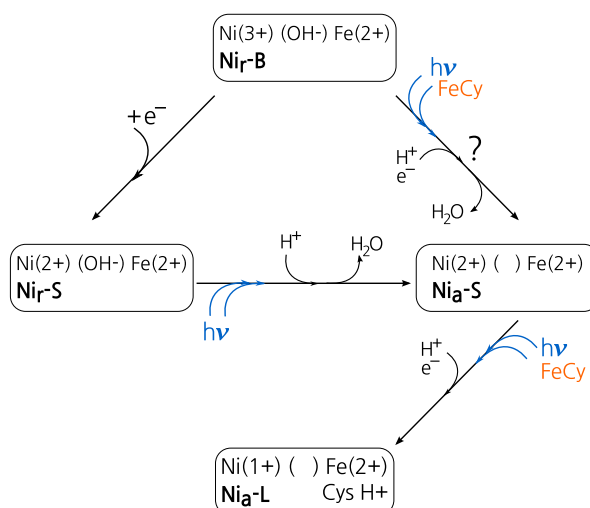
posed reactivation of oxidized redox states by light is recalled.[11, 116]

In the oxygen-sensitive [NiFe] hydrogenase from *Desulfovibrio vulgaris* Miyazaki F, the Ni<sub>r</sub>-S state was shown to undergo light-induced reactions at temperatures of 40 K. The efficiency of these reactions increases by a factor of two from 490 to 600 nm.[114] This wavelength-dependence of the photo-conversion matches the present results inasmuch as a substantially more intense RR spectrum was obtained at 568 than at 458 nm (Figure 6.2). However, the photo-products proposed by these authors, such as the Ni-SL state with a hydroxyl ligand coordinated to the nickel ion, were discarded in this study because of their instability in the QM/MM calculations. Instead, the comparison of the experimental to the theoretical Raman spectra strongly favors the association of the C<sub>NiX</sub> = C<sub>NiS</sub> component spectrum to Fe-CO/CN vibrations of the Ni<sub>a</sub>-S redox state. This assignment suggests that the high photon densities of the probe laser in the RR experiments causes the dissociation of the hydroxyl ligand from the bridging position of either the Ni<sub>r</sub>-B or the Ni<sub>r</sub>-S state (Figure 6.11).

The most plausible origin is the 15 – 20 % fraction of Ni<sub>r</sub>-S in the as-isolated MBH, which readily accounts for the experimental findings, since the Raman spectrum of Ni<sub>r</sub>-B as the main component is not resonance enhanced. The photo-conversion from the Ni<sub>r</sub>-S to the Ni<sub>a</sub>-S state solely requires the laser induced dissociation of the bridging ligand, whereby the oxidation state of Ni<sup>2+</sup> remains unchanged. However, a photo-conversion of the Ni<sub>r</sub>-B state, requiring both the Ni<sup>3+</sup> to Ni<sup>2+</sup> reduction and the removal of the hydroxyl ligand from the bridging position, cannot be ruled out completely. It might be that both events are induced by the action of the probe laser on the [NiFe] center, although the Ni<sup>3+</sup> state was found to be photo-stable in a previous study on the [NiFe] hydrogenase of *Desulfovibrio vulgaris* Miyazaki F.[83, 115] But there are indications for a lower photo-stability of Ni<sub>r</sub>-B in oxygen-tolerant hydrogenases. For the [NiFe] hydrogenase I of *Aquifex aeolicus*, a light-induced re-activation of the enzyme has been detected under turnover conditions at high potentials, which was tentatively explained by photo-induced hydroxyl ligand removal from Ni<sub>r</sub>-B to afford a Ni<sub>a</sub>-S state.[116] Such a process might also take place in MBH under the conditions of the present RR experiment.

An alternative mechanism for the photo-conversion is based on the decomposition of ferricyanide through the incident laser light. Ferricyanide is presumably present in locally enriched amounts in

**Figure 6.11.:** Proposed reaction pathway of the oxidized active site under the influence of light.



many crystalline samples used in this work. The photo-products of ferricyanide may act as reducing agents [206, 207, 208, 209, 210, 211] to convert for instance  $Ni^{3+}$  to  $Ni^{2+}$ , followed by a dissociation of the hydroxyl ligand from the [NiFe] active site or lead to a population of a further reduced species, such as Ni<sub>a</sub>-L. This is in line with the observation that a photo-reduction of the active site occurred in the presence of excess ferricyanide and illumination with the Raman probe beam. Interestingly, the relative intensity of the Fe-CO / CN vibrational modes of the Ni<sub>a</sub>-L redox state increased significantly, while no reliable statements can be made regarding the absolute intensities of the vibrations from the Ni<sub>a</sub>-S redox state as well as those from the superoxidized proximal cluster.

With this proven photo-induced reactivation of the active site the 'window of activity for H<sub>2</sub>-oxidation [11] in a fuel cell may be broadened and thus the performance of the biofuel cell increased.

In summary, this chapter presented an in-depth vibrational spectroscopic investigation on oxidized crystals of the oxygen tolerant MBH from *Ralstonia eutropha*.

1. Using FTIR spectroscopy it was shown that the redox-state of the active site of these crystals resembles that of the MBH in solution, namely a major fraction of Ni<sub>r</sub>-B and up to 20% of the Ni<sub>r</sub>-S redox-state. In addition, these infrared spectra are the first of a single protein crystal and thus, demonstrate another spectroscopic tool for the analysis of single protein crystals.
2. RR spectra of similar samples were shown to consist of three superimposed independent spectral components. Wavelength-dependent RR spectra suggested that two components derive

from modes of the active site and one from a FeS cluster. This latter component is associated with the superoxidized proximal cluster with a bound hydroxyl group at Fe1, as it was only observed in RR spectra of the as-isolated MBH and in the RR spectrum of the P242C MBH variant where this cluster remained unchanged. Notably, all genetically engineered MBH samples showed the unmodified modes of the active site.

3. In addition, the spectral components for an excitation at 458 nm were determined and compared to calculated Raman spectra (by Y. Rippers [204]), allowing the assignment of the experimental Raman bands to Fe-CO / CN modes of the Ni<sub>a</sub>-L and Ni<sub>a</sub>-S redox state and thus prove a photo-induced activation of the enzyme. The third component was assigned to Fe-OH and Fe-Cys modes of the proximal cluster with a hydroxyl group bound at Fe1. This is an additional spectroscopic prove for the existence of this group on the proximal cluster, which is discussed to be one of the keys for the exceptional oxygen-tolerance of the MBH from *Ralstonia eutropha*.
4. The experimental FTIR and RR spectra, the crystal structure and the calculated Raman spectra are all based on as-isolated MBH crystals of the very same preparations. This ensures a consistent analysis of the MBH structure and its function. Since each of the three techniques reflects different properties of the enzyme their combination can give further subtle but important insights into the structure and function of the MBH. Some of these informations are not accessible via x-ray crystallography, as will be shown in Chapter 8.

Based on the component spectra for 458 nm excitation, RR spectroscopy on hydrogenases now offers another experimental technique, apart from EPR spectroscopy, to investigate the FeS clusters and the active site at once. The ability to spectroscopically investigate *both* the active site and the proximal FeS cluster is crucial to unravel their structure-function relationship and in turn to efficiently use these enzymes for biofuel cells in the future.



# 7. Resonance Raman

## Characterization of FeS

### Stretching Modes

The previous two chapters focused on the Resonance Raman (RR) spectra of the reduced and as-isolated MBH. In concert with quantum mechanical / molecular mechanical (QM / MM) calculations the vibrational modes found in the spectral region from 400 to 700  $\text{cm}^{-1}$  were consistently assigned to Fe-CO / CN stretching and bending modes of the active site in the  $\text{Ni}_a\text{-L}$  and  $\text{Ni}_a\text{-S}$  redox state. Additionally, Fe-OH and Fe-Cys modes of the superoxidized proximal cluster  $[\text{4Fe3S}]_p\text{+OH}$  were identified.

The subject of this chapter is to discriminate the stretching modes of the three different FeS clusters in the electron transport chain of the MBH. Only vibrational modes of the oxidized FeS clusters will be investigated, as modes of the reduced clusters experience merely a weak resonance enhancement.[\[212, 37, 213\]](#)

The RR spectra of the as-isolated MBH exhibit a broad superposition of different FeS stretching modes in the spectral window below 400  $\text{cm}^{-1}$ . The individual bands originate from the three types of clusters from the MBH, namely  $[\text{4Fe3S}]$ ,  $[\text{3Fe4S}]$  and  $[\text{4Fe4S}]$  at the proximal, medial and distal position, respectively. Thus, three diverse clusters with FeS stretching modes at band positions, which may differ by not more than 1  $\text{cm}^{-1}$  and full widths at half maximum (FWHM) on the order of 10  $\text{cm}^{-1}$  contribute to the Raman spectrum. In addition the resonance conditions for all three clusters lie in the same energy window. It is therefore not possible to discriminate the vibrational modes of the individual clusters with the techniques used in the previous chapters. Instead, angle-dependent RR spectroscopy on single as-isolated MBH crystals is employed. This method has not yet been used to disentangle RR spectra of multifactor-protein complexes.

Before we turn to the in-depth analysis of the RR spectra, a brief summary of relevant results from the literature, details of the ex-

perimental setup and conventions used in this chapter will be given in Section 7.1. Then, the RR spectra of the as-isolated crystals will be compared to RR spectra of (re-)oxidized solubilized MBH samples in the bulk to verify that both preparation methods yield identical molecular structures and crystallization artifacts in the sample preparations can be excluded. (Section 7.2) Subsequently, the angle-dependence of the RR spectra from the MBH crystals is analyzed in detail to identify the band positions of FeS stretching modes in the different clusters. (Section 7.3) The angle-dependent RR analysis is complemented by RR spectroscopy of the MBH in different redox-states and with genetically engineered MBH variants in order to confirm the assignment. (Section 7.4) Using RR difference spectroscopy the results of the previous sections will be quantitatively corroborated and the approximate component spectra of each individual FeS cluster are acquired. (Section 7.5)

## 7.1. Preliminary Considerations

The broad superposition of bands in the spectral region from 325 to 380  $\text{cm}^{-1}$  in the RR spectrum of the as-isolated MBH originates from the three FeS cluster of the proteins electron transport chain. In the medial and distal position of this chain the widely studied [3Fe4S] and [4Fe4S] are found. RR spectra of such clusters were studied extensively in the 1980's and 1990's.[214, 213, 215, 37] Johnson and co-workers [214] have shown for ferredoxins of *Azotobacter vinelandii* and *Thermus thermophilus*, which both harbor a [3Fe4S] and a [4Fe4S] cluster, that the RR spectra excited at 458 and 488 nm are dominated by modes of the [3Fe4S] clusters. Here, the most intense [3Fe4S] bands were found at 347 and 368  $\text{cm}^{-1}$ . In comparison, bands of the [4Fe4S] cluster were detected as shoulders on the low frequency side with much lower intensities. Other groups [213, 215, 37] have confirmed that both clusters are characterized by two more or less equally intense bands and that the vibrational modes of the [4Fe4S] clusters are shifted by a less than 3  $\text{cm}^{-1}$  to lower frequencies with respect to the [3Fe4S] modes. This knowledge will help in the following to identify the [3Fe4S] and [4Fe4S] modes in the spectra of the as-isolated MBH. However, a consistent analysis of the spectra will independently yield the same results as in Reference [214].

In the proximal position, however, an [4Fe3S] cluster is found. This cluster is unique in oxygen-tolerant hydrogenases and is therefore related to their catalytic activity in the presence of oxygen.[43, 44,

color	cluster	band positions with $\Delta\nu = \pm 1 \text{ cm}^{-1}$	
black	$[4\text{Fe3S}]_{\text{p}}+\text{OH}$	344.5	356.5
gray	$[4\text{Fe3S}]_{\text{p}}$	346.0	368.0
blue	$[3\text{Fe4S}]_{\text{m}}$	342.0	366.0
orange	$[4\text{Fe4S}]_{\text{d}}$	336.6	364.0

**Table 7.1.:** The color code declares which bands are assigned to FeS stretching modes of the proximal, medial or distal cluster. At these positions vertical lines with the respective color are included in all figures of this chapter.

45, 46, 47] It is coordinated by six cysteines, instead of four as in oxygen-sensitive hydrogenases. One iron atom is bound to a backbone nitrogen and another one to a hydroxyl ligand.[47] In this work, the vibrational spectrum of the proximal  $[4\text{Fe3S}]$  cluster is investigated for the first time.

The subject of the following sections is to discriminate between the FeS stretching bands of the medial and distal FeS cluster, as well as the proximal cluster with and without a bound hydroxyl ligand. The final band positions of the FeS stretching bands will be marked with vertical lines in all of the following figures. The respective color code is defined in Table 7.1.

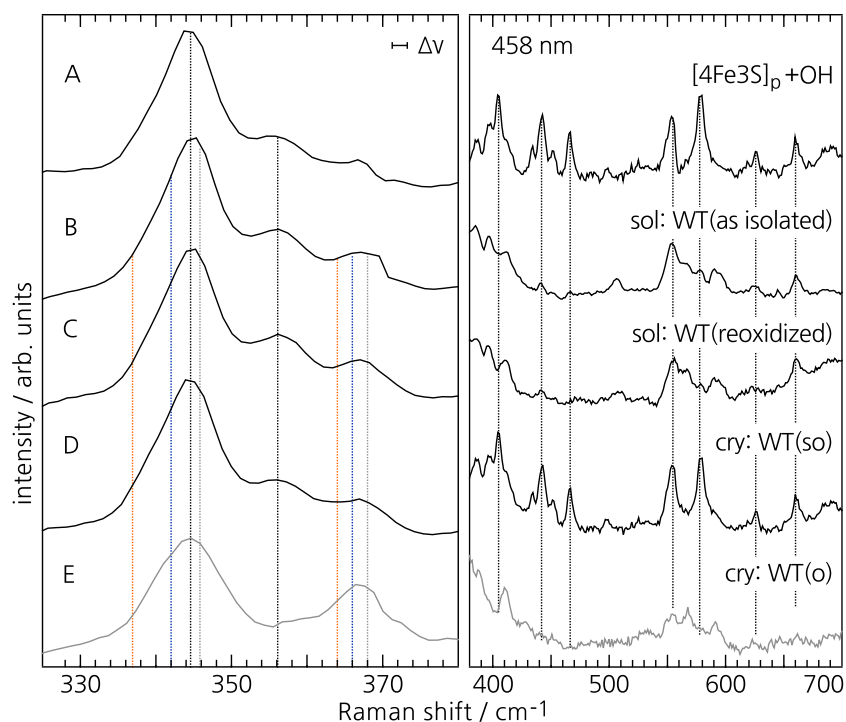
All RR spectra shown in this chapter were obtained with an excitation wavelength of 458 nm and at sample temperatures of 80 K. The electric field vector of the incident laser beam is parallel ( $\beta'=0^\circ$ ) to the c-axis of the single MBH crystal, if not stated otherwise. Occasionally a sharp peak  $369.0 \text{ cm}^{-1}$  appears in the spectrum. It is associated with with a photoluminescence of the quartz sample holder and marked with an asterisk. This peak and a further ice band at  $274.0 \text{ cm}^{-1}$  is used as an internal reference to calibrate the energy axis to an accuracy of at least  $\pm 1 \text{ cm}^{-1}$ . This is of great importance as the FeS stretching bands of the individual FeS clusters of the MBH will be shown to differ by not more than  $2 \text{ cm}^{-1}$  in some cases and have FWHM of 8 to  $10 \text{ cm}^{-1}$ .

## 7.2. Comparison of Crystalline and Solubilized MBH Samples

Numerous spectroscopic and electrochemical experiments confirmed the high quality of the as-isolated solubilized heterodimeric MBH preparations in terms of activity and oxygen-tolerance. During the reoxidation process the inactive redox species  $\text{Ni}_{\text{ia}}\text{-S}$  of the  $[\text{NiFe}]$  active site forms to about 30% (see Chapter 4), which implies that the reactivation is only partially reversible.[33, 89] In the present

**Figure 7.1.:** RR spectra excited at 458 nm of the MBH in its as-isolated, oxidized or reoxidation form. A) Extracted RR difference spectrum of the superoxidized proximal cluster  $[4\text{Fe3S}]_p+\text{OH}$ . (See Section 6.2.2) B and C) RR spectra of the as-isolated and reoxidized MBH in solution. D and E) RR spectra of two types of as-isolated MBH crystals, where the  $\text{OH}^-$  ligand is bound to the proximal cluster (WT(so)) and where it is absent (WT(o)). In case the hydroxyl ligand is bound, Fe-OH stretching modes appear above  $400\text{ cm}^{-1}$ . These bands are marked with dotted lines on the right hand side of the plot.

Proposed band positions of the FeS stretching modes for the  $[4\text{Fe3S}]_p+\text{OH}$ ,  $[4\text{Fe3S}]_p$ ,  $[3\text{Fe4S}]_m$  and  $[4\text{Fe4S}]_d$  cluster shown in black, gray, blue and orange, respectively. (See Table 7.1) Intensities in the right panel are increased by a factor of 3.0.



work it was shown with FTIR spectroscopy that the  $[\text{NiFe}]$  active site from as-isolated crystalline samples of the MBH resides with 83% in the  $\text{Ni}_I\text{-B}$  and with 17% in the  $\text{Ni}_{a/r}\text{-S}$  redox state. The corresponding spectrum is shown in Figure 6.1 (Chapter 6) in comparison to the solubilized as-isolated MBH. Additionally, it has been shown that the superoxidized proximal cluster of the chosen crystalline samples from the MBH has a hydroxyl ligand bound to Fe1 (Chapter 6). The complete component RR spectrum of this cluster,  $[4\text{Fe3S}]_p+\text{OH}$ , was obtained by mutual subtraction of RR spectra recorded at 458 nm. (Trace A in Figure 7.1) By means of QM/MM calculations the distinct bands between  $400$  and  $700\text{ cm}^{-1}$ , which are marked with dotted black lines, were assigned to Fe-OH and Fe-Cys modes of this specific cluster. Two characteristic bands at  $344.5$  and  $356.5\text{ cm}^{-1}$  (black lines) are observed in the spectral region of the FeS stretching modes. Accordingly, I assign them to the superoxidized proximal cluster.

To exclude that the hydroxyl ligand at the proximal cluster is a crystallization artifact, RR spectra from as-isolated and reoxidized heterodimeric MBH samples in bulk solution were measured, as shown in trace B and C of Figure 7.1.<sup>A</sup> Both spectra show the characteristic spectral signature that belongs to the superoxidized proximal cluster ( $[4\text{Fe3S}]_p+\text{OH}$ ) and show minor bands that were assigned to vibrational modes of the  $\text{Ni}_a\text{-S}$  redox state in Chapter 6. In turn that implies that the hydroxyl ligand at the proximal cluster is a native feature of the as-isolated MBH and not a

<sup>A</sup>The MBH samples in the heterodimeric form lack the electron acceptor cytochrome *b*. This is useful for the RR spectroscopic investigations, as the cytochrome would strongly overlap with the rather weak signal of the other MBH cofactors.

crystallization artifact. Secondly, the hydroxyl ligand is restored during the reoxidation process.

However, the overall intensity of the corresponding Fe-OH vibrational modes decreased slightly in the RR spectrum of the reoxidized sample (trace C). This indicates that the hydroxyl ligand did not rebind to the proximal cluster of each MBH macro-molecule, i.e. the reoxidation process is not completed. On the other hand, the reoxidation process of the MBH is always accompanied by a moderate formation of the inactivated Ni<sub>ia</sub>-S species of the active site. (See Chapter 4) These two observations indicate that the formation of the hydroxyl ligand during the reoxidation protects the active site from being irreversibly damaged under the influence of oxygen. In other words, if the hydroxyl ligand binds to the proximal cluster the less Ni<sub>ia</sub>-S redox species is formed at the active site. In accordance to that, this hydroxyl ligand is crucial for the oxygen-tolerance of the whole enzyme.

The spectrum of the single crystal is composed almost exclusively of the vibrational modes from the proximal cluster [4Fe3S]<sub>p</sub>+OH in its superoxidized state (Figure 7.1D). Crystalline MBH wildtype samples with such a Raman signature will be termed WT(so) in the following text. Here, (so) indicates that the proximal cluster resides in the superoxidized, i.e. the native form.

A RR spectrum of another aerobically grown MBH crystal measured under the same conditions is shown in trace E. The signature of the FeS stretching modes clearly differs from the one shown in trace D. A band at 344.5 cm<sup>-1</sup> is detected here, but the one at 356.5 cm<sup>-1</sup> is missing. Moreover, the high frequency modes related to Fe-OH and Fe-Cys vibrations of the superoxidized proximal cluster are not detected. In view of the QM / MM calculations, these modes disappeared in the calculated Raman spectra for the proximal FeS cluster when the hydroxide ligand at Fe1 was removed. (Figure 6.7C) Therefore, the spectrum in Figure 7.1E is initially assigned to an aerobically grown MBH crystal without a bound hydroxide ligand at the proximal cluster. Such MBH wildtype samples will be addressed as WT(o). The only difference to WT(so) is the missing hydroxide ligand at the proximal cluster, the structure of the medial and distal cluster are unchanged, as well as that of the active site.[189]

Notably, the detection of the hydroxide ligand in RR spectroscopy depends on the preparation batch of the measured samples, although the preparation and growth conditions for each sample series were identical. However, small variances, which in turn cause

<sup>B</sup>x-ray crystallography cannot distinguish between OH<sup>-</sup>, OH and O

the observed effect, cannot be ruled out completely. X-ray crystallographic data from a number of aerobically grown MBH crystals, which were obtained from the very same preparations as used for the RR experiments discussed here, revealed an occupancy of the oxygen ligand at the Fe1 of the proximal cluster between 30 to over 80%.<sup>B</sup> Thus, both RR spectroscopy and x-ray crystallography confirm that the formation of the hydroxide ligand in the as-isolated crystalline samples of the MBH is influenced by the preparation conditions. Also, a x-ray or light-induced reductive removal of this ligand can be ruled out as well.

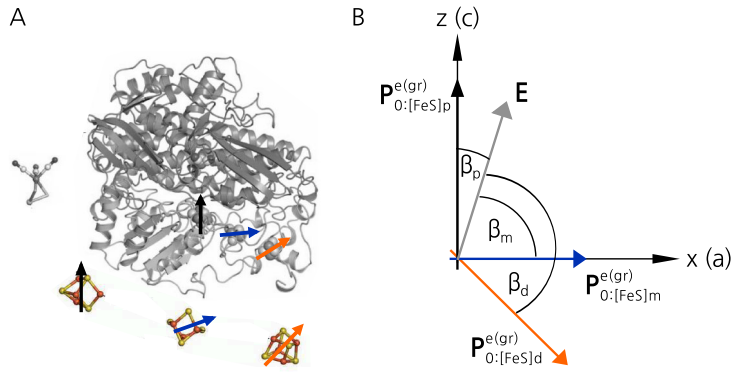
In view of these results, the two experimental techniques of RR spectroscopy and x-ray crystallography on single aerobically grown MBH crystals are capable to distinguish whether or not a hydroxide ligand is bound to the Fe1 of the proximal cluster. This enables further experiments regarding the origin of this ligand. In terms of the biochemical origin, several point-mutations in the vicinity of the proximal cluster have been performed already[43, 47, 203] and will be investigated with RR spectroscopy in Section 7.4. MBH wildtype samples labeled with D<sub>2</sub>O, H<sub>2</sub><sup>18</sup>O and <sup>18</sup>O<sub>2</sub> at various steps of the catalytic cycle will be investigated with RR spectroscopy in Chapter 8 and reveal the origin of the hydroxide ligand.

### 7.3. Angular Dependence of Resonance Raman Spectra

Electronic transitions within the FeS clusters are characterized by a broad absorption band between 380 and 500 nm in the UV-vis spectrum of the as-isolated solubilized MBH samples. (See Section 5.2) By choosing an excitation wavelength of 458 nm, which coincides with this absorption band, vibrational modes of all FeS clusters are resonantly enhanced.

In Section 3.4 the scattering effect for normal (pure) vibrational RR scattering is described theoretically. Contributions to the scattered intensity are restricted to the Franck-Condon Term (or A-Term) of the polarizability tensor. Under these presumptions, the scattered RR intensity for the  $k^{th}$  vibrational mode is proportional to:[157]

$$I_k^{scat} \sim \left| \mathbf{P}_0^{e(gr)} \cdot \mathbf{P}_0^{e(rg)} \cdot \mathbf{E} \right|^2 \frac{\left| \langle v_k^{f(g)} | v_k^{r(r)} \rangle \langle v_k^{r(r)} | v_k^{i(g)} \rangle \right|^2}{(\omega_{e(rg)} + \omega_{v_k(r)})^2 + \Gamma_r^2} \quad (7.1)$$



For a non-zero scattered intensity, not only the two Franck-Condon integrals  $\langle v_k^{f(g)} | v_k^{r(r)} \rangle \langle v_k^{r(r)} | v_k^{i(g)} \rangle$  have to non-zero, but also product of the two pure electronic transition moments  $\mathbf{P}_0^{e(gr)}$  and  $\mathbf{P}_0^{e(rg)}$ . The two vectorial quantities  $\mathbf{P}_0^{e(\cdot)}$  are non-zero, if the electronic transition  $|e^r\rangle \leftarrow |e^g\rangle$  is dipole allowed. The probability for this transition is given by:[161]

$$W_{gr} \sim \left| \mathbf{P}_0^{e(gr)} \cdot \mathbf{E} \right|^2 \sim \cos^2 \beta \quad (7.2)$$

where  $\beta$  is the angle between the electric field vector  $\mathbf{E}$  of the incident electromagnetic radiation and the electronic transition dipole moment  $\mathbf{P}_0^{e(gr)}$ . The transition probability and, accordingly, the scattered intensity is maximal (minimal) when both vectors are parallel (perpendicular) to each other.  $I_k^{scat}$  is proportional to the square cosine of the angle between the incident laser and the electronic transition dipole moment of the system under study.

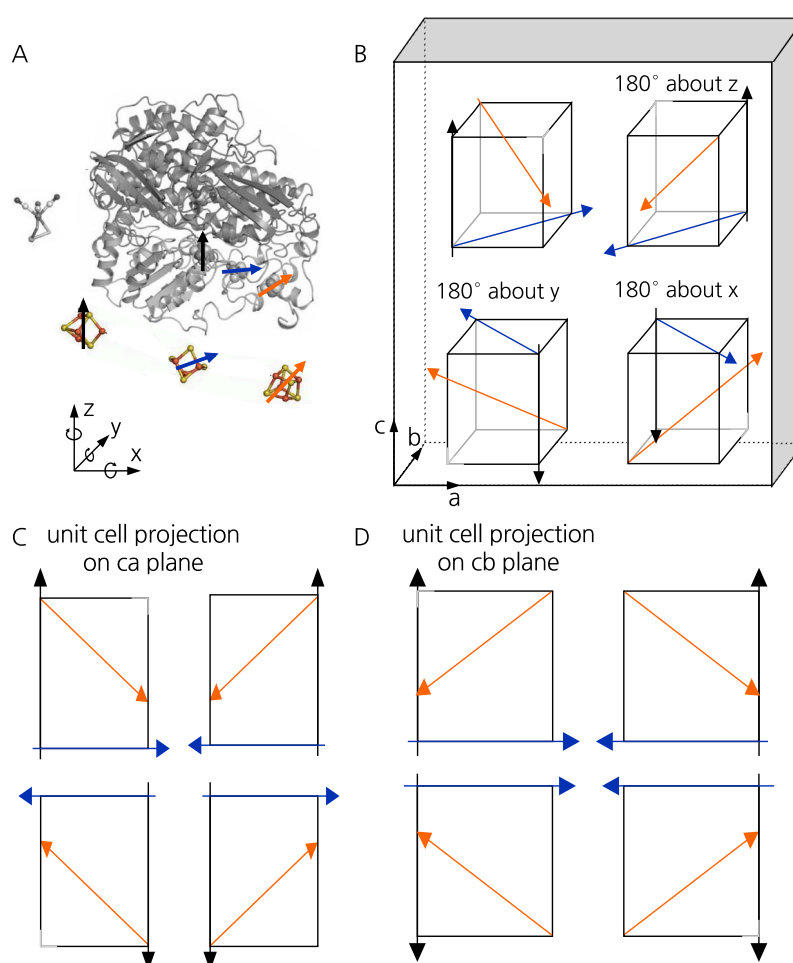
This angle-dependent effect of the scattered RR intensities will be used in this section to discriminate the vibrational modes of the three FeS cluster of the MBH. It is assumed, that the electronic transition dipole moments of the three individual FeS clusters point in different directions. Figure 7.2 illustrates this for three randomly chosen cases of  $\mathbf{P}_{0:[FeS]\diamond}^{e(gr)}$ .<sup>C</sup> The approximate projection of the pure electronic transition dipole moment for each FeS cluster, with respect to the c-axis of the crystal, is determined later in the text. However, the angle  $\beta_\diamond$  for the maximal transition probability is different for all three clusters. That results in the same angular-dependence of all vibrational modes of one specific cluster. This angular-dependence differs from that of another cluster.

The following RR spectra were obtained from aerobically grown MBH single crystals. Therefore, a number of highly ordered MBH macro-molecules is excited with the incident laser beam, whose

**Figure 7.2.:** A) Crystal structure of the MBH, with increased view of its cofactors – the [NiFe] active site and the three FeS clusters.[44, 47] The pure electronic transition dipole moments of each FeS cluster are illustrated by three differently colored arrows pointing in arbitrary directions. It is proposed that the pure electronic transition dipole moment points a in different directions for each of the three FeS clusters. B) Representation of the electric field vector  $\mathbf{E}$  of the incident laser and the pure electronic transition dipole moments  $\mathbf{P}_{0:[FeS]\diamond}^{e(gr)}$  of the FeS clusters in a Cartesian coordinate system. (With  $\diamond = p, m$  or  $d$ ) The probability  $W_{gr}$  for an electronic transition from a ground to an excited electronic state in the FeS cluster scales with the square of the scalar product of these two vectors. The transition probability in a specific FeS cluster is thus maximal whenever  $\mathbf{E}$  and  $\mathbf{P}_{0:[FeS]\diamond}^{e(gr)}$  are parallel to each other.

<sup>C</sup>with  $\diamond = p, m$  or  $d$ , for proximal, medial or distal FeS cluster. The proximal cluster is either in the  $[4Fe3S]_p+OH$  or  $[4Fe3S]_p$  configuration.

**Figure 7.3.:** A) Crystal structure of the MBH, with increased view of its cofactors – the [NiFe] active site and the three FeS clusters.[44, 47] The pure electronic transition moments of the FeS cluster are symbolized by three differently colored vectors. The MBH crystallizes in the  $P2_12_12_1$  space group with four asymmetric units per unit cell, which are represented by four boxes in part B) of the figure. Each of these four units harbors one MBH dimer and the corresponding electronic transition dipole moments of the three FeS clusters are again drawn as differently colored vectors. Three extreme cases have been chosen here just for illustrative matters. The correct vectors are not determined so far. Using RR spectroscopy the projection of the electronic transition moments either on the ca- or cb-plane of the crystal is probed. The respective projections are shown in part C) and D) for one unit cell. A large number of unit cells is probed in the RR experiment and the electronic transition dipole moments add up.



direction of propagation is perpendicular to either the ca- or the cb-plane of the crystal. Thus, only the projections of the electronic transition dipole moments on either one of these planes are probed. In Figure 7.3 the influence of the space group of the crystallized MBH on these projections is illustrated in a schematic way. The MBH crystallizes in the orthorhombic  $P2_12_12_1$  space group, like 75% of all protein crystals.[216] The space group provides the information on how the individual MBH macro-molecules are arranged in the crystal: The unit cell of the aerobically grown crystals is composed of four asymmetric units.<sup>D</sup> In the unit cell, the asymmetric unit is successively turned by  $180^\circ$  around the three orthogonal screw axes x, y and z, as shown in Figure 7.3B. As each asymmetric unit harbors one MBH-dimer, with electronic transition dipole moments for the three FeS clusters, the four boxes in part B of the figure also include differently colored vectors to symbolize these moments. Three extreme directions for the electronic transition dipole moments of the proximal, medial and distal cluster were chosen just to illustrate the effects. First – parallel to one of the axes of the unit cell, second – in the direction of one of

<sup>D</sup>with dimensions of  $a = 73 \text{ \AA}$ ,  $b = 95 \text{ \AA}$  and  $c = 119 \text{ \AA}$  with  $\alpha = \beta = \gamma = 90^\circ$ , [47]

the planes of the unit cell and third – with a random orientation. The correct vectors should be calculated in principal by elaborate quantum chemical means based on the crystal structure. Part C and D of Figure 7.3 show the projections of the three electronic transition dipole moments on the *ca*- and *cb*-plane from *one* unit cell of the crystal. In the experiment however, a larger number of unit cells are probed at once and thus the electronic transition dipole moments are added up.

Accordingly, the angle-dependent RR spectra of the as-isolated MBH can be discussed.

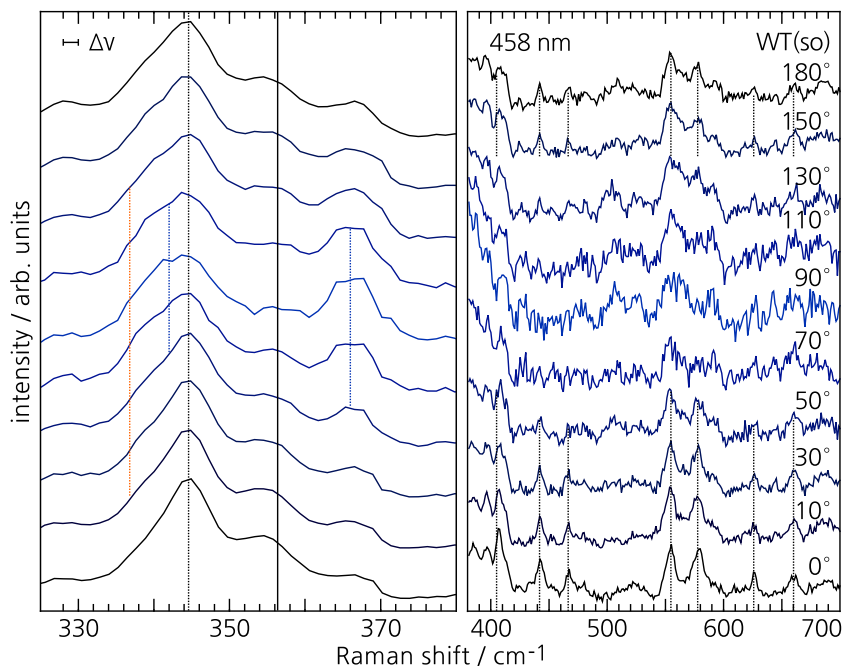
To emphasize the angle-dependent effects on the vibrational spectra of the three FeS clusters, the measured angle-dependent RR spectra shown in Figure 7.4 and 7.5 are normalized to the integral area of the most intense FeS stretching modes between 330 and 375  $\text{cm}^{-1}$ . Normally, the measured intensity is calibrated with respect to the sensitivity of the grating in the spectrograph, which is a complex function of the polarization of the incident light.[217] In Figure E.1 of Appendix E the RR spectra of the WT(so) MBH are scaled accordingly. More details regarding the calibration of the angle- and polarization-dependent RR measurement setup are described there as well.

In the previous section two distinct forms of aerobically grown MBH wildtype crystals have been discriminated. The WT(so) form, where the hydroxyl ligand is bound to the proximal FeS cluster of the MBH and the WT(o) form, where the  $\text{OH}^-$  is missing. Both samples have identical structures for the medial and distal cluster as well as identical active sites.[189] The angle-dependent spectra of both types of samples are shown in Figure 7.4 and 7.5, with increments of  $20^\circ$ . Here the excitation angle  $\beta'$  defines the angle between the *c*-axis of the crystal and the electric field vector of the laser beam.

The spectrum of the WT(so) crystal in Figure 7.4 shows the characteristic signature of the proximal  $[\text{4Fe3S}]_p + \text{OH}$  cluster at an excitation angle of  $\beta' = 0^\circ$ . The band positions of the FeS stretching modes are marked with vertical black lines at 344.5 and 356.5  $\text{cm}^{-1}$ . Additionally, the high frequency modes assigned to Fe-OH and Fe-Cys vibrations are detected between 400 and 700  $\text{cm}^{-1}$ , as shown in the right panel of the Figure. At  $\beta' = 180^\circ$  the spectrum is almost identical to the one measured at  $0^\circ$ . Small deviations are ascribed to a loss of the focus due to a thermal drift of the sample under the microscope objective over the entire measurement cycle of five hours.

**Figure 7.4.:** RR spectra of a single as-isolated MBH WT(so) crystal obtained at angles  $\beta'$  from 0 to 180° between the electric field vector of the incident laser and the c-axis of the crystal. The measured spectral intensities are normalized to the integral area between 330 and 375 cm<sup>-1</sup>. Dotted lines on the right side of the plot show the FeOH marker bands of the superoxidized proximal cluster.

Proposed band positions of the FeS stretching modes for the [4Fe3S]<sub>p</sub>+OH, [3Fe4S]<sub>m</sub> and [4Fe4S]<sub>d</sub> cluster shown in black, blue and orange, respectively. (See Table 7.1) Intensities in the right panel are increased by a factor of 3.0.



At an excitation angle of  $\beta' = 90^\circ$  the overall signature of the spectrum changes dramatically. The high frequency bands of the superoxidized proximal cluster decrease strongly in intensity and are in the range of the noise. The most intense FeS stretching band of the spectrum is broadened and shifted to a somewhat lower frequency at 342.0 cm<sup>-1</sup> (blue). Simultaneously the intensity of the band at 366.0 cm<sup>-1</sup> (blue) increases.

For excitation angles of 70 and 110° the shoulder at 336.5 cm<sup>-1</sup> (orange line) gains maximal relative intensity.

The angle-dependent RR spectra of a WT(o) type single MBH crystal are depicted in Figure 7.5. At a first glance, the overall spectral signature reveals no strong angular-dependence. However, the two main bands in the FeS stretching region found at 346.0 and 368.0 cm<sup>-1</sup> (gray lines) show a slight shift to lower frequencies at perpendicular (90°) excitation in comparison to the parallel excitation (0 or 180°). The high frequency region shows only one distinct band at 418 cm<sup>-1</sup> for all excitation angles. This band, which is not observed in the RR spectrum of the WT(so) sample, gains its maximal relative intensity at excitation angles between 60 and 140°.

Similar to the angle-dependent RR spectra of the WT(so) type crystalline sample in Figure 7.4 the modes at 342.0 and 366.0 cm<sup>-1</sup> (blue lines) gain their maximal relative intensity at perpendicular excitation angles. The shoulder at 336.5 cm<sup>-1</sup> (orange) has maximal intensity at 60 and 120° for the WT(o), similar to the WT(so) form.

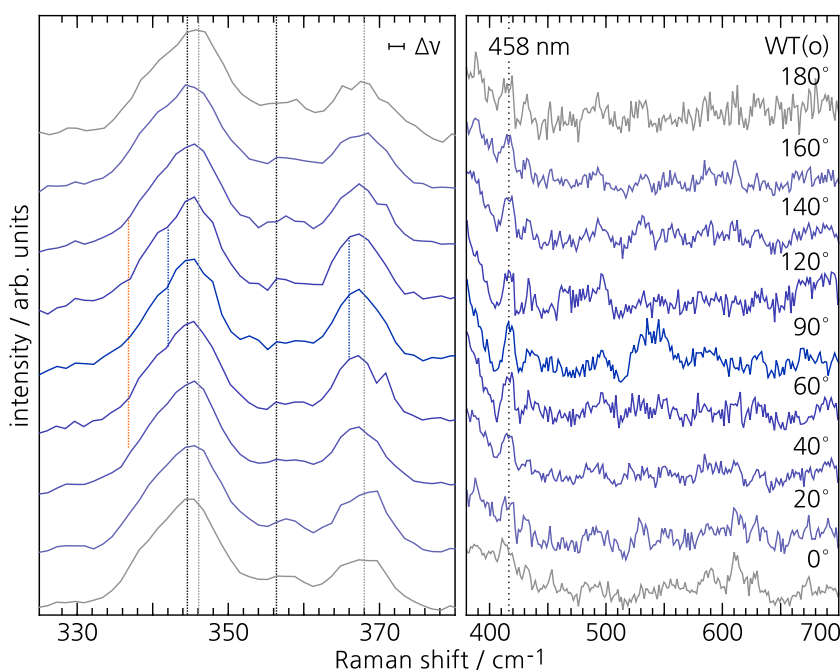


**Figure 7.5.:** RR spectra of a single as-isolated MBH WT(o) crystal obtained at angles  $\beta'$  from 0 to 180° between the electric field vector of the incident laser and the c-axis of the crystal. The measured spectral intensities are normalized to the integral area between 330 and 375  $\text{cm}^{-1}$ .

Proposed band positions of the FeS stretching modes for the  $[4\text{Fe}3\text{S}]_{\text{p}}+\text{OH}$ ,  $[4\text{Fe}3\text{S}]_{\text{p}}$ ,  $[3\text{Fe}4\text{S}]_{\text{m}}$  and  $[4\text{Fe}4\text{S}]_{\text{d}}$  cluster shown in black, gray, blue and orange, respectively. (See Table 7.1) Intensities in the right panel are increased by a factor of 3.0.

Based on the close inspection of the RR spectra shown in the last two figures, parts of the FeS stretching modes can be tentatively assigned to the three different FeS clusters.

At excitation angles of  $\beta' \sim 0^\circ$  mainly modes of the superoxidized proximal  $[4\text{Fe}3\text{S}]_{\text{p}}+\text{OH}$  cluster at 344.5 and 356.5  $\text{cm}^{-1}$  (black) are resonantly enhanced. Accordingly, the high frequency Fe-OH and Fe-Cys modes, which were assigned to this cluster in Chapter 6, gain their maximal relative intensities at parallel excitation angles as well.

As the medial and distal FeS clusters are identical in the WT(so) and WT(o) crystalline samples, their vibrational modes gain their largest resonance enhancement at the same excitation angles in both samples. The bands at 342.0 and 366.0  $\text{cm}^{-1}$  (blue) are therefore ascribed to the medial  $[3\text{Fe}4\text{S}]_{\text{m}}$  and the band at 336.5  $\text{cm}^{-1}$  (orange) to the distal  $[4\text{Fe}4\text{S}]_{\text{d}}$  cluster. This tentative assignment is supported by the finding of Johnson *et al.* that the vibrational modes of a  $[3\text{Fe}4\text{S}]$  cluster are more intense as those of a  $[4\text{Fe}4\text{S}]$  cluster at 458 nm excitation.[214] Furthermore, the  $[3\text{Fe}4\text{S}]$  modes have slightly higher frequencies as the  $[4\text{Fe}4\text{S}]$  modes.[214] Thus, modes of the  $[3\text{Fe}4\text{S}]_{\text{m}}$  cluster seem to be resonantly enhanced under perpendicular excitation ( $\beta' = 90^\circ$ ) and modes of the distal  $[4\text{Fe}4\text{S}]_{\text{d}}$  cluster gather their largest enhancement at excitation angles of 70 and 110°.

## 7.4. Attack of the Cluster Mutants

In the C120G/C19G variant of the MBH the proximal cluster adopts a cubane-like structure. The same transformation is achieved for the medial cluster in the P242C variant.[43] In case of the histidine variants H229A, H229M and H229Q a loss of the hydroxyl ligand at the proximal cluster is observed.[47, 203] Notably, the [NiFe] active site of all MBH variants remained unaffected and is identical to the wildtype form.[189] The molecular compositions of the individual FeS clusters for the MBH in different oxidized crystalline forms WT(so) and WT(o), as well as the MBH variants C120G/C19G, P242C and H229A are summarized in Table 7.2.

The RR spectra of the respective samples have contributions of all FeS clusters, if they are in their highest oxidation state. The spectral diversity of the FeS clusters in the samples is reduced, if mutation leads to a transformation of the proximal or medial cluster to a [4Fe4S] structure. Then the complexity of the RR spectrum of the respective sample decreases, assuming that the protein environment only slightly effects the frequencies of the vibrational modes from a specific cluster i.e. the [4Fe4S] cluster. Accordingly, the cluster is expected to exhibit the same vibrational frequencies independent from its position (proximal, medial or distal) relative to the [NiFe] active site of the MBH. The C120G/C19G and P242C variants of the MBH have indeed two [4Fe4S] clusters and thus a vibrational spectrum with a reduced complexity, as compared to the WT(so) form of the MBH, is expected. Table 7.2 also includes the expected contributions of the FeS clusters from a MBH wild-type sample (WT(asc)) incubated with 50 mM ascorbic acid. This treatment results in a partial reduction of the proximal cluster.[43] This partially reduced cluster only weakly contributes to the RR spectrum.[212, 37, 213]

In Figure 7.6 the RR spectra of the samples described in Table 7.2 are shown. Block A of this figure compares the RR spectra of the as-isolated C120G/C19G variant and the WT(asc) sample. Both spectra have a striking resemblance in the region of the FeS stretching modes, confirming the expected contributions from the different FeS clusters to the RR spectra shown in Table 7.2. EPR and FTIR spectroscopic investigations of the C120G/C19G variant from the MBH in comparison to the ascorbic acid treated WT(asc) carried out by Goris *et al.* revealed that the proximal cluster of the C120G/C19G variant exhibits only one one-electron redox transition, like in standard hydrogenases.[43] Later the x-

	proximal	medial	distal
WT(so)	[4Fe3S]+OH <sup>-</sup>	[3Fe4S]	[4Fe4S]
WT(o)	<u>[4Fe3S]</u>	[3Fe4S]	[4Fe4S]
WT(asc)	[4Fe3S]±OH <sup>-</sup>	[3Fe4S]	[4Fe4S]
C120G/C19G	<u>[4Fe4S]</u>	[3Fe4S]	[4Fe4S]
P242C	[4Fe3S]+OH <sup>-</sup>	<u>[4Fe4S]</u>	[4Fe4S]
H229A	<u>[4Fe3S]</u>	[3Fe4S]	[4Fe4S]

**Table 7.2.:** Individual contributions of the FeS clusters to the RR spectrum for different wildtype and genetically varied samples of the MBH. Cluster structures that differ from the native case WT(so) structure are underlined. Partially reduced FeS clusters are marked in gray. They do not or only weakly contribute to the RR spectrum.[212, 37, 213]

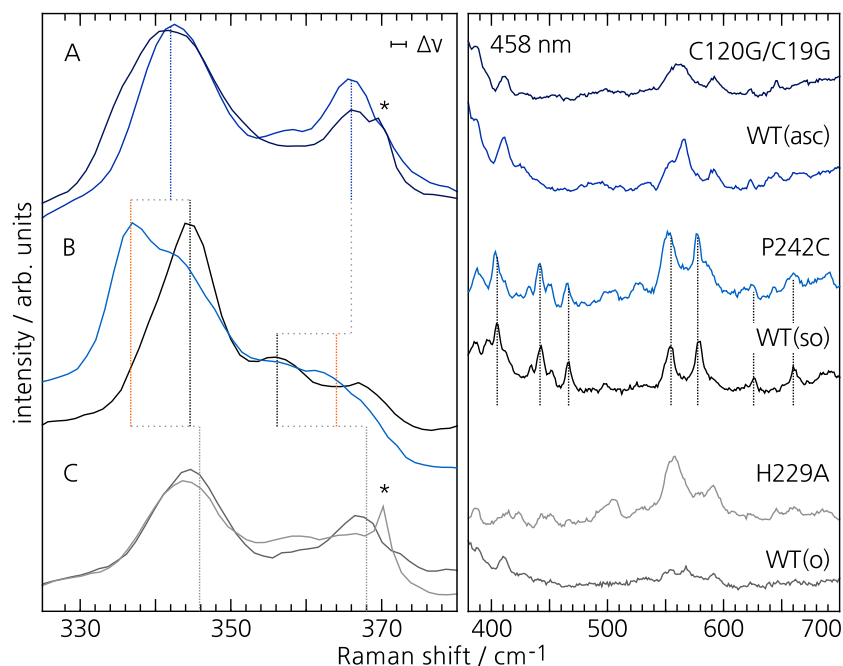
ray crystal structure confirmed, that by exchanging Cys120 and Cys19 to two glycines a [4Fe4S] cluster is formed at the proximal position of the C120G/C19G variant.[189] Thus, the RR spectrum of the as-isolated C120G/C19G has contributions from a [4Fe4S]<sub>p</sub>, [3Fe4S]<sub>m</sub> and a [4Fe4S]<sub>d</sub> cluster in the FeS stretching region. As partially reduced FeS clusters experience a decreased resonance enhancement [212, 37, 213], the RR spectrum of the WT(asc) sample is mainly composed of modes from the medial [3Fe4S]<sub>m</sub> and the distal [4Fe4S]<sub>d</sub> cluster. Moreover, the modes of the [3Fe4S]<sub>m</sub> cluster have an increased resonance enhancement at 458 nm than the modes of the [4Fe4S] cluster.[214, 213, 215, 37] Thus, the spectra of the C120G/C19G and the WT(asc) sample are dominated by the modes of the medial cluster.[214, 215, 37, 213] Modes of the [4Fe4S] cluster are slightly more pronounced and broadened in the RR spectrum of the C120G/C19G variant, because there are two [4Fe4S] clusters in each macro-molecule of this sample. Therefore, the two intense bands at 342.0 and 366.0 cm<sup>-1</sup>, marked by vertical blue lines in Figure 7.6A, must originate from the medial [3Fe4S] cluster. The spectrum of the C120G/C19G variant has a slightly more intense shoulder at the low frequency side of the band at 342.0 cm<sup>-1</sup>. This can be assigned to the low frequency mode of the two [4Fe4S] clusters in the proximal and distal position. The position of this band at 336.5 cm<sup>-1</sup> (vertical orange line in Figure 7.6B) will be further validated in the following text.

The assignment of this band to a mode of the [4Fe4S] cluster is further corroborated by the RR spectrum of the P242C variant of the MBH. (Figure 7.6B) In this variant of the MBH the Pro242 located in the vicinity of the medial cluster was substituted with a cysteine. Thus, the medial cluster is formed as a [4Fe4S] cluster and the corresponding RR spectrum is composed of vibrational modes of two [4Fe4S] clusters and the superoxidized proximal [4Fe3S]<sub>p</sub>+OH cluster. In trace B of Figure 7.6 the RR spectrum of the P242C

**Figure 7.6.:** Comparison of the RR spectra from MBH wildtype samples with various oxidation states of the proximal cluster and MBH samples with selected genetically induced variations at the proximal and medial cluster. The individual contributions of the FeS clusters to the RR spectrum for all samples are summarized in Table 7.2.

A) Spectrum of the C120G/C19G variant of the MBH and the wildtyp MBH partially reduced with 50 mM excess ascorbic acid. B) Spectra of the MBH wildtyp (WT(so)) compared to the spectrum of the P242C variant of the MBH. Both spectra exhibit the FeOH marker bands of the superoxidized proximal cluster, as illustrated by dotted lines on the right side of the plot. C) Spectra of an as-isolated wildtype crystal WT(o), which lacks the OH<sup>-</sup> ligand at the proximal cluster, in comparison to the H229A variant of the MBH.

Proposed band positions of the FeS stretching modes for the [4Fe3S]<sub>p</sub>+OH, [4Fe3S]<sub>p</sub>, [3Fe4S]<sub>m</sub> and [4Fe4S]<sub>d</sub> cluster shown in black, gray, blue and orange, respectively. (See Table 7.1) Intensities in the right panel are increased by a factor of 3.0.



variant is compared directly to the one of the wildtype MBH in the WT(so) form. The spectrum of the P242C variant shows a pronounced band at  $336.5\text{ cm}^{-1}$  (orange) which, thus must belong to the two [4Fe4S] clusters of that sample. Three further bands at  $344.6$ ,  $356.3$  and  $364.0\text{ cm}^{-1}$  (black, black and orange) are found in the spectrum of the P242C and WT(so) sample. It will be shown later, that the band at  $364.0\text{ cm}^{-1}$  belongs to the [4Fe4S] cluster as well. The first two bands are clearly enhanced in the spectrum of the WT(so) and both are not detected in the spectra of the C120G/C19G variant and the WT(asc) sample (Figure 7.6A) Therefore, the bands at  $344.6$  and  $356.5\text{ cm}^{-1}$  (black) must originate from the proximal cluster [4Fe3S]<sub>p</sub>+OH. This is also supported by the fact that the spectra of the WT(so) and P242C variant both exhibit the high frequency modes related to Fe-OH and Fe-Cys vibrations of the proximal cluster. (Chapter 6) These modes are not observed in the RR spectrum of the C120G/C19G and WT(asc).

The RR spectrum of the WT(so) shown in Figure 7.6B is one of the two extreme cases that were found for the aerobically grown MBH crystals in Section 7.2. The spectrum of the WT(so) is related to a superposition of all three clusters. Therefore, the most intense band at  $344.5\text{ cm}^{-1}$  (black) from the proximal cluster is broadened on the low frequency side of the spectrum due to less intense modes from the medial and distal cluster vibrating at slightly lower frequencies.

The other extreme is the case where the hydroxyl ligand is not

bound to Fe1 of the proximal cluster. In the RR spectrum of this WT(o) form, the Fe-OH and Fe-Cys vibrations of the superoxidized proximal cluster are absent. (Figure 7.6C) Although the overall spectral signature of the WT(o) sample seems to be similar to the spectra of the C120G/C19G variant and the WT(asc) sample in Figure 7.6A, a detailed inspection yields that the band positions differ from those initially assigned to the medial cluster. The band at  $346.0\text{ cm}^{-1}$  (gray line) is shifted by  $4\text{ cm}^{-1}$  to higher frequencies with respect to the bands of the medial cluster at  $342.0\text{ cm}^{-1}$  (blue line). Also the band at  $368.0\text{ cm}^{-1}$  (gray) is higher by  $2\text{ cm}^{-1}$  than the one of the medial cluster.

This assignment is corroborated by the RR spectrum of the as-isolated H229A variant (Figure 7.6C). The biochemical design of this variant, where the His229 at the proximal cluster was exchanged by an alanine, is described in [47]. The x-ray crystallographic data showed that the proximal cluster of this variant is identical to the one of the wildtype, except that it lacks the hydroxyl ligand bound at Fe1. Additionally, three water molecules were found at the side of the His229.[203] Therefore, the RR spectrum of the H229A variant is composed of modes from  $[4\text{Fe3S}]_p$ ,  $[3\text{Fe4S}]_m$  and a  $[4\text{Fe4S}]_d$ , which is nominally identical to the contributions of the FeS clusters to the spectrum of the WT(o) sample. Indeed, the similarity of the RR spectrum from the H229A variant and the WT(o) spectrum in Figure 7.6C is striking. Additionally, both spectra lack the high frequency Fe-OH and Fe-Cys modes of the superoxidized proximal cluster. Thus, the proximal cluster without the hydroxyl ligand is characterized by two almost equally intense modes at  $346.0$  and  $368.0\text{ cm}^{-1}$  (gray).

### 7.5. Extraction of FeS Component Spectra

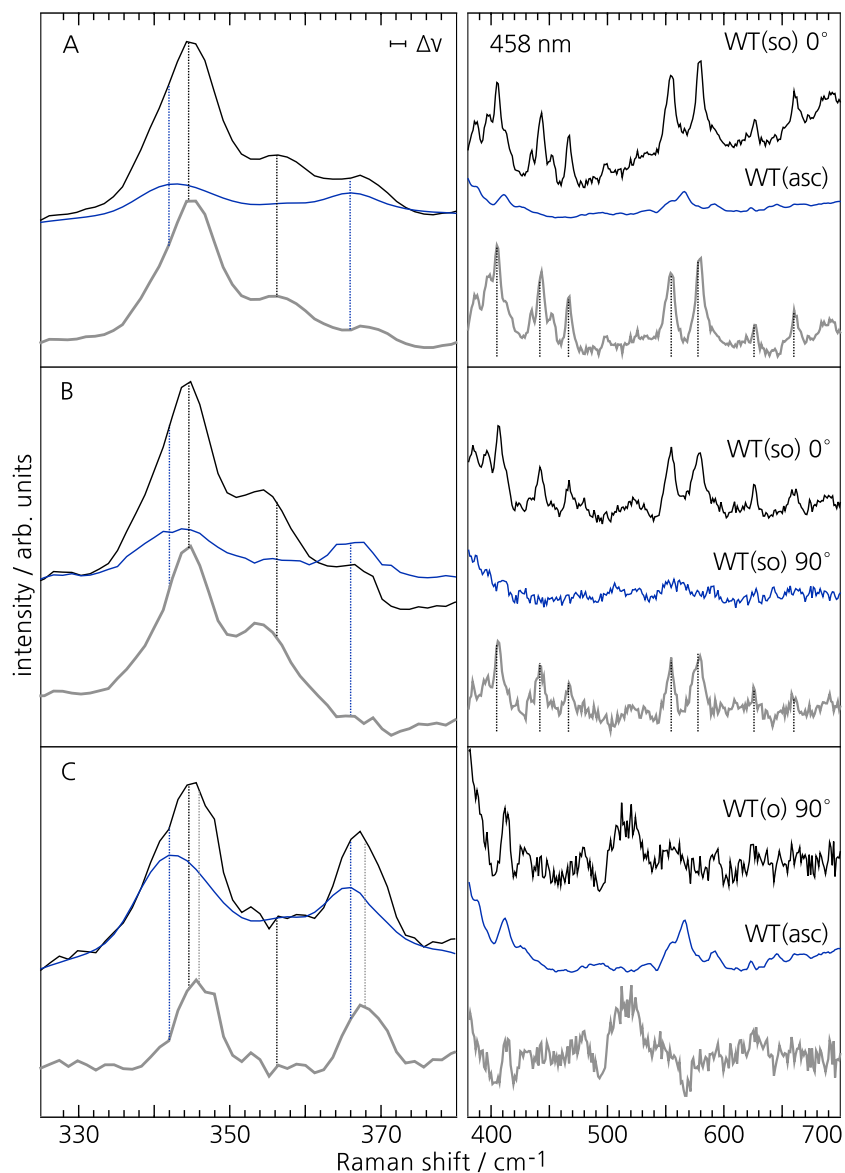
In this section RR difference spectroscopy is employed to verify the assignments made in Section 7.3 and 7.4. Approximate component spectra for each FeS cluster of the as-isolated MBH are determined, as well. As in the previous section it is assumed that the protein environment does not influence the vibrational frequencies of the FeS stretching modes of a specific cluster, regardless of its position in the electron transport chain of the protein.

The component spectra are calculated by mutual subtraction of selected RR spectra shown in Figures 7.4, 7.5 and 7.6. To ensure that artifacts are minimized no baseline was subtracted. Solely for illustrative matters a constant intensity offset was subtracted or

**Figure 7.7.:** Calculated differences between RR spectra of WT(so), WT(o) and WT(asc) shown as thick gray spectra at the bottom of each panel. A) Difference between the superoxidized MBH wildtype WT(so) at parallel excitation and the spectrum of the ascorbic acid incubated MBH wildtype sample WT(asc). B) Difference between the RR spectrum of WT(so) recorded under parallel and perpendicular excitation. Panel A and B, both show the approximate spectrum of the superoxidized proximal cluster  $[4\text{Fe3S}]_p+\text{OH}$  in the residual.

In contrast, the difference spectrum in C) displays the approximate positions of the FeS stretching modes of the proximal  $[4\text{Fe3S}]_p$  without a bound hydroxyl ligand. The vibrational spectrum of this cluster is characterized by two intense FeS stretching bands at  $346.0$  and  $368.0\text{ cm}^{-1}$  (gray vertical lines). Above  $400\text{ cm}^{-1}$  no distinct vibrations are related to this cluster.

Proposed band positions of the FeS stretching modes for the  $[4\text{Fe3S}]_p+\text{OH}$ ,  $[4\text{Fe3S}]_p$ ,  $[3\text{Fe4S}]_m$  and  $[4\text{Fe4S}]_d$  cluster shown in black, gray, blue and orange, respectively. (See Table 7.1) Intensities in the right panel are increased by a factor of 3.0.



added to the spectra in the following figures.

### The Proximal $[4\text{Fe3S}]_p+\text{OH}$ and $[4\text{Fe3S}]_p$ Clusters

The three RR difference spectra (gray traces) of Figure 7.7 confirm the assignment of the vibrational bands at  $344.5$  and  $356.5\text{ cm}^{-1}$  (black vertical lines) to the  $[4\text{Fe3S}]_p+\text{OH}$  and the bands at  $346.0$  and  $368.0\text{ cm}^{-1}$  (gray vertical lines) to the  $[4\text{Fe3S}]_p$  cluster. Moreover, the difference spectra show that the superoxidized proximal  $[4\text{Fe3S}]_p+\text{OH}$  cluster experiences the largest resonance enhancement whenever the excitation angle is parallel to the  $c$ -axis of the investigated as-isolated MBH crystal.

The RR spectrum of the WT(asc) crystalline sample obtained at an excitation of  $\beta' = 0^\circ$  serves as a reference for the difference spec-

tra shown in Figure 7.7A. The WT(asc) spectrum is dominated by bands from the medial cluster and has minor contributions from the distal cluster. (See Table 7.2) These contributions are eliminated in the RR difference spectrum with the WT(so) spectrum obtained under an excitation angle parallel to the c-axis of the crystal. The FeS stretching bands at 344.5 and 356.5  $\text{cm}^{-1}$  (black vertical lines), as well as the high frequency bands from Fe-OH and Fe-Cys stretching modes, remain in the residual. This residual displays the component spectrum of the superoxidized proximal cluster  $[4\text{Fe3S}]_p+\text{OH}$  with a hydroxyl ligand bound to Fe1.

The component spectrum of the  $[4\text{Fe3S}]_p+\text{OH}$  is again confirmed in the RR difference spectrum shown in Figure 7.7B, between the RR spectrum of the WT(so) sample taken under  $\beta' = 0^\circ$  and  $90^\circ$ . Similar to Panel A of Figure 7.7, only the modes of the  $[4\text{Fe3S}]_p+\text{OH}$  cluster remain in the residual. All minor contributions from the medial and distal cluster are eliminated.

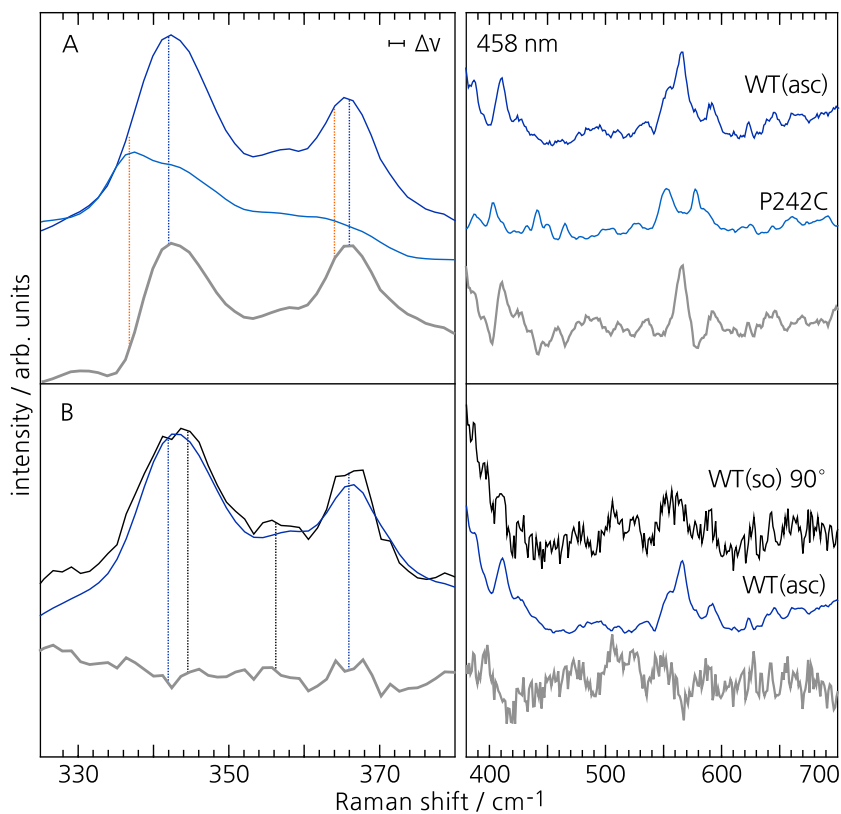
The residuals in Figure 7.7A and B reveal the first approximate component spectra of superoxidized  $[4\text{Fe3S}]_p+\text{OH}$  cluster, including its FeS, Fe-OH and Fe-Cys stretching modes. Its vibrational modes dominate the spectrum of the as-isolated MBH in the WT(so) form under parallel excitation. Thus, the projection of the electronic transition dipole moment of the proximal cluster must be parallel to the c-axis of the as-isolated, oxidized MBH crystal.

In panel C of Figure 7.7 the difference between the spectrum of a single oxidized MBH crystal without the hydroxyl ligand bound to the Fe1 of the proximal cluster (WT(o)) and the WT(asc) spectrum is shown. Two distinct bands at 344.6 and 368.0  $\text{cm}^{-1}$  (gray) remain in the region of the FeS stretching modes and no bands beyond 410  $\text{cm}^{-1}$  are detected. Therefore, the proximal cluster without an  $\text{OH}^-$  ligand is characterized by two almost equally intense bands at 346.0 and 368.0  $\text{cm}^{-1}$  and no distinct bands beyond 400  $\text{cm}^{-1}$ . From these spectra it can also be inferred that the proximal cluster in the WT(o) form is in a higher oxidation state, than in the WT(asc) form. Since the RR spectra of both samples shows different signatures in the spectral region of the FeS stretching modes.

### The Medial $[3\text{Fe4S}]_m$ Cluster

The difference spectra shown in Figure 7.8 reveal the approximate band positions at 342.0 and 366.0  $\text{cm}^{-1}$  (blue lines) of the FeS stretching modes from the medial cluster  $[3\text{Fe4S}]_m$ . The difference

**Figure 7.8.:** Calculated differences between RR spectra of WT(so), WT(asc) and the P242C variant of the MBH shown as thick gray spectra at the bottom of each panel. A) The difference between the RR spectra of WT(asc) and the P242C variant displays the approximate spectrum of the medial cluster. A) Subtracting the RR spectra of the WT(so) obtained under perpendicular excitation from the RR spectrum of the WT(asc) form of the MBH, results in a residual with no spectral features. This indicates, that the RR spectrum of the WT(so) measured under perpendicular excitation is dominated by modes from the medial [3Fe4S] and distal [4Fe4S] cluster. Proposed band positions of the FeS stretching modes for the [4Fe3S]<sub>p</sub>+OH, [4Fe3S]<sub>p</sub>, [3Fe4S]<sub>m</sub> and [4Fe4S]<sub>d</sub> cluster shown in black, gray, blue and orange, respectively. Intensities in the right hand panel increased by a factor of 3.0 with respect to the left hand side of the plot.



between the WT(asc)-sample, with contributions of the [3Fe4S]<sub>m</sub> and [4Fe4S]<sub>d</sub> clusters, and the spectrum of the P242C variant of the MBH (with one [4Fe3S]<sub>p</sub>+OH and two [4Fe4S]) is depicted in Figure 7.8 A. The residual shows the approximate spectrum of the medial [3Fe4S]<sub>m</sub> cluster. Minor contributions from the [4Fe3S]<sub>p</sub>+OH cluster are neglected, because the two [4Fe4S] clusters dominate the spectrum of the P242C variant. The medial [3Fe4S] cluster is characterized by two FeS stretching modes at 342.0 and 366.0 cm<sup>-1</sup> (blue). The intense band at 565 cm<sup>-1</sup> has been assigned to OH out-of-plane deformations or C-C ring stretching vibrations of ascorbic acid by Panicker *et al.* [218]

In Figure 7.8B the difference between the RR spectrum of WT(asc), which is mostly composed of modes from the [3Fe4S]<sub>m</sub> cluster, and the WT(so) sample excited perpendicular to the *c*-axis of the crystal, is illustrated. The residual shows no significant spectral signatures in the selected range from 325 to 700 cm<sup>-1</sup>. Thus, the RR spectrum of the WT(so) sample excited perpendicular to the *c*-axis exhibits mostly modes of the medial FeS cluster. Accordingly, its projection of the electronic transition dipole moment lies perpendicular to the *c*-axis. In contrast, the one of the superoxidized proximal cluster is parallel to this axis.

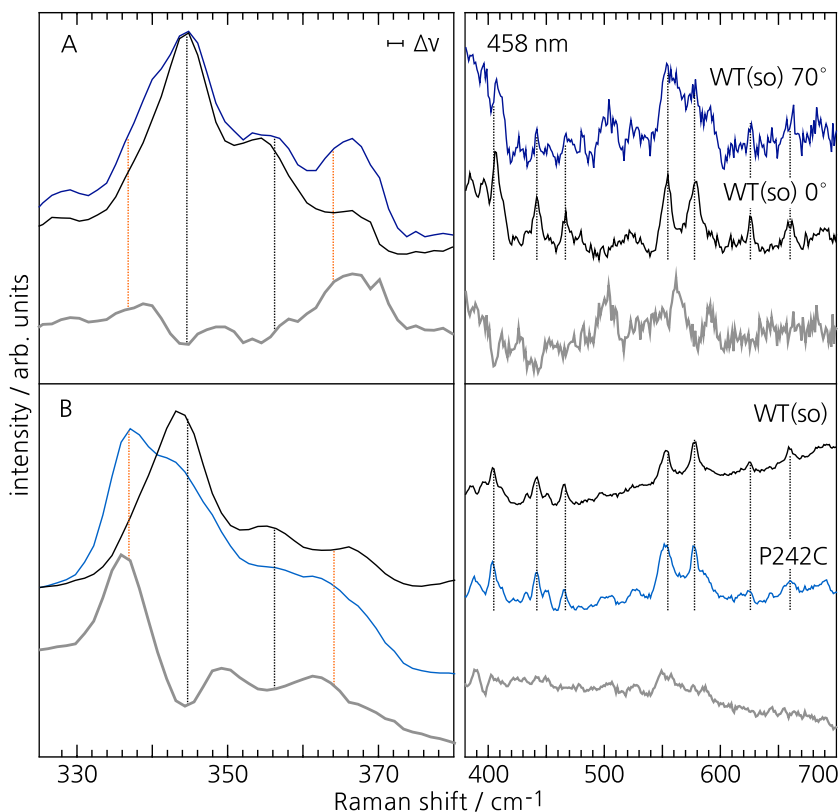


**Figure 7.9.:** Calculated differences between RR spectra of the WT(so) form of the MBH excited at  $0^\circ$  and  $70^\circ$  and the P242C variant of the MBH shown as thick gray spectra at the bottom of each panel. A) Spectrum of the WT(so) at an excitation angle of  $70^\circ$  subtracted from the one measured at  $0^\circ$  excitation. Shallow positive difference bands at the proposed positions of the distal  $[4\text{Fe}4\text{S}]$  cluster emerge in the residual. B) Difference spectrum between WT(so) and the P242C variant of the MBH. Both spectra were obtained at  $\beta' = 0^\circ$ . As in panel A) bands at the proposed positions of the distal cluster remain in the residual (orange vertical lines).

Proposed band positions of the FeS stretching modes for the  $[4\text{Fe}3\text{S}]_p + \text{OH}$ ,  $[3\text{Fe}4\text{S}]_m$  and  $[4\text{Fe}4\text{S}]_d$  cluster shown in black, blue and orange, respectively. (See Table 7.1) Intensities in the right panel are increased by a factor of 3.0.

### The Distal $[4\text{Fe}4\text{S}]_d$ Cluster

Finally, the approximate component spectrum of the distal  $[4\text{Fe}4\text{S}]_d$  cluster is obtained by mutual subtraction of the spectra shown in Figure 7.9. In panel A the RR spectrum of the WT(so) sample excited at  $\beta' = 0^\circ$  is subtracted from the one measured at  $70^\circ$ . It has been shown in Section 7.3 that the projection of the transition dipole moment of the distal  $[4\text{Fe}4\text{S}]_d$  cluster is tilted by about  $70^\circ$  and  $130^\circ$  to the  $c$ -axis. Indeed, the residual shows two weak bands in close vicinity to the proposed band position of FeS stretching modes of the distal cluster at  $336.5$  and  $364.0 \text{ cm}^{-1}$  (orange). The spectral quality is weak, but the assignment of the bands to the  $[4\text{Fe}4\text{S}]_d$  cluster can be further supported: In Figure 7.9B the RR spectrum of the WT(so) form and P242C variant of the MBH are subtracted from each other. Both spectra were obtained under parallel excitation with respect to the  $c$ -axis. Albeit noisy, the residual proves the previous assignment of the bands at  $336.5$  and  $364.0 \text{ cm}^{-1}$  (orange) to the distal  $[4\text{Fe}4\text{S}]$  cluster. The high frequency bands of the proximal cluster vanish in the residual as well, only weak bands that belong to the oxidized active site remain here.

## 7.6. Polarization Dependent Resonance Raman Spectra

In addition to the angle-dependent RR measurements on single as-isolated crystals of the MBH, polarized RR measurements on these samples were performed. Such measurements can be useful for vibrational mode assignments and may contain informations on the orientation of the differential polarizability  $(\partial\alpha/\partial Q_k)_0$ , that is the Raman tensor of the  $k^{th}$  vibrational mode which has the form of an ellipsoid.

Classically, the Raman effect is described by the equation  $\mathbf{P}^{ind} = \boldsymbol{\alpha} \cdot \mathbf{E}$ . The magnitude of the induced dipole moment depends on the polarizability  $\boldsymbol{\alpha}$  and according to Equation 3.17 also on the differential polarizability  $(\partial\boldsymbol{\alpha}/\partial Q_k)_0 = \boldsymbol{\alpha}'$  of the  $k^{th}$  vibrational mode. Due to the tensorial nature of the polarizability<sup>E</sup> and the vectorial nature of the electric field, the magnitude of  $\mathbf{P}^{ind}$  and thus the intensity of the scattered radiation depends on the angle between  $\boldsymbol{\alpha}$  and  $\mathbf{E}$  as well. The scattered Raman intensity is then proportional to [219]

$$I_k^{scat} \sim |\mathbf{e}_i \cdot \boldsymbol{\alpha}' \cdot \mathbf{e}_s|^2, \quad (7.3)$$

whereby  $\mathbf{e}_i$  and  $\mathbf{e}_s$  signify the unit vectors of the incident electric field vector and that of the analyzer, respectively. Thus, by carefully selecting the vectors of the incident laser light and the analyzed scattered light, directional information about the differential polarizability of the  $k^{th}$  vibrational mode of the molecule can be obtained. As each mode possesses an individual polarizability ellipsoid, polarization-dependent RR measurements may be useful for vibrational mode assignments as well.

The measurement of the depolarization ratio from a frozen anisotropic solution of the sample is of great importance to determine the shape of the differential polarizability ellipsoid. It is defined as

$$\rho = \frac{I_{\perp}}{I_{\parallel}} = \frac{3\bar{\gamma}^2}{45\bar{\alpha}^2 + 4\bar{\gamma}^2} \quad (7.4)$$

<sup>F</sup>

$$\begin{aligned} \bar{\alpha} &= \frac{1}{3} [\alpha'_{xx} + \alpha'_{yy} + \alpha'_{zz}] \\ \bar{\gamma} &= \frac{1}{2} \left[ (\alpha'_{xx} - \alpha'_{yy})^2 + (\alpha'_{yy} - \alpha'_{zz})^2 \right. \\ &\quad \left. + (\alpha'_{zz} - \alpha'_{xx})^2 \right. \\ &\quad \left. + 6(\alpha'^2_{xy} + \alpha'^2_{yz} + \alpha'^2_{zx}) \right]^{1/2} \end{aligned}$$

and  $\bar{\alpha}$  determines the mean radius of the ellipsoid and  $\bar{\gamma}$  its anisotropy.<sup>F</sup>

These two quantities are the invariants of the polarizability tensor under random rotation in 3D.

For the polarization-sensitive RR measurements an additional analyzer was inserted in the detection pathway of the setup. To account for the strong polarization-dependence of the gratings within

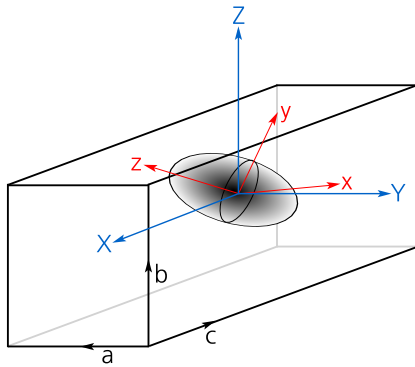


**Figure 7.10.:** Relationship between laboratory (XYZ), the crystal coordinate system (abc) and the principal axes (xyz) of the Raman scattering tensor  $(\partial\alpha/\partial Q_k)_0$  of one vibrational mode  $k$ . The orientation of tensor in the laboratory coordinate system is defined by the Euler angles.[164]

The incident laser propagates in the Z-direction and its electric field vector is adjusted to point in the X  $\hat{=}$  c or Y  $\hat{=}$  a direction with a half-wave plate.

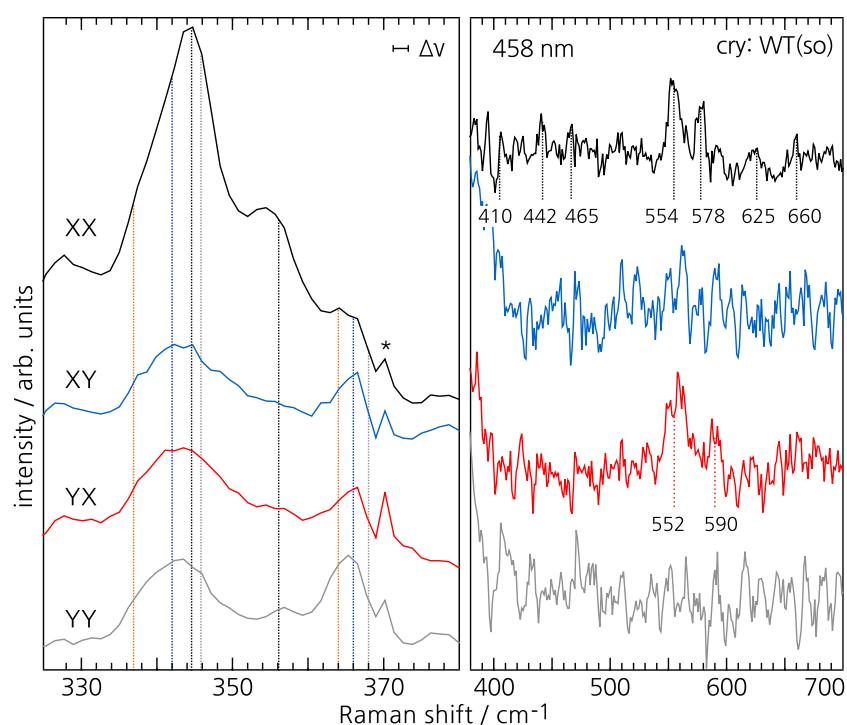
the spectrograph, a quarter-wave plate was placed behind the analyzer, at a fixed angle of  $45^\circ$  to create circularly polarized light that enters the spectrograph. The setup is sketched in Figure 3.6 of Section 3.5. Here, also the laboratory coordinate system is defined: The laser propagates along the Z-axis. Its electric field vector oscillates in the XY-plane and the angle within that plane is adjusted with a half-wave plate to point along the X- or Y-axis. The direction of the analyzer in the detection pathway is either parallel or perpendicular to electric field vector of the laser incident on the sample surface. In this respect, the four possible optical geometries for the polarized RR measurements may be written in Porto's notation[220]: Z(XX)Z, Z(XY)Z, Z(YX)Z and Z(YY)Z.

Prior to the polarization-dependent RR measurements on the MBH the polarization-sensitive throughput of the whole setup was carefully calibrated with the Raman band at  $521\text{ cm}^{-1}$  of a Si[111] and Si[001] sample, as well as with the Raman spectrum of  $\text{CCl}_4$ . (See Appendix E)

A single crystal of the MBH is placed into this system such that the c-axis (long axis) of the crystal coincides with the X-axis of the laboratory coordinate system. Correspondingly, the a- or the b-axis of the crystal is aligned parallel the Y-axis. Unfortunately, it is neither possible to distinguish between the a- and b- axis of the crystal during the measurement, nor to swap between the two, as the crystal is permanently frozen onto the sample holder. Figure 7.10 illustrates the relation between the laboratory and the abc-coordinate system of the crystal. Also the principal axes (xyz) of the Raman tensor for the  $k^{\text{th}}$  vibrational mode are illustrated. The Euler angles define its orientation within the crystal and accordingly, within the laboratory system.

Four polarized RR measurements, i.e. with the optical geometries of XX  $\hat{=}$  cc, XY  $\hat{=}$  ca, YX  $\hat{=}$  ac and YY  $\hat{=}$  aa (see Figure 7.10), were obtained from two different WT(so) crystals of the MBH. The re-

**Figure 7.11.:** Polarized RR spectra of a single as-isolated MBH WT(so) crystal. The spectrum obtained in the XX-configuration clearly shows the signature of the superoxidized  $[4\text{Fe3S}]_p+\text{OH}$  cluster. (Continuous and dotted black vertical lines) Bands at  $552$  and  $590\text{ cm}^{-1}$ , that were associated with the  $\text{Ni}_a\text{-S}$  redox state of the active site emerge in the spectrum measured in the YX-configuration. (Red dotted lines) Band positions of the FeS stretching modes for the  $[4\text{Fe3S}]_p+\text{OH}$ ,  $[4\text{Fe3S}]_p$ ,  $[3\text{Fe4S}]_m$  and  $[4\text{Fe4S}]_d$  cluster shown in black, gray, blue and orange, respectively. (See Table 7.1) Intensities in the right panel are increased by a factor of 3.0.



sulting RR spectra, with the intensities scaled according to the calibration factors (Table E.1) are shown in Figure 7.11 and 7.12. These spectra can be compared to the angle-dependent RR spectra with the same excitation geometry shown in Figure 7.4 for  $0^\circ \hat{=} X$  and  $90^\circ \hat{=} Y$ . There is no pronounced difference between the spectra of the WT(so) excited at  $90^\circ \hat{=} Y$  and measured polarization-sensitive with an analyzer either in the X or Y direction or without any analyzer in the detection pathway at all. Only the bands at  $552$  and  $590\text{ cm}^{-1}$  (red lines), which were assigned to vibrations of the  $\text{Ni}_a\text{-S}$  redox state, emerge in the spectrum of the WT(so) with the YX configuration. This finding possibly points towards a Raman tensor for the vibrational modes of the active site that is oriented approximately perpendicular to the c-axis of the crystal. In contrast, the Raman tensor of the vibrational modes of the superoxidized proximal cluster may be oriented parallel to the c-axis, as only the RR spectrum measured in the XY configuration differs strongly from the angle-dependent RR spectrum excited at  $0^\circ$ , while the RR spectrum measured in the XX configuration is almost similar to the latter.

However, the Raman tensors and their true orientation in the crystal cannot be obtained from these spectra with the procedure developed by M. Tsuboi and co-workers for single (uniaxial) protein crystals.[221, 222, 223, 224] Several circumstances render this notion almost impossible:

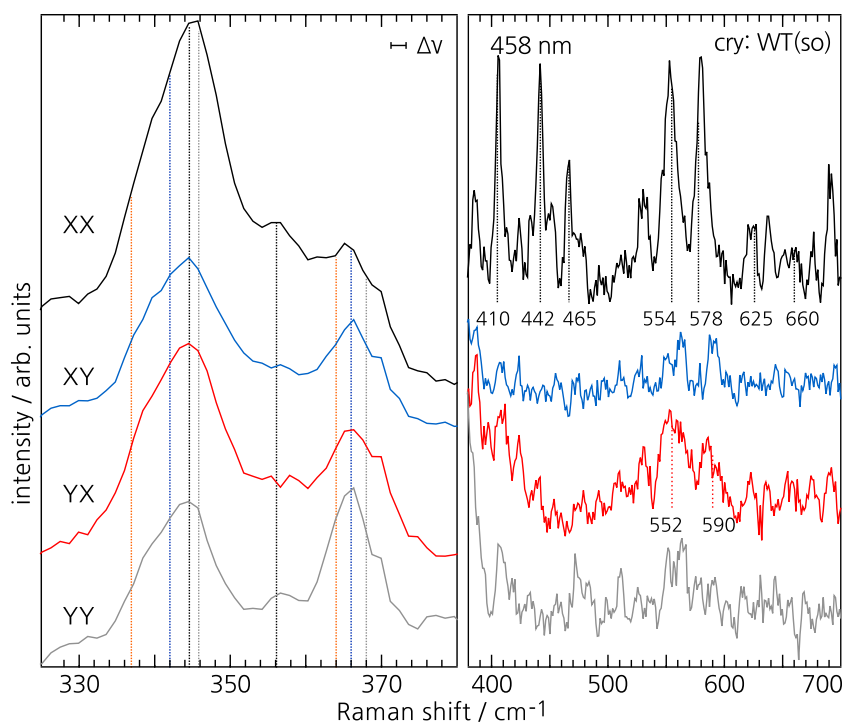


**Figure 7.12.:** Polarized RR spectra of another single as-isolated MBH WT(so) crystal. The spectrum obtained in the XX-configuration clearly shows the signature of the superoxidized  $[4\text{Fe3S}]_p+\text{OH}$  cluster. (Continuous and dotted black vertical lines) Bands at  $552$  and  $590\text{ cm}^{-1}$ , that were associated with the  $\text{Ni}_a\text{-S}$  redox state of the active site emerge in the spectrum measured in the YX-configuration. (Red dotted lines)

Band positions of the FeS stretching modes for the  $[4\text{Fe3S}]_p+\text{OH}$ ,  $[4\text{Fe3S}]_p$ ,  $[3\text{Fe4S}]_m$  and  $[4\text{Fe4S}]_d$  cluster shown in black, gray, blue and orange, respectively. (See Table 7.1) Intensities in the right panel are increased by a factor of 3.0.

1. The polarization-sensitive spectra were obtained under resonance conditions, such that the measured RR intensities are influenced by the directional properties of the electronic transitions in the FeS clusters, as well. As described in Section 7.3, parallel or perpendicular excitation lead to an almost selective enhancement of the proximal or medial cluster, respectively.
2. As the MBH does not crystallize in an uniaxial symmetry, polarized RR spectra from the ca- as well as the cb-plane have to be measured.[221, 223] As the MBH crystal is permanently frozen onto the sample holder it is not possible to swap between the two planes during the measurement.
3. The RR spectra of the MBH are comprised of a number of strongly overlapping bands, especially in the spectral region of the FeS stretching modes. Thus, the intensity ratios, that are important to determine the depolarization ratio  $\rho$  and the ratios  $r_1$  and  $r_2$  of the Raman tensor, can only be determined with high intrinsic errors.
4. The vibrating cofactors, i.e. the FeS cluster and the  $[\text{NiFe}]$  active site have no geometric symmetry at all. Thus, the Raman tensor  $(\partial\alpha/\partial Q_k)_0 = \alpha'$  is expected to be asymmetric as well, with different entries for all  $\alpha'_{\rho\sigma}$  components ( $\rho, \sigma = x, y, z$ ). Under these circumstances, we cannot learn

something about the character of the modes, except that they are highly anisotropic.

## 7.7. Conclusion

In this chapter two main results were elucidated: First, it was confirmed that the configuration with a bound hydroxide ligand at the proximal cluster  $[4\text{Fe3S}]$  represents the native molecular structure in the as-isolated MBH. (Section 7.2) All RR spectra of the as-isolated and reoxidized MBH in solution are dominated by the typical signature of the superoxidized proximal cluster in the  $[4\text{Fe3S}]_p+\text{OH}$  configuration. As-isolated heterodimeric MBH samples in solution from similar preparations are of high quality in terms of activity and oxygen tolerance.[33, 43, 79, 89] The observed RR signature from the as-isolated heterodimeric MBH in solution and the crystalline form thus corresponds to a native and functional configuration of the oxidized MBH. In addition, the  $[4\text{Fe3S}]_p+\text{OH}$  configuration is almost completely restored in the reoxidation process. Only a loss on the order of ten percent, with respect to the RR spectrum of the as-isolated MBH sample, is observed for the corresponding  $[4\text{Fe3S}]_p+\text{OH}$  vibrational modes. FTIR spectra of MBH samples reoxidized under similar conditions showed that parts of the active site are irreversibly damaged and the inactive  $\text{Ni}_{\text{ia}}\text{-S}$  redox species is formed to about 30 % with respect to the sum of all redox species. (Section 4.1) In contrast, the FTIR spectra of the as-isolated C120G/C19G variant of the MBH exhibited more than 30 % of the  $\text{Ni}_{\text{ia}}\text{-S}$  species. Moreover, this MBH variant was irreversibly inactivated when exposed to 20 % of oxygen, while the wildtype still showed hydrogen oxidation under such conditions in electrochemical experiments.[43] The proximal cluster of the C120G/C19G variant is in a cubane-like structure  $[4\text{Fe4S}]$ , as in standard hydrogenases. Accordingly, the  $[4\text{Fe3S}]_p+\text{OH}$  signature was not observed for the C120G/C19G variant of the MBH. Thus, the RR and FTIR spectra of the MBH wildtype and C120G/C19G variant indicate that the superoxidized proximal cluster protects the  $[\text{NiFe}]$  active site from irreversible oxidative damage and is thus crucial for the oxygen-tolerance of the whole enzyme.

On the other hand, the strongly overlapping FeS stretching modes of all three FeS cluster have been consistently assigned. (Section 7.3 to 7.5) This was achieved by angle-dependent RR spec-

cluster	band positions with $\Delta\nu = \pm 1 \text{ cm}^{-1}$		angle of max. intensity
$[4\text{Fe3S}]_p + \text{OH}$	344.5	356.5	$0^\circ$
$[4\text{Fe3S}]_p$	346.0	368.0	
$[3\text{Fe4S}]_m$	342.0	366.0	$90^\circ$
$[4\text{Fe4S}]_d$	336.6	364.0	$70$ and $130^\circ$

**Table 7.3.:** Assigned band positions for all three FeS clusters of the as-isolated MBH. For crystalline samples the projection of the electronic transition dipole moment onto the crystal surface is given as an angle with respect to the c-axis. The vibrational modes of a specific cluster experience maximal resonance enhancement if the crystalline sample is excited with electromagnetic radiation oscillating parallel to the specified angle.

troscopy, which allowed to selectively excite only specific types of the FeS clusters. I.e. those whose projections of electronic transition dipole moments are parallel to the electric field vector of the incident laser beam. This enabled initial band assignments and statements about the projections for each of the three cluster types onto the crystal surface. The electronic transition dipole moment of the proximal cluster is parallel to the c-axis of the crystal and RR spectra excited at  $\beta' = \beta_p \approx 0^\circ$  are dominated by vibrational modes of this cluster. These modes are no longer resonantly enhanced at excitation angles of  $\beta' = \beta_m \approx 90^\circ$ , but the vibrational modes of the medial cluster are selectively enhanced. Weak modes of the distal cluster were observed at excitation angles of  $\beta' = \beta_d \approx 70 / 130^\circ$ .

Based on that, the approximated component spectra for each cluster were obtained with RR spectra of MBH variants and RR difference spectroscopy.

Thus, by the end of this Chapter a complete decryption of the RR spectra from the as-isolated MBH in the spectral range from 325 to  $700 \text{ cm}^{-1}$  is provided. The vibrational modes in this region are correlated to stretching vibrations of the proximal, medial and distal FeS cluster in their highest oxidation state. (See Table 7.3) Furthermore, Raman active Fe-CO / CN stretching vibrations of the [NiFe] active site in the  $\text{Ni}_a\text{-S}$  and  $\text{Ni}_a\text{-L}$  redox state were identified in Chapter 5 and 6. This analysis also included the first RR spectroscopic investigation of the newly found superoxidized proximal cluster  $[4\text{Fe3S}]_p + \text{OH}$ .

With RR spectroscopy the existence of this hydroxyl ligand can now be directly verified by marker bands of the Fe-OH stretching modes. This finding allows a straightforward investigation of other oxygen-tolerant and -sensitive hydrogenases in terms of the existence of an  $\text{OH}^-$  group at the proximal cluster. RR spectroscopic investigation of hydrogenases from other organisms will show whether the hydroxyl ligand is a unique feature of the prox-

imal cluster in the MBH from *Ralstonia eutropha* or even of all oxygen-tolerant hydrogenases. This information is of great importance for the detailed understanding of the molecular basis for the oxygen-tolerance.

In view of Section 7.3, angle dependent RR studies on single crystals of other hydrogenases, as for instance Hydrogenase 1 from *Escherichia coli* or *Desulfovibrio vulgaris* Miyazaki F, may be decrypted with this approach. A comparison to the RR spectrum of the MBH from *Ralstonia eutropha* may shed further light on its remarkable oxygen-tolerance.

Altogether, RR spectroscopy is capable to provide additional informations on the structure of the MBH. These informations may not be accessible via x-ray crystallography and are complementary to the ones obtained by the established techniques of FTIR and EPR spectroscopy.

With RR, FTIR and EPR spectroscopy conclusions on the relationship between the structure of the MBH and insights regarding its function can be derived since spectra from samples at different states of the catalytic cycle, i.e. ready or activated, can be investigated.

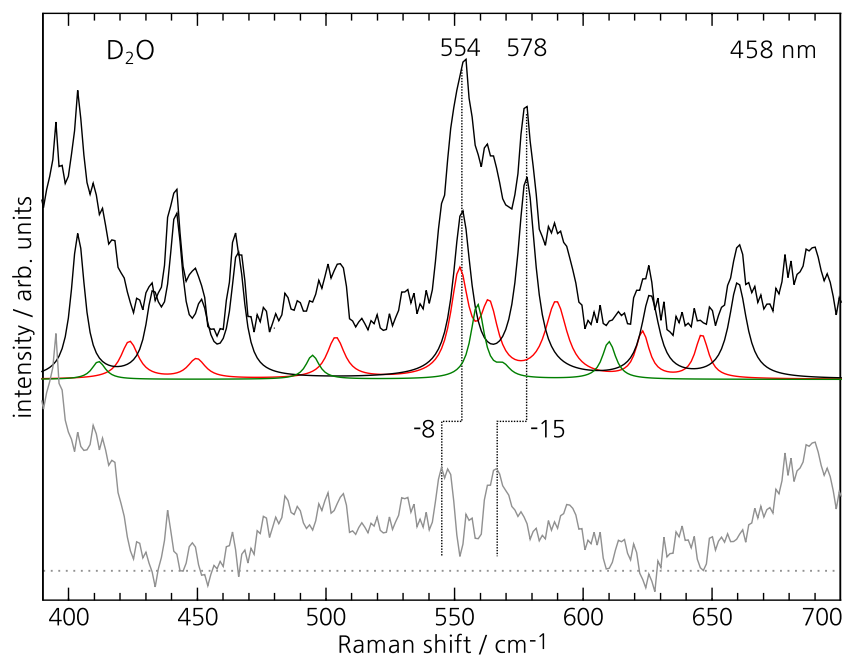
## 8. On the Origin of the OH<sup>-</sup> Ligand at the Proximal FeS Cluster

In the last three Chapters RR spectroscopy has been proven to be a suitable technique for probing the vibrational modes spectra of all MBH cofactors in the spectral range from 300 to 700 cm<sup>-1</sup>. In this Chapter the advanced understanding of the RR spectra from the MBH is used to identify the biochemical origin of the hydroxyl ligand at Fe1 of the superoxidized proximal FeS cluster.

The RR spectrum of the superoxidized proximal cluster with a hydroxyl ligand bound at Fe1 is characterized by FeS stretching modes with main components at 344 and 356 cm<sup>-1</sup>. (Chapter 7) In the spectral region above 400 cm<sup>-1</sup> stretching, bending and torsion modes of the Fe-OH moiety are found. The corresponding component spectrum  $C_{\text{FeS}}$ , with intense marker bands at 554 and 578 cm<sup>-1</sup>, was clearly distinguished from the vibrational modes of the active site in Chapter 6. In contrast, the vibrational spectrum of the oxidized proximal cluster without the hydroxyl ligand, is characterized by two almost equally intense bands at 346 and 368 cm<sup>-1</sup> in the FeS stretching mode region and no pronounced vibrational modes above 420 cm<sup>-1</sup> are detected.

Thus, RR spectroscopy allows to distinguish between the configuration of the proximal cluster with and without the hydroxyl ligand. Furthermore, the direct detection of the Fe-OH stretching modes enables isotopic labeling experiments with D<sub>2</sub>O, H<sub>2</sub><sup>18</sup>O and <sup>18</sup>O<sub>2</sub> of various redox conditions of the MBH, to identify whether the ligand is formed from water or reduced oxygen. RR spectroscopic experiments on genetically engineered MBH variants from *Ralstonia eutropha* will help to identify origin of this ligand. In addition, these experiments reveal long term effects at liquid nitrogen temperatures.

**Figure 8.1.:** RR spectrum of an as-isolated MBH crystal soaked in  $D_2O$ . The spectral components  $C_{NiL}$  (green) and  $C_{NiS}$  (red) of the active site and  $C_{FeS}$  (black) of the proximal cluster were fitted to the spectrum. The residuum (gray) exhibits two bands at 546 and 563  $cm^{-1}$ , that derive from the isotropically shifted bands at 554 and 578  $cm^{-1}$  related to the Fe-OH stretching vibration of the proximal cluster.



### 8.1. Isotopic Labeling Experiments at Various Redox States

To confirm the chemical nature of the ligand at the proximal FeS cluster  $D_2O$  labeling experiments were performed. At first, the as-isolated MBH crystals were soaked in  $D_2O$  buffer. This led to a partial H/D exchange at the ligand of Fe1, as shown in the corresponding RR spectrum of such a crystal displayed in Figure 8.1. The component spectra  $C_{NiS}$  and  $C_{NiL}$  of the active site and the component of the proximal cluster  $C_{FeS}$  were fitted to this spectrum. The resulting residuum displays the fraction of the sample that was successfully labeled with  $D_2O$ . It exhibits two bands above the signal-to-noise level at 546 and 563  $cm^{-1}$ , that derive from the isotropically shifted bands at 554 and 578  $cm^{-1}$ . The isotopic shifts of -8 and -15  $cm^{-1}$  of both bands are consistent with the results from QM/MM calculations (see Table D.2).

In view of the QM/MM data we can assume that the band at 578  $cm^{-1}$  corresponds to a nearly pure Fe-OH stretching mode. Badger's rule may be applied to relate the vibrational frequency to the Fe-O bond length obtained from x-ray crystallography.[225, 47] Indeed, the frequency of 578  $cm^{-1}$  corresponds to a bond length of 1.810 Å, which is in perfect agreement with the value of 1.81 – 1.82 Å for the Fe-O bond length derived from the crystal structures of the MBH.

To explore whether molecular oxygen can bind directly to the proximal cluster, crystalline samples of the MBH were first reduced

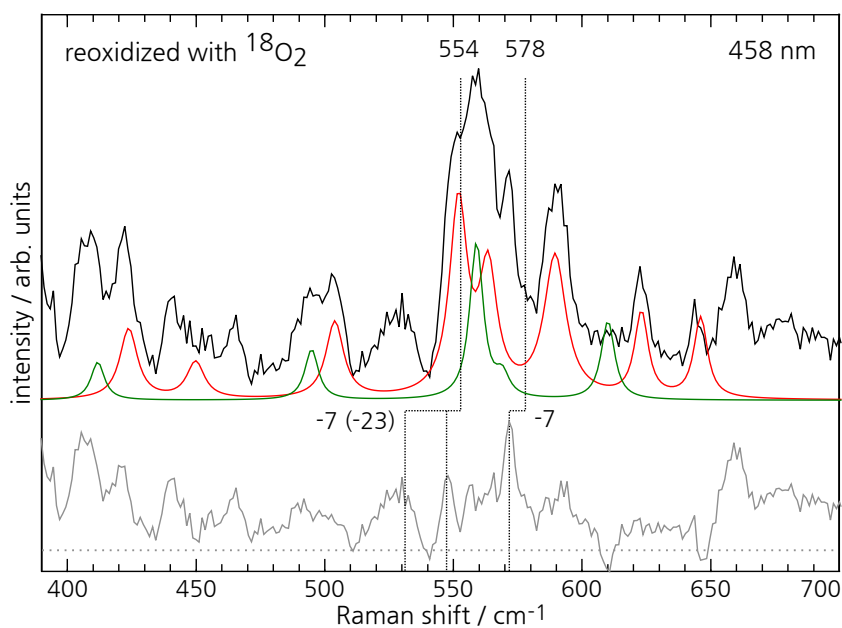
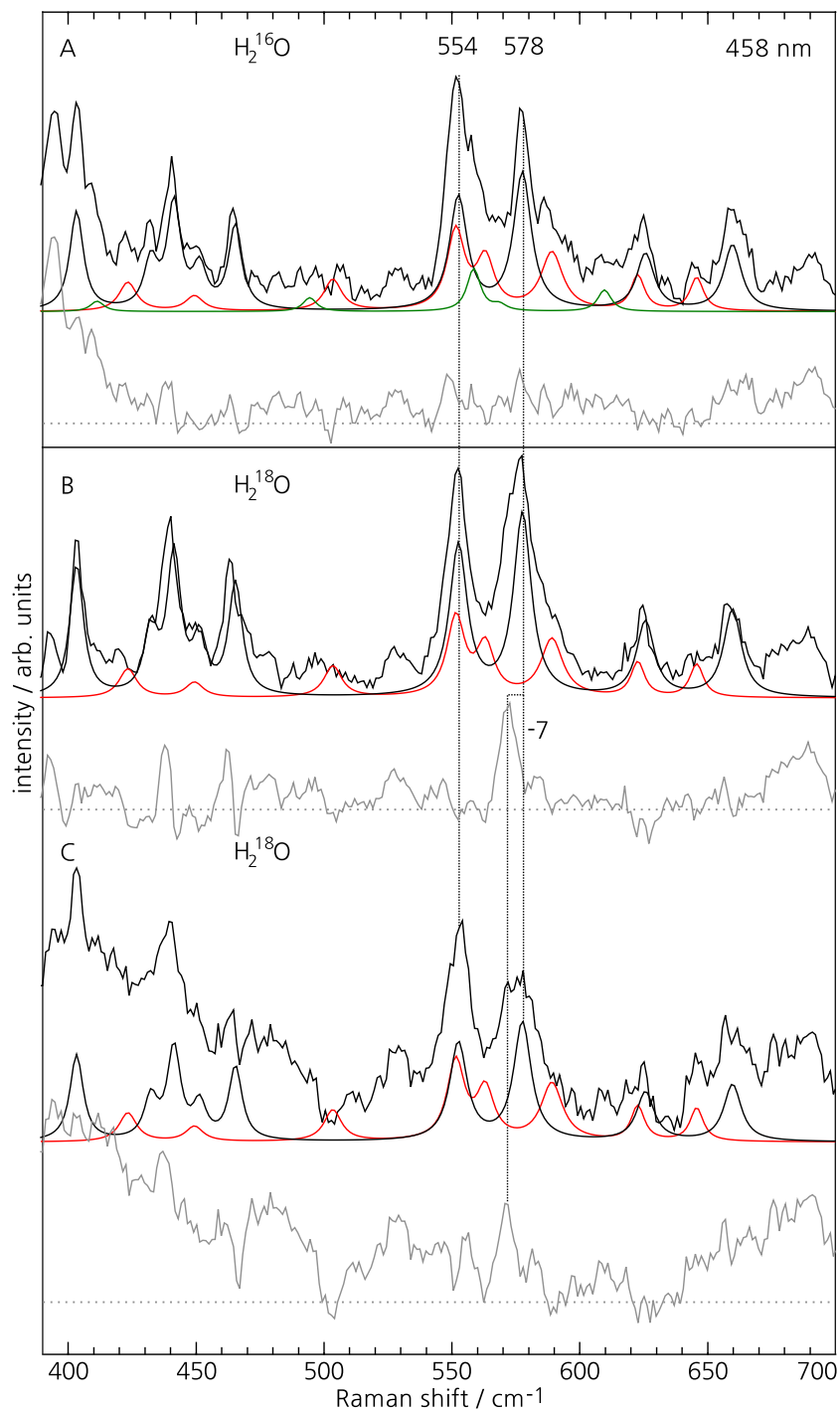


**Figure 8.2.:** RR spectrum of the MBH sample reoxidized with  $^{18}\text{O}_2$ . The component spectra  $C_{\text{NiL}}$  and  $C_{\text{NiS}}$  were fitted to the spectrum. The component spectrum  $C_{\text{FeS}}$  of the superoxidized proximal cluster, with the intense Fe-OH stretching bands at  $554$  and  $578\text{ cm}^{-1}$  is absent, due to a complete isotopic labeling of the respective bands. The residuum (gray) reveals that the  $554$  and  $578\text{ cm}^{-1}$  Fe-OH stretching bands shift by  $-23$  and  $-7\text{ cm}^{-1}$  to lower energies, respectively.

with  $\text{H}_2$  and subsequently reoxidized in the presence of  $^{18}\text{O}_2$ . The corresponding RR spectrum confirms a complete and exclusive isotopic labeling of the hydroxyl ligand at the proximal cluster. (See Figure 8.2) Both marker bands at  $554$  and  $578\text{ cm}^{-1}$  exhibit isotopic shifts to  $531$  and  $571\text{ cm}^{-1}$ , respectively.

In a next step, we will elucidate whether an  $\text{OH}^-$  derived from a water molecule in the vicinity of the proximal cluster can also bind under anaerobic conditions. Therefore, MBH crystals from aerobically purified protein in a buffer containing  $\text{H}_2^{18}\text{O}$  instead of  $\text{H}_2^{16}\text{O}$  were grown anaerobically in a reducing atmosphere. Afterwards the crystals were anaerobically reoxidized with ferricyanide, but trace amounts of oxygen cannot be excluded. A control experiment was done in the same way with unlabeled water. The RR spectra of both samples are displayed in Figure 8.3. Again, the component spectra  $C_{\text{NiS}}$  and  $C_{\text{NiL}}$  of the active site and the component of the proximal cluster  $C_{\text{FeS}}$  were fitted to the spectra, similar to the procedure for the other labeled MBH samples. The spectrum of the unlabeled sample (Panel A) can be represented by a linear combination of the three spectral components, as revealed by a residuum showing only noise. In contrast, the component fits for the RR spectra of two MBH samples labeled with  $\text{H}_2^{18}\text{O}$  displayed in panel B and C of Figure 8.3 show an isotopic shift of the Fe-OH stretching band at  $578\text{ cm}^{-1}$  by  $-7\text{ cm}^{-1}$ . The very same shift was observed for the  $^{18}\text{O}_2$  reoxidized MBH sample. Due to the low spectral quality an isotopic shift of the  $554\text{ cm}^{-1}$  band cannot be confirmed. However, the isotopic labeling is not complete. Portions of unlabeled Fe-OH stretching bands possibly originate

**Figure 8.3.:** RR spectra of anaerobically reoxidized MBH crystals in  $\text{H}_2^{16}\text{O}$  (panel A) as well as  $\text{H}_2^{18}\text{O}$  (two different samples in panel B and C). (see page 150 for more details on the sample preparation) Spectral components  $C_{\text{NiL}}$ ,  $C_{\text{NiS}}$  and  $C_{\text{FeS}}$ , displayed in green, red, and black, fitted to the spectra reveal an isotopic shift of  $-7\text{ cm}^{-1}$  in the respective residuals (gray) for the Fe-OH stretching mode at  $578\text{ cm}^{-1}$  in the  $\text{H}_2^{18}\text{O}$  labeled samples.



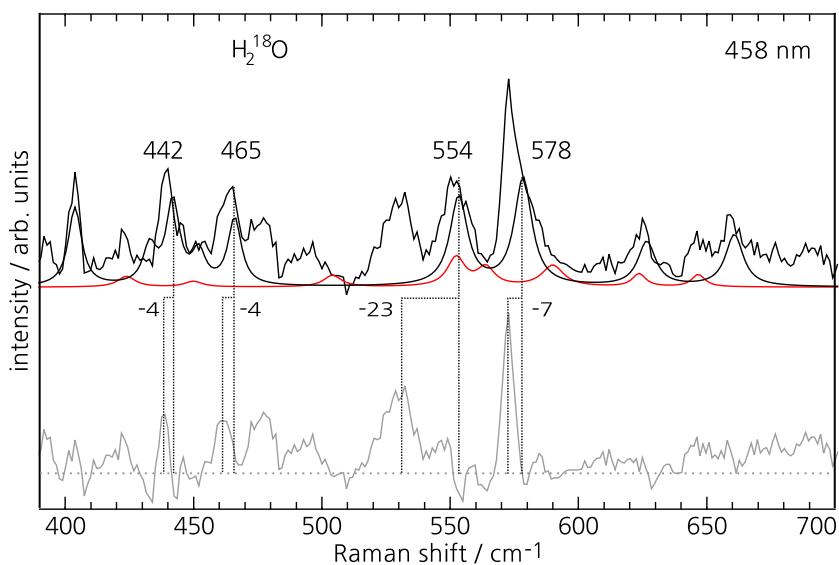


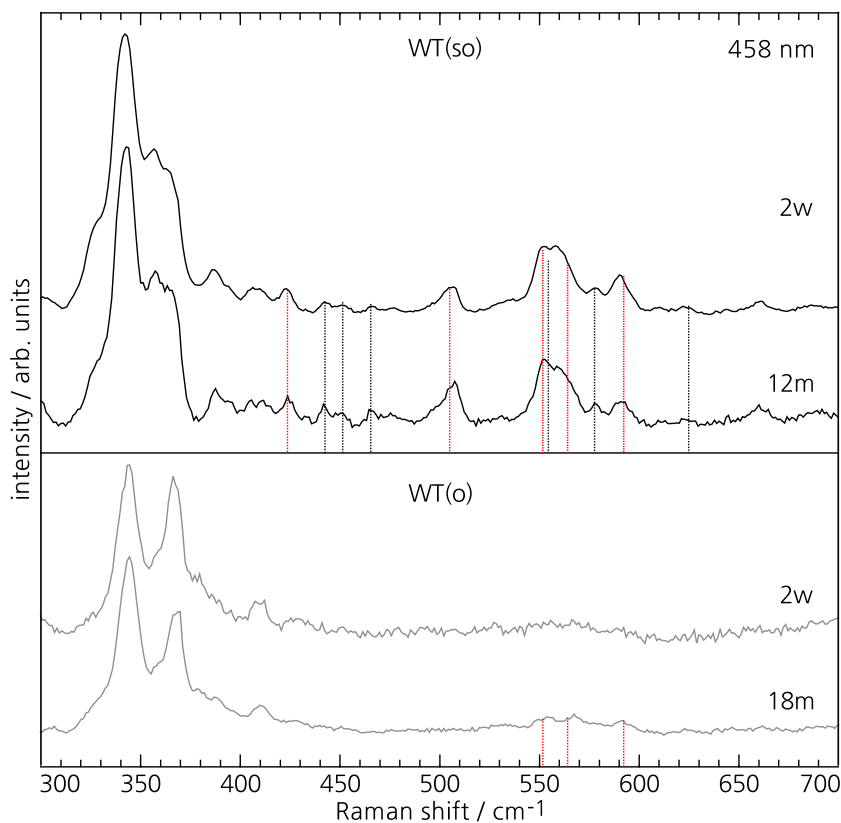
**Figure 8.4.:** RR spectrum of one anaerobically reoxidized MBH crystal in  $\text{H}_2^{18}\text{O}$  after a storage of two months in liquid nitrogen. An isotopic shift of  $-7\text{ cm}^{-1}$  can be clearly observed for the band at  $578\text{ cm}^{-1}$ . The  $554\text{ cm}^{-1}$  marker band of the Fe-OH stretching mode shows an isotopic down-shift of  $-23\text{ cm}^{-1}$  to  $531\text{ cm}^{-1}$ . In addition, shifts by  $4\text{ cm}^{-1}$  to lower frequencies are detected for the Fe-OH bands at  $442$  and  $465\text{ cm}^{-1}$ .

from trace amounts of oxygen during the sample preparation.

A control RR measurement of the  $\text{H}_2^{18}\text{O}$  labeled MBH samples was performed after storage of the samples in liquid nitrogen for two months. (Figure 8.4) The RR spectrum recorded at  $458\text{ nm}$  clearly verifies the isotopic downshift of  $-7\text{ cm}^{-1}$  for the Fe-OH stretching band at  $578\text{ cm}^{-1}$ . In addition, the isotopic shift of the band at  $554\text{ cm}^{-1}$  to  $531\text{ cm}^{-1}$  is now confirmed, as well. The very same isotopic shifts were observed for the  $^{18}\text{O}_2$  reoxidized MBH sample. From QM/MM calculations it is expected that the bands below  $500\text{ cm}^{-1}$  shift by approximately  $1\text{ cm}^{-1}$  to lower frequencies (Table D.2), experimentally the Fe-OH bands at  $442$  and  $465\text{ cm}^{-1}$  shift by  $-4\text{ cm}^{-1}$ .

In comparison to the previously shown RR spectrum in Figure 8.3B, the relative fraction of the fitted components  $C_{\text{FeS}}$  and  $C_{\text{NiS}}$  is essentially unchanged in the RR spectrum displayed in Figure 8.4 but the portion of the isotopically labeled Fe-OH stretching bands increased significantly. In general the spectra of as-isolated MBH crystals do not change after a prolonged storage at  $77\text{ K}$ , as shown in Figure 8.5A and B for an as-isolated MBH crystal with and without an  $\text{OH}^-$  ligand bound at the proximal cluster. Apparently, this is different for reoxidized samples, as the reoxidation process might be still incomplete at the time when the crystals are frozen to liquid nitrogen temperatures. A charge compensation process, as the driving force for the binding of the  $^{18}\text{OH}^-$  ligand derived from labeled water, can be a possible explanation. This process is delayed at liquid nitrogen temperatures, as the respective diffusion of water molecules is strongly decelerated here. These effects at cryogenic temperatures are further studied in the next section.

**Figure 8.5.:** RR spectra of as-isolated MBH crystals with (A) and without (B) an  $\text{OH}^-$  ligand bound at the proximal cluster. The RR spectra were measured after less than two weeks (2w) and twelve (12m) or eighteen months (18m) of storage in liquid nitrogen. The spectrum of the very same crystal does not change after that extended period of time. This also implies that the  $\text{OH}^-$  ligand does not bind, due to slow diffusion in the crystalline phase, to the proximal cluster of the oxidized wildtype crystal. Band positions of the Fe-OH modes from the superoxidized proximal cluster are marked in black. In red Fe-CO / CN modes of the  $[\text{NiFe}]$  active site in the  $\text{Ni}_a\text{-S}$  redox state are indicated.



### 8.1.1. Role of the His229 and Long Term Effects at 80 K

The  $\text{OH}^-$  ligand lies in hydrogen bonding distance (2.40 to 2.42 Å) to His229. To explore the role of this residue in the catalysis and oxygen-tolerance of the MBH, His229 was substituted by alanine (H229A), methionine (H229M) and glutamine (H229Q). The  $\text{H}_2$ -mediated methylene blue reduction activities of these MBH variants lie at 58, 31 and 15% of the wildtype level, respectively. These strains grew well only in the presence of 0.5% oxygen, but not at ten or more percent of oxygen. This suggested, that His229 is crucial of the oxygen-tolerance of the MBH.[47]

Exemplary, the RR spectra of the H229A and H229M variant recorded at 458 nm are displayed in Figure 8.6A. The respective samples were stored for one and two weeks in liquid nitrogen before the measurement. The two spectra are almost identical and exhibit vibrational modes of the  $C_{\text{NiL}}$  and  $C_{\text{NiS}}$  spectral components of the active site. The FeS stretching region in the RR spectrum is more similar to the spectrum of the oxidized, as-isolated wildtype without (WT(o)) a hydroxyl ligand than with (WT(so)). This observation is in agreement with the loss of the  $\text{OH}^-$  ligand found in all crystal structures of the histidine variants.[203, 189]

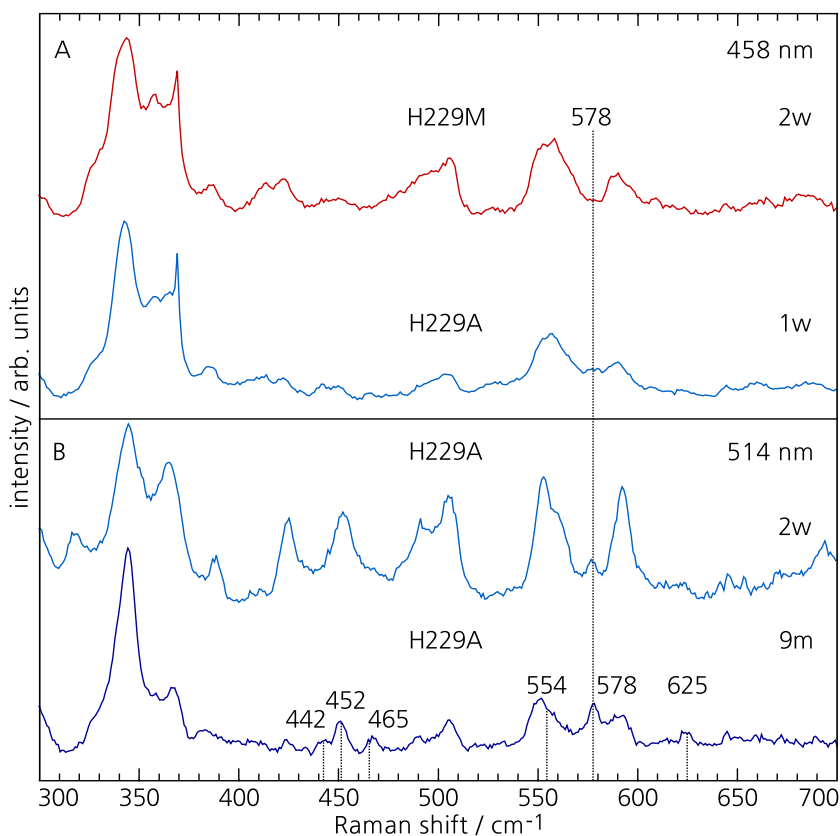


**Figure 8.6.:** A) RR spectra of the as-isolated MBH variants H229M and H229A recorded at 458 nm. The spectrum of the H229M and H229A variant shows no bands above the noise level at the band positions of the  $C_{\text{FeS}}$  spectral component from the superoxidized proximal cluster. The position of the intense FeOH stretching band at  $578\text{ cm}^{-1}$  is marked with a vertical line. B) RR spectrum recorded at 514 nm of the same MBH H229A crystal as shown in A, after storage for two weeks and nine months in liquid nitrogen, respectively. The intensity of the marker band for the  $C_{\text{FeS}}$  component clearly increases and the spectrum measured after nine months of storage is essentially identical to the spectrum of an as-isolated WT(so) crystal, as shown in Figure 6.2 page 82. Band positions of the  $C_{\text{FeS}}$  component spectrum are indicated with black vertical lines at the bottom.

(See also Section 7.4) The RR spectrum of the H229Q variant is very similar to the spectrum of the H229M variant and therefore not shown here.

However, a very weak shoulder, near the signal-to noise level at  $578\text{ cm}^{-1}$  is detected in the spectrum of the H229A variant. This is unexpected, as this band is one of the most intense marker bands of the  $C_{\text{FeS}}$  spectral component of the superoxidized proximal cluster and characteristic for the Fe-OH stretching. After another week in liquid nitrogen, the band intensity is clearly above the noise level for the spectrum of the H229A variant measured at 514 nm. (Figure 8.6B) The spectrum of the very same sample, stored for another nine months in liquid nitrogen, finally shows a RR spectrum that resembles that of the as-isolated MBH crystal in the WT(so) form. (See Figure 6.2) All major bands of the  $C_{\text{FeS}}$  component are detected on an adequate intensity level. Moreover, the spectral region of the FeS stretching modes has changed dramatically and is now wildtype like.

This can be explained in the following way:

First, it was suggested that the  $\text{OH}^-$  ligand derives from a water molecule in the vicinity of the proximal cluster.[47] The RR spectra of the anaerobically reoxidized  $\text{H}_2^{18}\text{O}$  labeled MBH samples corroborate this assumption. (Figure 8.3) However, this process

competes with the favored formation of the hydroxyl group from reduced oxygen. Secondly, we observed for the anaerobically re-oxidized MBH crystals that structural changes can even occur on time-scales ranging from weeks to several months at temperatures as low as 77 K. (Figure 8.4) Possibly an incomplete reoxidation process and a charge compensation served as the driving force for these effects.

In view of the first point, the crystal structure of the H229A variant is special in comparison to the other histidine variants and the MBH wildtype. Only in the crystal structure of the as-isolated H229A variant three water molecules in the vicinity of the proximal cluster are found.[189] At least one of these water molecules showed an extended flexibility in the crystal structure. Thus it is conceivable that the water molecule reorients, binds as an  $\text{OH}^-$  to the proximal cluster and forms the superoxidized redox state. At liquid nitrogen temperatures this may take an extended period of time, as diffusion and reorientation of selected water molecules is retarded.

Regarding the issue whether it is possible that individual water molecules in the crystal matrix reorient and bind as an  $\text{OH}^-$  to the proximal cluster at temperatures as low as 77 K, a short review on the characteristics of water ice is useful.

If frozen, water ice can exist in 16 crystalline and several amorphous phases, depending temperature and pressure.[226, 227] Under certain conditions, the individual water molecules cannot orient according to the 'ice rules'<sup>A</sup> and point defects (missing or extra hydrogen atoms) as well as ionic defects ( $\text{H}_3\text{O}^+$  or  $\text{OH}^-$ ) are very likely to develop.[228] As these defects move through the crystal, an increased orientational mobility and relaxation of the water molecules in the crystal is enabled.[228] It has been reported that the crystalline phase of water ice, called Ice Ic, undergoes reorientation effects at liquid nitrogen temperatures. The higher ordered form XI(c) is formed, which has a lower internal energy of about 1 kJ/mol.[229, 230, 231] However, this reorientation took several weeks at temperatures of 77 K and a pressure of 1 bar.

In the investigated MBH crystals for RR measurements as well as for the x-ray crystallography the water ice is presumably formed in the low density amorphous phase, as the crystals are rapidly frozen to liquid nitrogen temperatures at ambient pressure. Thus, a large number of point and ionic defects can be assumed. These defects may move through the MBH crystal and induce reorientations of the water molecules as described above. Therefore it is possible

<sup>A</sup>Ice rules: Each oxygen atom has four nearest neighbors (hydrogen atoms) in a tetrahedral arrangement. One hydrogen atom is placed between every two oxygen atoms and each of these hydrogen atoms is covalently bound to one oxygen and hydrogen bonded to the other oxygen atom.

that the water molecules in the MBH crystal rearrange, energy is released and a  $\text{OH}^-$  finally binds to the Fe1 of the proximal cluster, which may as well take weeks or months.

In conclusion, the superoxidized redox state of the proximal cluster appears to be an energetically favored configuration, as it is formed even at low temperatures due to the rearrangement of individual water molecules within the crystal structure. The effect of a rebinding of an  $\text{OH}^-$  ligand to the proximal cluster over an extended period of time is not observed for any crystalline samples of the as-isolated wildtype (Figure 8.5) or any other variant of the MBH such as H229M, C120G/C19G and P242C. Only crystalline samples of the H229A variant showed this effect. In contrast to the other samples, three water molecules are incorporated in the vicinity of the proximal cluster. Thus, the hydroxide ligand at the proximal cluster of the H229A variant might be in the present case a result of the reorientation of water molecules. In this context, protons are transferred via amino acids of the protein the matrix.

## 8.2. Conclusion

The above described RR spectra of isotopically labeled MBH samples as well as the observations made in the RR spectra of the H229A variant prove that the  $\text{OH}^-$  ligand at the superoxidized proximal cluster derives from reduced molecular oxygen or a water molecule in the vicinity of the cluster itself.

Of these two possibilities, the hydroxyl ligand at Fe1 is preferentially formed from molecular oxygen, which is reduced in a four-electron three-proton process. By the reduction of oxygen, the formation of reactive oxygen species, that may damage or block the [NiFe] active site, is avoided and oxygen-tolerant hydrogenases are enabled to maintain  $\text{H}_2$ -oxidation activity under aerobic conditions.[43, 137, 135] The continuously produced water molecules of this reaction effectively compete with  $\text{H}_2\text{O}$  from the solvent for the  $\text{OH}^-$  binding site at Fe1 of the proximal cluster. Here, the water molecule derived from the oxygen reduction has a clear advantage in this process, as it is already in direct proximity of the FeS cluster. The completely labeled Fe-OH marker bands of the MBH reoxidized with  $^{18}\text{O}_2$  corroborate this idea. Moreover, RR spectra of the anaerobically reoxidized MBH exhibited only partially labeled Fe-OH marker bands, which is in line with residual amounts of oxygen during the preparation. Thus, molecular oxygen has a high binding affinity to the proximal cluster, as even

traces of oxygen are bound under 'anaerobic' conditions. Previous quantum mechanical calculations also proposed that the proximal cluster can serve as an alternative target for the  $O_2$  binding.[232] Solvent water molecules in the vicinity of the proximal cluster are an alternative source for the hydroxyl ligand, as suggested previously.[47] However, this binding process is much slower than the formation of the Fe-OH bond from reduced molecular oxygen. In the H229A variants this effect was observed as a reorientation of at least one of the three water molecules in the vicinity of the proximal cluster with a subsequent binding of the  $OH^-$  to Fe1. An incomplete reoxidation of the anaerobically reoxidized MBH samples and the charge compensation at the proximal cluster served as a driving force for the formation of the Fe-OH bond. This leads to the conclusion, that the superoxidized redox state of the proximal cluster is the energetically favored configuration, as it is formed even at low temperatures due to the rearrangement of individual water molecules. The redox dependent reversible conformational changes at Fe4 together with the occurrence of the ligand at Fe1 in the superoxidized form stabilize the entire [4Fe3S] cluster in its highest oxidation state 5+. This process includes the release of two electrons. The remaining proton of the  $H_2O$  serving as the source of the  $OH^-$  is liberated and subsequently transferred via the amino acid residue H229 to the [NiFe] active site, where it is supposed to support the reductive removal of oxygen. Such a proton pathway has been described by Frielingsdorf *et al.* [47]

## 9. Summary and Outlook

Currently, the research on oxygen-tolerant hydrogenases is focused on the complex structure-function relationships and interactions between the enzyme's metal-inorganic cofactors during the reversible cleavage of molecular hydrogen into protons and electrons in the presence of oxygen. In this work the cofactors involved in the catalytic cycle of the membrane bound hydrogenase (MBH) from *Ralstonia eutropha*, i.e. the nickel-iron active site and iron-sulfurs clusters have been investigated by means of Infrared (IR) and Resonance Raman (RR) spectroscopy. RR spectroscopy has thereby been established as a powerful complementary vibrational spectroscopic technique for the investigation of highly complex biological molecules such as the MBH.

### Interconversion of Active Site Redox States

The redox transitions of the active site have been studied by IR transmission spectroscopy as a function of externally adjusted redox potentials. These potentials have been realized either by mixtures of the gaseous substrates hydrogen and oxygen or in a Spectro-Electro-Chemical (SEC) setup. Thus, it has been possible to visualize in time-resolved gas-exchange experiments the entire reoxidation process. A comparison of this process for the heterodimeric MBH attached to the membrane (MBH<sub>mem</sub>), i.e. in its natural environment, and the solubilized heterodimeric MBH without the natural electron acceptor cytochrome *b* (MBH<sub>sol</sub>), has revealed that the subunit including the cytochrome *b* is crucial for the reversibility of the proceeding redox process. A reversible redox process involves a conversion of the fully reduced Ni<sub>a</sub>-SR species via the reduced Ni<sub>a</sub>-C intermediate to the active or ready Ni<sub>a/r</sub>-S species. Upon further oxidation the Ni<sub>a/r</sub>-S species decays and the Ni<sub>r</sub>-B is formed as the dominant redox state. This entire process, with the decay and formation of the various redox states, has been successfully modeled with a set of coupled mono-exponential equations, thus confirming the presence of the underlying one-electron

The MBH<sub>mem</sub> reacts completely reversible with hydrogen and oxygen, the MBH<sub>sol</sub> not.  
Section 4.1

Under anaerobic conditions electrochemically induced processes are reversible for the MBH<sub>sol</sub>.  
Section 4.2

transitions.

Once the natural electron acceptor cytochrome *b* is lost, as in the MBH<sub>sol</sub> samples, the redox behavior could not be adequately described with coupled exponential equations. Moreover, the formation of the irreversibly inactive species Ni<sub>ia</sub>-S is triggered during the reoxidation process. A qualitative analysis has revealed that this species evolves from the decaying reduced redox species Ni<sub>a</sub>-C and presumably also Ni<sub>a</sub>-SR. Thus the MBH<sub>sol</sub> is not capable to react fully reversibly with hydrogen and oxygen, although the quality of the MBH<sub>sol</sub> preparation in the as-isolated form has been significantly improved regarding homogeneity and activity, as compared to earlier preparations.[33, 43, 79]

Interestingly, comparative SEC studies that have been carried out at pH 7.0, revealed that in the presence of redox mediators and under sufficiently high overpotentials a reactivation of significant amounts of the Ni<sub>ia</sub>-S to the Ni<sub>r</sub>-B redox state is possible. This demonstrates that the electro-chemically induced processes are reversible. However, a certain fraction Ni<sub>ia</sub>-S' of the Ni<sub>ia</sub>-S species has remained inactive under the present conditions. This irreversibly inactive species Ni<sub>ia</sub>-S' exhibits CN modes at lower frequencies than the Ni<sub>ia</sub>-S species, although both CO modes have the same frequency. Notably, the previously observed suppressed reactivation of Ni<sub>ia</sub>-S has been observed only in treatments of the MBH with its natural substrate hydrogen.

For a qualitative evaluation of the second derivative absorbance spectra, a superposition of second derivative Gaussian functions for the various redox states of the active site has been fitted to measured spectra. The relative population of each redox species has been determined as a function of applied potential in a reproducible way. Based on that, the midpoint potential of the Ni<sub>a</sub>-SR–Ni<sub>a</sub>-C redox couple at pH 7.0 has been obtained in satisfactory agreement with previous results on the oxygen-tolerant hydrogenase from *Aquifex aeolicus*. [85]

Furthermore, this approach has been successfully applied to gather the component spectra, i.e. the CO and CN band positions as well as their intensity ratios, for the various redox species including the Ni<sub>ia</sub>-S and Ni<sub>ia</sub>-S'. Thus, a powerful and efficient alternative to manual baseline corrections of the IR absorbance spectra has been established. Minor limitations regarding the fit of strongly overlapping bands, as for instance in the spectral region of the CN stretching bands, exist.

## Vibrational Spectroscopic Investigations of the Solubilized Heterodimeric MBH

The solubilized heterodimeric form of the MBH, i.e. MBH<sub>sol</sub> is preferred for electrochemical studies, as it can be efficiently adsorbed on electrode surfaces, which substitute for the missing electron acceptor cytochrome *b*. Also for RR spectroscopy the heterodimeric MBH<sub>sol</sub> form is favored, as the spectra will not be superimposed by the strong RR signals of the cytochrome's heme.

Recently the crystallization of the heterodimeric MBH<sub>sol</sub> in its reduced and several oxidized forms has been accomplished.[44, 47]

The first IR spectrum of a single as-isolated heterodimeric MBH<sub>sol</sub> crystal has been recorded with an IR microscope in this work and thus demonstrates another method to analyze single protein crystals. The active site of the as-isolated crystalline MBH<sub>sol</sub> resides, with a dominant Ni<sub>r</sub>-B fraction, in the same configuration as the MBH<sub>sol</sub> in bulk solution. This finding excludes any modifications at the active site due to packing defects in the crystallization process.

RR spectroscopy was so far only established for studies on the FeS clusters hydrogenase research. With the present work it has been proven that RR spectroscopy is a powerful complementary method to IR and EPR spectroscopy to selectively probe the vibrational modes of the FeS clusters *and* the metal ligand modes [NiFe] active site. A consistent assignment of the respective vibrational modes of the FeS clusters and the [NiFe] active site has been achieved supported by QM / MM calculations as well as isotopic labeling and adequate tools for the evaluation of the experimental RR spectra. With this advanced understanding of the experimental RR spectra new mechanistic and structural insights have been obtained, which even exceed the crystallographic information. Here, it is worth noting that the experimental RR spectra, the crystallographic data and in turn the calculated Raman spectra from QM / MM calculations refer to the crystalline MBH<sub>sol</sub>. Thus, results obtained from all three methods are directly correlated with each other.

Infrared spectrum of a single MBH<sub>sol</sub> crystal.  
Section 6.1

## Methods for Analyzing Resonance Raman Spectra of the MBH

RR spectra of the MBH<sub>sol</sub> exhibit a broad region of overlapping FeS stretching modes between 300 and 400 cm<sup>-1</sup> and distinct bands in the spectral region between 400 and 700 cm<sup>-1</sup>. In the hydrogen-

reduced samples contributions of FeS cluster related modes can be ruled out in the latter region. A sensitivity of the remaining bands in the RR spectrum of the hydrogen-reduced MBH<sub>sol</sub> to <sup>13</sup>C and <sup>15</sup>N isotopic labeling, has proven that these bands originate from vibrations of such moieties from the [NiFe] active site.

The analysis of RR spectra of as-isolated, oxidized samples has been complicated by the fact that some modes related to the superoxidized proximal FeS cluster are expected in a spectral range similar to that of the vibrations from the [NiFe] active site.[113] The vibrational modes from the active site, as well as from the superoxidized proximal cluster have been consistently discriminated with several methods of spectra analysis. Thereby, three component spectra have been identified. Two of them derive from the [NiFe] active site and one from the superoxidized proximal cluster with a hydroxyl group bound at Fe1.

The experimentally determined spectral components have been compared to Raman spectra calculated by means of QM/MM models, based on computationally refined crystal structures of the hydrogen-reduced and as-isolated MBH<sub>sol</sub> from *Ralstonia eutropha*. [191, 44, 103, 47] In conjunction with these calculations the experimental Raman bands have been assigned to Fe-CO / CN bending and stretching modes of the active site in the Ni<sub>a</sub>-L and Ni<sub>a</sub>-S redox state. Additionally Fe-OH and Fe-Cys modes of the superoxidized proximal cluster [4Fe3S]<sub>p</sub>+OH have been identified in the third component.

At frequencies between 300 and 400 cm<sup>-1</sup> the RR spectrum of the as-isolated oxidized MBH<sub>sol</sub> shows a superposition of vibrational modes from all three FeS clusters. The stretching modes of each cluster are shifted relative to each other, due to their different molecular configurations. Based on angle-dependent RR spectroscopy on single as-isolated MBH<sub>sol</sub> crystals, the FeS stretching modes for all three clusters have been discriminated. This method also allowed statements on the projection of the electronic transition dipole moments from each cluster relative to the crystal surface. The initial assignments obtained via angle-dependent RR spectroscopy have been confirmed with RR spectra from samples of MBH variants with genetically engineered FeS clusters and RR difference spectroscopy. This resulted in a consistent assignment of the most intense vibrational modes to all three FeS clusters. This also included the first vibrational spectroscopic description of the recently found proximal [4Fe3S]<sub>p</sub>+OH cluster in this region.

Finally, a complete assignment of the bands between 300 and

700 cm<sup>-1</sup> has been achieved. This allowed a consistent investigation of various samples of the MBH<sub>sol</sub> and its genetically engineered variants in terms of their [NiFe] active site configuration as well as the nature of the FeS clusters.

## Structural and Mechanistic Insights into the MBH Obtained by Resonance Raman Spectroscopy

First of all, is the resonance enhancement of active site vibrational modes related to Fe-CO metal-to-ligand charge transfer. This has been confirmed by the fact that the relative intensities of the calculated Fe-CO / CN Raman bands, weighted according to the contribution of the Fe-CO bending and stretching coordinates to the potential energy distribution (PED) of the individual modes for the Ni<sub>a</sub>-L and Ni<sub>a</sub>-S redox state, are in excellent agreement with the experimental data.

In view of the high local photon densities in the RR experiment, also light-induced process have been addressed. In this context an efficient photo-conversion of the reduced species to Ni<sub>a</sub>-L has been observed. The reaction mechanism for the hydrogen-reduced [NiFe] active site under the influence of light and at temperatures as low as 80 K proposes that Ni<sub>a</sub>-C converts to Ni<sub>a</sub>-L and the bridging ligand H<sup>-</sup> is liberated [108, 102, 100, 99] accompanied by the protonation of Cys597 [103]. As a result of the high photon densities in the RR experiment, Ni<sub>a</sub>-SR, which also has a protonated terminal cysteine, might be photo-converted to Ni<sub>a</sub>-L as well. The bridging hydride (H<sup>-</sup>) would then be released as one electron and proton. The remaining second electron changes the oxidation state at the nickel ion from 2+ to 1+.

Illumination of the as-isolated MBH<sub>sol</sub> samples in the RR experiment, resulted in the partial (re)activation of the [NiFe] active site to the Ni<sub>a</sub>-S, and under certain conditions even to the Ni<sub>a</sub>-L redox state. With this photo-reactivation of the active site the window of activity for H<sub>2</sub> oxidation in a fuel cell might be broadened and the performance of the fuel cell improved. [116, 11] As the bridging ligand is believed to be bound weaker in oxygen-tolerant hydrogenases [110] a photo-conversion of Ni<sub>r</sub>-S, which is present in minor amounts in oxidized samples, to Ni<sub>a</sub>-S is proposed. Depending on the excitation wavelengths and localized ferricyanide amounts, even the Ni<sub>r</sub>-B state might be photo-converted.

As-isolated MBH<sub>sol</sub> crystals soaked in solutions containing excess amounts of ferricyanide revealed, with increasing relative inten-

Resonance enhancement through metal-to-ligand charge transfer. Section 5.2, 5.3, 6.2.2 and 6.3

Efficient photo-conversion of all reduced species to Ni<sub>a</sub>-L. Section 5.3 and 5.4

Light-induced Reactivation of the as-isolated MBH<sub>sol</sub>. Section 6.4 and 6.5

sities of the Ni<sub>a</sub>-L Fe-CO / CN vibrational modes, a clear photo-reduction of the active site under the influence of the laser beam. Interestingly, the relative intensities of the Fe-CO / CN vibrational modes from the Ni<sub>a</sub>-S redox state as well as the Fe-OH stretching and bending modes from the superoxidized proximal cluster remained largely unchanged.

Another important issue has been the role and origin of the hydroxyl ligand at the proximal FeS cluster.

The native hydroxyl ligand of [4Fe3S]<sub>p</sub> is restored in the reoxidation process. Section 6.2, 7.2 and 7.4

With RR spectroscopy on the as-isolated and reoxidized MBH<sub>sol</sub> in solution it has been proven, that the hydroxyl ligand is the native configuration of the proximal cluster, and not a crystallization artifact. If the OH<sup>-</sup> ligand is absent, both the experimental RR as well as the calculated Raman spectrum exhibit no pronounced FeS cluster related modes in the spectral region between 400 and 700 cm<sup>-1</sup>. Also the FeS stretching modes are altered. This finding allows a straightforward investigation of other oxygen-tolerant and -sensitive hydrogenases (in solution and the crystalline form) in terms of the existence of an OH<sup>-</sup> group at the proximal cluster. This information is important for investigations regarding the oxygen-tolerance of other hydrogenases.

Additionally it has been shown, that the hydroxyl ligand is rebound to high amounts in the reoxidation process (with air). Similarly treated MBH<sub>sol</sub> samples at pH 5.5 exhibited in the respective IR spectra significant amounts of the irreversibly inactive redox species Ni<sub>ia</sub>-S. Thus, an incomplete reoxidation of the proximal cluster might favor the formation of the Ni<sub>ia</sub>-S species at the [NiFe] active site. In other words: The superoxidized proximal cluster in its [4Fe3S]<sub>p</sub>+OH configuration seems to protect the active site from an irreversible oxidative damage. This is also in line with previous combined IR and EPR studies at pH 7.0, where the effect is more pronounced and the oxidative damage found for the active site was also accompanied with modification (of the coupling behavior) in the proximal FeS cluster.[43]

The hydroxyl ligand derives from reduced molecular oxygen. Section 8.1

In order to elucidate the origin of the hydroxyl ligand at the superoxidized proximal FeS cluster, different isotopically labeled samples of the MBH<sub>sol</sub> have been prepared. First, reduced and H<sub>2</sub><sup>18</sup>O labeled MBH<sub>sol</sub> samples have been 'anaerobically' oxidized. Secondly, unlabeled reduced MBH<sub>sol</sub> samples have been oxidized with <sup>18</sup>O<sub>2</sub>. In both cases, this resulted in clear isotopic shifts of two Fe-OH stretching bands. As an exclusive labeling has been observed for samples oxidized with <sup>18</sup>O<sub>2</sub>, the hydroxyl ligand at Fe1 must be preferentially formed from molecular oxygen, which is reduced in

a four-electron three-proton process. This is also in line with the instantaneous binding of traces of  $^{16}\text{O}_2$ , which are present besides the  $^{18}\text{OH}^-$  derived from water during the 'anaerobic' oxidation  $\text{H}_2^{18}\text{O}$ . Thus, molecular oxygen has a high binding affinity to the proximal cluster. Previous quantum mechanical calculations also proposed that the proximal cluster can serve as an alternative target for the  $\text{O}_2$  binding.[232]

Solvent water molecules in the vicinity of the proximal cluster are an alternative source for the hydroxyl ligand. However, this binding process is much slower. In RR studies on crystals of H229A variants this effect has been observed as a reorientation of at least one of the three water molecules in the vicinity of the proximal cluster with a subsequent binding of the  $\text{OH}^-$  to Fe1 at liquid nitrogen temperatures. Under the same conditions an incomplete reoxidation process of the 'anaerobically' reoxidized  $\text{MBH}_{\text{sol}}$  samples was completed through a charge compensation which served as a driving force for the formation of the Fe-OH bond at the proximal cluster. Thus, the configuration with a bound hydroxyl group at Fe1 is the energetically favored configuration, as it stabilizes the entire cluster in an asymmetric form.

Binding affinity of  $\text{OH}^-$  from water is decreased, compared to  $\text{O}_2$  as source.  
Section 8.1.1

## Outlook

Exemplary IR-SEC measurements were successfully carried out for the  $\text{MBH}_{\text{sol}}$  at pH 7.0. In the future, studies of this kind under systematically varied (an)aerobic conditions, e.g. at different pH values and temperatures, should be performed. This will lead to an improved understanding of the catalytic mechanisms at the active site, its interaction with adjacent amino acids and structural changes in the surrounding protein matrix. Further aspects of interest are the molecular details in the oxygen-tolerance and the potential proton pathways. Therefore, the investigations in the bulk solution should be complemented, also with further IR microscopic studies on single crystals.

The advanced understanding of the  $\text{MBH}_{\text{sol}}$  RR spectra from *Ralstonia eutropha* demonstrated in this work will be the basis for future investigations of the wildtype enzyme and specific variants of the cofactors under varying experimental conditions, in order to elucidate further aspects of the catalytic cycle. The advantage of the present approach is that vibrational modes of both, the active site ( $\text{Ni}_a\text{-S}$  and  $\text{Ni}_a\text{-L}$ ) and all three FeS clusters ( $[\text{4Fe3S}]_p$ ,  $[\text{3Fe4S}]_m$ ,  $[\text{4Fe4S}]_d$ ) in their oxidized form are probed simultane-

ously. Based on the complementary information gained from IR and EPR spectroscopy, the structure-function relationships in the hydrogenase can be further unraveled for an efficient use of these enzymes in biofuel cells. In this context, also the sensitivity of RR spectroscopy for the hydroxyl ligand at the proximal cluster will allow further studies of its role in other oxygen-tolerant and oxygen-sensitive hydrogenases in solution or the crystalline form. Another focus could lie on angle-dependent RR spectroscopic investigations of single crystals of specific variants of the  $\text{MBH}_{\text{sol}}$ , as well as other related metallo-enzymes, such as the CO dehydrogenase. Here, the successfully established integrated approach of crystallographic data in combination with experimental and calculated Raman spectra could be applied. Notably, preliminary experiments showed that it is possible to investigate the same single ( $\text{MBH}_{\text{sol}}$ ) crystals with x-ray crystallography and RR spectroscopy.

With regard to the presented results, angle-dependent RR studies on single crystals of complex (biological) systems can be used to disentangle their RR spectra, due to differing electronic transition dipole moments of the cofactors.

# Appendix



# A. Protein Purification, Crystallization and Preparation

All heterodimeric MBH samples, as well as the genetically engineered variants C120G/C19G, P242C, H229A, H229M and H229Q used in this work were purified by J. Fritsch and S. Frielingsdorf as described in Reference [43, 79] and [47].

The purified MBH samples in solution were buffered in 50 mM KPO<sub>4</sub> buffer at pH 5.5 including 150 mM NaCl and concentrated to at least 0.7 mM for the RR experiments. For the acquisition of IR spectra protein concentrations were 0.4 mM.

For hydrogen-reduction of the solubilized MBH samples, the as-isolated enzyme, which was purified under aerobic conditions, was incubated anaerobically in an atmosphere of 5 % or 100 % H<sub>2</sub> for twenty minutes. These samples were reoxidized under a stream of water vapor saturated air for another twenty minutes at ambient temperatures.

Crystallization of the heterodimeric MBH was achieved by J. Fritsch, S. Frielingsdorf, A. Schmidt, J. Kalms and P. Scheerer. The mother liquor consists of the protein buffer at pH 5.5 with 40 mM KPO<sub>4</sub>, 150 mM NaCl and 10 % glycerin, as well as 25 % PEG 3350 and 0.1 mM BisTris. Crystals in the as-isolated state and genetically engineered variants, were grown from aerobically purified protein under air for two to three days as described in Reference [47]. Partially reduced crystals were likewise grown from aerobically purified protein. Afterwards the crystals were soaked for two to four hours in artificial mother liquor with dissolved sodium ascorbate of a final concentration of 50 mM.[47] MBH crystals in the reduced state were grown from aerobically purified protein under an anaerobic atmosphere with 5 % hydrogen and 95 % nitrogen for three days.[44]

### **Isotopic Labeling**

$^{13}\text{C}$ - and  $^{15}\text{N}$ -labeled MBH in solution was purified from cells cultivated in a media either containing  $^{13}\text{C}$ -labeled glycerol or  $^{15}\text{N}$ -labeled  $^{15}\text{NH}_4\text{Cl}$ , respectively.[43, 103]

For deuterium labeling, aerobically grown MBH crystals were soaked for three to four hours in artificial mother liquor, that was lyophilized and rehydrated using  $\text{D}_2\text{O}$  before soaking.[47]

### **Anaerobic Reoxidation with $\text{H}_2^{18}\text{O}$**

Crystals were grown anaerobically for two to three days in an atmosphere of 5% hydrogen and 95% nitrogen, from aerobically purified protein in a buffer containing  $\text{H}_2^{18}\text{O}$  instead of  $\text{H}_2^{16}\text{O}$ . Afterwards ferricyanide dissolved in  $\text{H}_2^{18}\text{O}$  was added to a final concentration of 5 mM to oxidize the crystals. To prevent a repeated reduction with hydrogen, the crystals are transferred to a gas tight vessel and the remaining hydrogen is removed under a stream of moistened nitrogen. Under these conditions the enzyme reoxidizes anaerobically. Finally the crystals were aerobically transferred within minutes from the mother liquor to quartz plate and frozen to liquid nitrogen temperatures.

A control experiment was done in the same way with unlabeled water.

### **Reoxidation with $^{18}\text{O}_2$**

Crystals were grown anaerobically for two to three days in an atmosphere of 5% hydrogen and 95% nitrogen from aerobically purified protein. The subsequent reoxidation was realized with a gas mixture of 20 %  $^{18}\text{O}_2$  and 80 % nitrogen.

### **Ferricyanide Treatment**

Crystals were either grown aerobically from purified protein in a mother liquor with dissolved ferricyanide of a final concentration of 1 mM or aerobically grown crystals were soaked for three and a half hours in an artificial mother liquor with dissolved ferricyanide of a final concentration of 5 or 10 mM.

## B. Appendix to Chapter 4

### Differential Equations to Describe the Reoxidation Process

In Figure B.1 the definition of the rate constants  $k_i$  for the first order reactions between the different active site species is declared. Based on this figure the rate Equations B.1 to B.8 are derived. The notation is simplified by omitting the Ni, Ni<sub>a</sub>-S and Ni<sub>r</sub>-S are denoted as  $S_a$  and  $S_r$ , respectively.

Between the fully reduced redox states Ni<sub>a</sub>-SR'', Ni<sub>a</sub>-SR' and Ni<sub>a</sub>-SR a fast equilibrium is considered. Furthermore, backreactions are not considered, since the redox potential is constantly increasing to more positive values in the reoxidation process. The only backreaction that is included, is the one with  $k'_3$  and  $k'_4$  between the Ni<sub>a</sub>-S and Ni<sub>r</sub>-S, since both states have the same redox potential.

$$\frac{dSR''(t)}{dt} = -k''_1 \cdot SR''(t) \quad (\text{B.1})$$

$$\frac{dSR'(t)}{dt} = -k'_1 \cdot SR'(t) \quad (\text{B.2})$$

$$\frac{dSR(t)}{dt} = -k_1 \cdot SR(t) \quad (\text{B.3})$$

$$\begin{aligned} \frac{dC(t)}{dt} = & +k''_1 \cdot SR''(t) & +k'_1 \cdot SR'(t) & +k_1 \cdot SR(t) \\ & -k_2 \cdot C(t) & -k'_2 \cdot C(t) \end{aligned} \quad (\text{B.4})$$

$$\frac{dS_i(t)}{dt} = +k'_2 \cdot C(t) \quad (\text{B.5})$$

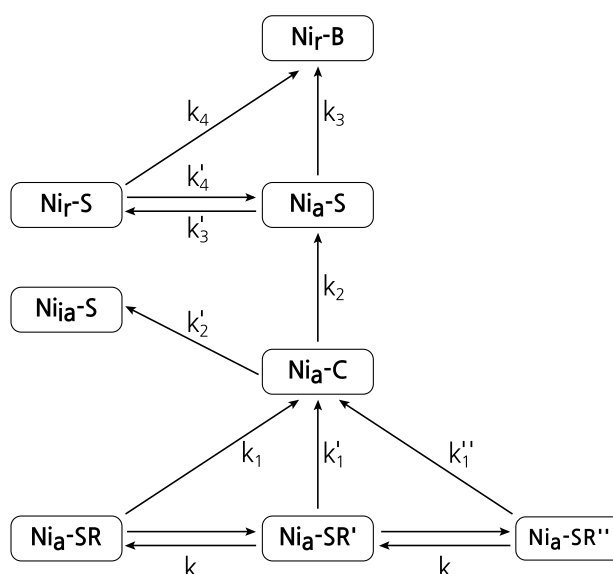
$$\begin{aligned} \frac{dS_a(t)}{dt} = & +k_2 \cdot C(t) & +k'_4 \cdot S_r(t) \\ & -k_3 \cdot S_a(t) & -k'_3 \cdot S_a(t) \end{aligned} \quad (\text{B.6})$$

$$\begin{aligned} \frac{dS_r(t)}{dt} = & +k'_3 \cdot S_a(t) \\ & -k_4 \cdot S_r(t) & -k'_4 \cdot S_r(t) \end{aligned} \quad (\text{B.7})$$

$$\frac{dB(t)}{dt} = +k_3 \cdot S_a(t) + k_4 \cdot S_r(t) \quad (\text{B.8})$$

These equations can be further simplified to describe the reoxidation process of the MBH<sub>mem</sub>.

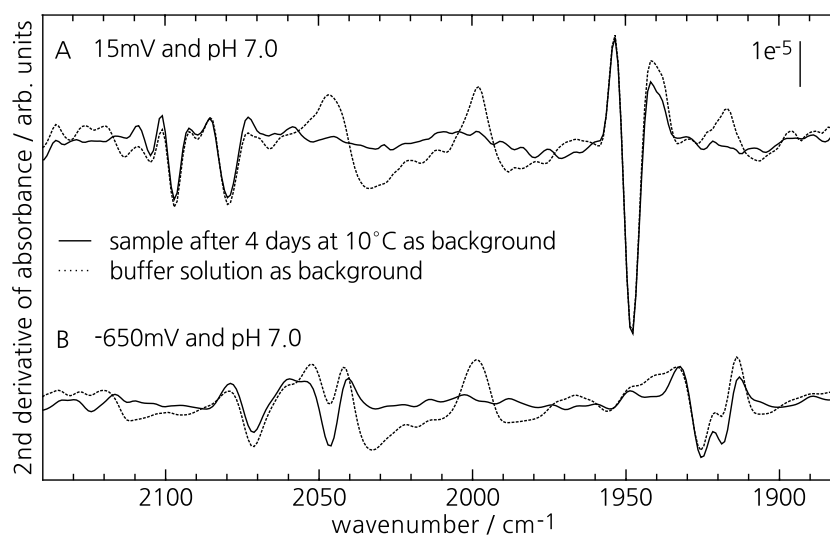
**Figure B.1.:** Definition of rate constants  $k_i$  for the reactions between the different active site species during the reoxidation process.



First, the  $\text{Ni}_a\text{-SR}$  species is hardly populated and contributions with  $k_1$  can be omitted. Secondly, no irreversibly inactive species  $\text{Ni}_{ia}\text{-S}$  is formed in the reoxidation process. Thus all terms with  $k_2'$  are neglected. And third, we cannot distinguish between the  $\text{Ni}_a\text{-S}$  and  $\text{Ni}_r\text{-S}$  redox state in the IR spectrum under the present conditions. Therefore, we refer to the detected state as  $\text{Ni}_{a/r}\text{-S}$  ( $S_{a/r}$ ) and neglect all terms with  $k_3'$ ,  $k_4'$  and  $k_4$ . The simplified Equations 4.1 to 4.5 are given in the main part of Chapter 4.

### Supplemental Data for the IR-SEC Experiments

**Figure B.2.:** Second derivative spectra of the MBH at 15 mV (A) and -650 mV (B). The dotted traces correspond to spectra where the spectrum of the buffer solution was used as a background. Continuous traces display the second derivative spectra where the spectrum of the very same sample after four days at 15 °C in the measurement cell was used as a background. This background spectrum lacks the CO and CN stretching vibrations but contains contributions of the mediator solution and other heterogeneities of the sample.



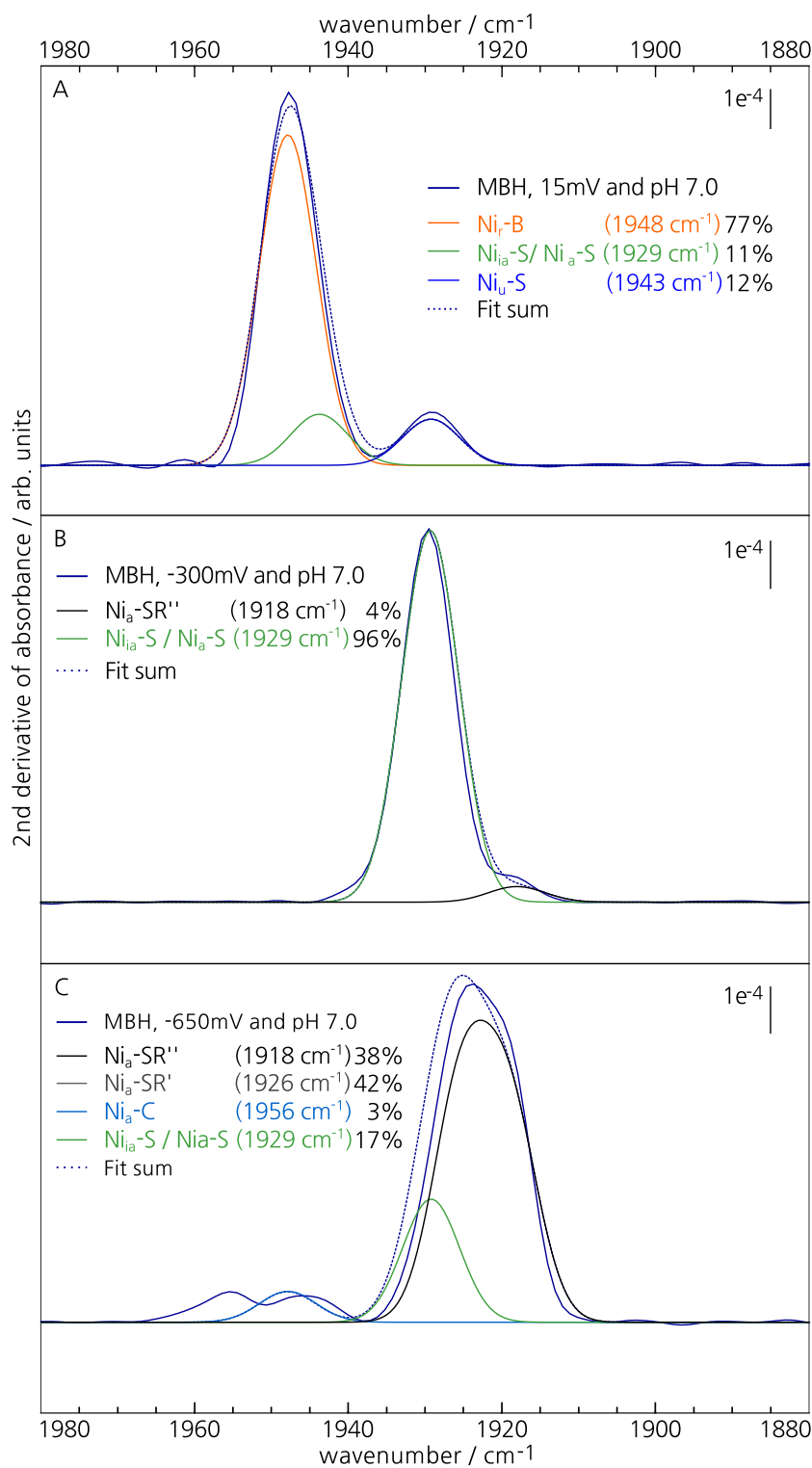
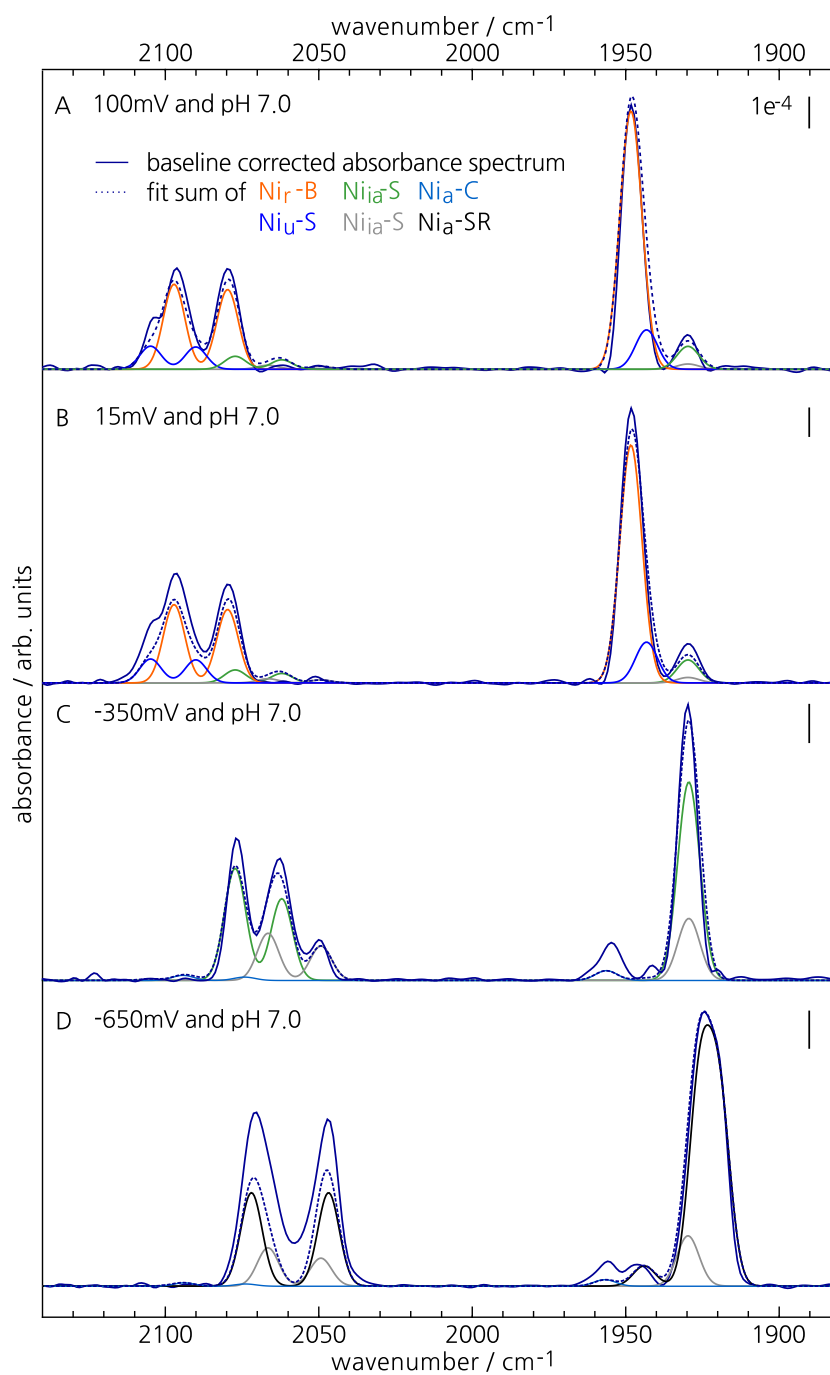


**Figure B.3.:** FTIR absorbance spectra after manual baseline correction in the spectral region of the CO stretching vibrations for the purified heterodimeric MBH at 15, -300 and -650 mV. A superposition of Gaussian functions was calculated with fit parameters obtained from the corresponding second derivative absorbance spectra shown in Figure 4.6. The relative band area is given in percent for each fitted redox species. Clearly the fitted bands match these spectra very well. Thus, the manual baseline correction of a large number of FTIR spectra is obsolete.

**Figure B.4.** FTIR absorbance spectra after manual baseline correction in the spectral region of the CO and CN stretching vibrations for the MBH at 100, 15, -350 and -650 mV. A superposition of Gaussian functions was calculated with fit parameters obtained from the corresponding second derivative absorbance spectra summarized in Table 4.4 and shown in Figure 4.6. Clearly the fitted bands match these spectra very well and a manual baseline correction of a large number of FTIR spectra can be avoided.



	$\nu_i$ cm <sup>-1</sup>	$z$	$V_m$ mV	$A_{max}^i$	$C$
Figure 4.7	1918	1	-529	0.42	0
	1926	1	-541	0.48	0
	1957 ↑	1	-550	0.17	0
	1957 ↓	1	-378	0.17	0
	1929 ↑	1	-520	0.88	0.05
	1929 ↓	1	-80	0.90	0.05
	1948	0.5	-120	0.91	0
	1948	0.5	-88	0.67	0
Figure 4.8	1918	1	-505	0.33	0.05
	1926	1	-523	0.41	0.03
	1929 ↑	1(2)	-503	0.80	0.17
	1929 ↓	1	-80	0.80	0.17
	1948	0.5	-22	0.90	0

**Table B.1.:** Fitted midpoint potentials  $V_m$  for the potential dependent infrared data shown in Figure 4.7 and 4.8. Equation 4.7 was fitted to the data points for each redox species. The midpoint potentials refer to a Ag/AgCl electrode. Low and high potential side of the Ni<sub>a</sub>-C and Ni<sub>a</sub>-S redox species are marked with ↑ and ↓, respectively. Due to the limited number of available data points, the number of transferred electrons was kept fixed at 0.5, 1.0 or 2.0.



## C. Appendix to Chapter 5

### Long Term LED Illumination Effects in FTIR Spectra

In Figure C.1 the FTIR spectra of the reduced MBH illuminated at 80 K are shown. The top spectra in panel A and B display the spectra of the MBH reduced with 5% and 100% hydrogen in the dark, respectively. The light-minus-dark difference spectra at the bottom of the figure obtained at the beginning and after ca. 30 minutes of the illumination with LEDs reveal the following:

The fraction of the CO stretching band of the Ni<sub>a</sub>-L species increases by about the same amount as the respective CO stretching mode of the Ni<sub>a</sub>-C species decreases.

Notably, a second CO band at 1932.6 cm<sup>-1</sup> shows an increasing intensity with illumination time. But a corresponding negative band, which would denote a further light sensitive redox state conversion is not observed.

### 413 nm Excitation

The RR spectra obtained at 413 nm turn out to be dominated by broad bands from the buffer between 400 and 550 cm<sup>-1</sup>, as illustrated in Figure C.2. Therefore, 413 nm excitation is not considered for the reduced and oxidized samples of the MBH throughout this work. In view of the UV-vis spectrum shown in Figure 5.4 the shoulder around 400 nm may correspond to the absorption of the incident light by certain compounds of the buffer solution.

At excitation wavelengths of 458 nm or higher the Raman active bands from the buffer are much lower in intensity or are hardly detectable and thus do not interfere with the Raman spectrum of the MBH in the studied spectral range of interest between 300 to 700 cm<sup>-1</sup>.

**Figure C.1.:** Top traces: FTIR spectra measured at 80 K of the MBH reduced either with 100 % or 5 % hydrogen in the dark.

Bottom traces: Light-Minus-Dark FTIR difference at the beginning and after ca. 30 minutes of LED illumination. The portion of the Ni<sub>a</sub>-L CO stretching band intensity increases with illumination time, while the Ni<sub>a</sub>-C intensity decreases approximately by the same amount. Interestingly another band at 1932.6 cm<sup>-1</sup> increases with the time of illumination.

Note the different scale bars in A and B, and that the intensity of the absorbance spectrum shown in panel A is divided by a factor of 16.

The positions of the CO bands are at: Ni<sub>a</sub>-C = 1958.3 cm<sup>-1</sup>, Ni<sub>a</sub>-S = 1940.6 cm<sup>-1</sup>, Ni<sub>a</sub>-SR' = 1927.0 cm<sup>-1</sup>, Ni<sub>a</sub>-L = 1910.7 cm<sup>-1</sup>. Another light induced species is characterized by a CO stretching band at 1932.6 cm<sup>-1</sup> (red line).

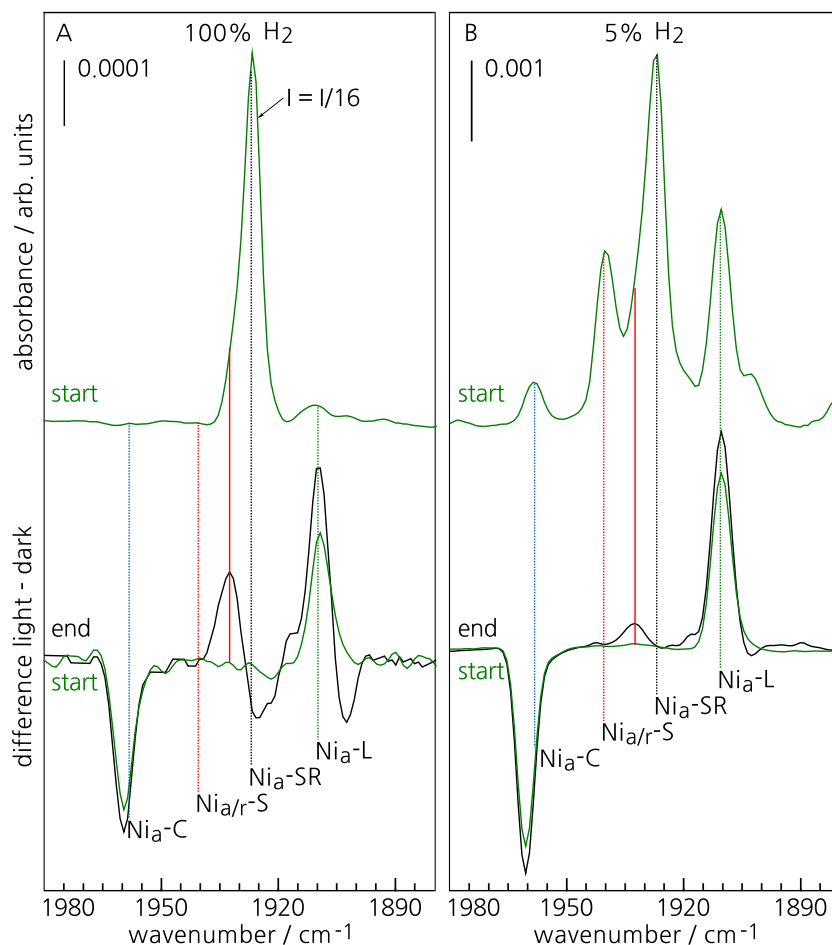
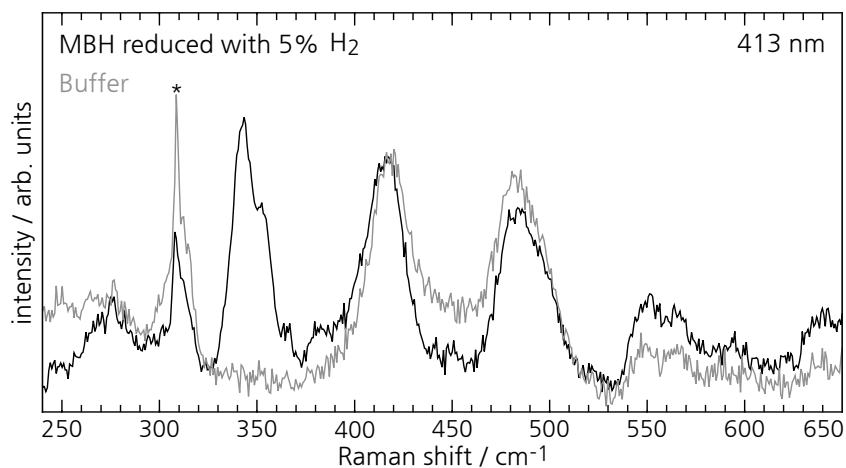


**Figure C.2.:** RR spectra of the H<sub>2</sub>-reduced MBH and its buffer solution at 80 K and an excitation wavelength of 413 nm. The spectrum of the MBH is dominated by broad vibrational bands from the buffer solution, apart from a weak signal around 350 cm<sup>-1</sup> derived from vibrations of the reduced FeS clusters. 413 nm is therefore not suited as an excitation wavelength for RR studies on the MBH from *Ralstonia eutropha*.



## H229M at Different Excitation Wavelengths

In Figure C.3 the RR spectra of the H<sub>2</sub>-reduced MBH wildtype and H229M variant recorded at wavelengths of 458, 514 and 568 nm are compared. The spectral region above 400 cm<sup>-1</sup> comprises the Raman active modes of Fe-CO / CN vibrations of the Ni<sub>a</sub>-L and Ni<sub>a</sub>-S redox species of the active site. Green and red vertical lines mark the band positions of these two components  $C_{\text{NiL}}$  and  $C_{\text{NiS}}$  in Figure C.3. The RR spectra of the MBH wildtype, C120G/C19G and H229M variant are almost identical, apart from minor differences between 250 and 400 cm<sup>-1</sup> derived from the alterations in the vicinity of the FeS clusters.

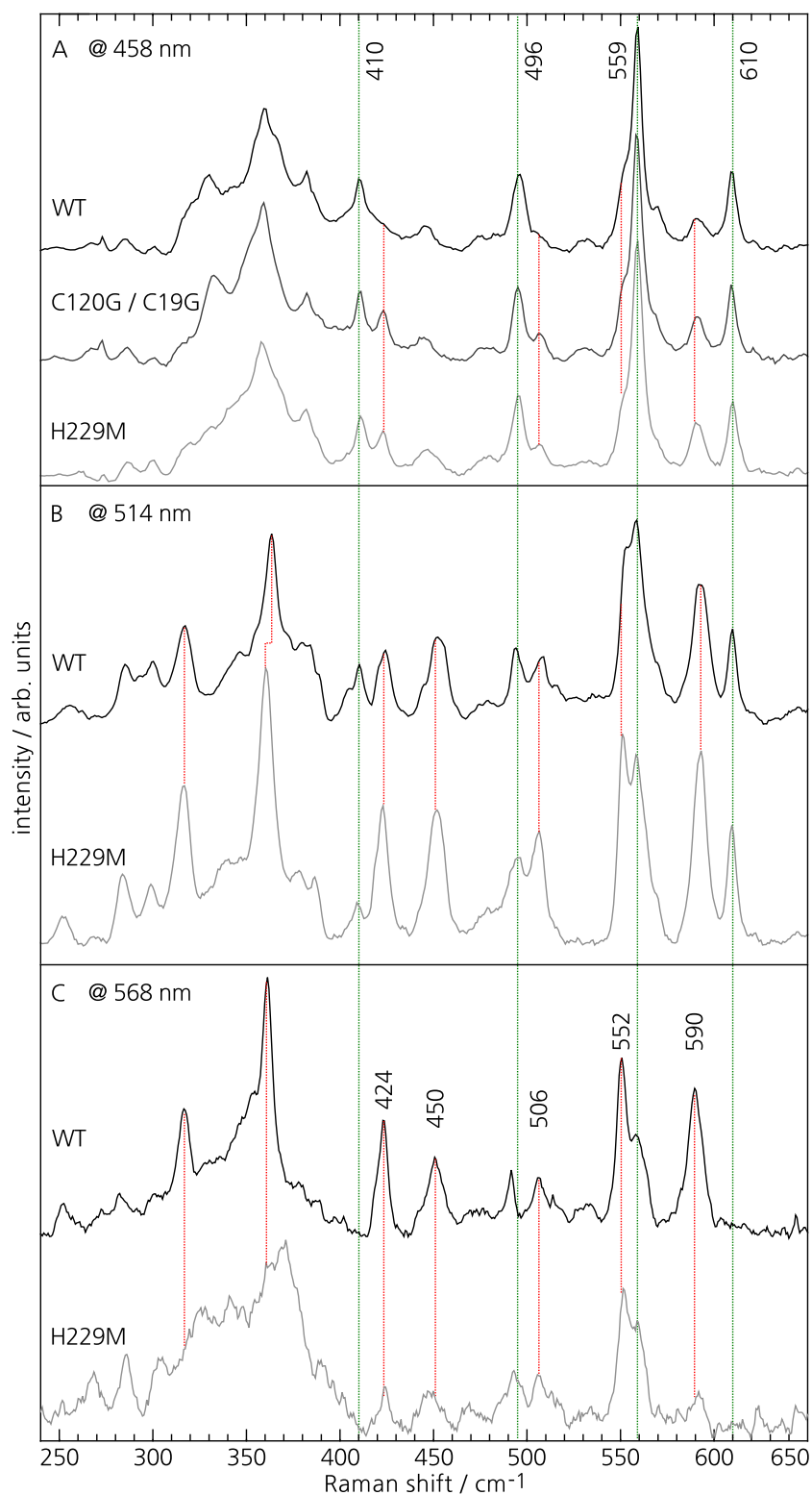
At wavelengths larger than 458 nm the broadened signal of the overlapping bands from the reduced FeS clusters disappears, but not those of the  $C_{\text{NiL}}$  and  $C_{\text{NiS}}$  compounds. Yet, the bands of the  $C_{\text{NiL}}$  compound decrease with increasing excitation wavelength and cannot be detected in the RR spectrum measured at 568 nm. The bands associated with Fe-CO / CN vibrations of the Ni<sub>a</sub>-S species show a reciprocal behavior. With increasing intensities of the bands related to the Ni<sub>a</sub>-S redox species, two sharp bands at 317 and 361 cm<sup>-1</sup> emerge for the wildtype and the H229M variant sample. Both bands are absent in the RR spectrum of the H229M variant obtained at 568 nm.

## QM / MM calculations

Raman spectra were calculated by Y. Rippers for various oxidation, spin and coordination states of the [NiFe] active site. Additionally different protonation states of the terminal Cys597 were simulated. The influence of these parameters on the calculated Raman spectrum for the Ni<sub>a</sub>-L redox state is illustrated in Figure C.4. Only the spectrum of the Ni<sub>a</sub>-L species with a protonated cysteine and nickel in oxidation state 1+ agrees remarkably well with the experimental spectrum. It is also worth noticing that an increasing oxidation state of the nickel is followed by a distinct blue shift of all calculated modes.

As described in the QM / MM part of Chapter 5, the calculated Raman intensities of the individual modes are approximated according to the contribution of the Fe-CO coordinates to the potential energy distribution. The respective normal coordinate contributions of the Fe-CO bending and stretching modes are illustrated in Figure C.4 as blue and red bars. For the Ni<sub>a</sub>-L redox species

**Figure C.3.:** Comparison of RR spectra from hydrogen reduced MBH wildtype as well as the C120G/C19G and H229M variants of the MBH at 458, 514 and 568 nm in panel A, B and C, respectively. Black vertical lines mark the band positions of the Ni<sub>a</sub>-L and red lines those of the Ni<sub>a</sub>-S redox state of the active site. (See also Chapter 6) Apart from minor differences, the signal of the reduced FeS clusters between 250 and 400 cm<sup>-1</sup> is very similar for the three samples at 458 nm. At higher excitation wavelengths the overlapping signals of the reduced FeS clusters decrease - as they no longer experience a resonant enhancement. With increasing laser wavelengths a set of new bands emerges in the spectra, at the expense of decreasing intensities for the Ni<sub>a</sub>-L vibrational bands. The nature of these marked in red bands is uncovered in Chapter 6.



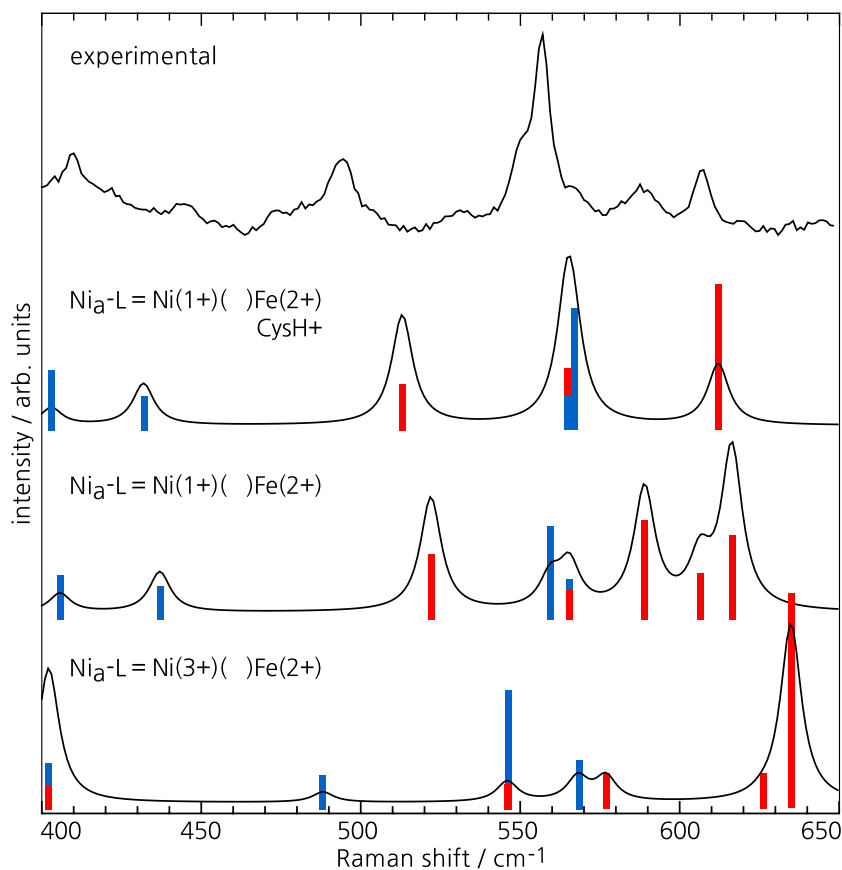


**Figure C.4.:** Theoretical Raman spectra derived by Yvonne Rippers with QM/MM calculations of the [NiFe] active site in various redox configurations. PED contributions from Fe-CO bending and stretching coordinates for different Ni<sub>a</sub>-L configurations are given by blue and red columns, respectively. Figure reproduced from Reference [103].

mode / cm <sup>-1</sup>	403.0	431.9	513.2	565.2	567.2	612.5
$\nu(\text{FeCO})$			10.9	14.8		34.3
$\delta(\text{FeCO})$	15.4	7.7		10.3	30.4	
$\nu(\text{FeCN})_{arg}$		12.7		5.1		
$\delta(\text{FeCN})_{arg}$	16.1	28.3		5.8		
$\nu(\text{FeCN})_{thr}$		6.1		7.8		
$\delta(\text{FeCN})_{thr}$	13.6	5.7	25.1	8.6		

**Table C.1.:** Reproduced from [103]: Normal coordinate contributions (larger 5%) to the PED of calculated normal modes for Ni<sub>a</sub>-L.  $\delta$  = bending and  $\nu$  = stretching modes, both are illustrated as blue and red bars in Figure C.4. (FeCN)<sub>arg</sub> and (FeCN)<sub>thr</sub> distinguish between the two different CN ligands of the Fe.

with a protonated cysteine, Table C.1 additionally summarizes the normal coordinate contributions of Fe-CN and Fe-CO modes.



# D. Appendix to Chapter 6

## Data Treatment and Statistical Analysis

The energy-axis of all spectra was carefully calibrated to an internal reference band at  $274.0\text{ cm}^{-1}$ . Afterwards a linear baseline was subtracted and all spectra were normalized to the area between  $325$  and  $375\text{ cm}^{-1}$ . At the band positions of 19 bands between  $380$  and  $640\text{ cm}^{-1}$  and the phenylalanine band at  $1005.0\text{ cm}^{-1}$  the integral in the limits of  $\pm 1\text{ cm}^{-1}$  at each selected position was calculated numerically with GNU Octave. Figure D.1 shows an example for two spectra.

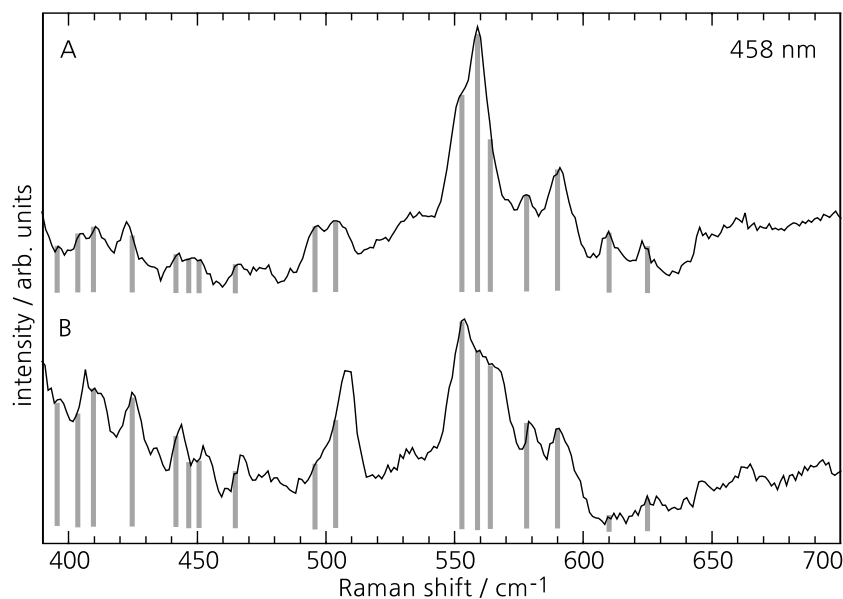
The cross-correlation between all two pairs of the selected band positions (variables) of the resulting  $65 \times 20$  matrix is described by their Spearman's rank correlation coefficients  $\rho_S$  in a  $20 \times 20$  matrix. We chose to determine Spearman's rank correlation coefficient  $\rho_S$  in contrast to the widely used Pearson's rank correlation coefficient.[202] The advantage of the  $\rho_S$  coefficient is that it is a parameter free measure of how well the the statistical relation between two variables (band positions) can be described by a monotone function. This function does not have to be linear. Furthermore, the numerical integral as a function of band position does not have to be normal-distributed.

If the function that describes the intensity relation between two variables (band positions) is strictly monotonically in- or decreasing the  $\rho_S$  is ideally  $\pm 1$  and the two variables are (anti-) correlated. Two variables show no correlation if their  $\rho_S$  is near zero.

Along with the Spearman coefficient  $\rho_S$  the so called p-value was calculated. This quantity describes the probability that the determined  $\rho_S$  is observed strictly by chance. That is, a p-value of less than 0.05 indicates that the probability for an observed strong correlation in  $\rho_S$  is observed to only 5% by chance. If the p-value is larger than that, it cannot be concluded from the data that the calculated correlation is real.

In Figure D.2 the p-values for the calculated Spearman coefficients shown in Figure 6.3 are displayed. In the statistical analysis, only

**Figure D.1.:** Two examples for numerical integration at selected band positions in the limits of  $\pm 1 \text{ cm}^{-1}$ .



$\rho_S$  were considered which are accompanied with p-values of less than 0.05. Clearly, all  $\rho_S$  coefficients of more than 0.35 are accompanied by p-values of less than 0.05. Gray and white colored areas in Figure D.2, that correspond to non-correlated variables, are mostly accompanied by p-values of more than 0.05. Therefore the interpretation of the  $\rho_S$  coefficients is limited to values between +1 and 0.

To interpret the  $\rho_S$  coefficients between +1 and 0 we have to consider a few possible errors and limitations of this data analysis method. At first the manual baseline correction may cause artificial intensity deviations at certain bands. Secondly, particular spectral ranges are characterized by strongly overlapping vibrational modes. Thus, the simple calculation of the numerical integral of  $\pm 1 \text{ cm}^{-1}$  at the selected band positions can only be a crude approximation of the actual area of this Lorentzian shaped band and the large cross-correlation coefficients between overlapping bands are an artifact of this analysis method. At last, the signal-to-noise ratio varies for each individual spectrum. Thus, a conservative interpretation would be that variables with a  $\rho_S$  of up to 0.5 are still fairly correlated. Variables with  $\rho_S$  coefficients of less than 0.35 will be considered as not correlated at all. Everything in between 0.5 and 0.35 is left open for discussion.

### Component Fits

Starting point of the fitting routine was the spectrum where component CFes was maximal and had no major superpositions from

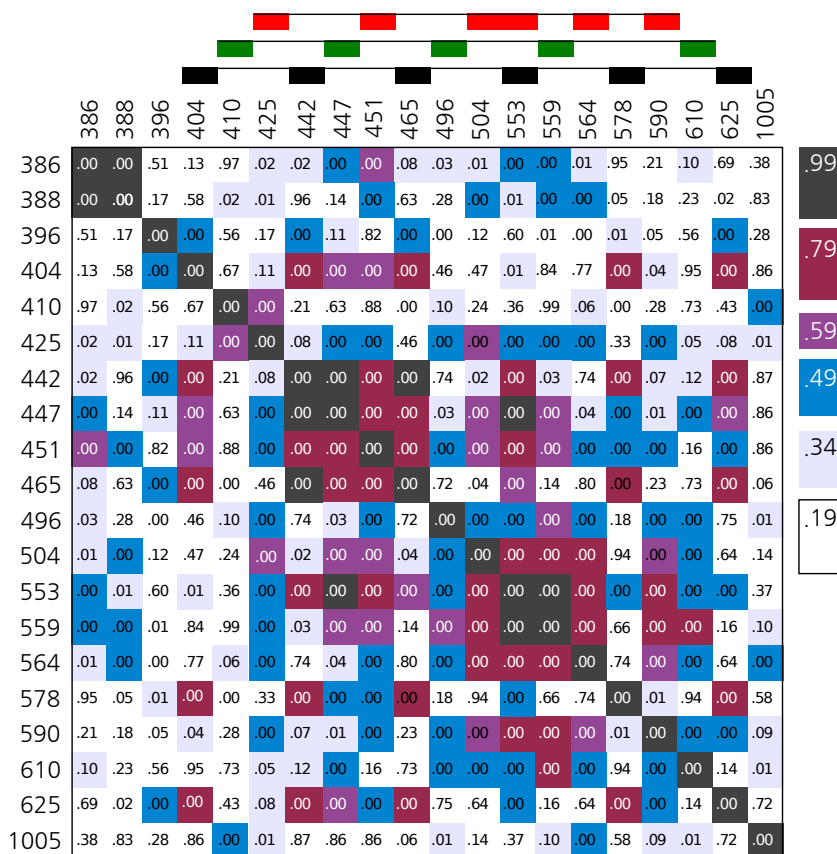


**Figure D.2.:** Calculated p-value for Spearman's rank correlation coefficient  $\rho_S$  shown in Figure 6.3. For comparison the color code for  $\rho_S$  was kept here and only such  $\rho_S$  were considered in the statistical analysis, which are accompanied by p-values of equal or less than 0.05.

other species (Figure 6.4A). Lorentzian bands with line-widths of up to  $10 \text{ cm}^{-1}$  were fitted at the band positions of the  $C_{\text{FeS}}$  species extracted from the statistical analysis. A clear band at  $554 \text{ cm}^{-1}$  had to be included as well as bands of lower intensities at the positions of the  $C_{\text{NiX}} = C_{\text{NiS}}$  component.

Lorentzian bands at the 496, 559 and  $610 \text{ cm}^{-1}$  were fitted to the spectrum with maximal intensities at the vibrational modes of species  $C_{\text{NiL}}$  (Figure 6.4B). Due to a superposition with the  $C_{\text{NiX}} = C_{\text{NiS}}$  species these modes were included as well. Also an extra band at  $569 \text{ cm}^{-1}$  was added to complete the fit. Subsequently, Lorentzian bands at the positions of the  $C_{\text{NiX}} = C_{\text{NiS}}$  species were fitted to a spectrum with maximal amounts of this species (Figure 6.4C).

The individual band parameters for all three spectra are summarized in Table D.1. For the sake of clarity, all bands are ordered in groups according to the proposed components. The entire fitting was done with the software Fityk.[169]

To cross-check the assignments of the statistical analysis the fitted band areas obtained from the three spectra were normalized to the area of a marker band of each proposed component. The last three columns of the table show, for each spectrum of Figure 6.4A-C, the values of all fitted band areas normalized to the area of a

marker band of each proposed component. That is the band at  $559\text{ cm}^{-1}$  for the  $C_{\text{NiL}}$ ,  $578\text{ cm}^{-1}$  for the  $C_{\text{FeS}}$  and  $590\text{ cm}^{-1}$  for the  $C_{\text{NiS}}$  component. If the intensity ratio for a group of bands with respect to one of the marker bands is comparable for all three selected spectra A-C, then this group must result from modes of one specific cofactor. As an example we may compare the normalized band areas of the  $C_{\text{FeS}}$  and  $C_{\text{NiS}}$  component in block A and C of Table D.1. In both blocks bands of the  $C_{\text{FeS}}$  component have comparable values when normalized to the marker band at  $578\text{ cm}^{-1}$  but differ by an order of magnitude when normalized to  $590\text{ cm}^{-1}$ . The situation is reversed when we turn to the last column of Table D.1, where only the group of bands proposed to belong to  $C_{\text{NiS}}$  have comparable ratios.

Regardless of the strong superpositions of a number of modes in certain spectral regions the approximate relative intensity ratios for each component  $C_{\text{FeS}}$ ,  $C_{\text{NiL}}$  and  $C_{\text{NiS}}$  are reproduced satisfactory in each fitted spectrum. This is yet another way to confirm the composition of the three components  $C_{\text{FeS}}$ ,  $C_{\text{NiS}}$  and  $C_{\text{NiL}}$ .

Component analyses as shown in Figure D.3 and 6.5 as well as the difference spectra depicted in Figure 6.6 were obtained with the home-written software Specmate.[170]

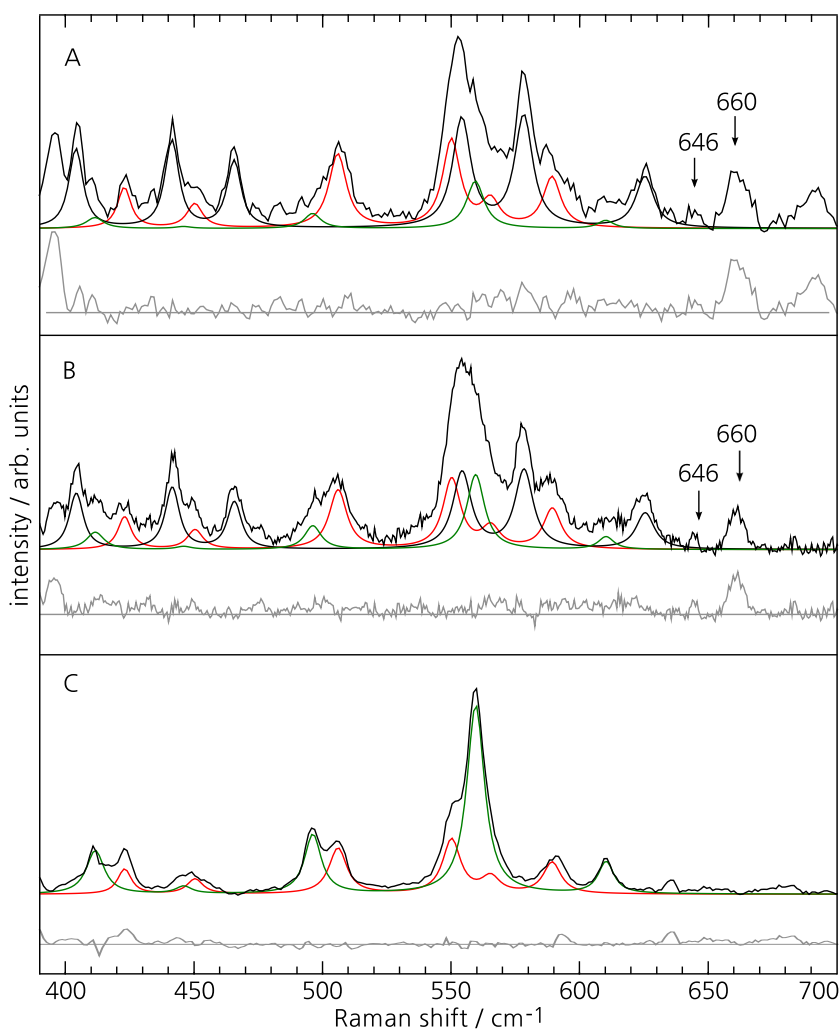


**Figure D.3.:** Selection of RR spectra of single MBH crystals, measured with 458 nm excitation. The spectra include the individual component spectra of  $C_{FeS}$  (black),  $C_{NiL}$  (green) and  $C_{NiX} = C_{NiS}$  (red). The residuals (gray) display unassigned bands at 649 and  $660\text{ cm}^{-1}$ . All three spectra exhibit a superposition of the reduced and oxidized component of the  $[NiFe]$  active site.

The spectra in Trace A and B were obtained from an incompletely re-oxidized sample and an as-isolated sample oxidized with additional ferricyanide. Trace C shows a spectrum of an incompletely reduced sample.

**Table D.1.:** For each spectrum of Figure 6.4A-C the values for the band position ( $\pm 0.5 \text{ cm}^{-1}$ ), FWHM ( $\pm 1.0 \text{ cm}^{-1}$ ) and area ( $\pm 10 \%$ ) of every Lorentzian shaped band is copied in the respective first four columns. The latter three columns present the values of the normalized fitted band areas, whereby the area of a marker band for each proposed component is used as the scaling factor. That is, the band at  $559 \text{ cm}^{-1}$  for the *CNiL*,  $578 \text{ cm}^{-1}$  for the *CFeS* and  $590 \text{ cm}^{-1}$  for the *CNiS* component. These are highlighted in bold.

		position	FW HM	area	realtive area with respect to		
					$559 \text{ cm}^{-1}$	$578 \text{ cm}^{-1}$	$590 \text{ cm}^{-1}$
spectrum Fig.6.4A	<i>CFeS</i>	404.2	6	0.065		0.58	3.59
		441.9	6	0.058		0.52	3.21
		465.8	6	0.043		0.39	2.40
		554.2	8	0.098		0.88	5.42
		<b>578.3</b>	8	0.111		<b>1.00</b>	6.18
		625.4	8	0.047		0.42	2.59
	<i>CNiS</i>	425.0	6	0.010		0.09	0.56
		450.4	7	0.015		0.13	0.83
		506.0	8	0.017		0.15	0.94
		550.0	8	0.033		0.30	1.83
		565.8	8	0.010		0.09	0.53
		<b>590.0</b>	10	0.018		0.16	<b>1.00</b>
spectrum Fig.6.4B	<i>CNiL</i>	411.6	8	0.142	0.25		4.29
		446.0	7	0.042	0.08		1.28
		496.1	7	0.174	0.31		5.28
		<b>559.5</b>	8	0.561	<b>1.00</b>		16.98
		610.2	7	0.140	0.25		4.23
	<i>CNiS</i>	424.0	6	0.048	0.09		1.45
		450.8	7	0.043	0.08		1.32
		506.0	8	0.039	0.07		1.18
		550.2	8	0.050	0.09		1.52
		565.8	8	0.018	0.03		0.55
		<b>590.5</b>	8	0.033	0.06		<b>1.00</b>
spectrum Fig.6.4C	<i>CNiL</i>	411.6	8	0.019	0.21	0.72	0.37
		496.3	8	0.025	0.28	0.95	0.50
		<b>559.3</b>	8	0.087	<b>1.00</b>	3.35	1.74
		610.2	7	0.006	0.06	0.22	0.11
	<i>CFeS</i>	404.2	6	0.013	0.15	0.52	0.27
		441.7	6	0.018	0.21	0.69	0.36
		465.6	6	0.014	0.16	0.54	0.28
		554.2	8	0.028	0.32	1.08	0.56
		<b>578.3</b>	8	0.026	0.30	<b>1.00</b>	0.52
		625.4	8	0.013	0.15	0.50	0.26
	<i>CNiS</i>	423.0	6	0.031	0.35	1.17	0.61
		450.4	7	0.021	0.24	0.81	0.42
		506.0	8	0.074	0.84	2.83	1.47
		550.2	8	0.087	0.99	3.33	1.73
		565.4	8	0.026	0.30	1.00	0.52
		<b>589.3</b>	8	0.050	0.57	1.92	<b>1.00</b>

### QM Models and Extracted PED values from QM / MM calculations

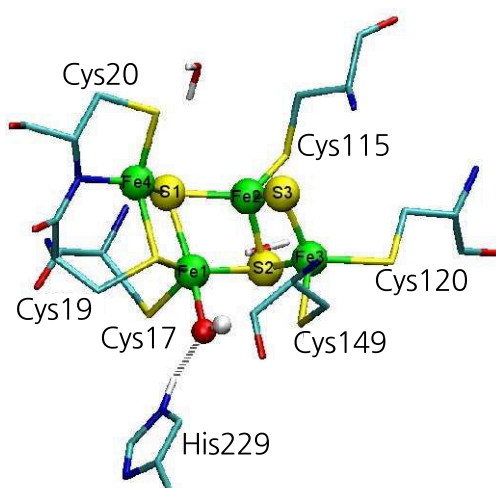
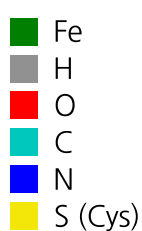


**Figure D.4.:** Stereo view of the QM/MM model for the [4Fe3S] cluster of the MBH, where Fe1 is bound to a  $\text{OH}^-$  group. Hydrogens are excluded for the sake of simplicity, except for the proton on the histidine residue and the hydroxyl group.

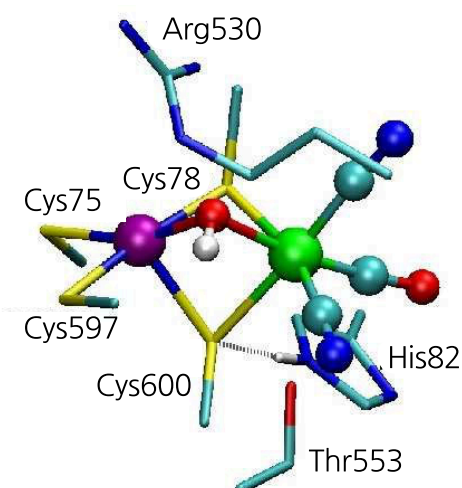


**Figure D.5.:** Stereo view of the QM/MM model for the MBH [NiFe] active site in the  $\text{Ni}_r\text{-B}$  redox state with a bridging  $\text{OH}^-$  ligand. Hydrogens are excluded for the sake of simplicity, except for the proton on the histidine residue and the bridging hydroxyl group.

**Table D.2.:** Calculated frequencies and extracted PED values for the QM/MM calculations of the proximal cluster with a hydroxyl group bound at Fe1 compared to the experimentally determined band positions of the CFeS component. CS(19) refers to the C-S stretching coordinate in Cysteine 19. The relative intensities  $I_{rel}$  refer to the most intense mode in this region.

Stretching and torsional coordinates are marked with a  $\nu$  and  $\tau$ , respectively.

Calculations						Experiment		
$\nu$	$I_{rel}$	PED %	mode	$\Delta^{18}O$	$\Delta D$	$\nu$	$\Delta^{18}O$	$\Delta D$
447	10	29	$\tau$ FeOH	-1	0	442	0	0
461	60	14	$\tau$ FeOH	-1	0	452	0	0
469	64	23	$\tau$ FeOH	-1	0	465	0	0
491	60	31	$\tau$ FeOH	-3	0	498	0	0
523	4	8	$\nu$ FeOH	-3	-1			
		21	$\nu$ FeOH					
543	16	16	$\nu$ FeN	-11	-9	554	-23	-8
		9	$\nu$ CS(19)					
557	96	62	$\nu$ FeOH	-20	-17	578	-7	-15
603	16	43	$\nu$ CS(19)	0	0	625	0	0
665	16	15	$\nu$ CS(19)	0	0	660	0	0

**Table D.3.:** Calculated frequencies and extracted PED values for the QM/MM calculations of the active site in the Ni<sub>a</sub>-L redox state to experimentally determined band positions of the CNiL component.

Stretching and bending coordinates are marked with a  $\nu$  and  $\delta$ , respectively.

Calculations					Exp. MBH	
$\nu$	$I_{rel}$	PED %	mode	$\Delta^{13}C$	$\nu$	$\Delta^{13}C$
		15	$\delta$ FeCO			
403	13	6	$\nu$ FeCN	-12	411	
		29	$\delta$ FeCN			
		8	$\delta$ FeCO			
432	31	13	$\nu$ FeCN	-11	424	
		29	$\delta$ FeCN			
442	13	20	$\nu$ FeCN	-13	447	-10
460	6	47	$\nu$ FeCN	-7	458	
468	25	24	$\nu$ FeCN	-5	458	
		24	$\nu$ FeCN			
478	25	7	$\delta$ FeOH	-7	481	
491	25	13	$\nu$ FeCN	-6	481	-13
		11	$\nu$ FeCO			
513	81	25	$\delta$ FeCO	-14	496	-11
		25	$\nu$ FeCO			
565	100	15	$\delta$ FeCN	-10	559	-14
		8	$\delta$ FeCO			
		31	$\delta$ FeCO			
567	25	8	$\nu$ FeCN	-15	569	-14
612	50	37	$\nu$ FeCO	-7	610	-10

$\nu$	Calculations			Exp. MBH
	$I_{rel}$	PED %	mode	$\nu$
423	5	6	$\nu$ FeCN	425
		26	$\delta$ FeCN	
		11	$\delta$ FeCO	
438	10	19	$\nu$ FeCN	440
		25	$\delta$ FeCN	
458	10	55	$\nu$ FeCN	450
		6	$\delta$ FeCN	
470	5	46	$\nu$ FeCN	474
		8	$\delta$ FeCN	
489	33	12	$\nu$ FeCN	490
		8	$\delta$ FeCO	
504	90	22	$\delta$ FeCN	504
		6	$\nu$ FeCO	
		6	$\nu$ FeCN	
		28	$\delta$ FeCO	
552	100	16	$\delta$ FeCN	552
		6	$\nu$ FeCO	
		12	$\nu$ FeS(Cys600)	
		6	$\nu$ FeCN	
572	12	6	$\nu$ FeCN	564
		9	$\delta$ FeCO	
587	90	12	$\nu$ FeCO	590
617	24	12	$\nu$ FeCO	615
626	19	37	$\nu$ FeCO	623

**Table D.4.:** Calculated frequencies and extracted PED values for the QM / MM calculations of the active site in the Ni<sub>a</sub>-S redox state to experimentally determined band positions of the CNiS component. Stretching and bending coordinates are marked with a  $\nu$  and  $\delta$ , respectively.



## E. Appendix to Chapter 7

### Setup for Polarization Sensitive RR spectroscopy

The setup for polarization-sensitive RR measurements is depicted in Figure 3.6. For angle-dependent RR spectroscopy the analyzer - half-wave plate couple in the detection pathway is removed.

Before polarization-dependent RR spectra can be acquired, the following polarization-sensitive optical components had to be calibrated.[217]

**Analyzer** Light of a specific polarization passes this optical filter and its intensity  $I$  is given by  $I = I_o \cos^2 \theta$ , where  $\theta$  is the angle between the electric field vector of the incident light, with an initial intensity of  $I_o$ , and the axis of the analyzer. Thus, the position of the analyzer (polarizer) axis in the rotation mount is identified by the maximal intensity of the laser beam passing through this filter.

**Half-wave plate** This optical device turns the electric field vector of the incident laser beam by a chosen angle, as light with a polarization parallel to the slow axis is retarded by half a wavelength or  $\pi$  with respect to light that is polarized perpendicular to that axis. The position of the slow axis of the half-wave plate in the rotation mount is obtained when the maximal intensity of the laser beam passes through the half-wave plate and an analyzer in a defined position. For this setup the slow axis of half wave plate lies at  $+5^\circ$  in the rotation mount.

**Quarter-wave plate** This optical device converts linearly polarized light into circularly polarized light, whenever the angle between the incident light and the slow axis is  $45^\circ$ . Light with a polarization parallel to the slow axis is retarded by a quarter of a wavelength or  $\pi/2$  with respect to light that is polarized perpendicular to that axis. For the detection pathway the optical axes of analyzer and the quarter-wave plate enclose a fixed angle of  $45^\circ$ , to ensure that light entering the

monochromator is always circularly polarized. With that, the polarization sensitivity of the grating is compensated to a certain extent. The polarization state of the light passing through this analyzer – quarter-wave plate couple was verified by constant light intensities, regardless of the position of second analyzer.

### **Polarization Sensitive Calibration of the Resonance Raman Setup**

In angle-dependent RR measurements the intensity of the measured spectrum typically has to be scaled according to the sensitivity of the monochromator grating, as it is a complex function of the polarization of the incident light.[217] The scaling factors for the measurement setup used in these experiments were determined with the unpolarized first order Raman peak at  $521\text{ cm}^{-1}$  of a Si[111] sample.[219] In addition, the determined scaling factors were cross checked with polarization sensitive measurements on Si[001] and  $\text{CCl}_4$ . Hereby, the Si[001] exhibits a polarized Raman peak at  $521\text{ cm}^{-1}$  and  $\text{CCl}_4$  a totally symmetric vibration at a frequency of  $463\text{ cm}^{-1}$  (polarized band) and two asymmetric vibrations with frequencies at  $220$  and  $318\text{ cm}^{-1}$  (unpolarized bands). The obtained scaling factors are found in Table E.1 and E.2. The accuracy of corrected intensity value is 5% with respect to deviating scaling factors for the  $0$  and  $180^\circ$  as well different XX measurement configurations. (Table E.1 and E.2) The scaling factors obtained for  $\text{CCl}_4$  yielded the same values within the error of 5%.

excitation $\lambda/2$	detection analyzer+ $\lambda/4$	measurement configuration	scaling factor
5°		0°	1.00
10°		10°	0.97
20°		30°	0.91
30°		50°	0.83
40°		70°	0.79
50°		90°	0.78
60°		110°	0.81
70°		130°	0.87
80°		150°	0.92
90°		170°	0.94
95°		180°	0.94
5°		0°	0.96
5°	95°	XX	1.00
5°	275°	XX	0.95
5°	5°	XY	0.50
5°	185°	XY	0.45
50°	5°	YY	0.77
50°	185°	YY	0.72
50°	95°	YX	0.68
50°	275°	YX	0.68

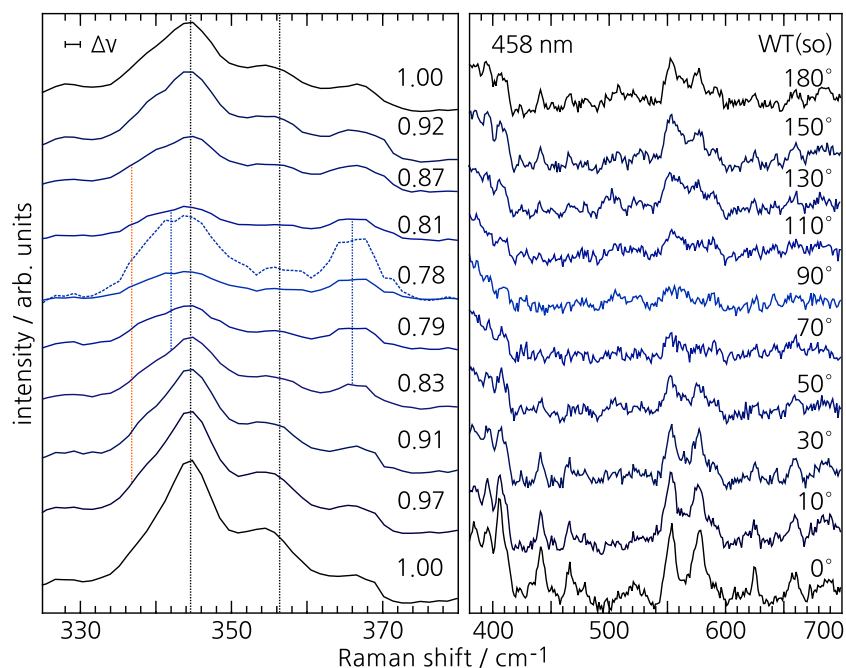
**Table E.1.:** Scaling factors for angle / polarization dependent RR spectroscopy obtained from a Si[111] surface. Here the band at  $521\text{ cm}^{-1}$  is unpolarized. In an ideal setup its intensity would be independent of the excitation angle. To account for the polarization sensitivity of the setup, the intensities of the measured spectra have to be divided by the given scaling factors.

In the first two columns the positions of the rotation mounts in the excitation and detection pathway of the setup are given.

excitation $\lambda/2$	detection analyzer+ $\lambda/4$	measurement configuration	scaling factor
5°	95°	XX	1.00
5°	275°	XX	0.96
5°	5°	XY	*
5°	185°	XY	*
50°	5°	YY	0.71
50°	185°	YY	0.65
50°	95°	YX	*
50°	275°	YX	*

**Table E.2.:** Scaling factors for polarization dependent RR spectroscopy obtained from a Si[100] surface. Here the band at  $521\text{ cm}^{-1}$  is polarized, therefore the band intensity drops to the noise level for the \* configurations. Nevertheless, the scaling factors of the XX and YY measurement configurations match with the values obtained for the Si[111] surface.

**Figure E.1.:** Angle dependent RR spectra of a single as-isolated MBH crystal scaled according to the detector sensitivity for different excitation angles. The scaling factors from Table E.1 are given for each spectrum in the left panel. For comparison the RR spectrum measured in the  $90^\circ$  configuration is also normalized to the area between  $330$  and  $375\text{ cm}^{-1}$ , as shown in Figure 7.4. This shows that the  $[3\text{Fe4S}]_m$  and  $[4\text{Fe4S}]_d$  clusters experience much less resonance enhancement than the  $[4\text{Fe3S}]_p+\text{OH}$ .



### Angle Dependent Effects on Vibrational Spectra

To demonstrate the angular dependent effects on the vibrational spectrum of the three FeS clusters the measured angle-dependent RR spectra shown in Figure 7.4 and 7.5 are normalized to the integral area of the most intense FeS stretching bands between  $330$  and  $375\text{ cm}^{-1}$ . Figure E.1 displays the effect when the spectra are scaled according to the polarization sensitivity of the grating in the spectrograph. Apparently, the resonance enhancement for the FeS cluster at perpendicular excitation drops significantly.

# Acknowledgement

Ich danke allen, die mich während meiner Promotion in unterschiedlicher Weise unterstützt haben.

- Prof. Dr. Peter Hildebrandt für die Betreuung während der Doktorarbeit, seine Gelassenheit und Unterstützung in jeglicher Hinsicht.
- Dr. Ingo Zebger – wo soll ich anfangen? Danke für die engagierte Unterstützung bei allen Widrigkeiten im Labor und der Interpretation der Daten. Für das Verständnis von Problemen außerhalb der Arbeit. Für das aufmerksame und kritische Korrekturlesen dieser Arbeit. Danke für die hervorragende Betreuung.
- Prof. Dr. Holger Dobbeck für die Übernahme der Zweitkorrektur dieser Arbeit.
- Yvonne Rippers für sämtliche QM/MM Berechnungen der MBH und die tolle Zusammenarbeit
- Dr. Johannes Fritsch, Dr. Stefan Frielingsdorf und Dr. Oliver Lenz für die Präparation und Bereitstellung unglaublicher Mengen an MBH Proben, die die Grundlage für diese Arbeit bildeten.
- Andrea Schimdt, Jacqueline Kalms und Dr. Patrick Scheerer für eine Vielzahl von MBH Kristallen für die RR Messungen
- Dr. Momme Winkelkemper für uneingeschränkte Unterstützung in guten und schlechten Zeiten. Das aufmerksame und kritische Korrekturlesen von Teilen dieser Arbeit, obwohl es gar nichts mehr mit Quantenpunkten zu tun hat. Und natürlich auch für das tolle Auswerte-Programm SpecMate.
- Marius Horch und Dr. Friedhelm Lenzian für ausgewählte IR und EPR Messungen an der MBH
- Dr. Uwe Kuhlmann für das Vertrauen beim Justieren von optischen Komponenten, sowie das Korrekturlesen von Teilen dieser Arbeit.
- Wiebke Meister, Sara Bruun, Yvonne Rippers, Johannes Salweski und Gal Schkolnik für die netten Kochabende
- Marina Böttcher, Barbara Gonzalez, Robert Götz, Sagie Katz, Jacek Kozuch, Jürgen Krauss, Khoa Ly, Maria Andrea Mroginski, Lars Paasche, Claudia Schulz, Michael Stolarski, Francisco Velazquez Escobar, Inez Weidinger und allen weit-

eren Mitgliedern des Max-Volmer Laboratoriums für die angenehme Arbeitsatmosphäre.

- Der Graduiertenschule BIG-NSE für die finanzielle Unterstützung.
- Die Juristen: Rike, Florian, Mara, Asha und Jessica für abwechslungsreiche Mittagspausen in der Mensa.
- meine Familie: Momme und Jannes sowie, Roland, Sabine, Nicole, Lutz, Leon und Luis für ihre uneingeschränkte Unterstützung in allen Lebenslagen.

# Bibliography

- [1] Dobson, C. (2004) *Seminars in Cell & Developmental Biology* **15(1)**, 3–16.
- [2] Wandrey, C., Lies, A., and Kihumbu, D. (2000) *Org. Proc. Res. Dev.* **4**, 286 – 290.
- [3] Schmid, A., Dordick, J., Hauer, B., Kiener, A., Wubbolts, M., and Witholt, B. (2001) *Nature* **409**, 258–268.
- [4] Zaks, A. (2001) *Curr. Op. Chem. Bio.* **5(2)**, 130–136.
- [5] Andreas Schmid, Frank Hollmann, J. B. P. and Bühler, B. (2002) *Curr. Op. Biotech.* **13(4)**, 359 – 366.
- [6] Crabtree, G. and Dresselhaus, M. (2008) *MRS Bulletin* **33(4)**, 421 – 428.
- [7] C. Koroneos, A. Dompros, G. R. and Moussiopoulos, N. (2004) *Int. J. Hydrogen Energy* **29**, 1443 – 1450.
- [8] Ross, D. K. (2006) *Vacuum* **80(10)**, 1084 – 1089.
- [9] Cammack, R., Frey, M., and Robson, R. (2011) *Hydrogen as a Fuel: Learning from Nature*, Taylor and Francis, London.
- [10] Frey, M. (2002) *Chem. Bio. Chem.* **2**, 153 – 160.
- [11] Vincent, K. A., Parkin, A., Lenz, O., Albracht, S. P. J., Fontecilla-Camps, J. C., Cammack, R., Friedrich, B., and Armstrong, F. A. (2005) *J. Am. Chem. Soc.* **127(51)**, 18179–18189.
- [12] Lubitz, W., Gastel, M., and Gaertner, W. volume **2**, of *Metal Ions in Life Sciences* chapter 7, pp. 279 – 322 John Wiley & Sons, Ltd (2007).
- [13] deLacey, A., Fernandez, V., Rousset, M., and Cammack, R. (2007) *Chem. Rev.* **107(10)**, 4304–4330.
- [14] Vincent, K., Parkin, A., and Armstrong, F. October 2007 *Chem. Rev.* **107(10)**, 4366–4413.
- [15] Siegbahn, P., Tye, J., and Hall, M. (2007) *Chem. Rev.* **107**, 4414 – 4435.
- [16] Burgdorf, T., Lenz, O., Buhrke, T., van derLinden, E., Jones, A., Albracht, S., and Friedrich, B. (2005) *J. Mol. Microbiol. Biotech.* **10(2-4)**, 181–196.

- [17] Guiral, M., Tron, P., Belle, V., Aubert, C. and Leger, C., Guigliarelli, B., and Giudici-Ortoniconi, M. T. (2006) *Int. J. Hydrogen Energy* **31**, 1424.
- [18] Parkin, A., Goldet, G., Cavazza, C., Fontecilla-Camps, J. C., and Armstrong, F. A. September 2008 *J. Am. Chem. Soc.* **130(40)**, 13410–13416.
- [19] Yoon, K.-S., Sakai, Y., Tsukada, N., Fujisawa, K., and Nishihara, H. (2009) *FEMS Microbiology Letters* **290(1)**, 114–120.
- [20] Lukey, M., Parkin, A., Roessler, M., Murphy, B., Harmer, J., Palmer, T., Sargent, F., and Armstrong, F. (2010) *J. Biol. Chem.* **285(6)**, 3928–3938.
- [21] Bleijlevens, B., Buhrke, T., van derLinden, E., Friedrich, B., and Albracht, S. (2004) *J. Biol. Chem.* **279**, 46686–46691.
- [22] Buhrke, T., Lenz, O., Krauss, N., and Friedrich, B. June 2005 *J. Biol. Chem.* **280(25)**, 23791–23796.
- [23] Ludwig, M., Cracknell, J., Vincent, K., Armstrong, F., and Lenz, O. (2009) *J. Biol. Chem.* **284(1)**, 465–477.
- [24] Karlin, K. (1993) *Science* **261**, 701–708.
- [25] Pershad, H., Duff, J., Heering, H., Duin, E., Albracht, S., and Armstrong, F. (1999) *Biochemistry* **38(28)**, 8992–8999.
- [26] Jones, A., Sillery, E., Albracht, S., and Armstrong, F. (2002) *Chem. Comm.* **21(8)**, 866–867.
- [27] Manor, B. and Rauchfuss, T. (2013) *J. Am. Chem. Soc.* **135(32)**, 11895 – 11900.
- [28] Simmons, T., Berggren, G., Bacchi, M., and Fontecave, M. Artero, V. (2014) *Coord. Chem. Rev.* **270**, 127 – 150.
- [29] Shafaat, H., Rüdiger, O., Ogata, H., and Lubitz, W. (2013) *Biochim. Biophys. Acta*.
- [30] Fritsch, J., Lenz, O., and Friedrich, B. (2013) *Nat. Rev.* **11**, 106 – 114.
- [31] Lubitz, W., Ogata, H., Rüdiger, O., and Reijerse, E. (2014) *Chem. Rev.* **114(8)**, 4081– 4148.
- [32] Lenz, O., Lauterbach, L., Frielingsdorf, S., and Friedrich, B. Biohydrogen chapter 4, pp. 61–96 De Gruyter (2015).
- [33] Saggi, M., Zebger, I., Ludwig, M., Lenz, O., Friedrich, B., Hildebrandt, P., and Lenzian, F. (2009) *J. Biol. Chem.* **284(24)**, 16264 – 16276.
- [34] Fichtner, C., Laurich, C., Bothe, E., and Lubitz, W. (2006) *Biochemistry* **45(32)**, 9706–9716.
- [35] Wisitruangsakul, N., Lenz, O., Ludwig, M., Friedrich, B., Lenzian, F., Hildebrandt, P., and Zebger, I. (2009) *Angew. Chem. Int. Ed.* **48(3)**, 611–613.

- [36] Germer, F., Zebger, I., Saggiu, M., Lenzian, F., Schulz, R., and Appel, J. (2009) *J. Biol. Chem.* **284**(52), 36462–36472.
- [37] Spiro, T., Czernuszewicz, R., and Han, S. (1988) Biological applications of raman spectroscopy John Wiley & Sons, Inc, New York.
- [38] Ogata, H., Mizoguchi, Y., Mizuno, N., Miki, K., Adachi, S.-i., Yasuoka, N., Yagi, T., Yamauchi, O., Hirota, S., and Higuchi, Y. (2002) *J. Am. Chem. Soc.* **124**(39), 11628–11635.
- [39] Galinato, M., Whaley, C., and Lehnert, N. (2010) *Inorg. Chem.* **49**, 3201–3215.
- [40] Stromberg, C. J., Kohnhorst, C. L., Van Meter, G. A., Rakowski, E. A., Caplins, B. C., Gutowski, T. A., Mehalko, J. L., and Heilweil, E. J. (2011) *Vib. Spectrosc.* **56**(2), 219–227.
- [41] Shafaat, H., Weber, K., Petrenko, T., Neese, F., and Lubitz, W. (2012) *Inorg. Chem.* **51**(21), 11787–97.
- [42] Goldet, G., Brandmayr, C., Stripp, S., Happe, T., Cavazza, C., Fontecilla-Camps, J., and Armstrong, F. (2009) *J. Am. Chem. Soc.* **131**(41), 14979–14989.
- [43] Goris, T., Wait, A. F., Saggiu, M., Fritsch, J., Heidary, N., Stein, M., Zebger, I., Lenzian, F., Armstrong, F. A., Friedrich, B., and Lenz, O. (2011) *Nat. Chem. Biol.* **7**(5), 310–318.
- [44] Fritsch, J., Scheerer, P., Frielingsdorf, S., Kroschinsky, S., Friedrich, B., Lenz, O., and Spahn, C. M. T. (2011) *Nature* **479**, 249 – 252.
- [45] Shomura, Y., Yoon, K.-S., Nishihara, H., and Higuchi, Y. (2011) *Nature* **479**, 253–256.
- [46] Volbeda, A., Amara, P., Darnault, C., Mouesca, J., Parkin, A., Roessler, M., Armstrong, F., and Fontecilla-Camps, J. (2012) *Proc. Natl. Acad. Sci.* **109**(14), 5305–5310.
- [47] Frielingsdorf, S., Fritsch, J., Schmidt, A., Hammer, M., Loewenstein, J., Siebert, E., Pelmenschikov, V., Jaenicke, T., Kalms, J., Rippers, Y., Lenzian, F., Zebger, I., Teutloff, C., Kaupp, M., Bittl, R., Hildebrandt, P., Friedrich, B., Lenz, O., and Scheerer, P. (2014) *Nat. Chem. Biol.* **10**, 378–385.
- [48] Schwartz, E., Fritsch, J., and Friedrich, B. The Prokaryotes chapter H2-Metabolizing Prokaryotes, pp. 119–199 Springer Berlin Heidelberg (2013).
- [49] Vignais, P., Billoud, B., and Meyer, J. (2001) *FEMS Microbiol. Rev.* **25**(4), 455 – 501.
- [50] Vignais, P. and Billoud, B. (2007) *Chem. Rev.* **107**, 4206–4272.
- [51] Tamagnini, P., Axelsson, R., Lindberg, P., Oxelfelt, F., Wuenschiers, R., and Lindblad, P. (2002) *Microbiol. Mol. Biol. Rev.* **66**(1), 1–20.

- [52] Tamagnini, P., Leitao, E., Oliveira, P., Ferreira, D., Pinto, F., Harris, D. J., Heidorn, T., and Lindblad, P. (2007) *FEMS Microbiol. Rev.* **31**, 692–720.
- [53] Thauer, R. K., Kaster, A.-K., Goenrich, M., Schick, M., Hiromoto, T., and Shima, S. (2010) *Annu. Rev. Biochem.* **79**, 507 – 536.
- [54] Fontecilla-Camps, J., Volbeda, A., Cavazza, C., and Nicolet, Y. (2007) *Chem. Rev.* **107**, 4273–4303.
- [55] Fontecilla-Camps, J. C., Amara, P., Cavazza, C., Nicolet, Y., and Volbeda, A. (2009) *Nature* **460**, 814–822.
- [56] Schwoerer, B., Fernandez, V., Zirngibl, C., and Thauer, R. (1993) *Eur. J. Biochem.* **212(1)**, 255–261.
- [57] Shima, S., Pilak, O., Vogt, S., Schick, M., Stagni, M. S., Meyer-Klaucke, W., Warkentin, E., Thauer, R. K., and Ermler, U. (2008) *Science* **321**, 572–575.
- [58] Happe, R., Roseboom, W., Pierik, A., Albracht, S., and Bagley, K. (1997) *Nature* **385**, 126–126.
- [59] Pierik, A., Hulstein, M., Hagen, W., and Albracht, S. (1998) *Eur. J. Biochem.* **258(2)**, 572–578.
- [60] Volbeda, A., Garcin, E., Piras, C., deLacey, A., Fernandez, V., Hatchikian, E., Frey, M., and Fontecilla-Camps, J. (1996) *J. Am. Chem. Soc.* **118(51)**, 12989–12996.
- [61] Stripp, S., Goldet, G., Brandmayr, C., Sanganas, O., Vincent, K., Haumann, M., Armstrong, F., and Happe, T. (2009) *Proc. Nat. Acad. Sci.* **106(41)**, 17331–17336.
- [62] Schwartz, E. and Friedrich, B. The Prokaryotes chapter The H<sub>2</sub>-metabolizing prokaryotes, pp. 496–563 Springer (2006).
- [63] Constant, P., Chowdhury, S., Hesse, L., Pratscher, J., and Conrad, R. (2011) *Appl. Environ. Microbiol.* **77(17)**, 6027–6035.
- [64] Conrad, R. (1996) *Microbiol. Rev.* **60**, 609–640.
- [65] Deckert, G., Warren, P., Gaasterland, T., Young, W., Lenox, A., Graham, D., Overbeek, R., Snead, M., Keller, M., and Aujay, M. (1998) *Nature* **392**, 353–358.
- [66] Sawers, G. (1994) *Antonie Van Leeuwenhoek* **66**, 57–88.
- [67] Pohlmann, A., Fricke, W. F., Reinecke, F., Kusian, B., Liesegang, H., Cramm, R., Eitinger, T., Ewering, C., Potter, M., Schwartz, E., Strittmatter, A., Vosz, I., Gottschalk, G., Steinbuchel, A., Friedrich, B., and Bowien, B. (2006) *Nat. Biotech.* **24(10)**, 1257–1262.

- [68] Lenz, O., Ludwig, M., Schubert, T., Bürstel, I., Ganskow, S., Goris, T., Schwarze, A., and Friedrich, B. (2010) *Chem. Phys. Chem.* **11**, 1107–1119.
- [69] Fontecilla-Camps, J. (1996) *J. Bio. Inorg. Chem.* **1(2)**, 91–98.
- [70] Fichtner, C., vanGastel, M., and Lubitz, W. (2003) *Phys. Chem. Chem. Phys.* **5**, 5507–5513.
- [71] Montet, Y., Amara, P., Volbeda, A., Vernede, X., Hatchikian, E., Field, M., Frey, M., and Fontecilla-Camps, J. (1997) *Nat. Struct. Biol.* **4**, 523–526.
- [72] Surerus, K., Chen, M., van derZwaan, J., Rusnak, F., Kolk, M., Duin, E., Albracht, S., and Muenck, E. (1994) *Biochemistry* **33(16)**, 4980 – 4993.
- [73] Huyett, J., Carepo, M., Pamplona, A., Franco, R., Moura, I., Moura, J., and Hoffman, B. (1997) *J. Am. Chem. Soc.* **119**, 9291–9292.
- [74] Volbeda, A., Charon, M. H., Piras, C., Hatchikian, E. C., Frey, M., and Fontecilla-Camps, J. C. (1995) *Nature* **373**, 580 – 587.
- [75] Bowman, L., Flanagan, L., Fyfe, P., Parkin, A., Hunter, W., and Sargent, F. (2014) *Biochem. J.* **458(3)**, 449–458.
- [76] Seefeldt, L., Hoffman, B., and Dean, D. (2009) *Annu. Rev. Biochem.* **78**, 78, 701–722.
- [77] Peters, J. (1997) *Biochemistry* **36**, 1181–1187.
- [78] Lanzilotta, W., Christiansen, J., Dean, D., and Seefeldt, L. (1998) *Biochemistry* **37**, 11376 – 11384.
- [79] Fritsch, J., Loescher, S., Sanganas, O., Siebert, E., Zebger, I., Stein, M., Ludwig, M., De Lacey, A. L., Dau, H., Friedrich, B., Lenz, O., and Haumann, M. (2011) *Biochemistry* **50(26)**, 5858–5869.
- [80] Lubitz, W., Reijerse, E., and vanGastel, M. (2007) *Chem. Rev.* **107(10)**, 4331–4365.
- [81] deLacey, A., Hatchikian, E., Volbeda, A., Frey, M., Fontecilla-Camps, J., and Fernandez, V. (1997) *J. Am. Chem. Soc.* **119(31)**, 7181–7189.
- [82] Pandelia, M.-E., Ogata, H., Currell, L., Flores, M., and Lubitz, W. (2009) *Biochim. Biophys. Acta* **1797**, 304–313.
- [83] Pandelia, M.-E., Ogata, H., and Lubitz, W. (2010) *Chem. Phys. Chem.* **11(6)**, 1127–1140.
- [84] Pierik, A., Roseboom, W., Happe, R., Bagley, K., and Albracht, S. (1999) *J. Biol. Chem.* **6**, 3331 – 3337.
- [85] Pandelia, M.-E., Fourmond, V., Tron-Infossi, P., Lojou, E., Bertrand, P., Leger,

- C., Giudici-Orticoni, M.-T., and Lubitz, W. (2010) *J. Am. Chem. Soc.* **132**(20), 6991–7004.
- [86] Fernandez, V., Hatchikian, E., and Cammack, R. (1985) *Biochim. Biophys. Acta - Protein Structure and Molecular Enzymology* **832**(1), 69–79.
- [87] Schneider, K., Patil, D., and Cammack, R. (1983) *Biochim. Biophys. Acta - Protein Structure and Molecular Enzymology* **748**(3), 353–361.
- [88] Frielingsdorf, S., Schubert, T., Pohlmann, A., Lenz, O., and Friedrich, B. (2011) *Biochemistry* **50**, 10836–10843.
- [89] Heidary, N. Ir-spectroscopic investigations on the redox behavior of oxygen-tolerant hydrogenases Master's thesis Technische Universitaet Berlin (2012).
- [90] Ogata, H., Hirota, S., Nakahara, A., Komori, H., Shibata, N., Kato, T., Kano, K., and Higuchi, Y. (2005) *Structure* **13**, 1635–1642.
- [91] Volbeda, A., Martin, L., Cavazza, C., Matho, M., Faber, B., Roseboom, W., Albracht, S., Garcin, E., Rousset, M., and Fontecilla-Camps, J. (2005) *J. Bio. Inorg. Chem.* **10**(3), 239–249.
- [92] vanGastel, M., Stein, M., Brecht, M., Schröder, O., Lenzian, F., Bittl, R., Ogata, H., Higuchi, Y., and Lubitz, W. (2006) *J. Bio. Inorg. Chem.* **11**, 41–51.
- [93] Saggu, M., Teutloff, C., Ludwig, M., Brecht, M., Pandelia, M.-E., Lenz, O., Friedrich, B., Lubitz, W., Hildebrandt, W., Lenzian, F., and Bittl, R. (2010) *Phys. Chem. Chem. Phys.* **12**, 2139–2148.
- [94] Ogata, H., Lubitz, W., and Higuchi, Y. (2009) *Dalton Transactions* **37**, 7577–7587.
- [95] Fernandez, V., Hatchikian, E., Patil, D., and Cammack, R. (1986) *Biochim. Biophys. Acta* **883**, 145–154.
- [96] Kurkin, S., George, S., Thorneley, R., and Albracht, S. (2004) *Biochemistry* **43**(21), 6820–6831.
- [97] Kraemer, T., Kampa, M., Lubitz, W., vanGastel, M., and Neese, F. (2013) *Chem. Bio. Chem.* **14**(14), 1898–1905.
- [98] Bagley, K., VanGarderen, C., Chen, M., Woodruff, W., Duin, E., and Albracht, S. (1994) *Biochemistry* **33**(31), 9229–9236.
- [99] Brecht, M., Gastel, v. M., Buhrke, T., Friedrich, B., and Lubitz, W. (2003) *J. Am. Chem. Soc.* **125**, 13075–13083.
- [100] Foerster, S., Stein, M., Brecht, M., Ogata, H., Higuchi, Y., and Lubitz, W. (2003) *J. Am. Chem. Soc.* **125**(1), 83–93.

- [101] Foerster, S., vanGastel, M., Brecht, M., and Lubitz, W. (2005) *J. Bio. Inorg. Chem.* **10(1)**, 51 – 62.
- [102] Stein, M. and Lubitz, W. (2001) *Phys. Chem. Chem. Phys.* **3(23)**, 5115–5120.
- [103] Siebert, E., Horch, M., Rippers, Y., Fritsch, J., Frielingsdorf, S., Lenz, O., Velazquez Escobar, F., Siebert, F., Paasche, L., Kuhlmann, U., Lenzian, F., Mroginski, M.-A., Zebger, I., and Hildebrandt, P. (2013) *Angew. Chem. Int. Ed.* **52(19)**, 5162–5165.
- [104] Ogata, H., Nishikawa, K., and Lubitz, W. (2015) *Nature* **520**, 571 – 574.
- [105] George, S., Kurkin, S., Thorneley, R., and Albracht, S. (2004) *Biochemistry* **43(21)**, 6808 – 6819.
- [106] Roberts, L. M. and Lindahl, P. A. (1995) *J. Am. Chem. Soc.* **117(9)**, 2565–2572.
- [107] van derZwaan, J., Albracht, S., Fontijn, R., and Slater, E. (1985) *FEBS Lett.* **179(2)**, 271 – 277.
- [108] Medina, M., Hatchikian, E., and Cammack, R. (1996) *Biochim. Biophys. Acta - Bioenergetics* **1275(3)**, 227 – 236.
- [109] Dole, F., Medina, M., More, C., Cammack, R., Bertrand, P., and Guigliarelli, B. (1996) *Biochemistry* **35(50)**, 16399–16406.
- [110] Pandelia, M.-E., Infossi, P., Stein, M., Giudici-Ortoni, M.-T., and Lubitz, W. (2012) *Chem. Commun.* **48**, 823–825.
- [111] Weber, K., Kraemer, T., Shafaat, H., Weyhermüller, T., Bill, E., vanGastel, M., Neese, F., and Lubitz, W. (2012) *J. Am. Chem. Soc.* **134(51)**, 20745–20755.
- [112] Kellers, P., Pandelia, M.-E., Currell, L. J., Gorner, H., and Lubitz, W. (2009) *Phys. Chem. Chem. Phys.* **11(39)**, 8680–8683.
- [113] Nakamoto, K. (2009) Infrared and raman spectra of inorganic and coordination compounds In *Applications in Coordination, Organometallic and Bioinorganic Chemistry* John Wiley & Sons, Inc, New York.
- [114] Pandelia, M., Ogata, H., Currell, L., Flores, M., and Lubitz, W. (2009) *J. Bio. Inorg. Chem.* **14**, 1227 – 1241.
- [115] Osuka, H., Shomura, Y., Komori, H., Shibata, N., Nagao, S., Higuchi, Y., and Hirota, S. (2013) *Biochem. Biophys. Res. Commun.* **430**, 284 – 288.
- [116] Ciaccafava, A., Hamon, C., Infossi, P., Marchi, V., Giudici-Ortoni, M.-T., and Lojou, E. (2013) *Phys. Chem. Chem. Phys.* **15**, 16463.
- [117] leGall, J., derVartanian, D., Spilker, E., Lee, J., and Peck, H. (1971) *Biochim. Biophys. Acta - Bioenergetics* **234(3)**, 525–530.

- [118] Nakos, G. and Mortenson, L. (1971) *Biochim. Biophys. Acta - Enzymology* **227(3)**, 576–583.
- [119] leGall, J., Ljungdahl, P., Moura, I., Peck, H., Xavier, A., Moura, J., Teixeira, M., Huynh, B., and derVartanian, D. (1982) *Biochem. Biophys. Res. Commun.* **106(2)**, 610–616.
- [120] Cammack, R., Patil, D., Hatchikian, E., and Fernandez, V. (1987) *Biochim. Biophys. Acta* **912**, 98 – 109.
- [121] Teixeira, M., Moura, I., Xavier, A., Moura, J., leGall, J., derVartanian, D., Peck, H., and IJuyun, B. (1989) *J. Biol. Chem.* **264(28)**, 16435–16450.
- [122] Mouesca, J., Noodleman, L., Case, D., and Lamotte, B. (1995) *J. Am. Chem. Soc.* **34(17)**, 4347–4359.
- [123] Cammack, R., Patil, D., and Fernandez, V. (1985) *Biochem. Soc. Trans.* **13**, 572.
- [124] Pandelia, M., Nitschke, W., Infossi, P., Giudici-Orticoni, M., Bill, E., and Lubitz, W. (2011) *Proc. Nat. Acad. Sci.* **108**, 6097 – 6102.
- [125] Knuettel, K., Schneider, K., Erkens, A., Plass, W., Mueller, A., Bill, E., and Trautwein, A. (1994) *Bull. Pol. Acad. Sci. Chem.* **42**, 495–511.
- [126] Roessler, M., Evans, R., Davies, R., Harmer, J., and Armstrong, F. (2012) *J. Am. Chem. Soc.* **134(37)**, 15581–15594.
- [127] Lukey, M., Roessler, M., Parkin, A., Evans, R., Davies, R., Lenz, O., Friedrich, B., Sargent, F., and Armstrong, F. (2011) *J. Am. Chem. Soc.* **133(42)**, 16881 – 16892.
- [128] Pandelia, M.-E., Lubitz, W., and Nitschke, W. (2012) *Biochim. Biophys. Acta - Bioenergetics* **1817(9)**, 1565–1575.
- [129] Pandelia, M., Bykov, D., Izsak, R., Infossi, P., Giudici-Orticoni, M.-T., Bill, E., Neese, F., and Lubitz, W. (2013) *Proc. Nat. Acad. Sci.* **110(2)**, 483–488.
- [130] Luo, X., Brugna, M., Tron-Infossi, P., Giudici-Orticoni, M., and Lojou, E. (2009) *J. Biol. Inorg. Chem.* **14**, 1275 – 1288.
- [131] Duche, O., Elsen, S., Cournac, L., and Colbeau, A. (2005) *FEBS* **272**, 3899 – 3908.
- [132] Cracknell, J. A., Wait, A. F., Lenz, O., Friedrich, B., and Armstrong, F. A. (2009) *Proc. Nat. Acad. Sci.* **106(49)**, 20681–20686.
- [133] Millo, D., Pandelia, M.-E., Utesch, T., Wisitruangsakul, N., Mroginski, M. A., Lubitz, W., Hildebrandt, P., and Zebger, I. (2009) *J. Phys. Chem. B* **113(46)**, 15344–15351.

- [134] Lamle, S., Albracht, S., and Armstrong, F. (2004) *J. Am. Chem. Soc.* **126**, 14899 – 14909.
- [135] Vincent, K., Cracknell, J., Lenz, O., Zebger, I., Friedrich, B., and Armstrong, F. (2005) *Proc. Nat. Acad. Sci.* **102(47)**, 16951–16954.
- [136] Friedrich, B., Fritsch, J., and Lenz, O. (2011) *Curr. Op. Biotech.* **22**, 358 – 364.
- [137] Lauterbach, L. and Lenz, O. (2013) *J. Am. Chem. Soc.* **135(47)**, 17897–17905.
- [138] Bernhard, M., Benelli, B., Hochkoeppler, A., Zannoni, D., and Friedrich, B. (2004) *Eur. J. Biochem.* **248(1)**, 179–186.
- [139] Evans, R., Parkin, A., Roessler, M., Murphy, B., Adamson, H., Lukey, M., Sargent, F., Volbeda, A., Fontecilla-Camps, J., and Armstrong, F. (2013) *J. Am. Chem. Soc.* **135(7)**, 2694–2707.
- [140] Schaefer, C., Friedrich, B., and Lenz, O. (2013) *Appl. Environ. Microbiol.* **79**, 5137 – 5145.
- [141] Schneider, K. and H.G., S. (1981) *Biochem. J.* **193**, 99 – 107.
- [142] Schneider, K. and H.G., S. (1976) *Biochim. Biophys. Acta.* **452**, 66–80.
- [143] Horch, M., Lauterbach, L., Mroginski, M., Hildebrandt, P., Lenz, O., and Zebger, I. (2015) *J. Am. Chem. Soc.* **137(7)**, 2555 – 2564.
- [144] Bernhard, M., Buhrke, T., Bleijlevens, B., deLacey, A., Fernandez, V., Albracht, S., and Friedrich, B. (2001) *J. Biol. Chem.* **276**, 15592–15597.
- [145] Liebgott, P., Leroux, F., and Burlat, B. (2010) *Nat. Chem. Biol.* **63(6)**, 63 – 70.
- [146] Liebgott, P., deLacey, A., and Burlat, B. (2011) *J. Am. Chem. Soc.* **133**, 986 – 997.
- [147] Abou Hamdan, A., Liebgott, P., and Fourmond, V. (2012) *Proc. Nat. Acad. Sci.* **109**, 19916 – 19921.
- [148] Ewald, P., Pauling, L., Robertson, J., Hume-Rothery, W., Wyckoff, R., Lonsdale, K., and Siegbahn, M. (1962) 50 Years of X-Ray Diffraction, International Union of Crystallography, .
- [149] Geschwind, S. (1972) Electron paramagnetic resonance, Plenum Press, New York.
- [150] Howe, I., Williams, D., and Bowen, R. (1981) Mass spectrometry: principles and applications, McGraw-Hill, New York 2 edition.
- [151] Hildebrandt, P. and Siebert, F. (2008) Vibrational Spectroscopy in Life Science, Tutorial in BiophysicsWiley VCH, .
- [152] Michelson, A. and Morley, E. (1887) *American Journal of Science* **34(203)**, 333 – 345.

- [153] Moss, D., Nabedyrk, E., Breton, J., and Maentele, W. (1990) *Eur. J. Biochem.* **187(3)**, 565–572.
- [154] Harrick, N. (1960) *J. Phys. Chem.* **64(9)**, 1110 – 1114.
- [155] Fahrenfort, J. (1961) *Spectrochim. Acta* **17(7)**, 698 – 709.
- [156] Bruker Optik GmbH Rudolf Planck Str. 27, 76275 Ettlingen HYPERION Benutzerhandbuch 3 auflage edition (2010).
- [157] Long, D. A. (2001) *The Raman Effect: A Unified Treatment of the Theory of Raman Scattering by Molecules*, John Wiley & Sons, Inc, New York, .
- [158] Smekal, A. (1923) *Die Naturwissenschaften* **43**, 873 – 875.
- [159] Raman, C. and Krishnan, K. (1928) *Nature* **121**, 501 – 502.
- [160] Tanaka, M und Young, R. (2006) *J. Mater. Sci.* **41**, 963–991.
- [161] Cohen-Tannoudji, C., Diu, B., and Laloe, F. (1999) *Quantenmechanik 1+2*, Gruyter, .
- [162] Born, M. and Oppenheimer, R. (1927) *Annalen der Physik* **389(20)**, 457–484.
- [163] Loudon, R. (1964) *Advances in Physics* **13(52)**, 423 – 482.
- [164] Roe, R. (1965) *J. Appl. Phys.* **36**, 2024.
- [165] Snyder, R. (1971) *J. Mol. Spectrosc.* **37**, 353 – 365.
- [166] Bower, D. (1972) *J. Pol. Sci.* **10**, 2135 – 2153.
- [167] Bower, D. (1976) *J. Phys. B.* **9**, 3275.
- [168] Porto, S. (1966) *J. Opt. Soc. Am* **56(11)**, 1585 – 1586.
- [169] Wojdyr, M. (2010) *J. Appl. Cryst.* **43**, 1126.
- [170] Winkelnkemper, M. <http://savannah.nongnu.org/projects/specmate>.
- [171] Vincent, K., Cracknell, J., Clark, J., Ludwig, M., Lenz, O., Friedrich, B., and Armstrong, F. (2006) *Chem. Comm.* **28**, 5033 – 5035.
- [172] Ihara, M., Nishihara, H., Yoon, K., Lenz, O., Friedrich, B., Nakamoto, H., Kojima, K., Honma, D., Kamachi, T., and Ichiro, O. (2006) *Photochem. Photobiol.* **82(3)**, 676 – 682.
- [173] Bleijlevens, B., vanBroekhuizen, F. A., De Lacey, A. L., Roseboom, W., Fernandez, V. M., and Albracht, S. P. J. (2004) *J. Bioinorg. Chem.* **9(6)**, 743–752.
- [174] Fritsch, J., Siebert, E., Priebe, J., Zebger, I., Lenzian, F., Teutloff, C., Friedrich, B., and Lenz, O. (2014) *J. Biol. Chem.* **289(11)**, 7982–93.
- [175] Atkins, P. and DePaula, J. (2014) *Atkins Physical Chemistry*, Oxford University Press, .

- [176] Garcin, E., Vernede, X., Hatchikian, E., Volbeda, A., Frey, M., and Fontecilla-Camps, J. (1999) *Structure* **7(5)**, 557 – 566.
- [177] Higuchi, Y., Ogata, H., Miki, K., Yasuoka, N., and Yagi, T. (1999) *Structure* **7(5)**, 549 – 556.
- [178] Fan, C., Teixeira, M., Moura, J., Moura, I., Hanh, H. B., Le Gall, J., Peck, H. D., and Hoffman, B. M. (1991) *J. Am. Chem. Soc.* **113(1)**, 20–24.
- [179] Medina, F., Salagre, P., Sueiras, J.-E., and Fierro, J. (1994) *J. Chem. Soc., Faraday Trans.* **90(10)**, 1455–1459.
- [180] Bruschi, M., Zampella, G., Fantucci, P., and deGioia, L. (2005) *Coord. Chem. Rev.* **249(15)**, 1620 – 1640.
- [181] Stein, M. and Lubitz, W. (2004) *J. Inorg. Biochem.* **98(5)**, 862–877.
- [182] Volbeda, A. and Fontecilla-Camps, J. (2006) Catalytic nickel-iron-sulfur clusters: From minerals to enzymes In Gerard Simonneaux, (ed.), Topics in Organometallic Chemistry, volume **17**, pp. 57–82 Springer Berlin Heidelberg.
- [183] Schmid, F. (2001) *eLS. John Wiley & Sons Ltd, Chichester.*
- [184] Gouterman, M. (1961) *J. Mol.Spectr.* **6**, 138 – 163.
- [185] Scott, R. and Mauk, A. (1996) Cytochrome C: A Multidisciplinary Approach, University Science Books, .
- [186] Gibney, B., Mulholland, S., Rabanal, F., and Dutton, P. (1996) *Proc. Natl. Acad. Scie.* **93(26)**, 15041–15046.
- [187] Kennedy, M. and Gibney, B. (2002) *J. Am. Chem. Soc.* **124**, 6826–6827.
- [188] Austin, R., Erramilli, S., Peticolas, W., Spiro, T., and Czernuszewicz, R. (1995) Biochemical Spectroscopy volume **246**, of Methods in Enzymology Elsevier, .
- [189] personal communication with a. schmidt and j. kalms.
- [190] Horch, M., Schoknecht, J., Mroginski, M., Lenz, O., Hildebrandt, P., and Zebger, I. (2014) *J. Am. Chem. Soc* **136(28)**, 9870 – 9873.
- [191] Rippers, Y., Horch, M., Hildebrandt, P., Zebger, I., and Mroginski, M. A. (2012) *Chem. Phys. Chem.* **13(17)**, 3852–3856.
- [192] Mroginski, M., Mark, F., Thiel, W., and Hildebrandt, P. (2007) *Biophys J.* **93**, 1885–1894.
- [193] Kamali, S., Wang, H., Mitra, D., Ogata, H., Lubitz, W., Manor, B., Rauchfuss, T., Byrne, D., Bonnefoy, V., Jenney, F., Adams, M., Yoda, Y., Alp, E., Zhao, J., and Cramer, S. (2012) *Angew. Chem. Int. Ed.* **52**, 724–728.
- [194] Ciaccafava, A., DePoulpiquet, A., Techer, V., Guidici-Orticoni, M.-T., Tingry, S., Innocent, C., and Lojou, E. (2012) *Electrochem. Commun.* **23**, 25–28.

- [195] Krishnan, S. and Armstrong, F. A. (2012) *Chem. Sci.* **3**(4), 1015–1023.
- [196] Xu, L. and Armstrong, F. (2013) *Energy and Environmental Science* **6**, 2166.
- [197] Grubel, K. and Holland, P. L. (2012) *Angew. Chem. Int. Ed.* **51**(14), 3308–3310.
- [198] Leger, C., Dementin, S., Bertrand, P., Rousset, M., and Guigliarelli, B. (2004) *JACS* **126**(38), 12162–12172.
- [199] Fourmond, V., Infossi, P., Giudici-Orticoni, M.-T., Bertrand, P., and Leger, C. (2010) *J. Am. Chem. Soc.* **132**(13), 4848–4857.
- [200] Cross, M., Xiao, Z., Maes, E. M., Czernuszewicz, R. S., Drew, S. C., Pilbrow, J. R., George, G. N., and Wedd, A. G. (2002) *J. Bio. Inorg. Chem.* **7**, 781–790.
- [201] Sanders-Loehr, J. Resonance Raman Spectroscopy of Iron-Oxo and Iron-Sulfur Clusters in Proteins chapter 3, pp. 49 – 60 ACS Symposium Series; American Chemical Society, Washington DC (1988).
- [202] Spearman, C. (1904) *The American Journal of Psychology* **15**(2), 201–292.
- [203] Kalms, J., Schmidt, A., and Scheerer, P. On the structure of the h229x variants of the mbh in preparation.
- [204] Rippers, Y. n.a. PhD thesis Technische Universitaet Berlin (2015).
- [205] Chakrabarti, M. and Pelhan Lindfield Roberts, E. (2008) *J. Chem. Soc. Pak.* **30**, 817.
- [206] Horio, T. and San Pietro, A. (1964) *Proc. Natl. Acad. Sci.* **51**, 1226 – 1231.
- [207] Balzani, V. and Carassiti, V. (1970) Photochemistry of Coordination Compounds, Academic Press, London, New York, .
- [208] Adar, F. and Yonetani, T. (1978) *Biochim. Biophys. Acta* **502**, 80–86.
- [209] Salmeen, I., Rimai, L., and Babcock, G. (1978) *Biochemistry* **17**, 800 – 806.
- [210] Cartling, B. (1983) *Biophys J.* **43**, 191–205.
- [211] Babcock, G., Ingle, R., Oertling, W., Davis, J., Averill, B., Hulse, C., Stufkens, D., Bolscher, B., and Wever, R. (1985) *Biochim. Biophys. Acta* **828**, 58–66.
- [212] Mino, Z., Loehr, T., Wada, K., Matsubara, H., and Sanders-Loehr, J. (1987) *Biochemistry* **26**, 8059 – 8065.
- [213] Fu, W., Drozdowski, P. M., Davies, M. D., Sligar, S. G., and Johnson, M. K. (1992) *J. Biol. Chem.* **267**(22), 15502–15510.
- [214] Johnson, M. K., Czernuszewicz, R. S., Spiro, T. G., Fee, J. A., and Sweeney, W. V. (1983) *J. Am. Chem. Soc.* **105**(22), 6671–6678.
- [215] Macor, K., Czernuszewicz, R., Adams, M., and Spiro, T. (1987) *J. Biol. Chem.* **262**(21), 9945–9947.

- [216] Wukovitz, S. and Yeates, T. (1995) *Nat. Struc. Biol.* **2**, 1062–1067.
- [217] Hecht, E. (2009) *Optik*, Oldenbourg Wissenschaftsverlag, 5 edition.
- [218] Panicker, C., Varghese, H., and Philip, D. (2006) *Spectrochim. Acta Part A: Mol. Biomol. Spectrosc.* **65**, 802–804.
- [219] Yu, P. and Cardona, M. (2001) *Fundamentals of Semiconductors: Physics and Materials Properties*, Advanced Texts in Physics Springer, 3rd edition.
- [220] Damen, T., Porto, S., and Tell, B. (1966) *Phys. Rev. B* **142**, 570–574.
- [221] Tsuboi, M., Ikeda, T., and Ueda, T. (1991) *J. Raman Spectrosc.* **22(11)**, 619–626.
- [222] Tsuboi, M. and Thomas, G. (1997) *Appl. Spectrosc. Rev.* **32**, 263 – 299.
- [223] Tsuboi, M., Benevides, J. M., Bondre, P., and Thomas, G. J. March 2005 *Biochemistry* **44(12)**, 4861–4869.
- [224] Tsuboi, M., Benevides, J. M., and Thomas, G. J. (2009) *Proc. Jpn. Acad.* **85**, 83 – 97.
- [225] Badger, R. M. (1935) *J. Chem. Phys.* **3**, 710 – 714.
- [226] Okabe, I., Tanaka, H., and Nakanishi, K. (1996) *Phys. Rev. E* **53**, 2638.
- [227] Petrenko, V. and Whitworth, R. (1999) *Physics of Ice*, Oxford University Press, .
- [228] Delvin, J. (2001) *J. Geophys. Res.* **106**, 333 – 349.
- [229] Abe, K. and Shigenari, T. (2011) *J. Phys. Chem.* **134**, 104506.
- [230] Raza, Z., Alfe, D., Salzmann, C., Klimes, J., Michaelides, A., and Slater, B. (2011) *Phys. Chem. Chem. Phys.* **13**, 19788 – 19795.
- [231] Geiger, P., Dellago, C., Macher, M., Franchini, C., Kresse, G., Bernard, J., Stern, J., and Loerting, T. (2014) *J. Phys. Chem.* **118**, 10989 – 10997.
- [232] Bruska, M., Stiebritz, M., and Reiher, M. (2013) *Dalton Trans.* **42**, 8729 – 8735.